TECHNISCHE UNIVERSITÄT MÜNCHEN

Max-Planck-Institut für Physik
(Werner-Heisenberg-Institut)

Calibration of the ATLAS Precision Muon Chambers and Study of the Decay $\tau \to \mu\mu\mu$ at the Large Hadron Collider

Jörg Horst Jochen von Loeben

Vollständiger Abdruck der von der Fakultät für Physik der Technischen Universität München zur Erlangung des akademischen Grades eines

Doktors der Naturwissenschaften (Dr. rer. nat.)

genehmigten Dissertation.

Vorsitzender:	Univ.-Prof. Dr. A. Ibarra
Prüfer der Dissertation:	
1.	Priv.-Doz. Dr. H. Kroha
2.	Jun.-Prof. Dr. L. Fabbietti

Die Dissertation wurde am 22. Juni 2010 bei der Technischen Universität München eingereicht und durch die Fakultät für Physik am 7. Juli 2010 angenommen.

Abstract

The Large Hadron Collider (LHC) is designed to collide protons at centre-of-mass energies of up to 14 TeV. One of the two general purpose experiments at the LHC is ATLAS, built to probe a broad spectrum of physics processes of the Standard Model of particle physics and beyond. ATLAS is equipped with a muon spectrometer comprising three superconducting air-core toroid magnets and 1150 precision drift tube (MDT) chambers measuring muon trajectories with better than 50 μm position resolution. The accuracy of the space-to-drift-time relationships of the MDT chambers is one of the main contributions to the momentum resolution. In this thesis, an improved method for the calibration of the precision drift tube chambers in magnetic fields has been developed and tested using curved muon track segments. An accuracy of the drift distance measurement of better than 20 μm is achieved leading to negligible deterioration of the muon momentum resolution.

The second part of this work is dedicated to the study of the lepton flavour violating decay $\tau \to \mu\mu\mu$. Lepton flavour violation is predicted by almost every extension of the Standard Model. About 10^{12} τ leptons are produced per year at an instantaneous luminosity of $10^{33}\mathrm{cm}^{-2}\mathrm{s}^{-1}$ and a centre-of-mass energy of 14 TeV. Simulated data samples have been used to evaluate the sensitivity of the ATLAS experiment for $\tau \to \mu\mu\mu$ decays with an integrated luminosity of $10\,\mathrm{fb}^{-1}$. Taking theoretical and experimental systematic uncertainties into account an upper limit on the signal branching ratio of $\mathcal{B}(\tau \to \mu\mu\mu) < 5.9 \cdot 10^{-7}$ at 90 % confidence level is achievable. This result represents the first estimation in ATLAS.

Contents

Chapter 1

Introduction

Exciting years are awaiting the research field of particle physics. The Large Hadron Collider (LHC), the most powerful particle accelerator ever constructed, has started its operation at the European Laboratory for Particle Physics (CERN[1]). It is designed to accelerate proton beams up to 7 TeV, allowing for proton-proton collisions with a centre-of-mass energy of 14 TeV. With these collisions, particle physicists from all around the world hope to find the answers to the most fundamental questions about the laws of nature such as the experimental prove of the last undetected particle of the Standard Model of particle physics: the Higgs boson. This discovery is crucial for the validation of the current understanding of matter, as this particle is supposed to give mass to all fundamental particles. Equally interesting questions concern phenomena beyond the Standard Model. The hope is to find hints towards an even more fundamental theory of nature, including for example Supersymmetry which can provide a promising dark matter candidate and elegantly solves the hierarchy problem.
Colliding highly energetic protons is only one part of the exercise, the other one is the meticulous reconstruction of the processes occurring in the collisions. For this purpose, the LHC is equipped with four particle detectors. The largest one is ATLAS[2], a general purpose detector which has been designed to exploit the full range of physics accessible at the LHC. Among its most distinct features is the muon spectrometer in a toroidal magnetic field created by superconducting air-core magnets. Since muons are produced in many interesting physics processes at the LHC, the precision of the momentum measurement of the muon spectrometer plays an important role.
After an introduction of the main properties of the LHC and ATLAS (Chapter 3) a precise method for the calibration of muon drift chambers in magnetic fields is presented in Chapter 4. Especially for muon momenta above about 100 GeV/c, the muon chamber calibration is one of the dominating contributions to the muon spectrometer resolution.
The second part of this work is dedicated to the search for lepton flavour violating decays $\tau \to \mu\mu\mu$. Lepton flavour violation is predicted by almost every extension of the Standard Model, including supersymmetric and so-called *Little Higgs* models. The lepton flavour violating decay rates predicted by these theories are becoming accessible at new colliders like the LHC. Chapter 2 gives an overview about lepton flavour violation in the Standard Model and in selected theories beyond the Standard Model. The LHC will produce about

[1] CERN - Conseil Europeen pour la Recherche Nucleaire.
[2] ATLAS - A Toroidal LHC ApparatuS.

10^{12} τ leptons during one year of stable data-taking, which motivates the study of the ATLAS sensitivity to the neutrinoless decay $\tau \to \mu\mu\mu$ presented in Chapter 5. After discussing the various sources of τ leptons in proton-proton collisions, a possible strategy for this search and the expected upper limit on the branching ratio accessible by ATLAS are discussed.

Chapter 2

Theoretical Background

2.1 The Standard Model of Particle Physics

The Standard Model forms the theoretical basis for the current understanding of the fundamental particles and forces. According to the Standard Model, all matter consists of twelve fundamental fermions with spin 1/2, six quarks and six leptons, which are grouped in three generations, each containing a quark and a lepton doublet. The first generation contains the up (u) and the down (d) quark and the electron (e) with the electron neutrino (ν_e), the second the charm (c) and the strange (s) quark, the muon (μ) and the muon neutrino (ν_μ) and the third the top (t) and the bottom (b) quark, the tau lepton (τ) and the tau neutrino (ν_τ). Charged fermions of the second and third generation are heavier than the fermions of the first generation and unstable. The matter surrounding us on earth is entirely composed of first-generation particles.
Interactions between the fundamental particles are described by the exchange of twelve spin 1 bosons. The electromagnetic interaction is mediated by the massless photon (γ), the weak interaction by the massive Z^0 and $W^\pm$ bosons and the strong interaction by eight massless gluons ($g_1, ..., g_8$). The Standard Model does not include the gravitational force as there is no satisfying quantum theory of gravitation yet. As the gravitational force is very weak compared to the other three forces, it can be neglected in the description of elementary particle physics at current accelerator energies, at least for only three spacial dimension, but plays an important role in cosmology. The fundamental particles and interactions are summarized in Table 2.1.
Besides the twelve bosons mediating the forces, the theory also requires the existence of a scalar particle, the Higgs boson (H), to give rise to the masses of the Z^0 and $W^\pm$ bosons and of the fermions in the so-called *Higgs mechanism* associated with the spontaneous breaking of the electroweak gauge symmetry. The Higgs boson is the only still undiscovered particle of the Standard Model.

Symmetry plays an important role in particle physics. All fundamental interactions of the Standard Model are described by gauge theories with the three symmetry groups

$$SU(3)_C \otimes SU(2)_L \otimes U(1)_Y$$

for the strong interaction (Quantum Chromodymamics) and the unified weak and electromagnetic interactions (Elektroweak Theory). According to Noether's theorem [2], con-

Table 2.1: The twelve matter particles (fermions) of the Standard Model and the four fundamental interactions with the corresponding mediators (gauge bosons). Gravitation is not included in the Standard Model and only listed for comparison. The undiscovered scalar Higgs boson H is not included in the table. Given masses coincide with the Particle Data Group [1].

Matter particles (spin 1/2) (Mass in GeV)				Force mediating particles (spin 1) (Mass in GeV)		
	Generation 1	2	3	Force	Relative strength	Mediator
Leptons	ν_e (~ 0)	ν_μ (~ 0)	ν_τ (~ 0)	Electromagnetic	10^{-2}	γ (0)
Leptons	e (0.0005)	μ (0.1)	τ (1.8)	Strong	1	$g_1, ..., g_8$ (0)
Quarks	u (0.004)	c (1.5)	t (174)	Weak	10^{-13}	$W^\pm, Z^0$ (81), (91)
Quarks	d (0.007)	s (0.15)	b (4.7)	Gravitation	10^{-38}	Graviton (spin 2) (0)

tinuous symmetries of the action in a physical system lead to corresponding conservation laws and hence, to associated conserved quantum numbers in a quantum theory.

2.1.1 Quantum Chromodynamics

Among the fundamental fermions, only the quarks are participating in the strong interaction which is described by the theory of Quantum Chromodynamics (QCD) [3–5]. In analogy to Quantum Electrodynamics (QED), the concept of colour charges was introduced to describe the strong interaction. In contrast to QED, which has only one electric charge and one massless neutral gauge boson, the photon, QCD requires three colour charges (commonly called *red, green, blue*) and eight massless gluons as force-mediating gauge bosons. The gluons carry combinations of colour and anti-colour charges and thus interact with each other themselves via the strong force.
The underlying gauge symmetry group of QCD is $SU(3)_C$. The strong gauge coupling constant α_s is the only free parameter of the theory. The non-abelian nature of $SU(3)_C$ and the resulting self-interaction of the gluons entail important implications of the theory: *asymptotic freedom* of quarks and gluons at short distances and their *confinement* in hadrons.
The strong coupling constant α_s is a function of the energy scale or momentum transfer Q of the process. With increasing energy scale, $\alpha_s(Q^2)$ decreases and vanishes asymptotically for $Q \to \infty$ (asymptotic freedom). In contrast, at low energy scales or large distances between coloured particles, α_s diverges. This behaviour is related to the phenomenon that no free colour carrying particles exist and they are rather confined in hadrons. When colour charges are separated from each other, the energy density eventually becomes large enough that quark-antiquark pairs are created from the vacuum, leading to the so-called *fragmentation* of quarks and gluons into hadrons, the *hadronization*. The observed hadrons are colour neutral (*white*) and can be classified either as quark-antiquark (*meson*) or three-

quark (*baryon*) bound-states.

2.1.2 The Electroweak Theory

The Standard Model is inspired by the local gauge invariant electromagnetic field theory of Quantum Electrodynamics (QED) which is based on the $U(1)_{em}$ symmetry group which leads to the conservation of the electric charge quantum number. In addition, the local gauge invariance also necessitates the introduction of an associated massless vector field, the photon.
The breakthrough in describing the weak interaction was achieved in the 1960's by Glashow [6], Weinberg [7] and Salam [8] by unifying the weak with the electromagnetic interaction in the Electroweak or GWS Theory. This theory is based on the local gauge symmetry group $SU(2)_L \otimes U(1)_Y$, which arranges the fundamental fermions in three generations of left-handed doublets and right-handed singlets of the fundamental $SU(2)_L$ representation. It comprises one $U(1)_Y$ gauge field B_μ and three $SU(2)_L$ or weak isospin gauge fields W_μ^i $(i = 1, 2, 3)$. B_μ couples to both left- and right-handed fermion fields, ψ_L and ψ_R, via the weak hypercharge Y, while the W_μ^i gauge fields only couple to the left-handed components. The left-handed projections of the fermion fields form the weak isospin doublets

$$\psi_{\mathrm{L}} = \begin{pmatrix} \nu_\ell \\ \ell^- \end{pmatrix}_{\mathrm{L}}, \begin{pmatrix} q_u \\ q_d \end{pmatrix}_{\mathrm{L}}, \tag{2.1}$$

with the weak eigenstates $\ell = e, \mu, \tau$, $\nu_\ell = \nu_e, \nu_\mu, \nu_\tau$, $q_u = u, c, t$ and $q_d = d, s, b$. The quark mass eigenstates (q'_u, q'_d) are related to the weak eigenstates (q_u, q_d) via unitary transformations and interact weakly via the Cabbibo-Kobayashi-Maskawa (CKM) mixing matrix:

$$(u', c', t') \cdot \underbrace{\begin{pmatrix} V_{ud} & V_{us} & V_{ub} \\ V_{cd} & V_{cs} & V_{cb} \\ V_{td} & V_{ts} & V_{tb} \end{pmatrix}}_{\text{CKM matrix}} \cdot \begin{pmatrix} d' \\ s' \\ b' \end{pmatrix}. \tag{2.2}$$

The right-handed projections form $SU(2)_L$ singlets:

$$\psi_{\mathrm{R}} = \ell_{\mathrm{R}}, \nu_{\ell\mathrm{R}}, q_{u\mathrm{R}}, q_{d\mathrm{R}}. \tag{2.3}$$

The distinction between left- and right-handed fermion fields corresponds to the maximal parity violation by the weak interaction. The individual fermions are characterized by the quantum numbers J and J_3 of the weak isospin vector $\boldsymbol{J} = (J_1, J_2, J_3)$ and the weak hypercharge Y. The electric charge is given by the Gell-Mann-Nishijima relationship

$$Q = J_3 + \frac{Y}{2}. \tag{2.4}$$

An overview of the fermion multiplets of the electroweak interaction and their quantum numbers is given in Table 2.2.

The gauge invariant Lagrangian of the electroweak theory $\mathcal{L}_{\mathrm{ew}}$ can be written as sum of the gauge field term $\mathcal{L}_{\mathrm{g}}$ and the fermion term $\mathcal{L}_{\mathrm{f}}$ and of two additional terms $\mathcal{L}_{\mathrm{h}}$ and $\mathcal{L}_{\mathrm{y}}$

Table 2.2: Fermion multiplets of the electroweak gauge symmetry with their quantum numbers. Because weak isospin and hypercharge commutate, the third component J_3 of the weak isospin is assigned such that the weak hypercharge is the same within each doublet fulfilling the Gell-Mann-Nishijima relationship.

	Fermion Multiplets			J	J_3	Y	Q
Leptons	$\begin{pmatrix}\nu_e\\e^-\end{pmatrix}_\mathrm{L}$	$\begin{pmatrix}\nu_\mu\\\mu^-\end{pmatrix}_\mathrm{L}$	$\begin{pmatrix}\nu_\tau\\\tau^-\end{pmatrix}_\mathrm{L}$	$1/2$ $1/2$	$1/2$ $-1/2$	-1 -1	0 -1
	e^-_R	μ^-_R	τ^-_R	0	0	-2	-1
Quarks	$\begin{pmatrix}u\\d\end{pmatrix}_\mathrm{L}$	$\begin{pmatrix}c\\s\end{pmatrix}_\mathrm{L}$	$\begin{pmatrix}t\\b\end{pmatrix}_\mathrm{L}$	$1/2$ $1/2$	$1/2$ $-1/2$	$1/3$ $1/3$	$2/3$ $-1/3$
	u_R	c_R	t_R	0	0	$4/3$	$2/3$
	d_R	s_R	b_R	0	0	$-2/3$	$-1/3$

which introduce masses for the weak gauge bosons according to the Higgs mechanism [9] and for the fermions via the Yukawa interactions with the Higgs field, respectively:

$$\mathcal{L}_\mathrm{ew} = \mathcal{L}_\mathrm{g} + \mathcal{L}_\mathrm{f} + \mathcal{L}_\mathrm{h} + \mathcal{L}_\mathrm{y}, \tag{2.5}$$

which will be described in the following.

Gauge Field Term $\mathcal{L}_\mathrm{g}$

The gauge field term of the electroweak Lagrangian reads

$$\mathcal{L}_\mathrm{g} = -\frac{1}{4}W^i_{\mu\nu}W_i^{\mu\nu} - \frac{1}{4}B_{\mu\nu}B^{\mu\nu} \tag{2.6}$$

With the field-strengths defined by

$$W^i_{\mu\nu} = \partial_\mu W^i_\nu - \partial_\nu W^i_\mu + g\epsilon^{ijk}W^j_\mu W^k_\nu, \tag{2.7}$$

$$B^i_{\mu\nu} = \partial_\mu B_\nu - \partial_\nu B_\mu, \tag{2.8}$$

where g is the weak $SU(2)_L$ gauge coupling constant, ϵ^{ijk} the totally antisymmetric pseudotensor, W^i_μ $(i = 1, 2, 3)$ the vector field triplet required by the local $SU(2)_L$ gauge symmetry and B_μ the vector gauge field of the $U(1)_Y$ gauge theory corresponding to the weak hypercharge Y.
Linear combinations of the four gauge fields B_μ and W^i_μ lead to the observable gauge bosons γ, Z^0 and $W^\pm$:

$$\begin{pmatrix}A_\mu\\Z_\mu\end{pmatrix} = \begin{pmatrix}\cos\theta_W & \sin\theta_W\\-\sin\theta_W & \cos\theta_W\end{pmatrix}\begin{pmatrix}B_\mu\\W^3_\mu\end{pmatrix}, \tag{2.9}$$

$$W^\pm_\mu = \frac{1}{\sqrt{2}}\left(W^1_\mu \pm iW^2_\mu\right), \tag{2.10}$$

with the weak mixing or Weinberg angle θ_W determined by the $SU(2)_L$ and $U(1)_Y$ coupling constants g and g' according to

$$\cos\theta_W = \frac{g}{\sqrt{g^2 + g'^2}}. \tag{2.11}$$

Fermion Term $\mathcal{L}_\mathrm{f}$

Interactions between fermions and the gauge fields are described by the Lagrangian

$$\mathcal{L}_\mathrm{f} = i\bar{\psi}_\mathrm{L}\gamma^\mu D_\mu \psi_\mathrm{L} + i\bar{\psi}_\mathrm{R}\gamma^\mu D_\mu \psi_\mathrm{R} \tag{2.12}$$

where γ^μ are the Dirac matrices and D_μ the covariant derivatives which ensure the local gauge invariance of the theory:

$$D_\mu = \partial_\mu + igJ_i W_\mu^i + ig' Y B_\mu. \tag{2.13}$$

For the left-handed fermion fields applies

$$D_\mu \psi_\mathrm{R} = \left(\partial_\mu + ig\frac{\sigma_i}{2}W_\mu^i + ig'\frac{Y}{2}B_\mu\right)\psi_\mathrm{L}, \tag{2.14}$$

where σ_i denote the Pauli-matrices, while for the right-handed fermions the covariant derivative is given by

$$D_\mu \psi_\mathrm{R} = \left(\partial_\mu + ig'\frac{Y}{2}B_\mu\right)\psi_\mathrm{R}. \tag{2.15}$$

Up to this point, all weakly interacting matter and force mediating particles are included in the theory. However, it has the severe problem that the theory contains no mass terms, which are forbidden by the electroweak gauge symmetry, in contradiction to the observations.

Higgs Term $\mathcal{L}_\mathrm{h}$

A possible solution is the so-called Higgs mechanism which allows for massive gauge bosons without violating the local electroweak gauge symmetry of the Lagrangian $\mathcal{L}_\mathrm{ew}$ by introducing a new complex scalar field

$$\phi = \begin{pmatrix}\phi^+ \\ \phi^0\end{pmatrix} \tag{2.16}$$

with hypercharge $Y = 1$ which couples to the electroweak gauge bosons and has a non-vanishing vacuum expectation value. It is described by the Lagrangian

$$\mathcal{L}_\mathrm{h} = (D_\mu\phi)^\dagger(D^\mu\phi) - V(\phi) \tag{2.17}$$

where D_μ is the covariant derivative introduced in Equation (2.13) and $V(\phi)$ the self-interaction potential of the scalar field

$$V(\phi) = \mu^2\phi^\dagger\phi + \lambda(\phi^\dagger\phi)^2, \tag{2.18}$$

where μ and λ are free parameters. For $\mu^2 < 0$, the ground state ϕ_0 (vacuum) is infinitely degenerated under the electroweak gauge transformations with vacuum expectation value $|\phi_0| =: v/\sqrt{2}$ different from zero with

$$v = \sqrt{\frac{-\mu^2}{\lambda}}. \tag{2.19}$$

By selecting one ground state of the scalar field the electroweak gauge symmetry is spontaneously broken. Three of the four components of the Higgs doublet become the longitudinal polarization components of the electroweak vector bosons, which then become massive. Only one component of the Higgs doublet remains and manifests itself as a massive neutral scalar, the Higgs boson H. The masses of the physical weak vector bosons are given by the gauge couplings g and g' and the vacuum expectation value of the Higgs field,

$$M_W = \frac{1}{2}gv, \quad M_Z = \frac{1}{2}\sqrt{g^2 + g'^2}\ v. \tag{2.20}$$

Thus, the ratio of the masses of the Z^0 and $W^\pm$ bosons is related to the electroweak coupling constants alone, independent of the Higgs potential:

$$\frac{M_W}{M_Z} = \frac{g}{\sqrt{g^2 + g'^2}} = \cos\theta_W. \tag{2.21}$$

The mass of the Higgs boson is given by

$$m_H = \sqrt{-2\mu^2}. \tag{2.22}$$

Yukawa Term $\mathcal{L}_\mathrm{y}$

Fermion masses are generated by Yukawa couplings of the fermion spinor fields to the scalar field ϕ. For instance, for the first generation of leptons the corresponding Yukawa term is:

$$\mathcal{L}_\mathrm{y} = -g_e \left[(\bar{\nu}_e, \bar{e})_\mathrm{L} \phi e_\mathrm{R} + \bar{e}_\mathrm{R} \phi^\dagger \begin{pmatrix} \nu_e \\ e \end{pmatrix}_\mathrm{L} \right] \tag{2.23}$$

which becomes after spontaneous symmetry breaking in the unitary gauge

$$\mathcal{L}_\mathrm{y} = -m_e \bar{e}e - \frac{g_e}{\sqrt{2}} \bar{e}eH \tag{2.24}$$

with g_e denoting the Yukawa coupling constant of electrons and $m_e = {}^{g_e v}/\sqrt{2}$. In general, the masses of the fermions f are given by

$$m_f = \frac{g_f v}{\sqrt{2}}. \tag{2.25}$$

2.1.3 Physics Beyond the Standard Model

The Standard Model of particle physics is very successful in describing experimental data at the highest precision. However, an extension of the model seems to be unavoidable due to several limitations, among which:

- The fourth known interaction, the gravitation, is not included in the theory.
- According to the current state of knowledge, only about 5 % of the mass in the universe is described by the fermions of the Standard Model while 23 % consist of so-called dark matter and 72 % of dark energy not included in the Standard Model.

- Radiative corrections quadratically diverging with the energy scale drive the Higgs boson mass to the largest possible scale, eventually the Planck scale of 10^{19} GeV. However, the electroweak precision measurements indicate a Higgs boson mass near the electroweak scale (∼100 GeV) [10]. Thus the quadratic divergence has to be compensated with unnaturally high accuracy, referred as *fine tuning*, to keep m_H at the electroweak scale.

So far no experimental evidence for physics beyond the Standard Model has been found, but further insight is expected from measurements by the LHC experiments.

2.2 Lepton Flavour Violation in the Standard Model

Besides the conserved charge quantum numbers of the gauge interactions—colour charge, weak isospin and weak hypercharge—additional conserved quantities and corresponding symmetries exist in the Standard Model. Lepton number conservation was proposed by Konopinski and Mahmoud [11] to explain why certain processes are allowed and others seem to be forbidden. The value $L = +1$ is assigned to every lepton and $L = -1$ to the antileptons. All other particles are assigned to the lepton number $L = 0$. The lepton number is an additive quantum number, its sum is conserved in particle interactions in the Standard Model. An example is the beta decay with:

$$\begin{aligned} & n \to p^+ + e^- + \bar{\nu}_e \\ L: \quad & 0 = 0 + 1 - 1 \end{aligned} \tag{2.26}$$

The conservation of the lepton number alone is not sufficient to explain why for example the decay

$$\begin{aligned} & \mu \to e^- + \gamma \\ L: \quad & 1 = 1 + 0 \end{aligned} \tag{2.27}$$

has never been observed. Hence, it is required to conserve the lepton numbers L_e, L_μ and L_τ for each generation separately, as for example in the decay of the muon:

$$\begin{aligned} & \mu \to e^- + \bar{\nu}_e + \nu_\mu \\ L: \quad & 1 = 1 - 1 + 1 \\ L_e: \quad & 0 = 1 - 1 + 0 \\ L_\mu: \quad & 1 = 0 + 0 + 1 \end{aligned} \tag{2.28}$$

Since the discovery of neutrino flavour oscillations it is known that the conservation of the lepton family number is not strict. A number of radio-chemical experiments including Homestake [12], GALLEX [13], GNO [14], and SAGE [15] and the real-time water Cherenkov experiments Kamiokande, Super-Kamiokande [16], and the Sudbury Neutrino Observatory [17] could prove a deficit in the flux of solar electron neutrinos while the total flux of neutrinos from the sun is consistent [17] with the expectations from the solar models. This can only be explained by solar neutrino oscillations. Other experiments, in particular the (Super-) Kamiokande experiment [18] discovered oscillations with atmospheric muon neutrinos produced in cosmic ray induced air showers, the KamLAND [19] experiment with muon neutrinos produced in nuclear reactors, and experiments like K2K [20], MINOS [21]

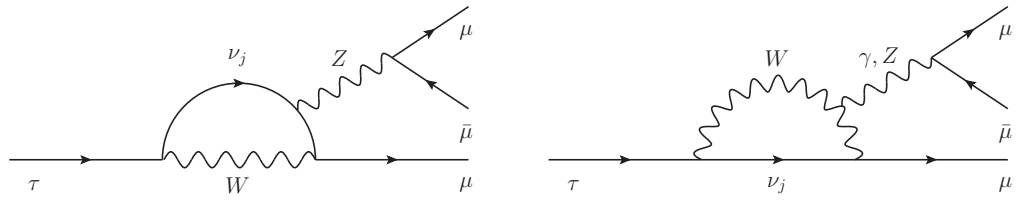

Figure 2.1: Feynman diagrams contributing to the lepton flavour violating decay $\tau \to \mu\mu\mu$ in the Standard Model with massive neutrinos which are able to change flavour periodically allowing changing neutral currents at a very low rate.

and OPERA [22] study neutrino oscillations in muon beams created by accelerators.
The discovery of the oscillating behaviour of the neutrino flavours has enormous consequences for the description of leptons in the Standard Model. It violates lepton family number or lepton flavour conservation, the neutrinos acquire masses and neutrino flavours mix in analogy to the CKM mixing of the quarks. The neutrino mass eigenstates ν_j $(j = 1, 2, 3)$ differ from the flavour eigenstates ν_ℓ $(\ell = e, \mu, \tau)$. Both are related by the unitary Pontecorvo-Maki-Nakagawa-Sakata (PMNS) mixing matrix:

$$\begin{pmatrix} \nu_e \\ \nu_\mu \\ \nu_\tau \end{pmatrix} = \underbrace{\begin{pmatrix} U_{e1} & U_{e2} & U_{e3} \\ U_{\mu 1} & U_{\mu 2} & U_{\mu 3} \\ U_{\tau 1} & U_{\tau 2} & U_{\tau 3} \end{pmatrix}}_{:= \text{PMNS matrix}} \cdot \begin{pmatrix} \nu_1 \\ \nu_2 \\ \nu_3 \end{pmatrix} \tag{2.29}$$

The mixing of the neutrinos also gives rise to flavour violation for the charged leptons. However, due to the unitarity of the mixing matrix, the tree level lepton decay is suppressed by the lepton sector analogue to the Glashow-Iliopoulos-Maiani (GIM) mechanism [23] and only allowed via higher order loop processes. Figure 2.1 shows two examples of Standard Model loop processes contributing to the lepton flavour violating decay $\tau \to \mu\mu\mu$. According to [24], the processes in Figure 2.1(a) dominate with a decay rate $\propto \log(m^2_{\nu_j}/m^2_W)$ while other contributions (see for example Figure 2.1(b)) are suppressed $\propto m^2_{\nu_j}/m^2_W$. This leads to a branching fraction of:

$$\mathcal{B}(\tau \to \mu\mu\mu) \geq 10^{-14},$$

depending on the neutrino mixing angles and mass differences. The $\tau \to \mu\mu\mu$ decay rate in the Standard Model is very small and beyond the sensitivity of current experiments. The observation of such a lepton flavour violating τ decay would thus be an unambiguous sign of new physics beyond the Standard Model.

2.3 Lepton Flavour Violation in Theories Beyond the Standard Model

There is a large number of theories beyond the Standard Model in which the rate of lepton flavour violating decays is significantly increased due to new particles and interactions. Mass-dependent couplings favour lepton flavour violation in the third generation. In general, the radiative decay $\tau \to \ell\gamma$ is more likely than the neutrinoless τ decay into three

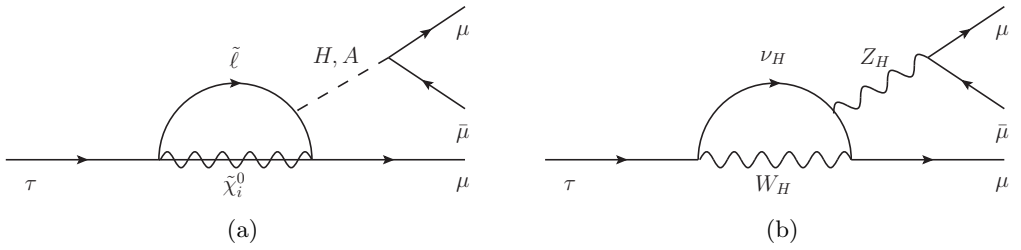

Figure 2.2: Two examples of Feynman diagrams of the lepton flavour violating decay $\tau \to \mu\mu\mu$ in (a) the Minimal Supersymmetric extension of the Standard Model and (b) in the Littlest Higgs Model.

leptons mediated by γ since the additional $\gamma\ell\ell$-vertex leads to a suppression of the decay rate proportional to the fine-structure constant α. However, if the decay is mediated by a new heavy particle, then also $\tau \to \ell\ell\ell$ can be favoured. The extensions of the Standard Model can be separated in two main classes: theories where charged-lepton flavour changing decays are still forbidden at tree level and theories where the tree level decays are allowed.

2.3.1 Models with Tree Level Suppressed Charged-Lepton Flavour Violation

The first category encompasses extensions of the Standard Model in which charged-lepton flavour violation is still suppressed at the tree level. But new particles can enter at the loop level replacing, for example, ν_j and γ, Z in Figure 2.1 and increasing the decay rate and branching ratio. Two examples of this class are the Minimal Supersymmetric extension of the Standard Model (MSSM) with massive neutrinos and the Littlest Higgs Model with $\mathcal{T}$-parity conservation.

Supersymmetry (SUSY)

Supersymmetry is a symmetry between fermions and bosons added to the Standard Model. This symmetry implies the existence of so-called superpartners for each particle of the Standard Model. Since the superpartners have not been observed so far, supersymmetry has to be broken in order to allow for superparticles much heavier than their corresponding Standard Model partners. A detailed introduction to Supersymmetry can be found, for example, in [25]. In the MSSM, two Higgs doublets have to be introduced to give masses to up- and down-type fermions which lead, after the spontaneous electroweak symmetry breaking, to five physical Higgs bosons, two charged ($H^{\pm}$) and three neutral ones (h, H, A). The superpartners of the Z boson (zino), the photon (photino) and the two neutral Higgs bosons (higgsinos) mix, resulting in four neutralinos ($\tilde{\chi}_1^0, \tilde{\chi}_2^0, \tilde{\chi}_3^0, \tilde{\chi}_4^0$) as mass eigenstates. The superpartners of the charged leptons ℓ are the sleptons $\tilde{\ell}$ and the superpartners of the quarks q are denoted squarks $\tilde{q}$. Dependent on the model parameters, charged-lepton flavour violation can be mediated by the neutral Higgs bosons, neutralinos and sleptons shown as example in Figure 2.2(a). Also the superpartners of the neutrinos (sneutrinos) and charginos ($\tilde{\chi}_1^{\pm}, \tilde{\chi}_2^{\pm}$), mixing of superpartners of $W^{\pm}$ (winos) and the two charged Higgs bosons (charged higgsinos), can contribute to the loop processes.

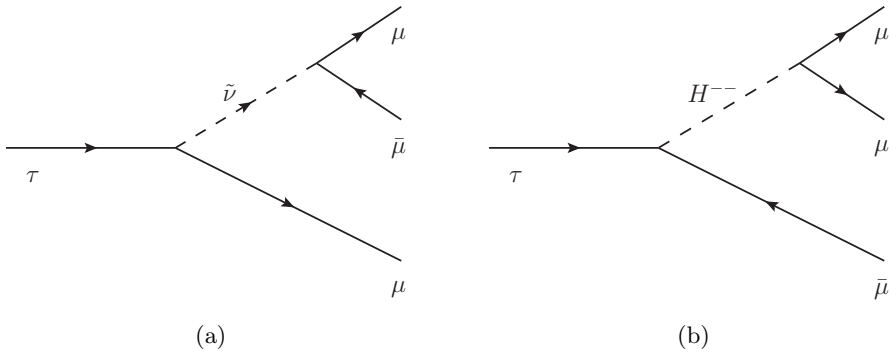

Figure 2.3: Two examples of tree level $\tau \to 3\mu$ decays in (a) supersymmetric models with $\mathcal{R}$-parity violation and (b) models with doubly charged Higgs bosons.

A prediction of the branching ratio of the $\tau \to \mu\mu\mu$ decay for specific assumptions on the model parameters is [26, 27]:

$$\mathcal{B}(\tau \to \mu\mu\mu) \lesssim 10^{-9}.$$

Littlest Higgs Model

The Littlest Higgs model is an alternative approach to generate electroweak symmetry breaking [28]. The theory predicts new mirror particles, for example $\nu \leftrightarrow \nu_{\mathrm{H}}$, $Z \leftrightarrow Z_{\mathrm{H}}$ and $W \leftrightarrow W_{\mathrm{H}}$, at the TeV scale. To avoid problems with electroweak precision measurements, a discrete $\mathcal{T}$-parity is introduced which allows only for pair production of the new particles (similar to the $\mathcal{R}$-parity of supersymmetric models, see below). An example of a Feynman diagram contributing to the $\tau \to \mu\mu\mu$ decay is shown in Figure 2.2(b). Also for this model, the prediction of the branching ratio depends strongly on the model parameters and can reach up to [29, 30]:

$$\mathcal{B}(\tau \to \mu\mu\mu) \lesssim 10^{-8}.$$

2.3.2 Models with Tree Level Charged-Lepton Flavour Violation

In the second category of extensions of the Standard Model, also tree level lepton flavour violating decays are allowed leading to larger branching ratios for instance for the τ lepton decays into three muons via the exchange of new heavy particles.

Supersymmetry with $\mathcal{R}$-Parity Violation

Conservation of the $\mathcal{R}$-parity has been introduced in supersymmetric theories to suppress lepton and baryon number violation which lead to the decay of the proton. In addition it guarantees that the lightest supersymmetric particle is stable and thus provides an excellent candidate for dark matter. Supersymmetric models with $\mathcal{R}$-parity violation are still possible within present experimental bounds on the proton lifetime and allow, for instance, for couplings between the sneutrino ($\tilde{\nu}$) and the charged Standard Model leptons (see Figure 2.3(a)) generating lepton flavour violation in the charged-lepton sector [31].

Models with Doubly Charged Higgs Bosons

Double charged Higgs Bosons ($H^{\pm\pm}$) can give rise to lepton flavour violation including the decay $\tau \to \mu\mu\mu$ through processes as shown in Figure 2.3(b). The resulting branching ratios are on the order of [32]:

$$\mathcal{B}(\tau \to 3\mu) \lesssim 10^{-7}.$$

This work concentrates on the lepton flavour violating decay $\tau \to \mu\mu\mu$ as muons provide a cleaner signature in the detector than electrons and the radiative decays $\tau \to \ell\gamma$. The latter is expected to be very difficult to distinguish from the huge background of hadron decays and bremsstrahlung photons.

Chapter 3

The Large Hadron Collider and the ATLAS Experiment

The Large Hadron Collider (LHC) [33] and the ATLAS experiment [34] were approved by the CERN council in December 1994. 15 years later, the first proton beams have been brought to collision on 23rd November 2009. The new particle accelerator will extend the accessible energy range with proton-proton collisions up to a centre-of-mass energy of $\sqrt{s} = 14\,\text{TeV}$ while reaching very high luminosities. ATLAS is one of the two general-purpose detectors at the LHC. CMS is the other one while ALICE and LHCb are dedicated to studies of heavy ion collisions and B meson physics, respectively. In this thesis simulations of the ATLAS detector performance are used to test a newly developed calibration algorithm for the precision muon drift chambers and to study the sensitivity on the decay $\tau \to \mu\mu\mu$. In the following, the LHC and ATLAS are introduced.

3.1 The Large Hadron Collider

The Large Hadron Collider at CERN near Geneva, Switzerland, is the highest-energy proton-proton and heavy ion collider equipped with superconducting dipole magnets. It is installed in an underground tunnel of 26.7 km circumference, at depths between 45 and 170 m (see Figure 3.1). The processes of main interest for the LHC experiments are rare compared to the backgrounds of Standard Model reactions. For instance, the expected cross section for the production of a light Higgs boson is only on the order 10 pb—thus only 1 out of 10^{11} proton-proton collisions contains a Higgs boson. Hence the challenge for the LHC is to provide an as high as possible event rate for the experiments. This rate is given by:

$$\frac{dN}{dt} = \mathscr{L} \cdot \sigma(\sqrt{s})$$

where σ is the cross section of the process studied depending on the centre-of-mass energy $\sqrt{s}$ and $\mathscr{L}$ is the instantaneous luminosity which depends on the beam parameters according to

$$\mathscr{L} = \frac{N_b^2 n_b f}{A},$$

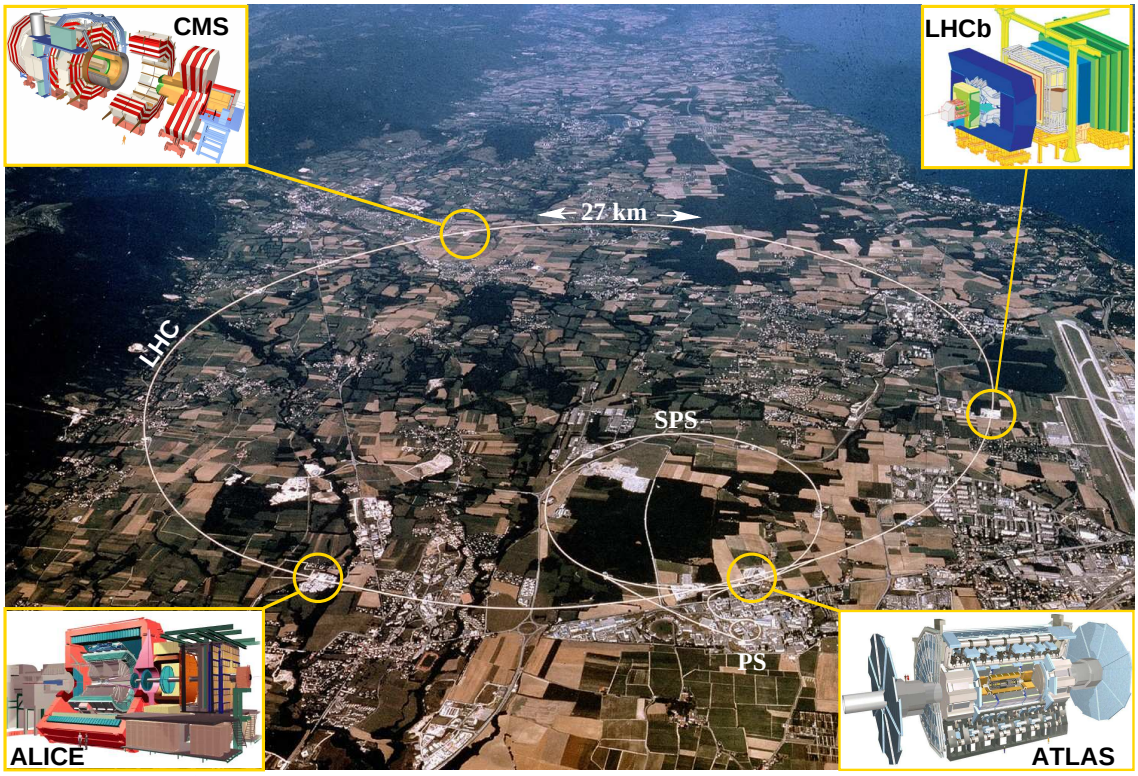

Figure 3.1: Aerial view of the region around CERN. The locations of the LHC ring and the previous accelerators SPS and PS used for injecting protons into the LHC are indicated, as well as the locations of the four experiments ALICE, CMS, LHCb and ATLAS.

where f is the revolution frequency, n_b the number of proton bunches per beam in the storage ring, N_b the number of particles in each bunch and A the cross section of the beams. The most important beam parameters for the peak luminosity of $\mathscr{L} = 10^{34}$ cm^{-2}s^{-1} for which the LHC is designed are listed in Table 3.1.
In the first years, the LHC will run at lower energies and lower instantaneous luminosities to fully understand the accelerator and the experiments. After the incident during the commissioning phase in September 2008 the LHC program officially restarted on the 20th November 2009. After first collisions at $\sqrt{s} = 900\,\text{GeV}$ in 2009, a two year period of operation at a centre-of-mass energy of $\sqrt{s} = 7\,\text{TeV}$ takes place in 2010 and 2011 to be followed by a one year long shut-down to install additional safety and quench protection systems and to train the superconducting magnets for highest currents. This is necessary to ensure safe operation of the LHC up to the design beam energy.
The high interaction rates leads to a challenging environment for the experiments with very high radiation doses and particle multiplicities. Two of the four LHC experiments

- ATLAS (A Toroidal LHC ApparatuS) [34] and
- CMS (Compact Muon Solenoid) [35]

are general-purpose detectors designed to fully exploit the LHC physics potential up to highest luminosity of $\mathscr{L} = 10^{34}$ cm^{-2}s^{-1}. The other two have specialized physics programs at lower instantaneous luminosities:

- ALICE (A Large Ion Collider Experiment) is designed to study the creation of quark gluon plasma in highly energetic heavy ion collisions at a luminosity of $\mathscr{L} = 10^{27}$ cm^{-2}s^{-1} [36].
- LHCb (Large Hadron Collider beauty) is devoted to the study of beauty physics at a luminosity of $\mathscr{L} = 10^{32}$ cm^{-2}s^{-1} [37].

Table 3.1: LHC beam parameters for the peak luminosity of $\mathscr{L} = 10^{34}\,\text{cm}^{-2}\text{s}^{-1}$ [33].

	Unit	Injection	Collision
Number of particles / bunch	–	$1.15 \cdot 10^{11}$	
Number of bunches / beam	–	2808	
Circulating beam current	(A)	0.582	
Proton Energy	(GeV)	450	7000
RMS transverse beam size	(μm)	375.2	16.7
Stored beam energy	(MJ)	23.3	362
Bunch crossing frequency	(MHz)	–	40

3.2 The ATLAS Experiment

This section gives an overview of the different detector technologies used in the ATLAS experiment and of their expected performance and introduces the most important physics goals.

3.2.1 Physics Goals and Detector Performance

The LHC provides a rich physics program, ranging from the measurement of Standard Model processes with high precision to a large variety of new physics searches. The most important studies are summarized below which serve to define the requirements for the ATLAS detector system.

Tests of the Standard Model The high luminosity and increased cross sections at the LHC compared to previous colliders[1], enable precision measurements of QCD and electroweak processes, and of flavour physics. The top-quark will be produced at a rate of about 10 Hz at the peak luminosity providing the opportunity to test its couplings and spin.

Search for the Standard Model Higgs Boson This search is the main motivation for the LHC experiments and is a benchmark for the performance requirements of the ATLAS detector systems. Depending on the production and decay mode, the detection of the Higgs boson requires efficient identification and accurate energy and momentum measurement of electrons and muons. In addition, a hermetic detector for precise missing energy determination and the identification of b- and τ-jets is needed.

[1] For instance, the Tevatron at the Fermilab close to Chicago, the highest energy hadron collider before the LHC, achieves a peak luminosity of $3 \times 10^{32}\,\text{cm}^{-2}\text{s}^{-1}$ with proton-anti-proton collisions at $\sqrt{s} = 1.96\,\text{TeV}$.

Discovery of Supersymmetric Particles In most models studied, the supersymmetric particles produced decay in cascades to Standard Model particles and the stable lightest supersymmetric particle (LSP). The typical signature therefore is large missing transverse energy due to the weakly interacting LSP together with several jets and, frequently, leptons.

Other New Physics Searches The LHC opens up a new energy range where searches for any kind of new particles and physics processes can be performed. Theories beyond the Standard Model predict for instance new heavy gauge bosons Z' and W' which are accessible up to masses of about 6 TeV. Searches for flavour changing neutral currents and lepton flavour violation through $\tau \to \mu\gamma$ or $\tau \to \mu\mu\mu$ as well as measurements of rare B decays like $B_s^0 \to \mu\mu$ may open a window to new physics.

All processes mentioned above have small cross sections or decay rates which is the reason for the high design luminosity of the LHC. For the experiments this implies serious difficulties as the inelastic proton-proton cross section is about 80 mb. Hence the LHC will produce a total rate of up to 10^9 events per second with a bunch-crossing frequency of 40 MHz at the peak luminosity. This implies that every hard collision event will on average be accompanied by 23 inelastic interactions, an effect called *pile-up*. This leads to the following requirements to the detector:

- Fast, radiation-hard electronics and detector elements.
- High detector granularity is needed to cope with the high particle fluxes and to reduce the influence of pile-up events.
- Hermetic detector coverage around the interaction point up to the very forward regions in order to measure the decay products and the energy released in the collisions as completely as possible.
- High charged-particle energy and momentum resolution and reconstruction efficiency in particular for electrons and muons over a wide energy range from few GeV to about 1 TeV.
- High tracking accuracy close to the interaction region to assign particles to the primary hard scattering process, to select the decay products of unstable particles like B mesons or τ leptons and to identify pile-up events.
- Highly efficient trigger on electron, muon and jet signatures down to low momenta with sufficient suppression of the background.

3.2.2 The ATLAS Detector

This section provides an overview of the magnet system, the detector technologies and the trigger system of the experiment. The overall layout of the ATLAS detector is shown in Figure 3.2 with its main performance characteristics listed in Table 3.2. The detector is forward backward symmetric with respect to the interaction point. Like most of the general purpose particle detectors at colliders, it consists of three main measurement layers: closest to the collision region is the inner tracking detector, followed by the calorimeters and finally the muon spectrometer as outermost layer.

Table 3.2: General performance characteristics of the ATLAS detector [34]. The units of E and p_{T} are GeV and GeV/c. The pseudorapidity (η) covered by the sub-detectors are given for the particle measurement and, if applicable, in parentheses for the trigger.

Sub-detector	Resolution	$\lvert\eta\rvert-$range
Inner Tracker	$\sigma_{p_{\mathrm{T}}}/p_{\mathrm{T}} = 0.05\,\%/p_{\mathrm{T}} \oplus 1\,\%$	< 2.5
EM calorimetry	$\sigma_E/E = 10\,\%/\sqrt{E} \oplus 0.7\%$	< 3.2 (< 2.5)
Hadronic calorimetry		
barrel and end cap	$\sigma_E/E = 50\,\%/\sqrt{E} \oplus 3\,\%$	< 3.2 (< 3.2)
forward	$\sigma_E/E = 100\,\%/\sqrt{E} \oplus 10\,\%$	$3.1 - 4.1$ ($3.1 - 4.1$)
Muon Spectrometer	$\sigma_{p_{\mathrm{T}}}/p_{\mathrm{T}} = 10\,\%$ at $p_{\mathrm{T}} = 1\,\mathrm{TeV}$	< 2.7 (< 2.4)

The ATLAS Coordinate System

The right-handed ATLAS coordinate system is defined as follows:

- The origin at the nominal interaction point at the of the detector.
- The positive x-direction points towards the center of the LHC ring.
- The positive y-direction points upwards.
- The z-direction is oriented in direction of the beam line.

The azimuthal and polar angles are denoted by ϕ and θ. A commonly used variable in collider experiments is the Lorentz invariant pseudorapidity η:

$$\eta := -\ln\tan\left(\frac{\theta}{2}\right).$$

Distances in the $\eta - \phi$ space,

$$\Delta R := \sqrt{\Delta\eta^2 + \Delta\phi^2},$$

define opening angles between particles produced at the interaction point. Important variables are defined in the x-y plane transverse to the beam: The transverse momentum p_{T}, the transverse energy E_{T} and the missing transverse energy $E_{\mathrm{T}}^{\mathrm{miss}}$. These variables are Lorentz invariant under boosts along the z-direction which is important for hadron collider experiments as the collision products are usually boosted in beam direction. The transverse momenta and energies of all particles analysed in the detector should also add up to zero while energy is always lost in the longitudinal directions in the beam pipe.

3.2.3 The Magnet System

Special for the ATLAS detector is its superconducting magnet system consisting of a solenoidal field for the inner detector and a toroidal magnetic field in the muon spectrometer. The layout of the system is shown in Figure 3.3. The central solenoid [38] surrounds the inner tracking detector and provides it with a homogeneous magnetic field of up to 2 T parallel to the beam line. To minimize the radiation lengths of material in front of the calorimeters, the coil is only 10 cm thin and shares the vacuum vessel with the barrel

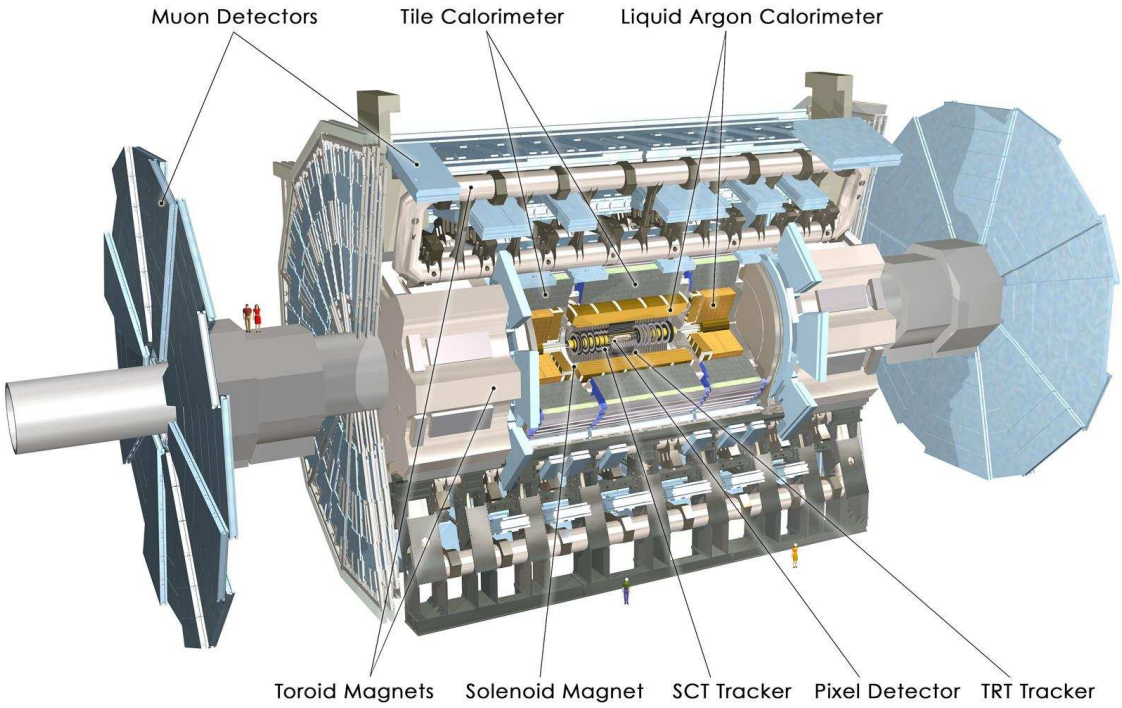

Figure 3.2: Cut-away view of the ATLAS detector. It measures 44 m in length, 25 m in diameter and weights almost 7 000 tons [34].

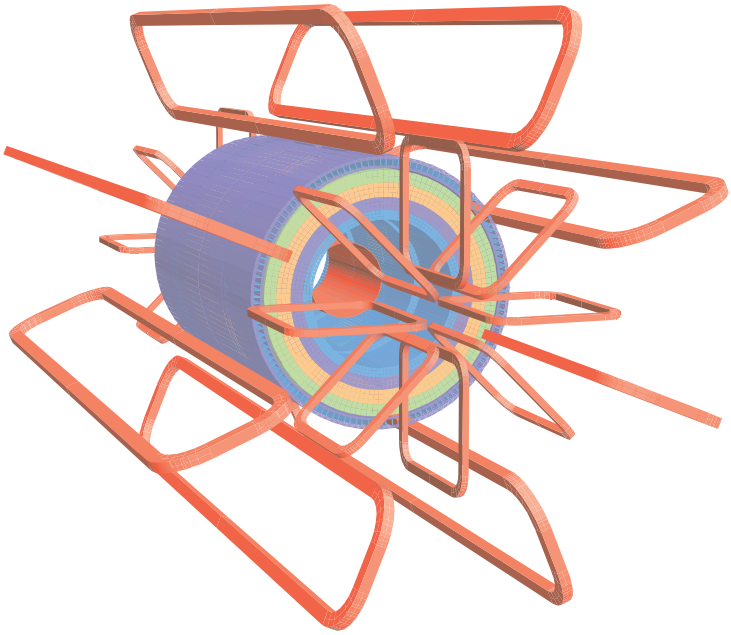

Figure 3.3: Schematic view of the superconducting coils of the ATLAS magnet system (red) eight in the barrel part and eight in each end cap toroid. The iron in the calorimeter system serves as return yoke for the central solenoid which lies inside the barrel calorimeter [34].

electromagnetic calorimeter.
In ATLAS, the muon spectrometer has its own magnet system with a toroidal field configuration with a mean field strength of 0.5 T. The system consists of three separate magnets:

- One barrel toroid consisting of eight 25 m long coils, each one in a separate cryostat.
- Two end cap toroids, each consisting of eight coils sharing a common cryostat.

Due to the limited number of coils, the toroidal magnetic is not uniform. It is essential for good momentum resolution to have knowledge about the field distribution with a relative accuracy on the order of $(2-5)\cdot 10^{-3}$. The field configuration has two major advantages:

- The air-core magnet design minimizes multiple scattering of the muons inside the spectrometer.
- The momentum resolution is largely independent of the pseudorapidity up to the very forward regions.

Table 3.3 summarizes the main parameters of the ATLAS magnet system.

Table 3.3: Main Parameters of the ATLAS magnet system.

Feature	Unit	Solenoid	Barrel toroid	End cap toroids
Inner diameter	(m)	2.46	9.4	1.65
Outer diameter	(m)	2.56	20.1	10.7
Axial length	(m)	5.8	25.3	5.0
Number of coils	–	1	8	2×8
Nominal current	(kA)	7.73	20.5	20.5
Stored magnetic energy	(GJ)	0.04	1.08	2×0.25
Field strength	(T)	$0.9-2.0$	$0.2-2.5$	0.2–3.5

3.2.4 The Inner Tracking Detector

The inner detector is designed to reconstruct trajectories of charged particles with high precisions and serves two main purposes: to measure the particle momenta and to determine the origin of the particle (production vertex) and to distinguish between particles from the primary hard interaction, from a secondary vertex due to the decay of long lived particles or from additional inelastic proton-proton collisions. Since the inner detector is permeated by the field of the central solenoid, the tracks of charged particles are bent in the transverse plane allowing for momentum measurement from the track curvature.
The ATLAS inner detector combines three different but complementary detector technologies providing efficient and accurate track reconstruction up to $|\eta| = 2.5$. Figure 3.4 shows a cut-away view of the inner detector.
Closest to the interaction region is the silicon pixel detector. To deal with the high particle densities in the immediate vicinity of the proton-proton collisions, the pixel detector has with 80.4 million read-out channels the highest granularity of all ATLAS subdetectors. It consists of three concentric cylinders around the beam axis in the central part ($|\eta| < 2.0$) and of 3 disks perpendicular to the beam axis in each of the forward regions

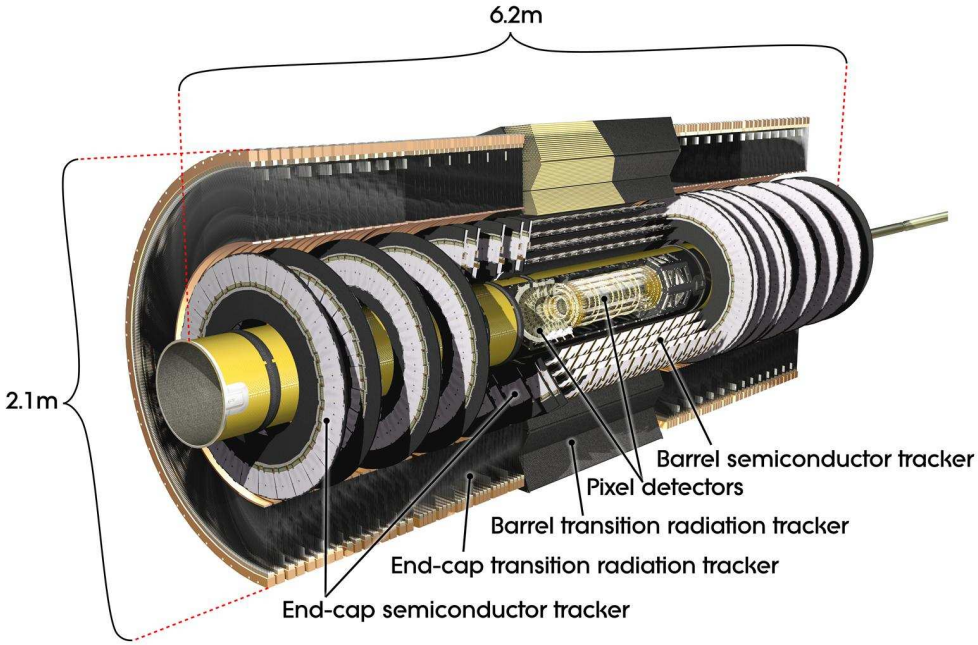

Figure 3.4: Cut-away view of the ATLAS inner detector [34].

$(2.0 < |\eta| < 2.5)$. Each pixel has the size of $50 \times 400\,\mu$m allowing for a spatial resolution of the pixel sensors of $10\,\mu$m in the $R - \phi$ bending plane and of $115\,\mu$m in the z-direction in the barrel and radial direction in the end caps.

Table 3.4: Main parameters of the three detector technologies of the ATLAS inner detector.

Technology	Point resolution (μm)	No. of space points per track	No. of read-out channels
Pixel	$10\,(R-\phi),\ 115\,(z,R)$	3	$80.4 \cdot 10^6$
SCT	$17\,(R-\phi),\ 580\,(z,R)$	$4-9$	$6.3 \cdot 10^6$
TRT	$130\,(R-\phi)$	36	$3 \cdot 10^5$

The pixel detector is surrounded by the semiconductor tracker (SCT) which consists of almost 16 000 silicon strip sensors with in total 6.3 million read-out channels. Four cylindrical layers of small-angle stereo strip detectors in the barrel ($|\eta| < 1.1$) and 9 disks in each of the end cap regions ($1.1 < |\eta| < 2.5$) measure at least 4 space points for each track. The strip pitch of $80\,\mu$m allows for a spatial resolution of the strip sensors of $17\,\mu$m in the $R - \phi$ plane.

The outermost part of the inner detector is the Transition Radiation Tracker (TRT). This gas detector consists of over 300 000 straw drift tubes. Polyimide tubes of 4 mm diameter are filled with the gas mixture $Xe/CO_2/O_2$ (70/27/3) at $5 - 10$ mbar overpressure and contain a $35\,\mu$m diameter gold-plated tungsten-rhenium anode wire in the center. The straw tubes, with an intrinsic resolution of $130\,\mu$m, are arranged in 73 layers in the barrel ($|\eta| < 1.0$) and in 160 layers in each end cap ($1.0 < |\eta| < 2.0$) contributing on average 36

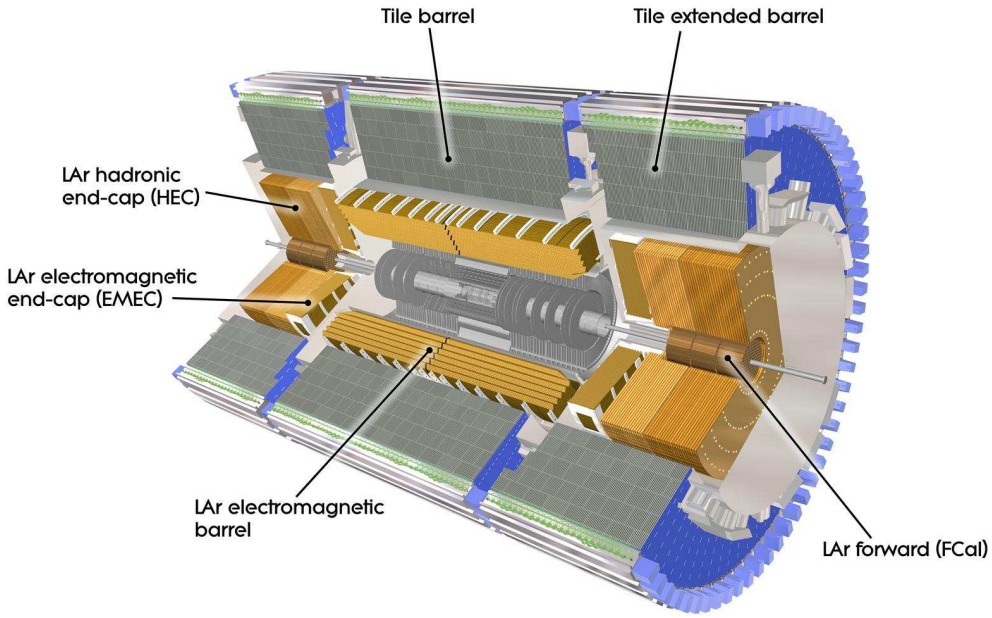

Figure 3.5: Cut-away view of the ATLAS calorimeter system [34].

space points to the track reconstruction. Between the tube layers polypropylene fibres and foils are embedded in the barrel and end caps, respectively, causing traversing electrons to emit transition radiation while the heavier muons and hadrons are passing essentially without radiation emission. By requiring the charge deposition around the track of a charged particle to exceed 2 GeV, electrons can be separated from hadrons, in particular from charged pions. The main parameters of the different detector technologies used in the inner detector are listed in Table 3.4.

3.2.5 The Calorimeters

All ATLAS calorimeters are sampling calorimeters with full ϕ-acceptance and η-coverage up to $|\eta| = 4.9$. They are characterized by high granularity and are realized with different active and absorber materials matched to their purpose. Figure 3.5 shows a cut-away view of the calorimeter system.
Located just outside the superconducting solenoid coil of the inner detector is the electromagnetic (EM-) calorimeter, consisting of a barrel part ($|\eta| < 1.5$) and two end caps (EMEC) extending up to $|\eta| = 3.2$, and complemented by two forward electromagnetic calorimeters (FCal1) in the high pseudorapidity regions $3.2 < |\eta| < 4.9$. The active medium of all electromagnetic calorimeters is liquid argon which combines intrinsic radiation hardness, stability over time and linear response. Special for the ATLAS EM-calorimeters in barrel and end caps are the accordion-shaped lead absorbers and read-out electrodes. This design allows for homogeneous response and fast signals without inefficient regions for read-out cables. For precise spatial and energy resolution, the electrode segmentation in the η-region also covered by the inner detector ($|\eta| < 2.5$) is very fine

($\Delta\eta \times \Delta\phi = 0.025 \times 0.025$). The highest granularity of $\Delta\eta = 0.003$ is implemented in the first of the three layers of the EM-calorimeter, the so-called η-strip layer.
The EM-calorimeters are surrounded by hadron calorimeters. In the barrel ($|\eta| < 1.1$) and extended barrel ($0.8 < |\eta| < 1.7$) this is a scintillating tile calorimeter using steel absorbers and plastic scintillators as active medium. The tile calorimeter consists of three layers with a granularity of $\Delta\eta \times \Delta\phi = 0.1 \times 0.1$. At higher pseudorapidities ($1.5 < |\eta| < 3.2$) two hadronic end cap calorimeters (HEC) are used for the energy measurement. They consist of copper plates with liquid argon as active medium and have the same granularity as the tile calorimeter for $|\eta| < 2.5$ and a granularity of $\Delta\eta \times \Delta\phi = 0.2 \times 0.2$ for $2.5 < |\eta| < 3.2$. The largest pseudorapidities are covered by the forward hadron calorimeters (FCal2 and FCal3) with a tungsten absorber matrix with liquid argon filled boxes and with cell sizes of $\Delta x \times \Delta y = 3.3 \times 4.2$ cm^2 and $\Delta x \times \Delta y = 5.4 \times 4.7$ cm^2, respectively.
The total thickness of the calorimeter system is more then 22 radiation lengths (X_0) and about 10 hadronic interaction lengths. This ensures a good energy resolution for highly energetic jets, precise reconstruction of the missing transverse energy and minimizes the punch through of particles to the muon spectrometer. The total number of read-out channels of the ATLAS calorimeter system is about 260 000. Its main parameters and quantities are summarized in Table 3.5.

Table 3.5: Parameters for the ATLAS calorimeters. The energy resolutions are from test-beam measurements [39–41] and well inside the specifications of ATLAS (see Table 3.2).

Name	$\|\eta\|$−range	Absorber / active material	Energy resolution (E in GeV) (stochastic)	(constant)
EM	<1.5	lead/LAr	$(10.1\pm0.4)\,\%/\sqrt{E}$	$(0.2\pm0.1)\,\%$
EMEC	1.5−3.2	lead/LAr	$(10.1\pm0.4)\,\%/\sqrt{E}$	$(0.2\pm0.1)\,\%$
Tile	<1.7	steel/scint.	$(52.0\pm1.0)\,\%/\sqrt{E}$	$(3.0\pm0.1)\,\%$
HEC	1.5−3.2	copper/LAr	$(70.6\pm1.5)\,\%/\sqrt{E}$	$(5.8\pm0.2)\,\%$
FCal1	3.2−4.9	copper/LAr	$(28.5\pm1.0)\,\%/\sqrt{E}$	$(3.5\pm0.1)\,\%$
FCal2+3	3.2−4.9	tung./LAr	$(94.2\pm1.6)\,\%/\sqrt{E}$	$(7.5\pm0.14)\,\%$

3.2.6 The Muon Spectrometer

Hadrons are interacting via the strong force and are thus absorbed almost completely in the calorimeters. Charged leptons on the other hand loose their energy mainly through ionization of atoms and bremsstrahlung in the Coulomb field of nuclei on their way through the detector. As the energy loss due to the latter is proportional to $1/m^2$, electrons are absorbed in the EM-calorimeters, while the 207 times heavier muons are traversing the inner parts of the detector mostly with only minor energy losses[2] and are detected in the muon spectrometer.
It is the muon spectrometer (see Figure 3.6) which defines the impressive size of the ATLAS detector with 44 m in length and 25 m in diameter. It is designed to provide an independent muon trigger and a high-precision muon momentum measurement up to

[2]The dominating process is energy dependent: In the range from a few GeV to about 100 GeV muons mainly loose their energy due to ionization. For muons with larger energy, the energy losses are mainly radiative through pair production, bremsstrahlung and knock-on electron (δ-rays).

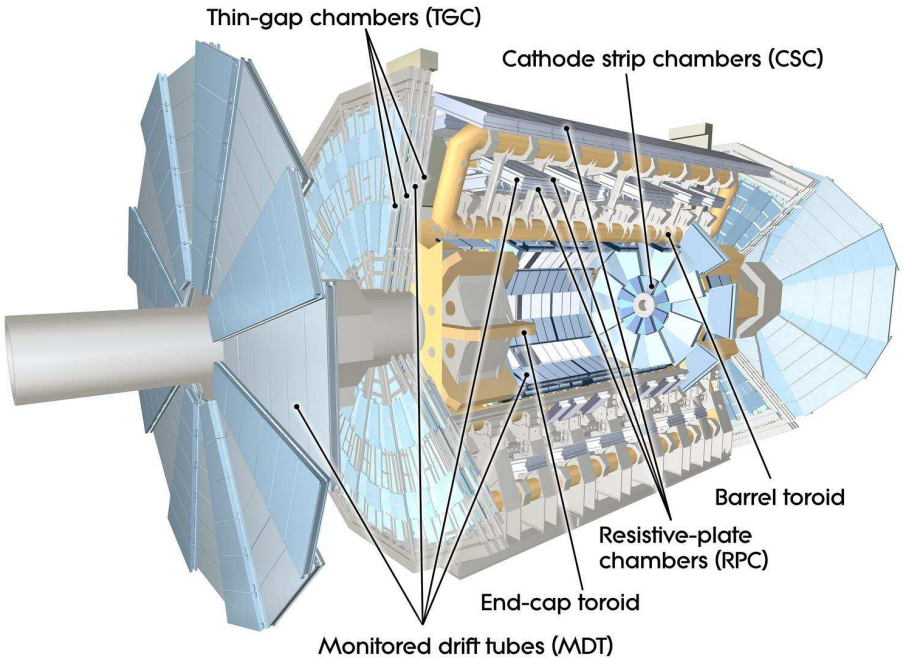

Figure 3.6: Cut-away view of the ATLAS muon spectrometer [34].

the TeV scale. By using three superconducting air-core toroid magnets to provide the bending field (see Section 3.2.3), multiple scattering is minimized. Muons are detected by three layers of dedicated trigger and precision tracking chambers. In the barrel part (pseudorapidity range $|\eta| < 1.0$) the fast trigger information is provided by Resistive Plate Chambers (RPC) and in the end cap region ($1.0 < |\eta| < 2.4$) by three layers of Thin-Gap Chambers (TGC). The precision tracking coordinate measurement in the bending plane of the magnetic field is realized by Monitored Drift Tube (MDT) chambers for most of the muon spectrometer acceptance. Only in the innermost end cap layer at $|\eta| > 2.0$, Cathode Strip Chambers (CSC) are installed to ensure precise measurement of the track-points at high background rates. The precision chambers cover the pseudorapidity range up to $|\eta| < 2.7$. In the following, a more detailed description of the momentum measurement and of the functionality of the muon trigger is given, including an explanation of the detector technologies used. As the first part of this work is devoted to the precise calibration of the ATLAS MDT chambers, this detector system will be described in detail in Section 3.3.

Precision Momentum Measurement

The ATLAS muon spectrometer consists of three layers of precision tracking chambers which provide track points for measuring the curvature and momentum of the muon tracks. The chambers in the barrel region are arranged in three concentric cylindrical shells around the beam axis at radii of approximately 5 m, 7.5 m and 10 m. In the two end cap regions, the muon chambers form wheels perpendicular to the beam axis located at distances of $|z| \approx 7.4$ m, 10.8 m, 14 m and 21.5 m from the interaction point. Figure 3.7 shows a cross section of a quadrant of the muon system. In the barrel region, the muon

momentum is determined from the sagitta of the track, in the end caps from a point-angle measurement (see Figure 3.7). To achieve the high standalone momentum resolution of better than 10 % for transverse momenta up to the TeV scale, each chamber layer has to measure a track-point with an accuracy of better than $\sigma = \sqrt{\sigma_{\text{pos}}^2 + \sigma_{\text{ch}}^2} = 50\,\mu\text{m}$ (see Appendix A for a discussion of contributions to the momentum resolution of the ATLAS muon spectrometer). To reach this precision, the uncertainty of the knowledge of the relative positions of MDT wires and CSC strips, respectively, along the muon trajectory (σ_{pos}) and the intrinsic resolution of the MDT and CSC chambers (σ_{ch}) must be better than $^{50\,\mu\text{m}}/_{\sqrt{2}} \approx 35\,\mu\text{m}$. A high-precision optical alignment system with about 12 000 sensors monitors the relative positions and internal deformations of the MDT chambers. It is complemented by track-based alignment algorithms. The high tracking resolution is ensured by two different detector types.

Monitored Drift Tube Chambers (MDT) Monitored drift tube chambers are the precision muon tracking detectors over most of the muon spectrometer acceptance. In total 1150 chambers with 354 000 drift tubes are covering an active region of almost 5500 m^2. The MDT chambers consists of six or eight layers of drift tubes with a spatial resolution of 80 μm leading to a chamber resolution of about 35 μm in the track bending plane. Their functionality is explained in detail in Section 3.3.

Cathode Strip Chambers (CSC) The limit for reliable operation of MDT chambers is at counting rates of about $500\,^{\text{Hz}}/_{\text{cm}^2}$, which will be exceeded in the innermost layer of the very forward region ($2.0 < |\eta| < 2.7$) due to background hits from neutrons and photons produced by particle interactions in the detector, mainly the calorimeters. There, in total 32 Cathode Strip Chambers are used to ensure efficient muon tracking at high counting rates up to $1700\,^{\text{Hz}}/_{\text{cm}^2}$. Each chamber provides four independent measurements in η and ϕ along each track. The CSCs are multi-wire proportional chambers with a segmented cathode read-out. A chamber spatial resolution of 40 μm is achieved in R- and of 5 mm in ϕ-direction as well as a time resolution of 7 ns.

Muon Trigger

An essential design criterion of the muon system is the capability to trigger on muon tracks. The trigger chambers provide fast information about traversing muons to the level-1 muon trigger logic allowing to discriminate low and high momentum muons up to a pseudorapidity of $|\eta| = 2.4$ and over the whole ϕ-range. In addition, the trigger chambers identify the bunch crossing to which the muons belong and measure the coordinates along the drift tubes. Two different detector technologies are used for the trigger chambers in the barrel and the end cap regions of the detector.

Resistive-Plate Chambers (RPC) In the barrel part of the ATLAS muon spectrometer, the fast trigger information is provided by 606 RPCs. They consist of two parallel resistive plates of Bakelite with a gas gap of 2 mm in between which is filled with a $C_2H_2F_4$/Iso-C_4H_{10}/SF_6 gas mixture. To ensure high rate capability, the RPCs are operated in avalanche mode with an electric field of 4.9 $^{\text{kV}}/_{\text{mm}}$ between the Bakelite plates,

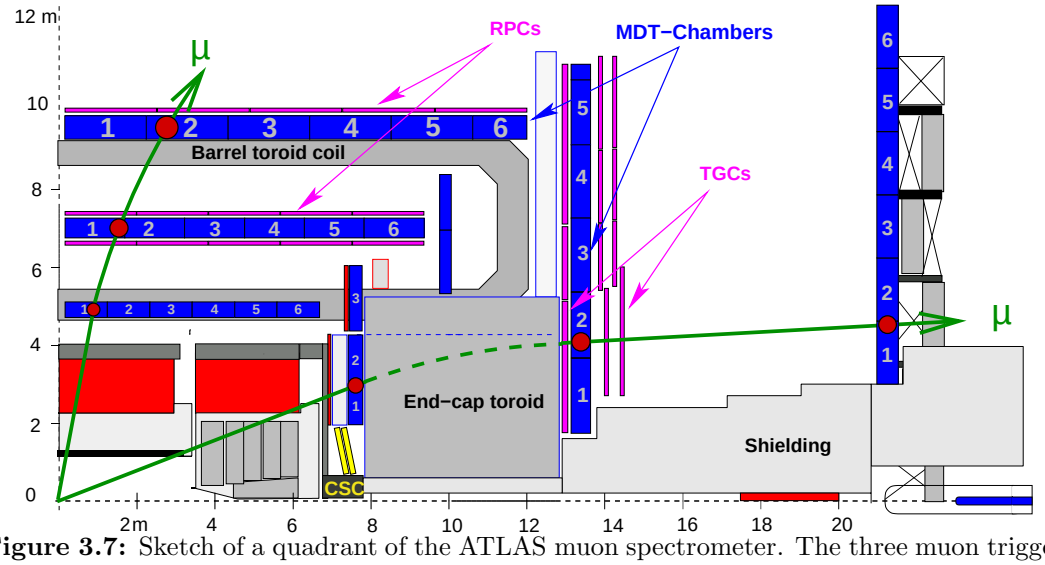

Figure 3.7: Sketch of a quadrant of the ATLAS muon spectrometer. The three muon trigger chamber (RPC and TGC) layers are indicated as well as the precision tracking chambers (MDT and CSC). The interaction point is at the origin of the coordinate system.

leading to an excellent time resolution of 1.5 ns. The signal is read-out via capacitive coupling to metallic strips on the outside of the Bakelite plates providing a spatial resolution of 10 mm in z and ϕ, respectively.

Thin-Gap Chambers (TGC) In total 3588 TGCs are used as fast trigger chambers in the end cap region of the muon spectrometer. TGCs are multi-wire proportional chambers operated with a strongly quenching gas mixture of CO_2 and n-pentane (n-C_5H_{12}) at a relatively low gas-gain of 3×10^5. With a wire-to-cathode distance of 1.4 mm, which is smaller than the wire-to-wire distance of 1.8 mm, a good time resolution of 4 ns and a spatial resolution between $2 - 7$ mm in R and ϕ is achieved.

In the barrel, three layers of trigger chambers are implemented while in the end caps a fourth TGC layer (TGC I) is added to the innermost MDT layer for second coordinate measurement and to increase the robustness of the tracking in case of high background. The schematic layout of the trigger system is shown in Figure 3.8. In the barrel, two RPC layers (RPC1 and RPC2) enclose the MDT chambers of the middle layer, while the third RPC layer is located on the outer MDT layer. In the end caps, the three TGC layers are in front of (TGC1) and behind (TGC2 and TGC3) the middle MDT wheel. The trigger information is generated by fast coincidences between the outer three trigger layers along the muon trajectory. The coincidence patterns correspond to certain deviation of the tracks from straightness used as criteria for the tracks to exceed pre-defined momentum thresholds. The working principle of the trigger is in detail:

- A muon hit in the reference layer (*pivot-point*) is connected to the nominal interaction point by a straight line. The reference layer (*pivot-plane*) is the second layer in the barrel (RPC2) and the last layer in the end cap (TGC3) (cp. Figure 3.8).

- A search road around this straight line is defined by extrapolating a cone from the

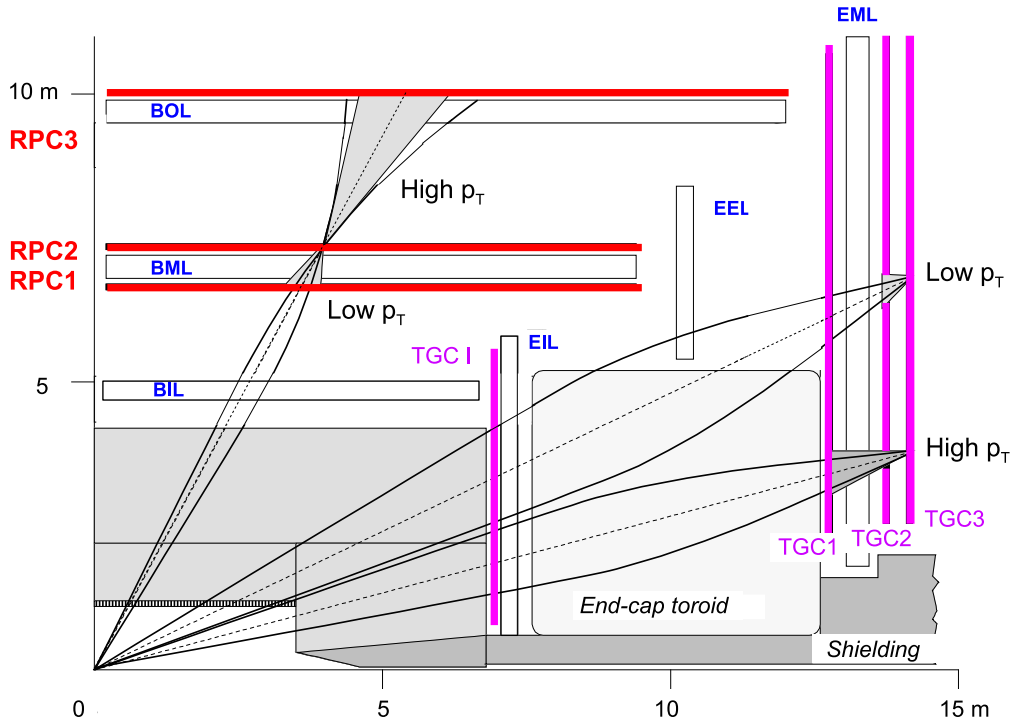

Figure 3.8: Schematic layout of the muon trigger system. RPC2 and TGC3 are the reference (pivot) planes for the barrel and end cap triggers, respectively [34].

pivot-point to the RPC1 and TGC2 layer, respectively, for the low p_T trigger and to the RPC3 and TGC1 plane, respectively, for the high p_T trigger. When a hit is found inside the extrapolated region a muon with minimum transverse momentum related to the road width has been found.

- A system of programmable coincidences allows for three adjustable p_T thresholds for both, the low p_T $(6-9\,\mathrm{GeV/c})$ and for the high p_T $(9-35\,\mathrm{GeV/c})$ muon trigger.

The intersection of the extrapolated trigger road with the trigger chamber plane is called region of interest (ROI). Due to the higher granularity of the TGCs compared to the RPCs, the size of a ROI in the end cap is a dimension of $\Delta\eta \times \Delta\phi = 0.03 \times 0.03$ while it is $\Delta\eta \times \Delta\phi = 0.1 \times 0.1$ in the barrel. The ROIs are used as starting point for the level-2 and offline muon track finding and reconstruction.

Overview of the Muon Detector Parameters

Table 3.6 summarizes the parameters of the detector technologies used in the ATLAS muon spectrometer.

3.3 Monitored Drift Tube Chambers

Monitored drift tube chambers are the precision muon tracking detectors over the most part of the muon spectrometer acceptance.

Table 3.6: Parameters of the ATLAS muon detectors [34]. The quoted spatial resolutions (columns 3,4) do not include chamber-alignment uncertainties. Column 5 lists the intrinsic time resolution of each chamber type.

Type	Function	Chamber resol. (RMS) in z/R	ϕ (mm)	t (ns)	Track points barrel	Track points end cap	Number of chambers	Number of channels
MDT	tracking	35 μm (z)	–	–	20	20	1150	$354 \cdot 10^3$
CSC	tracking	40 μm (R)	5	7	–	4	32	$31 \cdot 10^3$
RPC	trigger	10 mm (z)	10	1.5	6	–	606	$373 \cdot 10^3$
TGC	trigger	2-6 mm (R)	3-7	4	–	9	3588	$318 \cdot 10^3$

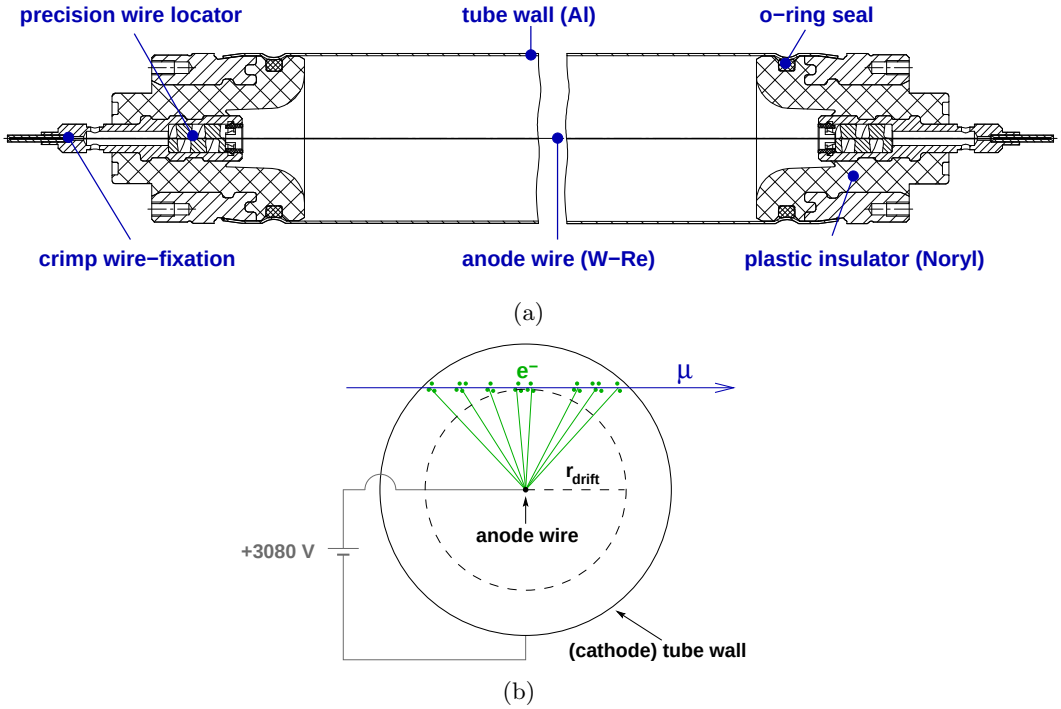

Figure 3.9: MDT tube cross sections (a) along and (b) perpendicular to the wire.

3.3.1 Drift Tube Principle

The basic cells of an MDT chamber are aluminium drift tubes with outer diameter of 29.970 mm and 400 μm wall thickness. A gold-plated tungsten-rhenium wire with 50 μm diameter is centred in each tube (cp. Figure 3.9). Each tube is closed by two end plugs which are used to position the wires with an accuracy of 10 μm. The tubes are filled with a gas mixture of Ar/CO_2 (93 % / 7 %) at an absolute pressure of 3 bar. Around 500 ppm of water are added to the mixture to prevent cracks in the plastic insulator of the end plugs due to drying-out and to improve the HV stability. A drift gas without hydrocarbons was selected to prevent ageing of the drift tubes due to the formation of polymers on the wires under high radiation doses at the LHC [42–44]. The length of the tubes varies between 70 cm for chambers in the innermost layer and 630 cm for the largest MDT chambers in the outer end cap layer.
A high voltage of 3080 V is applied between the anode wire and the grounded tube wall,

creating a radially symmetric electric field. When a muon traverses the tube, it ionizes the gas along its path. The ionization is a statistical process leading to ion clustering along the muon trajectory. On average, 105 clusters per centimetre are produced under nominal operating conditions with on average 2.7 electron-ion pairs per cluster [45]. These primary electrons are moving, while being accelerated by the electric field and decelerated by the scattering on gas atoms, with a mean drift velocity of about 0.02 $^{\mathrm{mm}}/_{\mathrm{ns}}$ to the anode wire. In a small region of about 150 μm radius around the wire, the field is strong enough that the electrons gain sufficient kinetic energy for secondary ionization between collisions with the gas atoms. This leads to an avalanche multiplication of the primary ionization charge produced by the traversing muon. For the high voltage of 3080 V, the gas amplification is 2×10^4, chosen to keep the charge collected per centimetre on the wire as small as possible to prevent ageing effects.
The drift of the secondary ion cloud induces a measurable electronic signal on the anode wire, while the contribution of the secondary electrons can be neglected due to the small potential difference to the wire. The start time of the signal coincides with the start of the avalanche, i.e. with the arrival time of the first primary electrons at the anode. The time at which the detected muon traverses the tube is known from an external source. In the case of ATLAS the proton-proton collision time defined by the accelerator bunch crossing clock corrected with the time-of-flight of the muon to the MDT chamber is used. The time difference between the tube signal and the crossing muon can thus be determined. It is the sum of two effects:

- The drift time of the primary electrons produced closest to the wire and
- a time offset due to signal propagation along the wire and in the read-out electronics and cables.

When the time offset is subtracted, the remaining drift time is a direct measure of the shortest distance between the muon trajectory and the anode wire, the drift radius), if the relationship between the drift time and the drift distance is know, the so-called space-to-drift-time or r(t) relationship. The determination of the r(t) relationship with high accuracy is crucial to reach the intended muon detector and momentum resolution of the ATLAS muon spectrometer (see Chapter 4). With a precise r(t) calibration, the ATLAS drift tubes reach an average spatial resolution of 80 μm.

3.3.2 Chamber Design

The ATLAS Monitored Drift Tube chambers, apart from a few exceptions, consist of two multilayers of the described aluminium drift tubes which are glued on both sides of an aluminium support frame. Each chamber of the middle and the outermost layer has three densely packed tube layers per multilayer. To improve the tracking efficiency in the higher background environment just outside the hadron calorimeters, the chambers of the innermost layer are equipped with four drift tube layers per multilayer. Figure 3.10 shows the layout of an MDT chamber for the barrel region of the spectrometer. The chamber design for the end cap regions is very similar, only with a trapezoidal instead of a rectangular shape.
The light-weight aluminium support frame consists of two long beams oriented along the tube axes and three cross-plates perpendicular to them at equal distance. All tubes are

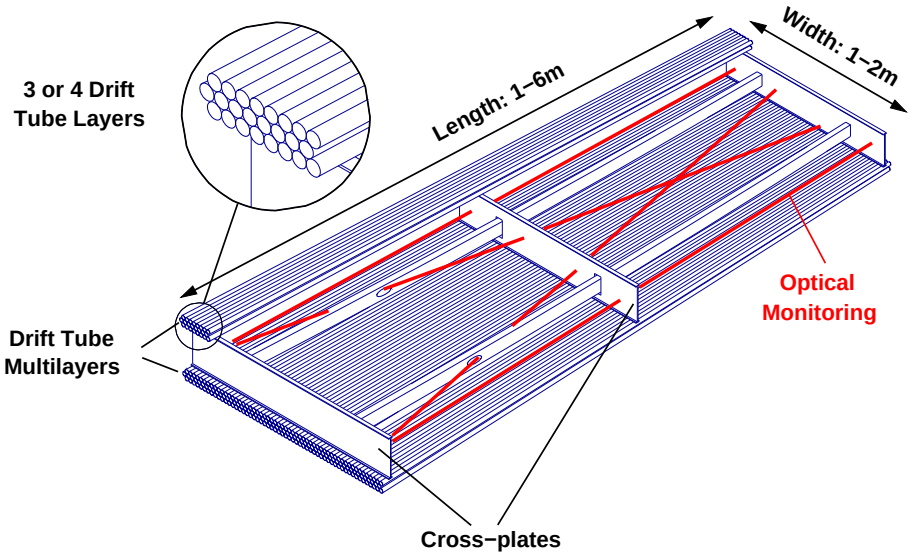

(a)

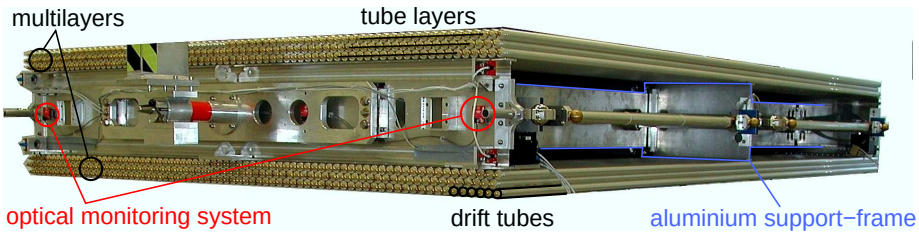

(b)

Figure 3.10: An ATLAS MDT chamber from the barrel region presented in a schematic drawing (a) and an illustrated photography (b).

connected to the high voltage on one side (HV) and are read out at the opposite side (RO).
To reach the intended momentum resolution of the ATLAS muon spectrometer, a tracking accuracy of 35 μm per chamber is needed. This high precision is achieved with the following way:

- Operation at a gas pressure of 3 bar (absolute) to improve the drift tube resolution by suppressing diffusion effects of the drifting electron clouds.
- Positioning of the anode wires with an accuracy of 10 μm at the centre of end plugs [46–48] and with an accuracy of 20 μm within a chamber.
- With high-precision X-ray tomograph measurements of the wire positions ∼15 % of the 1150 MDT chambers the accuracy of the drift tube assembly during chamber construction has been verified [49].
- Knowledge of the wire sag with an accuracy of 20 μm by precise adjustment of the wire tension equivalent to 350 g.
- To measure deformations of the chambers during the operation, e.g. due to temperature gradients, with a precision of 5 μm the MDT chambers are equipped with an

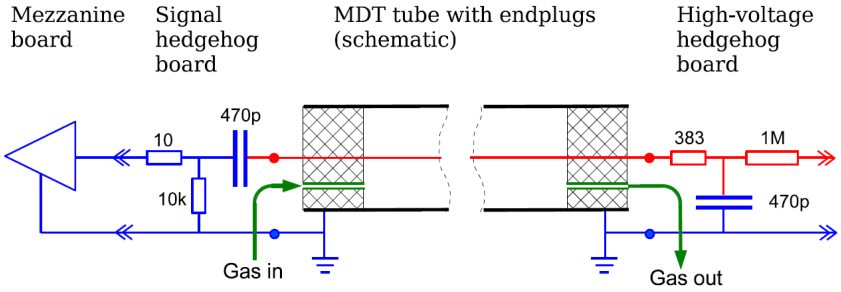

Figure 3.11: Diagram of the main service connections to an MDT tube. At the HV side the wire is terminated with the equivalent transmission line impedance of the tube (383 Ω) to avoid reflections [51].

optical monitoring system based on RasNik sensors [50].

- Adjustment of the multilayer gravitational sag to the wire sag for the MDT chambers in the barrel and in the outermost end cap layers, thus ensuring a centred anode wire along the tube.

- As the environmental conditions influence the drift velocity of the electrons, the chambers are equipped with up to four hall probes for the three dimensional measurement of the magnetic field as well as with up to 28 temperature sensors. These measurements are used to improve the r(t) calibration of the tubes (see Section 4.3).

3.3.3 MDT Chamber Electronics

An overview of the service connections of a single MDT tube is given in Figure 3.11 and a read-out diagram is shown in Figure 3.12. The different components are described in the following paragraphs.

Hedgehog Boards On the HV side, 24 drift tubes (3×8 for three- and 4×6 for four-layered chambers) are connected to a so-called HV hedgehog board which supply the high voltage to each tube. These front-end boards are directly plugged onto the signal pins of the tube end plugs terminating the open end of the wire with a 383 Ω resistor, the tube's characteristic transmission line impedance, to avoid signal reflections. In addition, a 470 pF capacitor and a 1 MΩ resistor form a low-pass-filter for each channel to suppress high-frequency (> 500 Hz) noise in the high voltage connection. In case of an electrical short, for instance a broken wire touching the tube-wall, the 1 MΩ resistor is limiting the current to 3 mA.
On the hedgehog boards connected to the opposite tube ends, the RO-side, the signals are decoupled from the high voltage on the wire and routed to the read-out electronics. The hedgehog boards on both sides are surrounded by Faraday cages shielding them against electronic pick-up noise and dust.

Mezzanine Boards A so-called mezzanine board carrying three ASD[3]-chips responsible for the further signal processing is connected to every RO-hedgehog board. Each chip

[3] Amplifier-Shaper-Discriminator

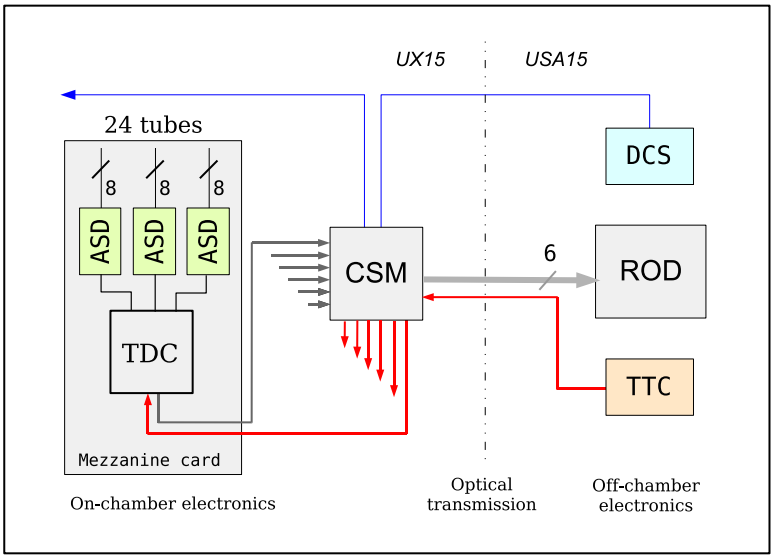

Figure 3.12: Diagram of the MDT read-out electronics. Each CSM (Chamber Service Module) serves up to 18 mezzanine boards depending on chamber size, each MROD (Muon Read-Out Driver) up to 6 CSMs [51].

contains tunable pre-amplifiers, shapers and discriminators. When a signal is passing an adjustable threshold, a digital pulse is passed to a time-to-digital converter (TDC) on the board measuring the signal arrival time relative to the bunch crossing time. In the TDC, the bunch crossing interval of 25 ns is subdivided by 32 resulting in a so-called *fine time* period of $^{25}/_{32} = 0.78$ ns leading to an RMS timing error of 0.23 ns in measuring the signal arrival times. The programmable parameters of both the ASD and the TDC are initialized using the JTAG[4] protocol. In addition, the charge of the signal pulse is measured by a Wilkinson-ADC[5].

Chamber Service Module (CSM) The mezzanine boards of an MDT chamber are connected for information transfer and low-voltage supply to a central Chamber Service Module (CSM) through high density 40 pin twisted pair cables. The CSM collects the information of all tubes per chamber and transmits them via an optical fibre to the MDT read-out drivers (MROD) which are installed in the underground counting room USA15 close to the detector cavern UX15. Furthermore, the CSM forwards JTAG information to the ASD-chips, as for example the discriminator thresholds. On a second optical fibre, the timing, trigger and control (TTC) clock signal is sent from the counting room to the CSM and transmitted to the mezzanine boards to synchronise all TDCs to the bunch crossing clock. The signal information from each tube is stored in a buffer memory on the CSM with a tube identifier and only sent to the MROD if the TTC sends the trigger signal.

Detector-Control-System (DCS) Each chamber contains a DCS interface connected via a CAN[6]-bus allowing for the external programming of the read-out electronics. In addi-

[4] JTAG - Joint Test Action Group.
[5] ADC - Analog-to-Digital-Converter.
[6] CAN - Controller-Area-Network.

tion, the information from the on-chamber sensors (Hall-probes and temperature sensors) is collected there and sent for central processing via the CAN-bus connection.

RasNik Multiplexer (RasMux) The information from the on-chamber optical alignment system is collected in the so-called RasMux and transmitted to the counting room for the further analysis.

3.3.4 MDT Chamber Naming Scheme

Each of the 1150 MDT chambers has a name which encodes its position in the muon system. Especially for Chapter 4, it is useful to be familiar with this naming convention. The scheme which fits for most of the chambers is briefly described here. For a full overview see Appendix B.

- A '**B**' or '**E**' as first letter distinguished barrel and end cap chambers region.
- The second letter defines the chamber layer, **I**nner, **M**iddle and **O**uter.
- The spectrometer consists of 16 azimuthal sectors. The third letter distinguishes **L**arge sectors with odd numbers and **S**mall sectors with even numbers.
- There are up to 8 chambers per sector and layer in each hemisphere of the barrel and up to 6 chambers radially in end caps wheels. The fourth position in the chamber identifier indicates the sequential chamber numbers in z-direction in the barrel starting at $z = 0$ and with increasing radius in the end caps (η-positions; see also the chamber numbering in Figure 3.7).
- The fifth letter distinguishes chambers in hemisphere **A** (positive z) and **C** (negative z).
- The last two digits give the azimuthal sector number clockwise around the z-axis.

Thus, a chamber name like 'BOS1A02' reads like: '**B**arrel **O**uter **S**mall, η-position **1**, side **A**, sector **2**'.

3.4 Trigger and Data Acquisition

The ATLAS trigger and data acquisition system is based on three levels of event selection designed to capture the events of interest with high efficiency from the collisions occuring at a rate of 40 MHz. The selection at the three trigger levels must provide sufficient rejection to reduce the event rate to 200 Hz (about 300 $^{\mathrm{MB}}/_{\mathrm{s}}$ of data) compatible with the available computing power and storage capacity. In the following, the three levels of the trigger system are described:

1. The level-1 trigger system (L1) is hardware based and uses muon spectrometer (TGC and RPC) and calorimeter information to select events with muons, electrons, photons and jets exceeding predefined p_{T} or energy thresholds. In addition, the total transverse energy, the missing transverse energy and the multiplicity of the measured objects are used as trigger criteria. The L1 trigger receives data at the LHC

bunch crossing rate of 40 MHz and must take a decision within 2.5 μs. The system determines regions of interests (ROI) and passes them to the next trigger level with a maximal output rate of 100 kHz (75 kHz during ATLAS start-up).

2. The second trigger level (L2) is software based and refines the search for signatures in the ROIs passed from the L1 trigger using the full detector information. For example, a fast muon reconstruction using the MDT and CSC precision track coordinate measurement is performed. The L2 trigger software runs on a computing farm with about 500 quad-core CPUs enabling a trigger decision within 100 μs. The L2 trigger system must provide an additional rejection after L1 of about 40 to reduce the accepted event rate down from 100 (75) kHz to 2 (1) kHz for nominal (start-up) operation.

3. The final offline trigger selection is performed by the Event Filter (EF) on a farm of 1800 dual quad-core CPUs. An average processing time of 4 s per event is available to provide additional rejection to reduce the output rate to 200 Hz. The output rate of the Event Filter is only limited by the offline computing and storage capacity.

Figure 3.13 gives an overview of the expected event rates for interesting physics processes at LHC design luminosity. The maximum allowed trigger rates system are indicated.
All events accepted by the trigger are recorded on disk and can be analysed via the world-wide computing grid [53]. Several thousand terabytes of data have to be stored per year and kept available.

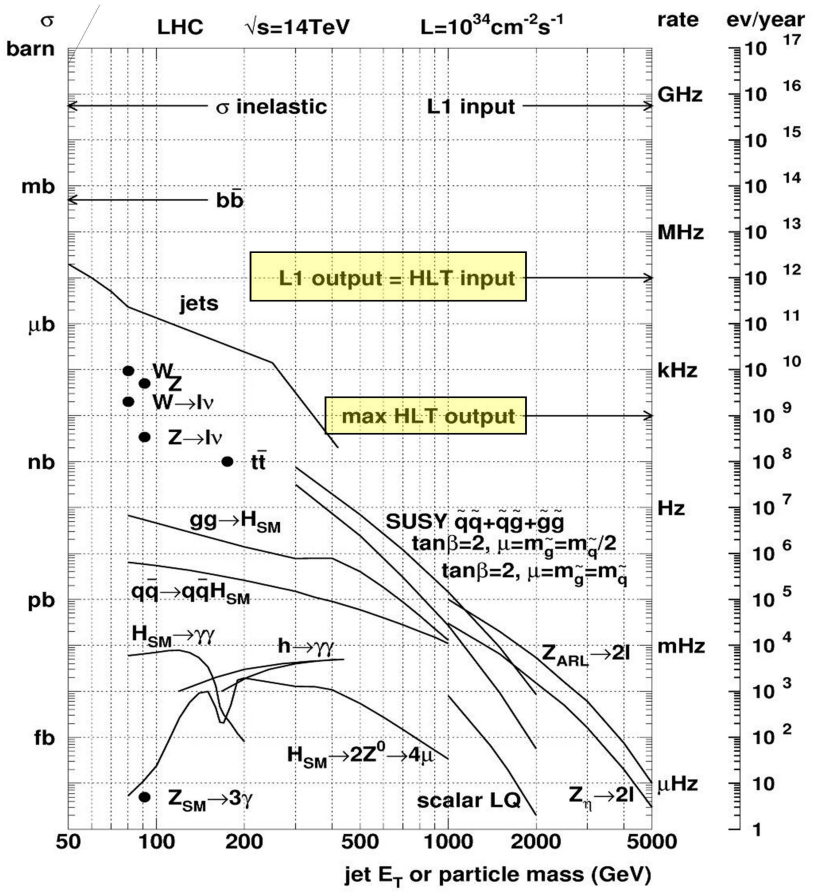

Figure 3.13: Cross sections and expected event rates at the LHC design luminosity for various physics processes as a function of the mass of the produced particles. For comparison, the maximum allowed input and output rates of the first-level trigger (L1) as well as of the higher-level trigger (HLT), L2 and EF are indicated [52].

Chapter 4

Calibration of the Monitored Drift Tube Chambers

The ATLAS muon spectrometer has been designed to provide an independent muon trigger and high precision muon momentum resolution over a wide momentum range from few GeV/c up to about 1 TeV/c. Several effects limit the momentum resolution of the spectrometer which are shown in Figure 4.1. For low p_{T}, the dominant effect are energy loss fluctuations, i.e. the uncertainty in the energy loss of the muon when traversing the inner detector and the calorimeters (on average about 3 GeV). In the p_{T} range from about 20 GeV/c to 200 GeV/c mainly multiple scattering limits the resolution to about 3.5 %. For muon momenta of several hundreds of GeV/c up to about 1 TeV/c, the intrinsic spacial resolution including the calibration accuracy and the relative alignment of the precision muon tracking MDT chambers are the dominating effects.
The goal for the momentum resolution at $p_{\mathrm{T}} = 1\,\mathrm{TeV/c}$ is 10 % to measure the masses of possible new heavy particles decaying into muons, like new heavy gauge bosons Z' with a $5 - 15\,\%$ resolution in the mass range $m_{Z'} = 0.5 - 5\,\mathrm{TeV}$. With an average spatial resolution of 80 μm of a tube, corresponding to a chamber resolution of 35 μm, the drift tube calibration accuracy has to be better than 30 μm in order to be negligible compared to the intrinsic tube resolution.
The calibration of the space-to-drift-time relationship is performed in-situ by using muon tracks (so-called autocalibration) and is a crucial step in order to reach the performance goals for the ATLAS muon spectrometer. A new autocalibration method is discussed in this chapter which uses curved track segments in the MDT chambers for the calibration. The challenges for the muon spectrometer calibration are explained in Sections 4.1 to 4.4. In Section 4.5, the new autocalibration method is discussed before the performance of the algorithm is tested with simulated data in Sections 4.6 and 4.7. In Section 4.8, the influence of the calibration on the momentum resolution of the ATLAS muon spectrometer is studied for the highest muon momenta. The chapter is completed with the validation of the autocalibration procedure with cosmic ray muons in Section 4.9.

4.1 Introduction

The task of MDT chamber calibration is to provide calibration constants and functions to translate measured times into drift radii. The time measurement of the TDC (t_{TDC})

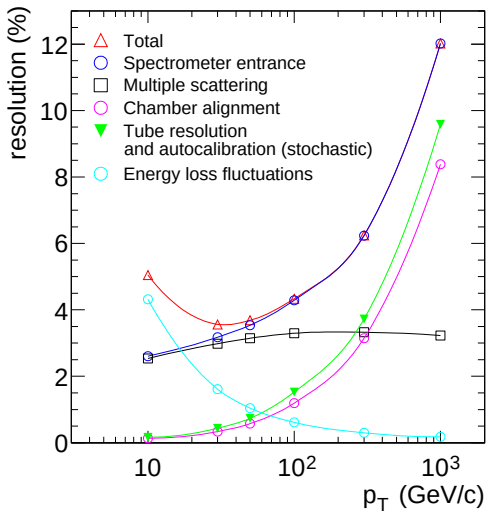

Figure 4.1: Contributions to the momentum resolution of the muon spectrometer as a function of transverse momentum for $|\eta| < 1.5$. The alignment contribution corresponds to an uncertainty of 30 μm in the track sagitta reconstruction [52].

comprises not only the drift time t_{drift} of the electron to the anode wire itself but also the time of flight t_{TOF} of the muon from the proton-proton interaction point to the drift tube, the propagation time t_{prop} of the signal in the tubes from the hit position along the tube to the read-out electronics at the tube end and an offset to signal delays t_0 in cables specific for each channel:

$$t_{\text{TDC}} = t_{\text{TOF}} + t_{\text{drift}} + t_{\text{prop}} + t_0.$$

The individual contributions are described in the following.

Time of Flight (t_{TOF}) The time elapse between the LHC bunch crossing (i.e. the collision) and arrival of the muon at the MDT chamber is:

$$t_{\text{TOF}} = \frac{s}{c},$$

where s is the distance between the interaction point and the hit tube and c is the speed of light in vacuum (the approximate muon velocity). The chambers closest to the interaction region are the BIS chambers with $s = 4.5 - 6.5\,\text{m}$. The chambers in the outer end cap layer are the farthest away with $s = 16.0 - 19.5\,\text{m}$. Hence the time of flight varies between 15 and 65 ns.

Signal Propagation Delay (t_{prop}) The signal propagation time t_{prop} is the time between the arrival of the ionization electrons on the anode wire and the arrival of the signal pulse at the front-end electronics. As the propagation speed is $0.9c$, the largest correction is $t_{\text{prop}} = 23\,\text{ns}$ for the longest drift tubes of the EOL6 chambers with 6.2 m length. For the calculation of this correction, the coordinate along the drift tube measured by the corresponding trigger chamber is used. For MDT chambers without associated trigger chambers (the BI and EO chambers), the hit position is determined by extrapolating the

muon track from the other chamber layers. The uncertainty in the propagation time determination thus depends on the spatial resolution of the RPC or TGC chambers of about 10 mm. Consequently it is well below 0.05 ns for MDT chambers with trigger chambers and still below 0.5 ns for a pessimistic estimation of the extrapolation error of 10 cm for the BI and EO chambers.

Time Offset (t_0) The measured time t_{TDC} for each channel has a fixed offset t_0 due to signal delays in the read-out electronics and cables. The offset varies typically by a few nanoseconds between the different channels of an MDT chamber by several 10 ns between different chambers. It has thus to be measured for each tube by recording the drift time spectrum and determining the start time of the spectrum. In this way the channels are synchronized within an uncertainty of 0.5 ns [54]. In practice, also the time of flight is absorbed in t_0 as it is almost constant for the different tubes.

Drift Time (t_{drift}) The essential measurement is the time the first ionization electrons need to drift from the point of the primary ionization to the wire. The determination of the space-to-drift-time relationship for the translation of drift times t_{drift} into drift radii r_{drift} is the subject of this chapter.

4.2 The Drift Time Spectrum

Figure 4.2(a) shows a typical drift time spectrum of the ATLAS MDT tubes operated at standard conditions with a gas mixture of 93 % Argon, 7 % CO_2 and $\lesssim 500$ ppm of H_2O at 3 bar absolute pressure and a high voltage of 3080 V between the tube wall and the anode wire. It was recorded for cosmic muons in a BML chamber in October 2009 while the magnetic field of the spectrometer was turned off. The mean temperature of the drift gas was measured to be 24.7° C. The figure shows the distribution of the measured drift times for in total $7.5 \cdot 10^5$ recorded hits before t_0 subtraction. The bin size of $^{25}/_{32}$ ns corresponds to the fine time period of the TDC.
Drift times in the rising edge of the spectrum correspond to muons which are passing close to the wire. The width of the rising edge is about 8 ns and a measure of the intrinsic resolution of the tube. The maximum drift time corresponds to electrons from primary ionizations along tracks close to the tube wall which arrive after about 740 ns[1] at the anode wire. The drift time is very sensitive to small variations of the operational parameters of the drift tubes (see Section 4.3). Thus, the temperature and the gas mixture are constantly monitored during ATLAS operation. In addition the drift times measured by the individual chambers are monitored to detect possible time or position dependent changes during the data taking.

Determination of t_0 and t_{max} For the precise determination of the minimum drift time t_0 a modified Fermi function

$$F(t) = \frac{A_0}{1 + e^{-\frac{t-t_0}{T_0}}} + b, \tag{4.1}$$

[1] The admixture of water to the drift gas decreases the drift velocity. Test beam measurements have been mainly performed with pure Ar/CO_2 (93/7) with a maximum drift time of about 700 ns.

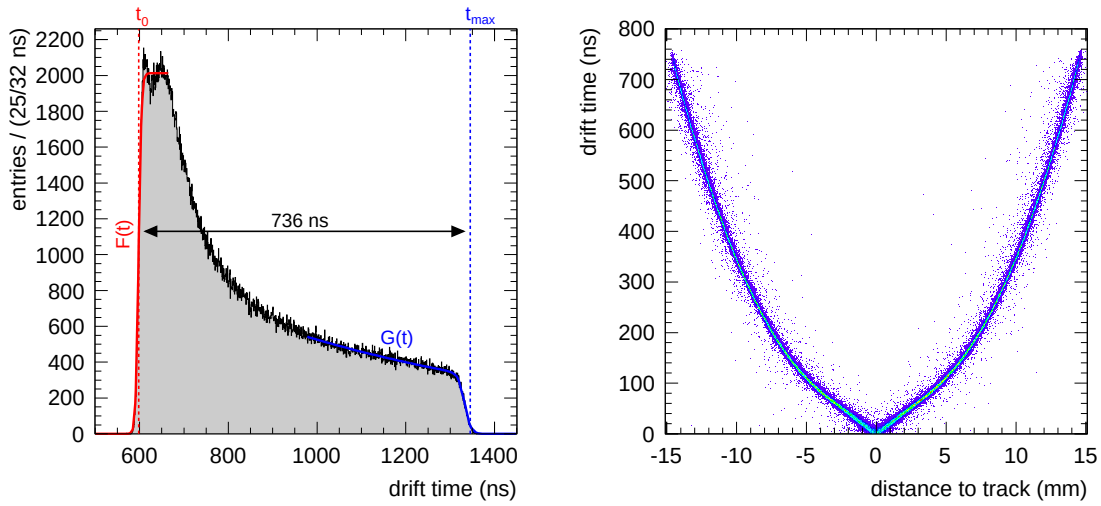

(a) (b)

Figure 4.2: (a) Typical drift time spectrum for ATLAS MDT drift tubes before t_0 subtraction with the fitted curves applied to determine t_0 and the maximum drift time $t_{\max}$. (b) The drift time as a function of the distance of the muon track to the anode wire. The non-linearity of the relationship for the MDT drift gas Ar/CO_2 (93/7) at 3 bar absolute is clearly visible. The data are from cosmic muons in one ATLAS MDT chamber.

is fit to the rising edge of the drift time spectrum. The function has four free parameters: The offset b is a measure of the accidental hit rate due to electronic noise and possible background radiation. A_0 describes the amplitude of the drift time spectrum, for $t \to \infty$, the function approaches the value $A_0 + b$. The parameter $1/T_0$ measures the slope of the rising edge and thus characterizes the intrinsic time resolution of the tube. The inflexion point of the Fermi function defines the start time t_0 of the drift time spectrum with $F(t_0) = A_0/2 + b$ corresponding to the most likely drift time of muons crossing the wire. The time t_0 is subtracted from the measured time $t_{\text{TDC}} - t_{\text{TOF}} - t_{\text{prop}}$, to synchronise the drift time measurements of all tubes of the muon spectrometer. By definition, the space-to-drift-time relationship has a fixed point $r(t_0) = 0$. Due to the definition of t_0, also negative drift times after t_0 substraction are allowed. As corresponding negative drift radii are non-physical, they are defined to be $r(t < t_0) = 0$.
As the drift time spectrum is not constant on the left-hand side of the trailing edge, the Fermi function $G(t)$, used to fit the trailing edge and to determine $t_{\max}$, is multiplied by an exponential $p_1 \cdot e^{-p_2 \cdot t}$ instead of a constant:

$$G(t) = \frac{p_1 \cdot e^{-p_2 \cdot t}}{1 + e^{\frac{t - t'_{\max}}{T_{\max}}}} \tag{4.2}$$

The slope parameter $1/T_{\max}$ of the function is smaller than $1/T_0$ due to efficiency losses close to the tube wall. The maximum drift time is defined as:

$$t_{\max} = t'_{\max} + 2 \times T_{\max}, \tag{4.3}$$

where $t'_{\max}$ is the inflexion point of $G(t)$. The details of the fitting algorithm of the drift time spectrum are described in [54].

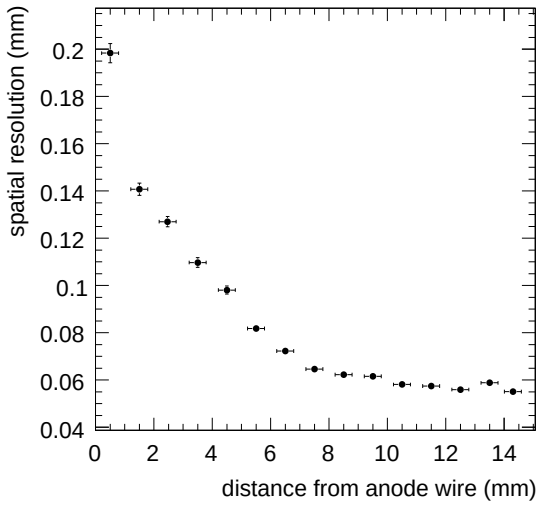

Figure 4.3: Dependence of the drift tube resolution on the drift radius determined from muon test beam measurements [56].

An alternative method is described, fitting the whole drift time spectrum with a single function in [55] but will not be used in this work.

The Space-to-Drift-Time Relationship The drift velocity of the electrons is not constant for the $Ar/CO_2/H_2O$ gas mixture but depends on the non uniform electric field in the drift tubes resulting in a non-linear space-to-drift-time relationship r(t) (see Figure 4.2(b)). The non-linearity complicates the r(t) calibration and makes the accurate knowledge of it particularly important for high drift tube resolution. However, this gas mixture prevents ageing effects in the drift tubes under the high irradiation doses at the LHC even in the muon spectrometer [42–44] and was thus chosen as MDT drift gas. The precise determination of the r(t) relationship at highest precision has been studied in this work.

Drift Tube Resolution The spatial resolution $\sigma(r)$ of the drift tubes depends on the drift radius r due to the non-linearity of the gas mixture, the clustering of the primary ionizations and the diffusion of the electrons along their drift to the anode wire. The resolution is about 200 μm for tracks crossing the tube close to the anode wire and improves to about 50 μm for tracks crossing close to the tube wall. The resolution curve as a function of r shown in Figure 4.3 has been determined in test beam measurements [56] corresponding to an average drift tube resolution of 80 μm.

4.3 The MDT Calibration Model

This section describes the procedure adopted by ATLAS for the calibration of the MDT chambers [57] with the aim to translate the times measured in the tubes by the TDC (t_{TDC}) into drift radii with a precision of about 30 μm independent of the tube positions. The procedure consists of three main tasks needed for precise muon tracking:

1. Correction of t_{TDC} for each hit for t_{TOF}, t_{prop} and the time slewing t_{slew} (see below).
2. Determination of t_0.
3. Determination of the r(t) relationship and of the resolution $\sigma(r)$.

While the corrections of the first point can be performed immediately from a look-up table, the other two steps require for collection of sufficient statistics of muon track segments in a chamber.
The determination of t_0 is described in Section 4.2. Eventually it has to be determined for each tube separately once sufficient statistics has been collected. Especially in the LHC start-up phase, tubes with similar expected offset are grouped together (e.g. the tubes read out by the same ASD-chip or mezzanine board) to reach the minimum of about 10 000 recorded drift times needed to achieve the required accuracy.
The model adopted for the r(t) calibration is to divide the spectrometer into suitable regions with common r(t) relationship of the drift tubes. The regions cannot be chosen arbitrarily small for the following reasons. First, the autocalibration procedure requires track segments from at least 3 tube layers. A spread of track incidence angles is also required for good performance of the r(t) calibration (see Section 4.5.6). Finally, the autocalibration algorithm needs a minimum number of tracks to converge. In order to repeat the calibration frequently to follow changes of the environmental conditions, tubes have again to be grouped together to collect sufficient statistics. It is necessary according to these criteria to optimize the size of the calibration regions. A typical calibration region is one MDT multilayer.
Five effects remain which affect the drift time within a calibration region and have to be corrected for:

Time Slewing The TDC measures the time when the signal in a drift tube crosses the discriminator threshold relative to the accelerator clock. The threshold-crossing occurs earlier for larger pulse heights and thus depending on the amount of charge created in the tube (see Figure 4.4) which is proportional to the number of ionization clusters created along the muon path in the tube. The time slewing effects are on the order of 3 ns (rms) and can be corrected for by using the correlation with the signal charge measurement of the ADC [58].

Wire Sag The anode wire is centred at the tube ends with an accuracy of 10 μm. The wire tension of 350 g corresponds to a maximum sag of 500 μm (corresponding to about 20 ns) for the longest drift tubes. All chambers (except the middle layer of end cap chambers) for which this effect would significantly influence the tube resolution were mechanically adjusted such that the sag of the tubes follows the gravitational sag of the wire. This compensation was applied with a precision of better than 50 μm [59] such that the influence on the track position measurement can be neglected. For the EM chambers, the drift time is corrected offline for this effect during the calibration procedure [60].

Irradiation The tube resolution degrades with increasing background rate [56] of ionizing radiation. The space charge from this ionization alters the electric field inside the drift tube and reduces the electric field near the wire and consequently the gas amplification, signal charge and spatial resolution. Fluctuations of the ionization and of the space

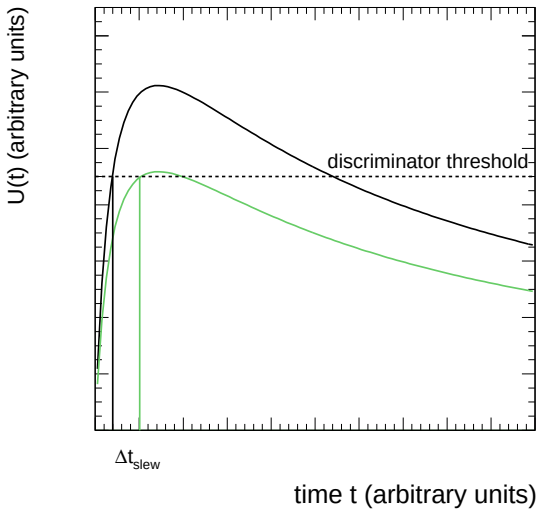

Figure 4.4: Illustration of the time slewing effect. Signals with larger pulse heights cross the discriminator threshold earlier.

charge due to the background radiation cause fluctuations of the r(t) relationship which deteriorate the spatial resolution. The background flux depends on the instantaneous LHC luminosity which decreases during an accelerator run. The strategy to cope with this effect is to frequently recalibrate the r(t) relationships for the whole spectrometer such that this effect becomes negligible within a calibration cycle. A new determination of the r(t) relationship every hour is intended for this purpose.

Temperature The gas pressure in the tubes is regulated to be 3 bar absolute. Consequently, the gas is getting less dense when the temperature rises leading to a longer mean free path-length for the drifting electrons and thus to an increased drift velocity and shorter drift time. The magnitude of this effect is $^{\Delta t_{\mathrm{drift}}}/_{\Delta T} = -2.34 \pm 0.06\ ^{\mathrm{ns}}/_{\mathrm{K}}$ [61].

Magnetic Field The largest effect is caused by the component of the magnetic field perpendicular to the drift path which deflects the drifting electrons on their path to the anode wire and thus prolongs their drift times. Especially for MDT chambers installed directly on the toroid magnet coils the field strength along the tubes and across individual tube layers is quite inhomogeneous leading to a variation of the maximum drift time by $70\,\mathrm{ns}\,^{B^2}/_{\mathrm{T}^2}$ or by up to 25 ns along the tubes of certain chambers [62].

As it is not advantageous to choose the calibration regions smaller than one MDT multilayer, the strategy to correct for the last two effects is to determine calibration constants for $|\vec{B}| = 0$ and a mean chamber temperature. It has been shown that a precision of better than 1 ns on the drift time prediction within a calibration region can be reached [61,63,64]. The accuracy of the Lorentz-angle correction is studied with cosmic muons in Section 4.9.4.

4.3.1 Required Statistics

In several studies summarized in the following the amount of data necessary for the determination of the calibration parameters with the required statistical accuracy have been investigated [54, 63–65].

Determination of t_0 About 10 000 drift time measurements are needed in a drift time spectrum to determine t_0 with a precision of 0.5 ns. Since a muon track from the interaction point crosses about 20 tubes in the spectrometer, roughly $2 \cdot 10^8$ good muon tracks are required to determine t_0 separately for each tube. However, t_0 differences between the 24 tubes connected to the same mezzanine board are only about 1 ns, and stable in time. The combination of tubes with similar t_0 values allows a reduction of the required statistics to about $3 \cdot 10^7$ muon tracks.

r(t) Calibration In a conservative estimation, about 5 000 tracks are needed per calibration region to achieve 30 μm precision everywhere in the muon spectrometer. Each muon crosses about 6 MDT multilayers; thus about $2 \cdot 10^6$ good muon tracks are required for computing r(t) relationships for the whole spectrometer. The dependence of the performance of the autocalibration algorithm on the available number of muon tracks is studied in Section 4.6.7.

4.3.2 Muon Calibration Stream

Due to the total rate limit, the maximum rate of muon triggered events recorded on disk is 40 Hz, or about 360 muons per hour and MDT chamber. In order to obtain enough statistics to follow possible variations of the drift properties with time, muon events are extracted at the second trigger level with a rate of 1 kHz which corresponds to several thousands of muons per chamber and hour. With this rate, a daily t_0 determination and an hourly recalibration of the r(t) relationships is feasible. Figure 4.5 shows the expected trigger rates for different level 1 (L1) p_{T} thresholds for a luminosity of $\mathscr{L} = 10^{31}\,\mathrm{cm}^{-2}\mathrm{s}^{-1}$ in the LHC start-up phase. The muons are mainly produced in charm, beauty and π/K-decays and their p_{T} spectrum drops exponentially with transverse momentum. To collect sufficient statistics for the calibration of the MDT chambers, the lowest possible L1 single muon trigger threshold of $p_{\mathrm{T}} > 4\,\mathrm{GeV/c}$ is used during the start-up phase of the LHC. The cumulative rate is expected to be 1730 Hz [52] and sufficient to perform the calibration. For increasing LHC luminosities, the p_{T} thresholds will be raised accordingly to stay within the acceptable data rates.

4.3.3 Performance Goals

The performance goals for the r(t) calibration are on the one hand defined by the desired momentum resolution of the muon spectrometer of 10 % for $p_{\mathrm{T}} \simeq 1\,\mathrm{TeV/c}$ and on the other hand constrained by the limited available statistics for an hourly recalibration and the required size of the calibration regions. To achieve this momentum resolution a spatial resolution of the MDT chambers of 35 μm is required. The average single drift tube resolution is 80 μm, thus the calibration accuracy has to stay within 30 μm including all corrections on t_{TDC} and t_{drift}. Hence, a r(t) accuracy of $\lesssim 20\,\mu$m is intended to leave margin for the accuracy of the drift time corrections.

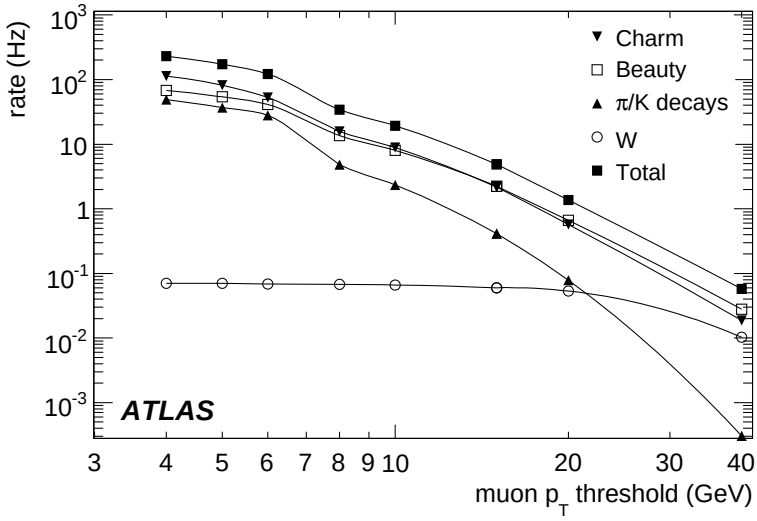

Figure 4.5: Estimated single muon trigger rate and its contributions for a luminosity of $\mathscr{L} = 10^{31}\,\mathrm{cm}^{-2}\mathrm{s}^{-1}$ depending on the muon p_T threshold [52].

4.4 Calibration of the Space-to-Drift-Time Relationship

The strategy for the determination of the r(t) relationship with high accuracy consists of two steps:

1. Determination of an initial r(t) relationship. It is usually directly calculated from the drift time spectrum using the so-called *integration method* described below but could also be calculated, e.g. with the drift detector simulation program Garfield [66, 67], or taken from previous calibrations, for example in test beam measurements.

2. The initial space-to-drift-time relationship is used to reconstruct muon track segments within an MDT chamber or multilayer. The residuals of the hits belonging to track segments are used to iteratively refine the r(t) relationship. This procedure using muon tracks in the MDT chambers without external reference is called *autocalibration*.

4.4.1 Integration Method

The integration method provides a fast and simple way to derive the r(t) relationship directly from the measured drift time spectrum with derivative:

$$\frac{dN}{dt} = \frac{dN}{dr}\,\frac{dr}{dt}. \tag{4.4}$$

Assuming that the muons are traversing the tube uniformly in r, $^{dN}/_{dr}$ is constant and can be replaced by $^{N}/_{r_\mathrm{max}}$ where N is the total number of collected drift times in the spectrum and r_max is the maximum drift radius, 14.6 mm in the MDT case. The r(t) relationship is

calculated by integrating Equation (4.4) from t_0 to $t_{\max}$ (see Section 4.2):

$$r(t)^{\text{initial}} = \int_{t_0}^{t_{\max}} \frac{dr}{dt'} dt'. \tag{4.5}$$

$$r(t)^{\text{initial}} = \int_{t_0}^{t_{\max}} \frac{r_{\max}}{N} \frac{dN}{dt'} \, dt'. \tag{4.6}$$

4.4.2 Principle of Autocalibration

All autocalibration methods use the redundant information of muon track fits through several tube layers (at least three) to determine the r(t) relationship. This can be illustrated in the following way: The initial r(t) relationship is used to reconstruct straight track segments within an MDT multilayer assuming a preliminary tube resolution function $\sigma(r)$. Using the track parameters, the residuals

$$\Delta(t) = r(t) - d \tag{4.7}$$

are calculated for each tube hit where r(t) is the measured drift radius according to the r(t) relationship and d is the shortest distance of the track to the respective anode wire (cp. Figure 4.6).
If the r(t) relationship is not correct, the drift radii obtained from it deviate systematically from the correct drift radius $r(t)^{\text{true}}$:

$$r(t)^{\text{true}} = r(t) + \epsilon(t). \tag{4.8}$$

As the muon track is determined by fitting to the (incorrect) drift radii, also d deviates from the correct distance of the ionizing track to the anode wire by an amount δ:

$$d^{\text{true}} = d + \delta. \tag{4.9}$$

Inserting $\epsilon(t)$ and δ into equation (4.7),

$$\Delta(t) = r(t)^{\text{true}} - \epsilon(t) - \left(d^{\text{true}} - \delta\right) \tag{4.10}$$

and using $r(t)^{\text{true}} = d^{\text{true}}$, the residual can be written as

$$\Delta(t) = \delta - \epsilon(t). \tag{4.11}$$

Both deviations, $\epsilon(t)$ and δ, have a statistical as well as a systematic component. Two algorithms have been investigated in order to determine the systematic component of $\epsilon(t)$: The standard and an improved, so-called *analytic* autocalibration method.

Standard Autocalibration

The original autocalibration procedure [68, 69] assumes that the statistical components of $\epsilon(t)$ and δ vanish once a sufficient number of muon tracks has been collected. The r(t) relationship is corrected by the mean value of the residual distributions as a function of the drift time (in intervals Δt). As $\epsilon(t)$ and δ are strongly correlated, the method is

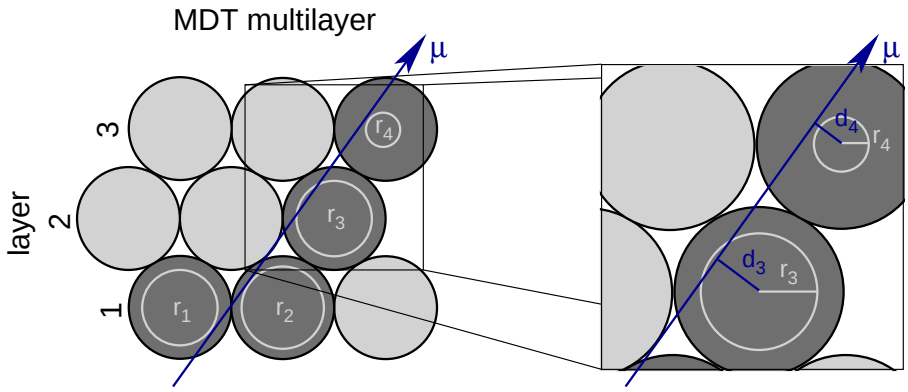

Figure 4.6: Illustration of a muon traversing an MDT chamber multilayer with three tube layers with hits in four tubes. A straight track is fit to the four drift radii. As visible in the magnified region, the distances between track and wires is different from the drift radii. These differences are the track residuals, which are the criterion for the autocalibration to improve the r(t) relation.

applied iteratively. The measured drift radii $r^i(t)$ of iteration i are corrected by the mean residuals $\langle \Delta^i(t) \rangle$, resulting in an improved relationship $r^{i+1}(t)$:

$$r^{i+1}(t) = r^i(t) - \langle \Delta^i(t) \rangle \,. \tag{4.12}$$

Depending on the available statistics, after about 10 iterations, the method stops to further improve the r(t) relationship. While the residuals calculated with $r(t)^{\text{initial}}$ are shifted systematically by up to 500 μm, the residual distributions after autocalibration are centred at zero within about 20 μm independent of the drift time. However, this method only converges to the correct r(t) relationship when the incidence angles of the muons used for the calibration have sufficient spread. As it turns out that this is not the case for all calibration regions in the muon spectrometer such that this method does not always converge to the correct r(t) relationship (see Section 4.6.4).

Analytic Autocalibration

While the standard method applies average corrections to the r(t) relationship, this improved autocalibration method [63, 64, 70] takes into account the correlations between the different hits on a track as well as correlations between different tracks. The correlation matrices are calculated analytically to first approximation in order to speed up the iteration and minimize the number of tracks required for the autocalibration to converge. The method shows improved performance for the difficult calibration regions and only needs about 3 000 tracks to reach the required calibration accuracy of 20 μm while the standard method requires about 10 000 tracks for similar accuracy. It is the basis of the method presented in this work and is discussed in detail in the following sections.

4.5 Autocalibration with Curved Tracks

The autocalibration algorithms discussed so far use straight track fits on the hits of only one MDT multilayer for two reasons. First, the trajectories of the muons traversing an

MDT chamber are bent in the magnetic field. The sagitta of a muon track is

$$s = \frac{p'}{B_\perp} - \sqrt{\left(\frac{p'}{B_\perp}\right)^2 - \frac{l^2}{4}} \tag{4.13}$$

where $B_\perp$ is the azimuthal component of the toroidal magnetic field perpendicular to the track bending plane, l is the track length and p' the muon momentum at the entrance of the muon spectrometer. For middle barrel chambers with an average magnetic field strength of $B_\perp = 0.5\,\mathrm{T}$ and a minimum momentum of muons at the interaction point of about $p_\mathrm{T} = 4\,\mathrm{GeV/c}$ needed to reach them as well as $p' = p - 3\mathrm{GeV/c}$ [2], the track sagitta across whole chamber ($l = 500\,\mathrm{mm}$) is $s = 4.8\,\mathrm{mm}$ whereas it is $s = 120\,\mu$macross each multilayer ($l = 80\,\mathrm{mm}$).
The second reason is the better stability and uniformity of the operational parameters within a multilayer, such as temperature, magnetic field and gas composition. However, the performance of the autocalibration algorithms, especially of the analytic method, is considerably increasing with the number of hits included in the track fit. In particular for the calibration of the majority of the chambers with three tube layers per multilayer, the algorithms are operating at the limit of the available information as already two hits are needed to define the straight track. Especially at the LHC design luminosity, the high background counting rate together with the electronics dead time significantly reduces the efficiency of detecting the correct muon hit in a tube. If hits on the track are lost, the straight track fit restricted to multilayers cannot be used for the calibration of the ATLAS muon spectrometer. As corrections for temperature and magnetic field gradients on the r(t) calibration reach an accuracy of better than 1 ns [61–63], the extension of the analytical autocalibration procedure to curved track fits across both multilayers of the MDT chambers has been studied. The significant bending of the tracks has to be taken into account in this case by using polynomials of order P for the track fit. The straight track fit is a special case with $P = 1$.

4.5.1 Working Principle

The principle of the autocalibration with curved tracks is to collect N muon tracks and use their information to correct the r(t) relationship such that the weighted sum of all measured residuals becomes minimal. The advantage to the existing approaches is the full information of the muon tracks and their residuals is used. The procedure consists of four steps:

- **Track fit:** The first step is to fit a polynomial of order P to the hits in a chamber. With this so-called track-segment, the residual $\Delta(r_k)$ of the $\mathrm{k^{th}}$ hit on the segment is expressed with a parametrized form of the distance d_k between track and wire.
- **Influence on small shifts:** The dependence of the residual $\Delta(r_k)$ on small errors $\delta r_{k'}$ on the radii $r_{k'}$ included in the segment fit is determined. This leads to a matrix equation for the residuals, where the matrix elements are determined analytically.
- **Correction function:** The shifts δr_k are used to correct the r(t) relationship such that the residuals are minimized. In general the matrix equation for the residuals

[2] Note that on average muons loose about 3 GeV/c of momentum in the detector layers in front of the muon spectrometer.

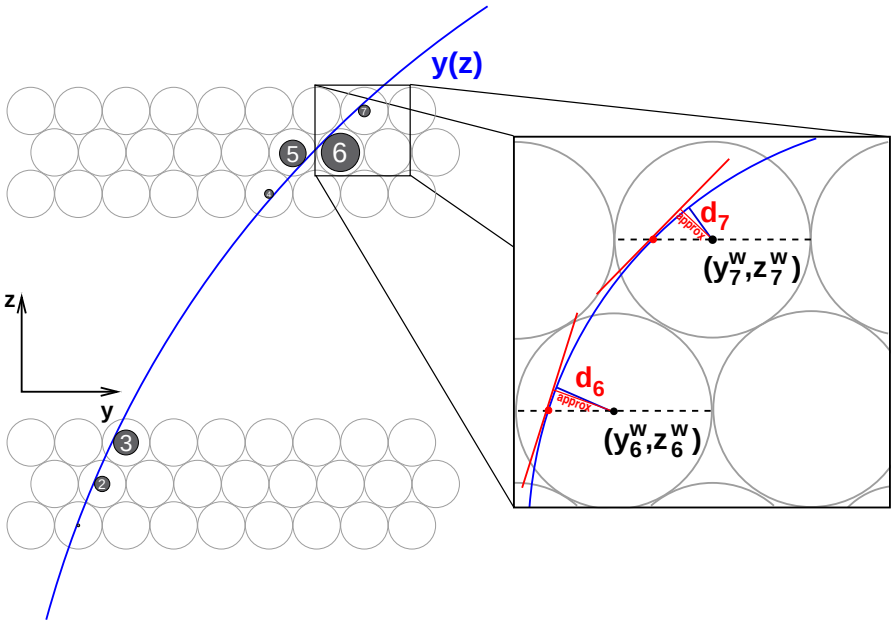

Figure 4.7: The drawing shows a schematic view of an MDT chamber with a parabolic fit on 7 driftradii. The smaller, magnified area points out how d_k is defined as the distance between the tangents on the curved track and the appropriate anode wires.

does not have an analytic solution. Thus the δr_k are parametrized by expanding them as a linear combination of orthonormal functions (e.g. Legendre polynomials) with coefficients determined by minimizing the weighted sum of the residuals of all tracks.

- **Iteration:** Already one application of the corrections improves the initial r(t) relationship significantly. However, to obtain r(t) with the required accuracy of 20 μm, the procedure has to be iterated to account for approximations in the analytical expressions. The iteration converges to $\delta r_k \approx 0$ after typically 5 iterations.

4.5.2 Curved Track Fit

A well performing track fit is crucial for accurate autocalibration. In particular the ambiguities if a muon passes the anode wire on its left- or right-hand side have to be resolved. Most muons used for calibration will be relatively low energetic with transverse momenta between 4 and 10 GeV/c (see section 4.3.2). They are following curved trajectories with a sagitta of up to about 5 mm within chambers. A curved track is fitted to all K hits associated in an MDT chamber by minimizing the χ^2 function

$$\chi^2 = \sum_{k=1}^{K} \frac{(r_k - d_k)^2}{\sigma(r_k)^2}. \tag{4.14}$$

In the numerator is the residual $\Delta(r_k)$ squared with $r_k = r(t_k)$ (see Equation (4.7)). In the denominator is the drift tube resolution $\sigma(r_k)$ squared. The aim is to find a suitable parametrization for d_k and to determine the parameters from the χ^2 fit.
In general the track can be described by a polynomial of order P in the $y-z$ plane of the

chamber coordinate system (see Figure 4.7):

$$y(z) = \sum_{p=0}^{P} \alpha_p u^p(z). \tag{4.15}$$

The shortest distance d_k between the track $y(z)$ and the k^{th} anode wire at the position (y_k^w, z_k^w) can be expressed analytically by replacing it into good approximation for the small curvature by the distance between the wire and the tangent to the trajectory in the point $y(z_k^w)$,

$$t(z) = y'(z_k^w)(z - z_k^w) + y(z_k^w) \tag{4.16}$$

with

$$y'(z_k^w) \equiv \frac{dy}{dz}(z_k^w) =: m_k, \tag{4.17}$$

with the result

$$d_k = \frac{|-y_k^w + t(z_k^w)|}{\sqrt{1+m_k^2}} = \frac{|y(z_k^w) - y_k^w|}{\sqrt{1+m_k^2}} \tag{4.18}$$

which is the parametrization in Equation (4.15):

$$d_k = \frac{1}{\sqrt{1+m_k^2}} \left| \sum_{p=0}^{P} \alpha_p u^p(z_k^w) - y_k^w \right|. \tag{4.19}$$

The derivative m_k from the initial track fit is treated as a constant to good approximation during χ^2 minimization and iteration of the track fit. The parameters α_p are determined by minimizing the χ^2 function of Equation (4.14) analytically resulting in the expression for the residual of the k^{th} hit (see Appendix C.1 for the derivation):

$$\boxed{\Delta(r_k) = r_k - \frac{1}{\sqrt{1+m_k^2}} \left| \sum_{p=0}^{P} \sum_{q=0}^{P} M_{pq}^{-1} b_q u^p(z_k^w) - y_k^w \right|.} \tag{4.20}$$

Both, M_{pq}^{-1} and b_q, include the sum over all hits on the track and can be called hit-matrix and hit-vector, respectively. They are defined to get a simple expression for the fit parameters α_p:

$$\alpha_p = \sum_{q=0}^{P} M_{pq}^{-1} \cdot b_q. \tag{4.21}$$

4.5.3 Sensitivity of the Residuals to the Drift Radii

With Equation (4.20) an expression for the residuals has been found which depends on all hits on the track since it is the solution of the χ^2 minimization for the track fit. The interesting question for the r(t) calibration is, how the residual $\Delta(r_k)$ changes, when small offsets $\delta r_{k'}$ are added to any of the drift radii $r_{k'}$ on the track (including $k' = k$):

$$\tilde{r}_{k'} = r_{k'} + \delta r_{k'}. \tag{4.22}$$

The residual $\tilde{\Delta}_k$ including these offsets is to first order:

$$\tilde{\Delta}(r_k) \simeq \Delta(r_k) + \sum_{k'=1}^{K} \left.\frac{\partial \Delta(r_k)}{\partial r_{k'}}\right|_{(r_1,\ldots,r_K)} \delta r_{k'} \tag{4.23}$$

or

$$\tilde{\Delta}(r_k) \simeq \Delta(r_k) + \sum_{k'=1}^{K} D_{kk'}\, \delta r_{k'} \tag{4.24}$$

with

$$D_{kk'} = \left.\frac{\partial \Delta(r_k)}{\partial r_{k'}}\right|_{(r_1,\ldots,r_K)} \tag{4.25}$$

calculated analytically in Appendix C.2, Equation (C.13). Expression (4.24) with Equation (C.13) can be used to determine corrections to the measured drift radii using the information from the residual of the track hit.

4.5.4 The Correction Function

In general $\delta r_k\, (k = 1, ..., K)$ cannot be determined on a track-by-track basis. For segments with K hits, there are K equations like (4.24) with K variables δr_k. With $P+1$ Equations (C.5)–(C.7) the χ^2 minimization determines uniquely for $K > P + 1$ the $P + 1$ track parameters and $K-(P+1)$ parameters remain for the determination of δr_k. The equation system is thus under-determined and corrections $\delta r(t)$ to the drift radii are parametrized as a linear combination of base functions $v(t)$ of the drift time t, for instance, Legendre polynomials:

$$\delta r(t) = \sum_{a=0}^{A} \beta_a v_a(t). \tag{4.26}$$

To determine $\delta r(t)$, the information from N fitted muon tracks is taken into account with the χ^2 function

$$\chi^2 = \sum_{n=1}^{N} \sum_{k=1}^{K^n} \frac{\left(\Delta^n(r_k) + \sum\limits_{k'=1}^{K^n} \sum\limits_{a=0}^{A} \beta_a D^n_{kk'} v_a(t^n_{k'})\right)^2}{\sigma^2(r^n_k)} \tag{4.27}$$

or

$$\chi^2 = \sum_{n=0}^{N} \left| \boldsymbol{\Delta}^n + \sum_{a=0}^{A} \beta_a \boldsymbol{D}^n \boldsymbol{v}^n_a \right|^2 \tag{4.28}$$

with the definitions:

- Residual vector: $\boldsymbol{\Delta}^n := \left(\frac{\Delta_1^n}{\sigma^2(r_1^n)}, ..., \frac{\Delta_K^n}{\sigma^2(r_K^n)}\right)$
- Residual matrix: $\boldsymbol{D}^n := \frac{D_{kk'}^n}{\sigma^2(r_k^n)}\Big|_{(k,k'=1,...,K^n)}$
- Base function vector: $\boldsymbol{v}_a^n := (v_a(t_1^n), ..., v_a(t_K^n))$

The coefficients β_a are then determined by requiring:

$$\frac{\partial\chi^2}{\partial\beta_{a'}} = 2\sum_{a=0}^{A}\beta_a \underbrace{\sum_{n=0}^{N}\boldsymbol{D}\boldsymbol{v}_a^n\cdot\boldsymbol{D}^n\boldsymbol{v}_{a'}^n}_{:=N_{aa'}} - \underbrace{2\sum_{n=0}^{N}\boldsymbol{\Delta}^n\cdot\boldsymbol{D}^n\boldsymbol{v}_{a'}^n}_{:=B_{a'}} \stackrel{!}{=} 0 \tag{4.29}$$

$$\Rightarrow \boxed{\beta_a = \sum_{a'=0}^{A} N_{aa'}^{-1}B_{a'}} \tag{4.30}$$

4.5.5 Iteration and Convergence

Equation (4.30) together with Equation (4.26) determine the correction function $\delta r(t)$ for the r(t) relationship. Because of the linear approximation used in Equation (4.24), the optimum r(t) relationship cannot be found in one step by analytical autocalibration, but the r(t) relationship has to be corrected iteratively:

$$r^{i+1}(t) = r^i(t) - \delta r^i(t). \tag{4.31}$$

The iterations are stopped when the χ^2 from Equation (4.28) divided by the number of tracks used is not further improving in successive iterations and when in addition the correction function $\delta r(t)$ is sufficiently close to zero as quantitatively defined in Section 4.6.3.

4.5.6 Fixed Points

Even if the correction function to an arbitrary r(t) relationship cannot be determined analytically, there are track configurations containing the information about the exact r(t) relationship for particular radii. These so-called fixed points depend on the incidence angle of the muon trajectory and its position relative to the wires. As an example, Figure 4.8 shows four possible fixed point configurations.
During standard operation, only muons from collisions are used by the autocalibration. As they originate from the interaction vertex, the position and the size of an MDT chamber defines the range of incidence angles of tracks for the calibration region. The muons are mainly low energetic, such that the angular range is slightly enlarged by the fact that oppositely charged muons are deflected at opposite angles by the magnetic field. As the density of fixed points depends on the incidence angles of the tracks and their spread within a calibration region, there are calibration regions with many, but also regions with nearly no fixed points.

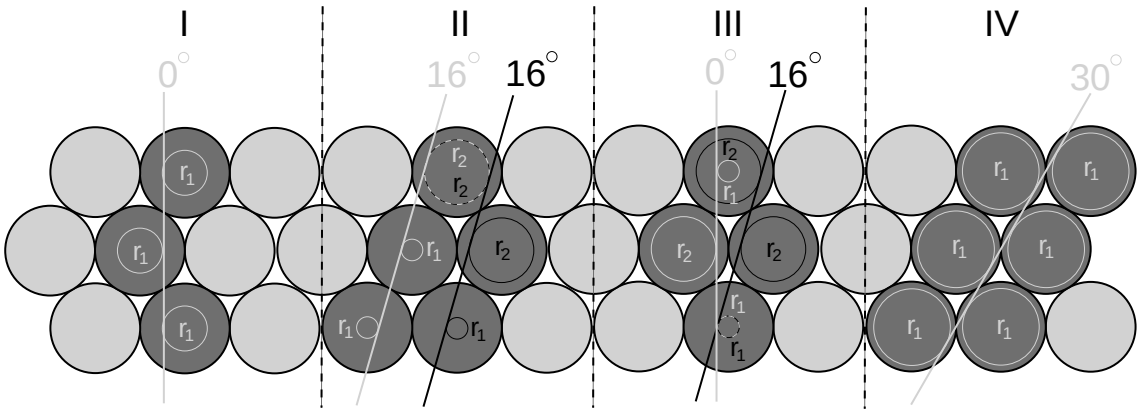

Figure 4.8: Four examples of track configurations which exactly determine the r(t) relationship for particular radii for three tube layers. One track can be sufficient if all measured drift times are equal (I and IV). Using the correlations between two different tracks, two different drift radii can be determined (II and III).

Tracks around 30 Degrees

The most difficult case is for tracks with incidence angles of 30 degrees where only one fixed point exists (see Figure 4.8, IV). Even worse, the residuals of tracks at 30 degree, which do not also cross the neighbouring tubes, are by definition equal to zero because the distances of the track from all anode wires are the same. Therefore it is impossible for the autocalibration to improve the r(t) relationship with tracks at this angle and it is very challenging to calibrate MDT chambers, for which the track angles are spread around 30 degrees.

Increasing the Number of Fixed Points

The number of fixed points is increasing with the number of hits on the track, which is an additional motivation for using the full MDT chamber for the autocalibration.

In principle the number and position of the fixed points as a function of the track parameters can be calculated (see [70]). In reality, the possible track configurations for MDT chambers are too complex to be well predictable for each MDT chamber of the ATLAS muon spectrometer. Nevertheless, the exact information about the r(t) relationship for these particular radii is taken into account by the analytic autocalibration as the correlation between all tube hits is included in the track fit resulting in faster convergence of the method in calibration regions with high fixed points density.

4.6 Performance Tests of the Autocalibration with Simulated Muons

In this section the performance of the new autocalibration method is tested using the ATLAS detector simulation with a dedicated dataset of single muons. The algorithm is tested for two representative MDT chambers before determining the r(t) accuracies for

every calibration region and their influence on the momentum resolution of the muon spectrometer in Section 4.8.

4.6.1 The Dataset for the Performance Tests

For the calibration of the MDT chambers, a dedicated muon calibration data stream is extracted at the second trigger level (see Section 4.3.2) with a maximum rate of 1 kHz. The data stream is distributed to three calibration centres in Ann Arbor (Michigan, USA), Munich (Germany) and Rome (Italy). Track segments are reconstructed in the computing centres using standard calibration constants from previous calibration. The data are stored in a dedicated format (Calibration Ntuples), which includes, in addition to the detector raw data, preliminary track segments. The performance of the autocalibration is tested with a sample of 5 million simulated single muons at fixed transverse momenta of 4, 6 and 10 GeV/c. For the event generation, the detector simulation and the event reconstruction the ATLAS software framework Athena [71] version 14.2.21 has been used. The detector simulation is based on the software tool-kit GEANT4 [72]. The muons of different transverse momenta are mixed according to their expected relative trigger rates at an instantaneous LHC luminosity of $\mathscr{L} = 10^{31}\,\mathrm{cm}^{-2}\mathrm{s}^{-1}$ (compare Figure 4.5). The rates at the first trigger level have been estimated in [52] and are summarized in Table 4.1. The statistics of the Monte Carlo dataset corresponds to almost one hour of data taking in the start-up phase of the LHC. The muons in the sample are uniformly distributed in the range $|\eta| < 3.0$ and $0 < \phi \leq 2\pi$ covering the full geometrical acceptance of the ATLAS muon spectrometer.

Table 4.1: Estimated muon rates and number of events generated corresponding to about one hour of data taking for different L1 trigger thresholds at a luminosity of $\mathscr{L} = 10^{31}\,\mathrm{cm}^{-2}\mathrm{s}^{-1}$ [52] as used for the autocalibration performance study.

L1 threshold (GeV/c)	4	6	10	15	20	40
Rate (Hz)	1730	640	360	30	20	10
Fractions	1.00	0.37	0.13	0	0	0
Total nb. of events ($\times 10^6$)	5.00	1.85	0.65	0	0	0

Hit Distribution

Even if the generated four-vectors of the muons are uniformly distributed in the acceptance region of the detector, several effects reduce the hit rates in certain regions of the spectrometer. A rough estimate assuming an equal distribution across 1088 MDT chambers in three layers leads to $5 \cdot 10^6/(1088/3) \approx 1.4 \cdot 10^4$ muons per chamber. A fraction of the low-energetic muons loose too much energy in the calorimeters to reach the muon spectrometer or all three layers of it. In addition there are detector regions where no MDT chambers are installed, or installed yet, e.g. the transition region between the barrel and the end caps. Thus the estimated number has to be corrected by 10–15 %. Figure 4.9 gives an overview of the muon spectrometer with the numbers of muons crossing the individual MDT chambers:

- **Inner layer:** About 10 000 track segments are reconstructed in most of the chambers of the inner layer. Exceptions are BIS chambers at $|\eta|$-positions larger than five, where the muon rate is decreased due to the solid angle the chambers are covering. The same argument is true for the inner end cap chambers in sectors 1, 9, 11 and 15 which are smaller than chambers in the neighbouring sectors. Furthermore, barrel chambers in sectors 11 and 15 have a reduced muon rate due to the additional material of the calorimeter rails in front of them.
- **Middle layer:** Barrel chambers in the middle layer have decreased muon hit rate with respect to the inner chambers (about $3000 - 5000$ muons). Very low-energetic muons are bent too much in the magnetic field in order to reach the middle layer. In addition, track segments have to be discarded due to bad quality of the preliminary straight-segment fit for the curved tracks in the middle chambers which are inside the magnetic field in contrast to the inner and outer chambers. The middle end cap chambers in general have a larger muon hit rate (about 10 000 track segments). An exception are chambers in the small sectors at largest radius where muons can be bent out of the acceptance by the barrel magnetic field (the same is true for the outermost small end cap chambers EOS).
- **Outer layer:** Chambers of the large sectors generally have larger statistics than the ones of small sectors due the lower bending power of the magnetic field and less material in front of them. The additional material in the feet region of the detector, together with smaller chamber dimensions, explains the lower muon rate in sectors 12 and 14 of the barrel.

4.6.2 Testing Procedure

With the simulated single muon data set described above, the accuracy of the autocalibration with curved tracks will be tested for all calibration regions. First, a suitable definition of the accuracy of the r(t) relationship is given.

Definition of the r(t)-Accuracy

To compare r(t) relationships with each other, two definitions are used to quantify their accuracy:

1. The average quadratic deviation from the correct drift radii r^{true} in the simulation:

$$\rho := \sqrt{\frac{1}{|r_{\max} - r_{\min}|} \int_{r_{\min}}^{r_{\max}} (r' - r^{\text{true}})^2 dr'}. \tag{4.32}$$

2. The resolution-weighted average quadratic deviation from the correct drift radii:

$$\hat{\rho} := \frac{\sqrt{\frac{1}{|r_{\max} - r_{\min}|} \int_{r_{\min}}^{r_{\max}} \omega(r')^2 (r' - r^{\text{true}})^2 dr'}}{\frac{1}{|r_{\max} - r_{\min}|} \int_{r_{\min}}^{r_{\max}} \omega(r') dr'} \tag{4.33}$$

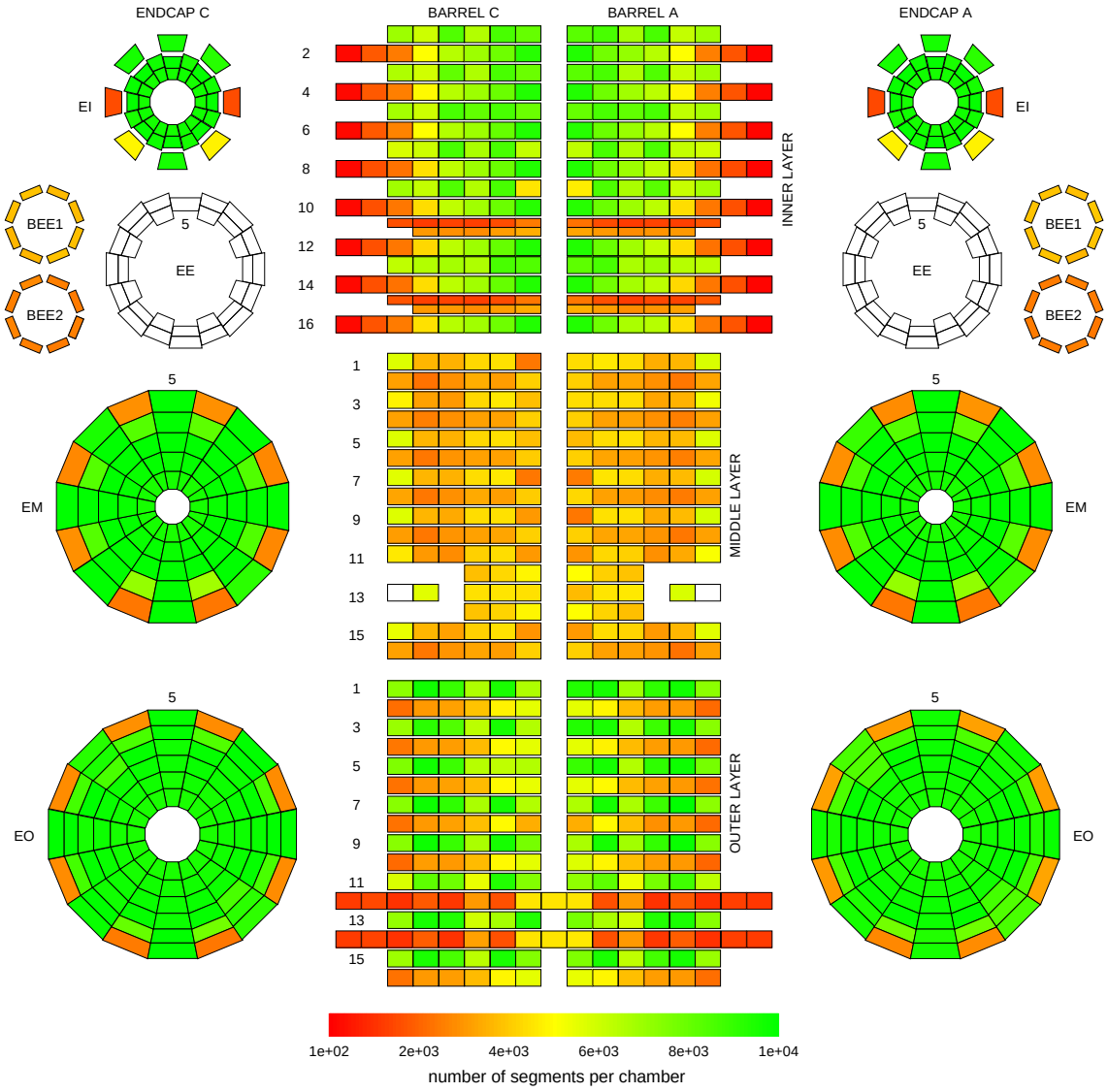

Figure 4.9: Numbers of track segments per MDT chamber in three layers of each barrel hemisphere A and C, in the three main layers of each end cap and in special chambers in the transition regions between barrel and end caps for $5 \cdot 10^6$ generated single muons. The EE chambers of the transition region are not fully installed yet and not included in the simulation. In the barrel layers, the horizontal rows correspond to azimuthal sectors with small (even numbers) and large (odd numbers) chambers. The same clock-wise numbering viewing from the interaction point is used for the sectors of the end cap wheels. The η-numbers (columns) are numbers from inside ($z = 0$) out in each barrel hemisphere and from small to large radii in each end cap wheel.

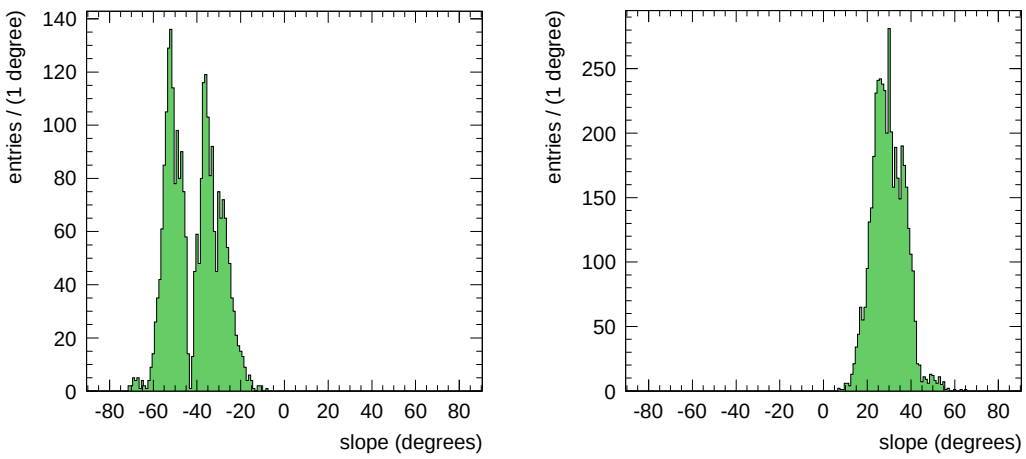

(a) BOS5C04 (b) BML3A01

Figure 4.10: Distributions of the incidence angles of muons crossing the BOS5C04 (a) and BML3A01 (b) chambers.

with $\omega(r) := \frac{1}{\sigma(r)}$.

The first definition is a measure of the absolute accuracy of the r(t) calibration. The second takes into account the effect of the r(t) accuracy on the muon track fit which depends on spatial drift tube resolution $\sigma(r)$. To reach a resolution of the transversal momentum of 10 % for highly energetic muons in the TeV scale, the precision of the r(t) relationship shall be better than 20 μm.

Overview of the Performance Tests

The ATLAS muon spectrometer consists of 1150 MDT chambers. For the autocalibration with curved muon tracks, each of them constitutes a calibration region with its own environmental conditions and challenges. To demonstrate the robustness of the r(t) calibration, two MDT chambers with different challenges of the r(t) calibration are chosen:

BOS5C04 is a chamber with three tube layers per multilayer in the outermost barrel layer installed on one of the toroid coils resulting in a rather inhomogeneous magnetic field along the drift tubes. Due to its η-position in the spectrometer, the angular acceptance is small, but the bending of oppositely charged muons in the magnetic field leads to a rather broad two peak distribution of muon incidence angles (see Figure 4.10(a)).

BML3A01 is a chamber in the middle barrel MDT layer with 3 tube layers per multilayer. Its position in between the barrel toroid coils corresponds to a relatively strong but homogeneous magnetic field distribution along the drift tubes. In addition, the η-position in the spectrometer implies a distribution of muon incidence angles around 30 degrees as shown in Figure 4.10(b). The two facts together make this chamber one of the most difficult to calibrate.

The end cap chambers are easier to calibrate because they are not embedded in the magnetic field and the tracks are not curved within a chamber. For the same reason and because of their eight tube layers autocalibration of the inner MDT chambers is less challenging.

Increasing the Statistics Even if the total number of simulated muons of $5 \cdot 10^6$ is relatively large, only 3500 muons cross the BOS5C04 and 5200 the BML3A01 chamber. As the ATLAS muon spectrometer is azimuthally symmetric, except for the feet region, the chambers BOS5C02, BOS5C04, BOS5C06 and BOS5C08 as well as BML3A01, BML3A03, BML3A05, BML3A07 with the same condition are combined for testing the calibration in order to increase the number of muons when needed. This combination of calibration regions is only possible for simulation studies, as the operating conditions (gas temperature, pressure, magnetic field) are not the same for the different MDT chambers in the real experiment. The number of real muons needed for an adequate r(t) calibration is determined in Section 4.6.7.

4.6.3 Determination of the Convergence Criterion

The selection of a suitable convergence criterion is crucial for a well performing autocalibration algorithm: First it has to be ensured that the best possible r(t) relationship is found by the algorithm and second that no unnecessary iterations are performed without improving the r(t) accuracy in order to safe computing time. To monitor the evolution of the r(t) accuracy in the simulation, the differences between the drift radii obtained by the autocalibration and the correct drift radii are analysed as a function of the correct drift radius. For the initial r(t) relationship $r(t)^{\text{initial}}$, the correct r(t) relationship is modified by subtracting a parabola with amplitude A

$$r(t)^{\text{initial}} = r(t)^{\text{true}} - A \cdot \frac{4}{r_{\max}} \cdot r(t)^{\text{true}} \left(\frac{r(t)^{\text{true}}}{r_{\max}} - 1 \right), \tag{4.34}$$

with the inner tube radius $r_{\max} = 14.6\,\text{mm}$ (see Figure 4.11(a)). For these first tests, the amplitude A is chosen such that the accuracy of the initial r(t) relationship is $\rho = A/\sqrt{2} = 250\,\mu\text{m}$.
As in the real data the correct r(t) relationship is unknown, suitable parameters have to be found to evaluate the quality of the r(t) relationship. One of them is the χ^2 of the residuals after each iteration of the autocalibration from Equation (4.27), divided by the number N of muon tracks used (χ^2/N_{dof}). The second information about convergence of the r(t) calibration is provided by the root mean square $\sigma(\delta r(t))$ of the correction function $\delta r(t)$ (see Section 4.5.4). It is a quantitative measure of by how much the autocalibration changed the r(t) relationship in the last iteration. How to combine these two variables into a robust convergence criterion will be exemplary demonstrated for the selected BOS and BML chambers (see Section 4.6.2):

BOS Chambers Figure 4.11(a) shows the difference $r - r^{\text{true}}$ as a function of r^{true} for the BOS5C04 chamber for successive iterations of the autocalibration. The r(t) accuracies ρ ($\hat{\rho}$) are significantly improving with the first two iterations from 255 (264) μm to 11.4 (9.7) μm. After the fourth iteration, the autocalibration improves the r(t) relationship

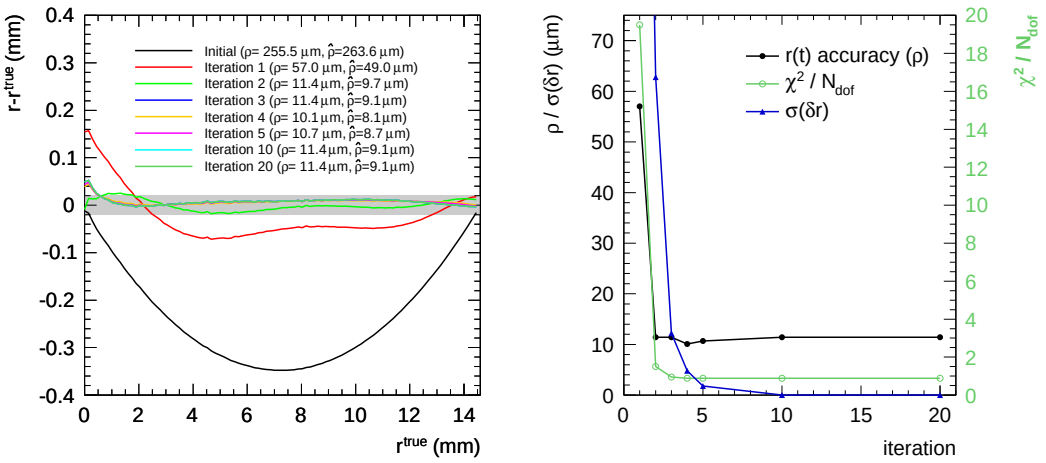

(a) (b)

Figure 4.11: (a) Deviation of the calibrated r(t) relationship from the correct one for increasing number of iterations for the BOS5C04 chamber. The shaded band around zero marks the required accuracy of $\pm 20\,\mu$m. (b) The r(t) accuracy ρ, the rms $\sigma(\delta r(t))$ of the correction function and the χ^2/N_{dof} of the residuals as a function of the number of iterations.

only marginally. This behaviour is also reflected in the parameters χ^2/N_{dof} and $\sigma(\delta r(t))$ (see Figure 4.11(b)). As expected, the evolution of χ^2/N_{dof} follows well the one of the r(t) accuracy ρ and converge to χ^2/N_{dof}=0.9 and $\rho = 10\,\mu$m, respectively, in iteration 4. The average quadratic deviation $\sigma(\delta r(t))$ of the correction function $\delta r(t)$ on the other hand, steadily decreases with increasing number of iterations and converges to zero after iteration 9.

The autocalibration thus only needs three iterations to determine an r(t) relationship to better than $\pm 20\,\mu$m (absolut maximal deviation) for $r > 0.5$ mm. Only close to the wire the deviation is about $50\,\mu$m. How to improve the precision at very small drift radii is studied in Section 4.6.5. The accuracy of the r(t) relationship after 3$^{\mathrm{rd}}$ iteration of $\rho = 11\,\mu$m is well below the required $20\,\mu$m. The corresponding weighted r(t) accuracy is $\hat{\rho} = 9\,\mu$m.

BML Chambers The more difficult track configuration in the BML3A01 chamber is reflected in the higher number of iterations for the autocalibration algorithm to converge after 8 iterations to $\rho = 11\,\mu$m and $\hat{\rho} = 7\,\mu$m(see Figure 4.12(a)). As for the BOS chambers, the r(t) relationship determined by the autocalibration only differs by more than $20\,\mu$m from the correct one for drift radii smaller than 0.5 mm. As shown in Figure 4.12(b), the χ^2/N_{dof} drops from 14.5 after the first iteration to 0.92 after iteration 4 and slowly converges to 0.88 after iteration 7. The comparison of Figure 4.12(a) and 4.12(b) shows that the quadratic mean $\sigma(\delta r(t))$ of the correction function is a good parameter to determine after which iteration the r(t) relationship remains unchanged by the autocalibration.

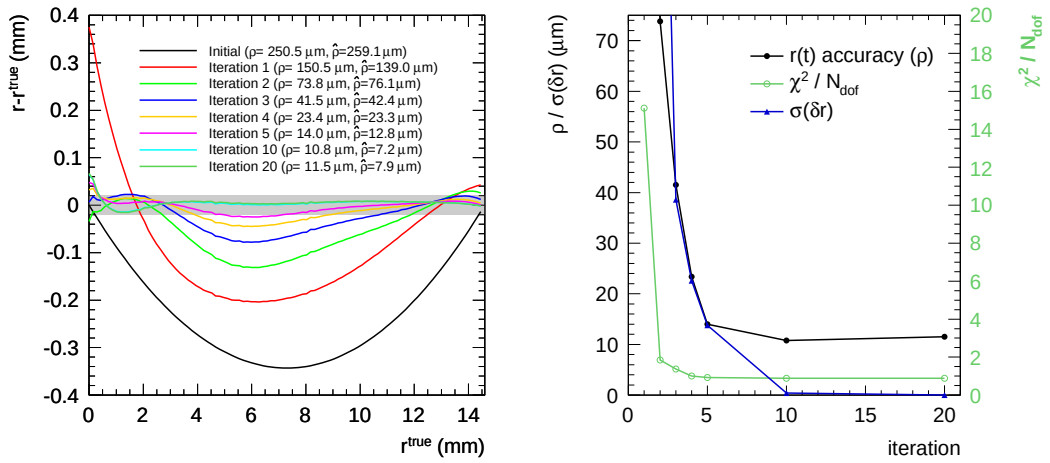

(a) (b)

Figure 4.12: (a) Deviation of the calibrated r(t) relationship from the correct one for increasing number of iterations for the BML3A01 chamber. The shaded band around zero marks the required accuracy of $\pm 20\,\mu$m. (b) The r(t) accuracy ρ, the rms $\sigma(\delta r(t))$ of the correction function and the χ^2/N_{dof} of the residuals as a function of the number of iterations.

Conclusion

Considering the above example cases a convergence criterion is defined which takes into account the χ^2/N_{dof} as well as the quadratic mean $\sigma(\delta r(t))$ of the correction function $\delta r(t)$. The autocalibration is stopped after iteration i, if the following two requirements are fulfilled:

- $(\chi^2/N_{\mathrm{dof}})^i \geq (\chi^2/N_{\mathrm{dof}})^{i-1}$,
- $\sigma(\delta r(t))^i \leq 1\,\mu$m.

The criterion is chosen such that the iteration stops at a minimum of $(\chi^2/N_{\mathrm{dof}})^i$. The second requirement ensures that the autocalibration only stops if the rms of the corrections for the last iteration is smaller than $1\,\mu$m. This is important to ensure continuation of the iteration in case only a local minimum of $(\chi^2/N_{dof})^i$ has been found. In addition, a maximum number of iterations can be defined to make sure that the autocalibration always stops. For the BOS chambers, the convergence is reached after four iterations (with $\rho = 10.1\,\mu$m) and for the BML chambers, the criterion is fulfilled after eight iterations (with $\rho = 10.8\,\mu$m). The fact that two times the number of iterations are needed for BML chambers can be explained by the restricted range of track incidence angles around 30 degrees with a low density of fixed points.

4.6.4 Dependence of the r(t) Relationship on the Initial Values

To verify that the autocalibration always converges to the correct r(t) relationship independently of the initial r(t) relationship, the algorithm is tested for different initial values.

Initial r(t) Relationship from the Integration Method

Determining the initial r(t) relationship by the integration method (see Section 4.4.1) is the standard method and the benchmark for the autocalibration with curved tracks. The integration bounds t_0 and $t_{\max}$ are determined with a precision of better than 1 ns (see Section 4.2) leading to an accuracy of better than 40 μm in the point $r(t_0) := 0$. How much the accuracy of the t_0-fit influences the r(t) calibration accuracy is studied in Section 4.6.5; the boundary condition $r(t_0) = 0$ will be considered exact until then.
To constrain also the end-point $r(t_{\max}) = r_{\max}$, a parabola is fitted to the initial r(t) bins in the range $r(t_1) = 11.6\,\text{mm}$ to $r(t_2) = 13.6\,\text{mm}$ and extrapolated over the last millimetre to the point $r(t_{\max}) = r_{\max} = 14.6\,\text{mm}$. The end-point in this way is not fixed, but included as additional point in the fit.
In Figure 4.13, the deviations of the initial r(t) relationship determined with the integration method and of the final r(t) relationship after performing the autocalibration from the correct one are plotted as a function of r^{true} for the selected BOS and BML chambers. In addition, the distributions of the residuals of the track fit for the initial and the final r(t) relationship are shown as a function of the distance of the track to the wire. The initial r(t) relationship shows a parabola-shaped deviation from the correct relationship. The maximum deviations of about 200 μm for the BOS and of about 600 μm for the BML chamber are near $\sim r_{\max}/2$.

BOS Chamber The initial r(t) relationship determined by the integration method for the BOS chamber(see Figure 4.13(a)) has an accuracy of only $\rho = 125.5\,\mu\text{m}$ while the deviations of the final r(t) relationship to the correct one after the autocalibration are centred at zero with an accuracy of $\rho = 13.8\,\mu\text{m}$. Hence the final r(t) relationship is less precise by 3.7 μm than the r(t) relationship determined in the previous section where the modified correct r(t) relationship with an accuracy of $\rho = 150\,\mu\text{m}$ was used as initial relationship. The reason are small deviations, e.g. at $r \approx 10.5\,\text{mm}$ visible in the initial and as well as in the final r(t) relationships. This effect will be studied in the following section.
The track residual distributions as a function of the distance d of the track to the wires for the initial r(t) relationship determined by the integration method are well correlated with the deviations of the drift radii from the correct values (see Figure 4.13(c)). Thus, the r(t) relationship can also be improved using the standard autocalibration method.
Figure 4.13(e) shows the residuals after autocalibration. Even though they are well centred at zero, small deviations in the final r(t) relationship are visible also in the residual distribution, as e.g. at $d \approx 10.5\,\text{mm}$ and near the wire.
The colours of the scatter plots (Figures 4.13 (c,d,e,f)) indicate the numbers of measured residuals while the black markers represent the mean values of the residual distribution for each distance d. Due to un-physical values $\Delta(r) < -d$ of the residuals $\Delta(r) = r - d$, their mean values increase to larger residuals at small distances. The situation is similar close to the tube wall, where $\Delta(r) > r_{\max} - d$ is un-physical.

BML Chamber Even though the accuracy $\rho = 402.1\,\mu\text{m}$ of the r(t) relationship determined by the integration method is about four times worse than for the BOS chamber (see Figure 4.13(b)), the r(t) relationship after autocalibration deviates only for $r < 1\,\text{mm}$ and $r \approx 4\,\text{mm}$ by more than 20 μm from the correct relationship. Two observations can be made: First, also for this chamber the fine structure from the initial r(t) relationship

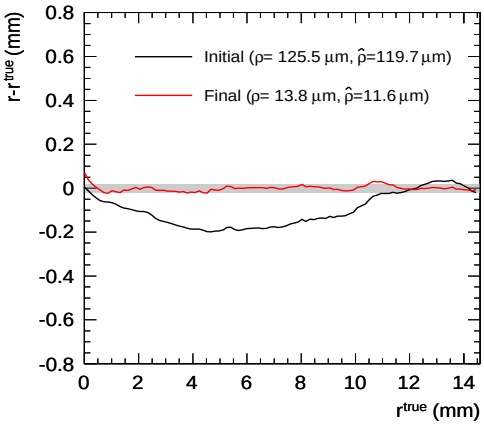

(a) BOS5C04.

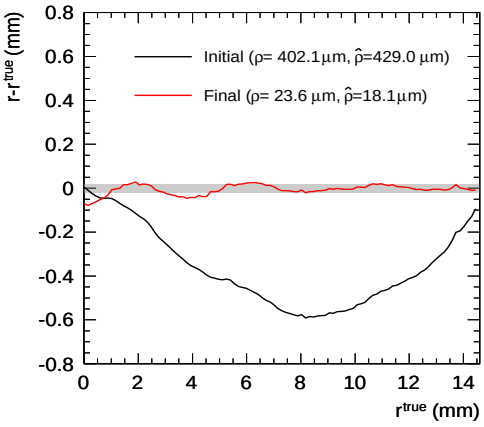

(b) BML3A01.

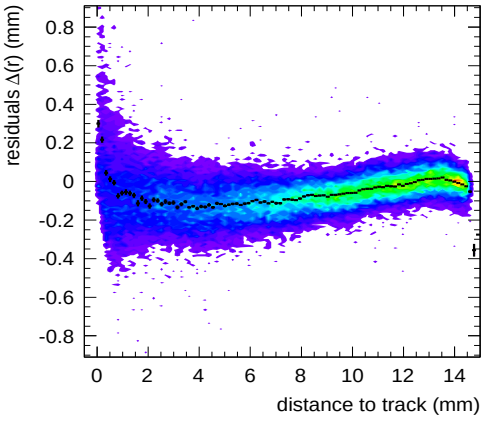

(c) BOS5C04: residuals using initial r(t).

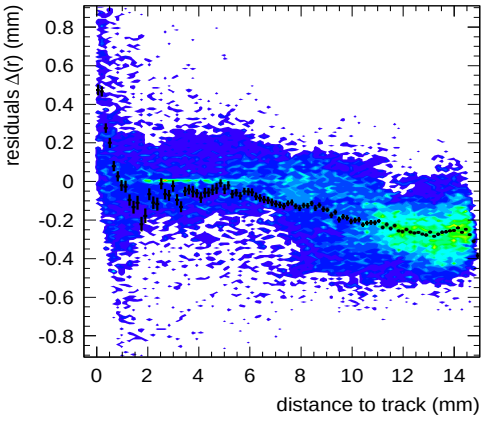

(d) BML3A01: residuals using initial r(t).

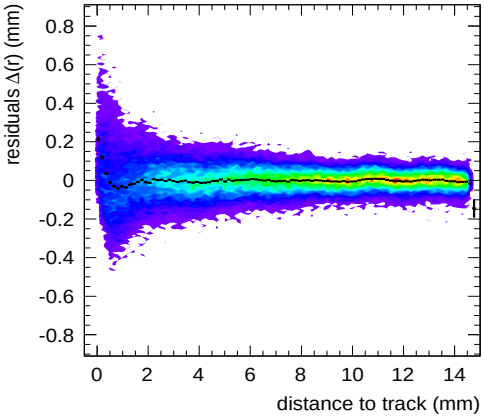

(e) BOS5C04: residuals using final r(t).

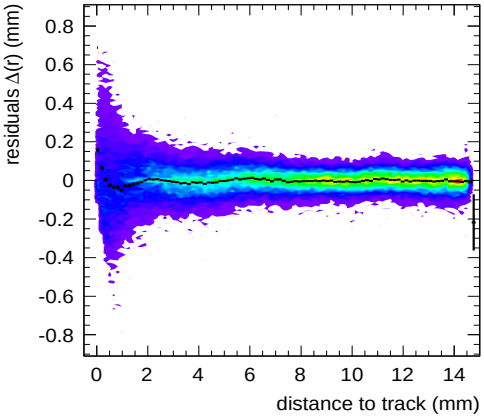

(f) BML3A01: residuals using final r(t).

Figure 4.13: Deviations as a function of the correct drift radius of the r(t) relationships before and after autocalibration from the correct relationship starting with integration of the drift time spectrum for (a) the BOS5C04 and (b) the BML3A01 chamber. While the residuals of the track fit for the initial r(t) relationship reflect well the deviation from the correct r(t) relationship for the BOS chamber (c), the residuals are not correlated with the deviation of the drift radii for the BML chamber (d). After autocalibration, the residuals are centred zero independently of the distance d between track and wire in both cases (e,f).

is still visible after the autocalibration. Second the final r(t) relationship oscillates with a maximal deviation of about 50 μm around the correct r(t) relationship.
Comparing the deviations of the initial r(t) relationship from the correct one with the residuals in Figure 4.13(d), demonstrates the necessity to use the full tracking information for the autocalibration and that correcting the r(t) relationship only according to the mean values of the residual distributions can be insufficient. While the deviation of the initial r(t) relationship increases from $r - r^{\text{true}} \approx 0\,\mu$m close to the wire to $r - r^{\text{true}} \approx 600\,\mu$m at a radius of 8 mm, the mean of the residual distribution is deviating only little from zero in this region. Hence it is impossible for the standard autocalibration method to improve the initial r(t) relationship for drift radii smaller than 8 mm. Only for distances to the track larger than 8 mm a larger deviation to negative values occur. The reason is that the probability of the muon to pass more than three tubes per multilayer increases in this case, where the track passes one tube on the opposite side of the wire than the other three.
Figure 4.13(e) shows the residuals after autocalibration with curved tracks. Very similar to the BOS chamber, also the residuals for the BML chamber are centred at zero independently of r. The oscillations observed in the deviations of the final r(t) relationship are also visible in the residuals as a function of track distance to the wires.

Initial r(t) Relationship with Additional Fine Structure

To study the ability of the autocalibration with curved tracks to correct for fine structure in the initial r(t) relationship, a combination of a parabola and a sine-function is added to the correct r(t) relationship:

$$r(t)^{\text{initial}} = r(t)^{\text{true}} - \underbrace{A_1 \cdot \frac{4}{r_{\max}} \cdot r(t)^{\text{true}} \left(\frac{r(t)^{\text{true}}}{r_{\max}} - 1 \right)}_{\text{I}} + \underbrace{A_2 \sin\left(f \cdot r(t)^{\text{true}}\right)}_{\text{II}}, \qquad (4.35)$$

The first term is the same as in Equation (4.34), a parabolic deviation from the correct r(t) relationship with amplitude $A_1 = 353\,\mu$m. The second term is a sine function with amplitude $A_2 = 75\,\mu$m and oscillation frequency $f = 10 \cdot (2\pi / r_{\max})$. While the autocalibration with curved tracks perfectly corrects for the parabolic offset, the oscillations remain as shown in Figure 4.15(a) for the BOS5C04 chamber (for the BML chamber it is similar). The reason for the insensitivity of the algorithm to higher frequency deviations is the order of the polynomial correction function. A linear combination of Legendre polynomials of order of 7 was used. Polynomial of order 20 or larger would be needed to correct for the 10 oscillation periods of the deviation (20 inflexion points). Even though this is in principle possible, polynomials this high are not practical. The computing time increases linearly with the order of the polynomial function. The autocalibration with 10 000 tracks takes about 9 s per iteration using polynomials of order 7 as correction function and about 24 s for order 20 polynomials. Still, it can not be excluded that the order of the polynomial function is still too low to correct for local irregularities in the initial r(t) relationship.
A solution can be the standard autocalibration method, which uses the deviations of the means of the residual distributions as a function of the drift time or radius for correcting the r(t) relationship which clearly show the oscillating behaviour (see Figure 4.15(b)). This possibility is discussed in the following section.

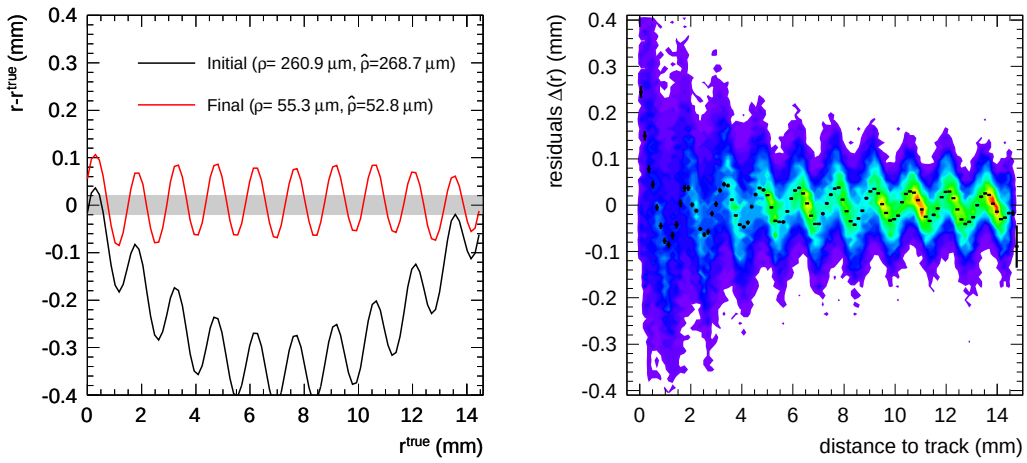

(a) (b)

Figure 4.14: Differences of the initial r(t) relationship as well as the r(t) relationship after autocalibration (final) from the correct r(t) relationship (a). In Figure (b) the residual distribution after the autocalibration is plotted. The autocalibration is unable to correct the sinusoidal deviation, as the frequency is larger as the order of the correction function used in the algorithm. See text for details.

4.6.5 Refinement of the Autocalibration Method

As discussed in the previous section, due to the limited order of the polynomial correction function, the analytic autocalibration is insensitive to variations for higher order perturbations of the r(t) relationship. As these perturbations are also visible in the residuals, the possibility of improving the r(t) accuracy by smoothing of the dependence of the residual as a function of the drift distance has been studied.

Smoothing of the Residuals

Smoothing of the residuals follows the concept of the standard autocalibration method. It will be applied after the analytic autocalibration has converged. The mean values of the residual distributions are calculated in bins of the distance between track and wires and are subtracted from the r(t) relationship. The method is applied iteratively until the radial dependence of the residuals is sufficiently flattened. To refine the r(t) relationship in this way, the following procedure is used:

- Also for the smoothing curved tracks are fitted to the hits in both multilayers of the MDT chambers.
- To improve the r(t) relationship via smoothing of the residuals, at least 1000 muon track segments ($\gtrsim$ 5000 residuals) are needed.
- The radial bin size is optimized by requiring $N_{\text{bins}} = \sqrt{N_{\text{segments}}}$.
- The largest and smallest 1 % of the residuals in each bin are considered as outliers and discarded.

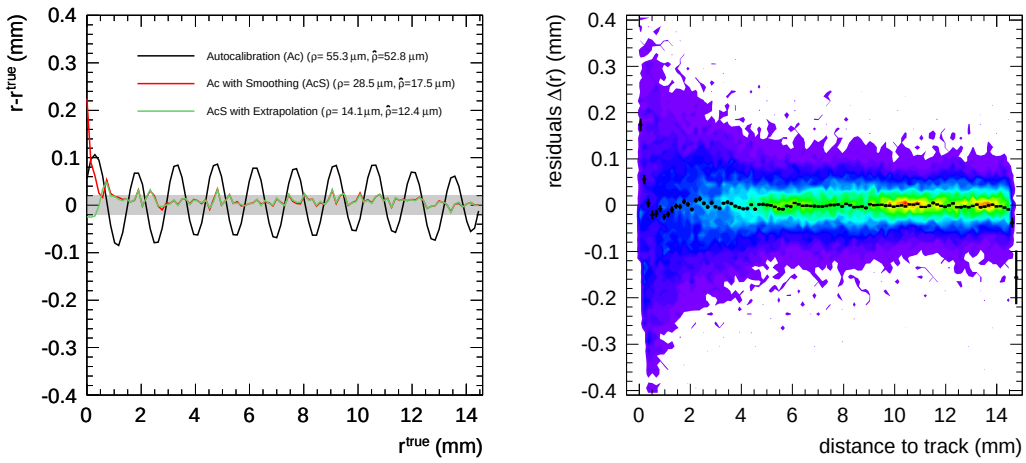

(a) (b)

Figure 4.15: (a) Deviation of the calibrated r(t) relationship from the correct one after the autocalibration (Ac) with additional residual smoothing (AcS) and including parabolic extrapolation to the end-points for the BOS5C04 chamber. (b) Residual distributions as a function of the distance between track and wires after smoothing and extrapolation have been applied.

- The smoothing is applied iteratively until the root mean square of the difference between two succeeding r(t) relationships is less than 1 μm.

Applying the autocalibration with curved tracks with additional residual smoothing to the initial r(t) relationship in Equation (4.35) of the previous section leads to an agreement between final calibrated and correct r(t) relationship of better than 20 μm for drift radii larger than 0.5 mm (see Figure 4.15(a)). However, the smoothing method fails to improve the r(t) relationship for radii smaller than 0.5 mm. This is caused by the asymmetric distribution of the residuals at small radii which has two reasons: residuals with values $\Delta(r) < -d$ are un-physical (corresponding to $r < 0$) and the drift time distributions for tracks passing close to the wire is also asymmetric (see Figure 4.16) as the statistical distribution of the primary ionization clusters along the tracks.

Parabolic Extrapolation to the End-Points

To improve the r(t) accuracy for drift radii smaller than 0.5 mm, the smoothing is not applied for drift radii smaller than 0.5 mm. Instead, a polynomial of order 2 is used to extrapolate the r(t) relationship to small radii after convergence of the autocalibration and smoothing of the residuals. Two assumptions are made for this extrapolation:

- The point $r(t_0) = 0$ is known with an accuracy of $\lesssim 40\,\mu$m from the determination of t_0.
- The r(t) relationship of the Ar/CO_2 gas mixture can be approximated with sufficient precision by a parabola for $r \lesssim 5$ mm.

The parabola is fitted to the r(t) bins in the range r=1 to 3 mm, the point r(t_0)=0 is included as constraint in the fit.

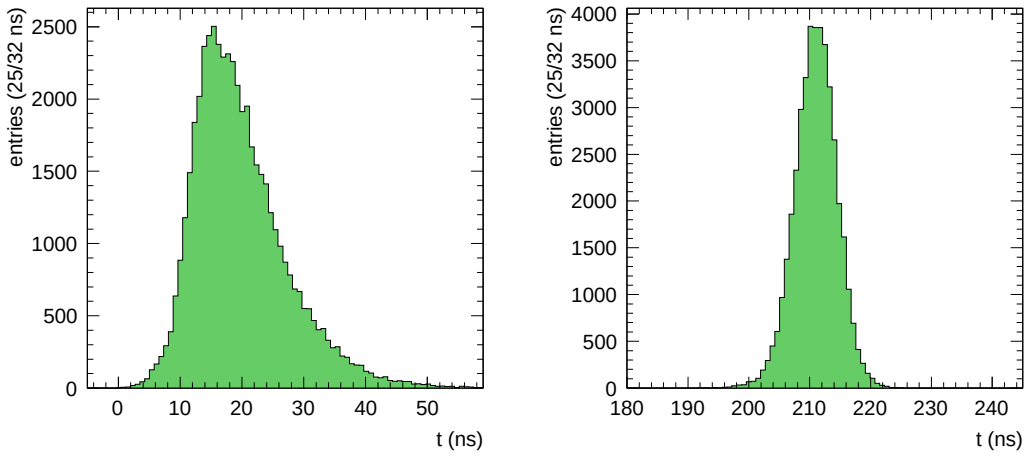

(a) (b)

Figure 4.16: Distributions of the drift times for tracks passing the anode wire at distances (a) between 0 mm and 0.1 mm and (b) between 7.5 mm and 7.6 mm from the simulated single muon events.

Similarly the r(t) relationship is extrapolated at its end. A polynomial of order 2 is fit to the r(t) bins in the range $r(t_{max})-3$ mm to $r(t_{max})-1$ mm after autocalibration and residual smoothing. In this case, the point $r(t_{max})$ is not included in the fit.
The reason for the parabolic extrapolation is the fact that higher order polynomials used for parametrization of the autocalibration correction function tend to oscillate with non-negligible amplitudes at the end points.
With the parabolic extrapolation to the end points, the accuracy of the r(t) relationship improves from $\rho = 25.5\,\mu$m ($\hat{\rho} = 17.5\,\mu$m) without to $\rho = 14.1\,\mu$m ($\hat{\rho} = 12.4\,\mu$m). As shown in Figure 4.15(a), the improvement is achieved for small drift radii $r < 0.5$ mm while the end-point for $r(t) = r(t_{max})$ agree with the correct values even without extrapolation for the BOS5C04 chamber. In Figure 4.15(b) the residuals after smoothing and extrapolation are shown as a function of the distance of the tracks from the anode wires. The residuals are distributed uniformly around zero for all distances. Only for tracks close to the wire, the mean values are shifted positive values due to the asymmetry of the residuals in this range.

4.6.6 Standard Autocalibration Procedure

The results of the previous sections lead to the following standard procedure for the autocalibration and the further tests:

- The initial r(t) relationship is determined by the integration method.
- A polynomial correction function of order 7 is used.
- After convergence of the autocalibration, the r(t) relationship is further improved by smoothing the residuals if more than 1000 muon tracks are available within the calibration region.

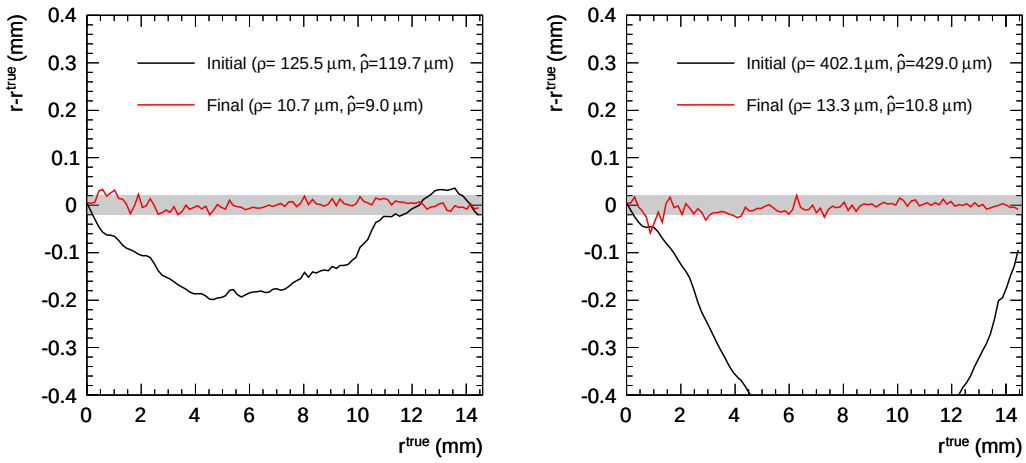

(a) BOS5C04 (b) BML3A01

Figure 4.17: Deviations of the initial and final calibrated r(t) relationships from the correct ones for the (a) BOS5C04 and (b) the BML3A01 chamber. The accuracies achieved are well below the target precision of 20 μm.

- To improve the precision at the end-points, the first and last millimetre of the r(t) relationship are extrapolated by fitting a 2$^{\text{nd}}$ order polynomial close to the end-points. The starting point $r(t_0) = 0$ is included in the fit while the end-point $r(t_{\max})$ is left free.

With this procedure, r(t) accuracies of $\rho = 10.7\,\mu$m ($\hat{\rho} = 9.0\,\mu$m) are achieved for the BOS5C04 chamber and of $\rho = 13.3\,\mu$m ($\hat{\rho} = 10.8\,\mu$m) for the BML3A01 (see Figure 4.17).

4.6.7 Dependence of the Autocalibration Precision on the Number of Muon Tracks

It is important to determine how many muon tracks are necessary per calibration region to reach sufficient autocalibration accuracy. Especially for the high luminosity phase of LHC ($\mathscr{L} = 10^{34}\,\text{cm}^{-2}\text{s}^{-1}$), the background irradiation influences the drift properties significantly. As the instantaneous luminosity decreases during an LHC run, the irradiation of the drift tubes changes and the r(t) relationship has to be recalibrated frequently while the maximum L2 trigger rate limits the calibration stream to 1 kHz. The number of muon tracks required for the autocalibration determines the time intervals between successive recalibrations.
During the LHC start-up phase on the other hand, the muon rate is limited by the interaction rate and the inclusive muon cross section. The muon rates are expected to increase from about 0.1 Hz for $\mathscr{L} = 10^{28}\,\text{cm}^{-2}\text{s}^{-1}$ and $\sqrt{s} = 900\,\text{GeV}$ at the start of LHC operation at the end of 2009 to about 1.5 kHz for $\mathscr{L} = 10^{31}\,\text{cm}^{-2}\text{s}^{-1}$ and $\sqrt{s} = 7\,\text{TeV}$ during the 2010/2011 run. Thus the autocalibration is running at low statistics for the first ATLAS physics runs.
To study the dependence of the autocalibration on the available statistics, the two selected MDT chambers are calibrated with increasing number of simulated muon tracks. The t_0 values have been determined only once with maximum available statistics. In order to per-

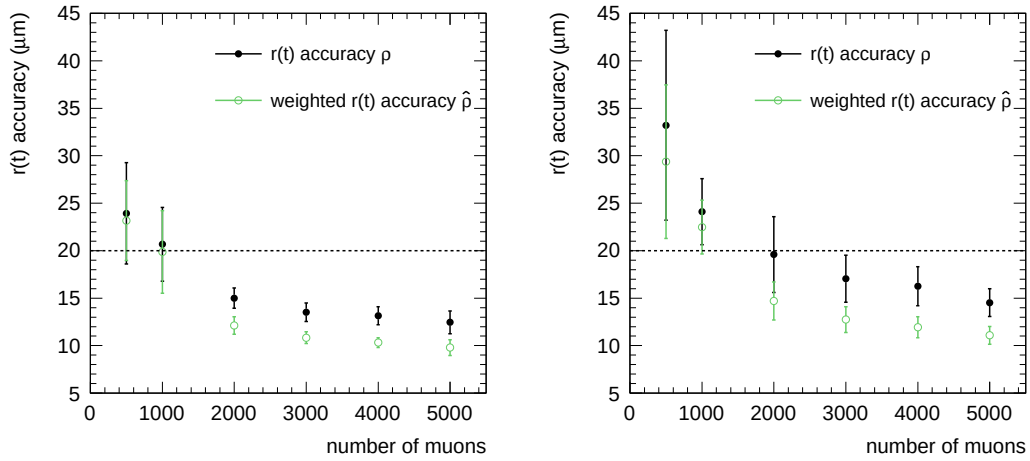

(a) Average of BOS5 calibration regions. (b) Average of BML3 calibration regions.

Figure 4.18: Dependence of the autocalibration accuracy on the number of muon tracks used for (a) BOS5 and (b) BML3 chambers. To reach the required r(t) accuraciy of 20 μm, 2000–3000 muon tracks are sufficient. Note that no residual smoothing is performed for 500 and 1000 tracks.

form a statistically meaningful test with the available dataset of simulated single muons, the following strategy was used:

- Always two MDT chambers of the same type and η-position (e.g. the BOS5C02 and BOS5C04) are combined to one form one calibration region.
- The opposite detector hemisphere (e.g. the BOS5A02 and BOS5A04) is also added. Hence there are 6 BOS5-type and 8 BML3-type calibration regions (the BOS chambers in sectors 12 and 14 have a different geometry due to their position in between the detector feet and are therefore excluded from this test).
- The integration and autocalibration are performed with the number of muon track segments increasing from 500 to 5000 for each calibration region.
- The mean values and standard deviations of the r(t) accuracies achieved for the different calibration regions are determined as a function of the number of muon tracks used.

The results are shown in Figure 4.18. As expected, the calibration accuracy is steadily improving with the number of muons. Already with 500 tracks the autocalibration significantly improves the initial r(t) relationships ($\rho^{\text{initial}} \simeq 100$ and 500 μm) to accuracies on the order of 30 μm. With 2000 tracks, the accuracies for the BOS5 chambers are with $\rho = 15.0 \pm 1.1\,\mu$m ($\hat{\rho} = 12.1 \pm 0.9\,\mu$m) well below the goal of 20 μm while the more difficult track configuration for the BML3 chambers requires 3000 tracks to reach an accuracy of better than 20 μm, $\rho = 17.1 \pm 2.5\,\mu$m ($\hat{\rho} = 12.7 \pm 1.4\,\mu$m). With the highest available statistics of 5000 muons per calibration region, the mean r(t) accuracies for BOS5 and BML3 chambers are $\rho = 12.5 \pm 1.2\,\mu$m ($\hat{\rho} = 9.8 \pm 0.8\,\mu$m) and $\rho = 14.5 \pm 1.5\,\mu$m ($\hat{\rho} = 11.1 \pm 0.9\,\mu$m), respectively.

The minimum number of 3000 muon track segments needed to reach the required r(t) accuracy is available for most chambers, except in some special regions discussed in Section 4.6.1. Thus about five million muons have to be collected for the r(t) calibration of all MDT chambers in the ATLAS muon spectrometer.
The dataset of single muons with $p_T = 4, 6$ and $10\,\mathrm{GeV/c}$ was chosen to simulate the calibration stream at $\mathscr{L} = 10^{31}\,\mathrm{cm^{-2}s^{-1}}$. As the p_T threshold will be raised to $6\,\mathrm{GeV/c}$ for higher LHC luminosity, the muons will be distributed more uniformly over the different chamber layers.

4.6.8 Calibration Accuracies Across the Muon Spectrometer

The Monte Carlo sample of five million single muons, which corresponds to about one hour of data taking at $\mathscr{L} \simeq 10^{31}\,\mathrm{cm^{-2}s^{-1}}$, is used to determine r(t) relationships for the MDT chambers in the muon spectrometer in order to study systematic effects due to different detector regions. The different calibration steps—the determination of t_0, the integration of the drift time spectrum and the autocalibration itself—are performed with the full available statistics per chamber (see Figure 4.9) and the r(t) accuracy ρ is calculated. Figure 4.19 gives an overview of the accuracies reached.
For most of the chambers an r(t) accuracy between 5 and $15\,\mu$m is achieved. Even for chambers with relatively low statistics in the sample (BIS, EIL, EMS, EOS at large $|z|$ and R, respectively, as well as the chambers installed in the detector feet) the autocalibration precision is better than $30\,\mu$m. In particular there is no accuracy loss in the barrel at η-position 3 where muons cross the MDT chambers at incidence angles close to 30°. As BIS chambers at η-position 8 only have one multilayer with three tube layers and the muon rate is expected to be the smallest in the whole spectrometer, they are combined with the BIS at η-position 7 for the autocalibration.
As discussed in Section 4.3.3, an accuracy of the r(t) calibration of better than $30\,\mu$m is required within each calibration region including the corrections for the drift time measurement. These systematic effects have not been included in the study of the r(t) accuracies so far and will be discussed in the following section.

4.7 Systematic Effects

The autocalibration with curved tracks has been optimized and tested for stable nominal operating conditions resulting in r(t) accuracies in the range of $5-15\,\mu$m depending on the calibration region. In this section systematic effects on the accuracy of the r(t) calibration are studied including the accuracy of the t_0 and drift time measurements and deviations of the chambers from their nominal geometry. The r(t) accuracy including these effects is required to be better than $30\,\mu$m to avoid a degradation of the muon momentum resolution at highest muon energies.

4.7.1 Effect of the Drift Time Resolution

The resolution of the drift time measurement is limited by the digitization steps of $^{25}/_{32}\,\mathrm{ns}$ of the TDC. A number of other effects can degrade the precision of the drift time measurement, like the Lorentz-angle correction or changes of the drift time due to variations of the environmental conditions. During the commissioning of the MDT chambers with

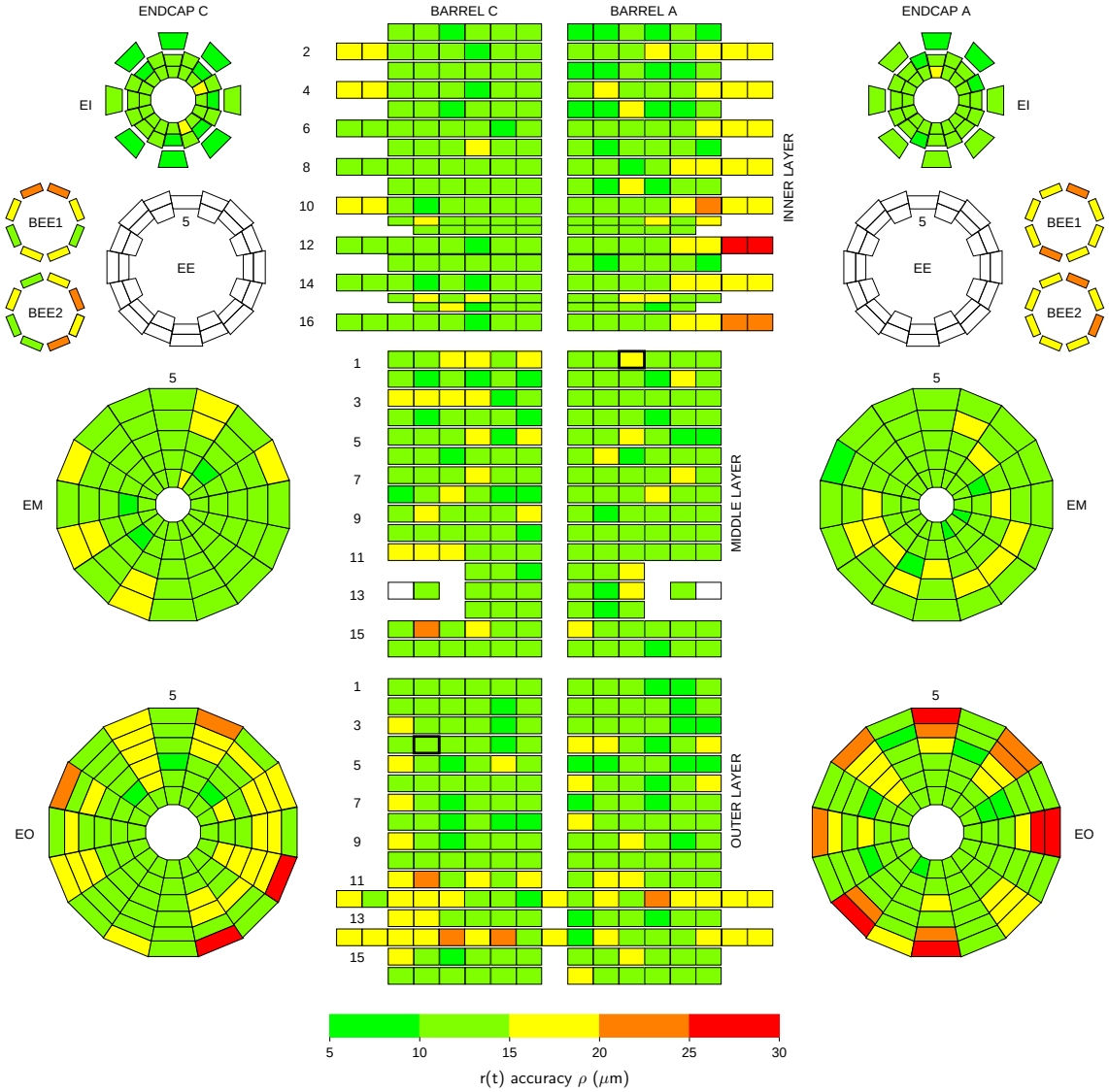

Figure 4.19: r(t) accuracies ρ achieved using the five million simulated single muon events corresponding to one hour of data taking at $\mathscr{L} \geq 10^{31}\,\mathrm{cm}^{-2}\mathrm{s}^{-1}$for the 1088 MDT chambers which are included in the geometry description of the simulation. The η-position of the chambers in the barrel are counted horizontally in both detector hemispheres starting at $z = 0$ in the centre and radially in the end cap wheels.

,

cosmic ray muons, each measured drift time had a varying offset of up to ± 12.5 ns, since these muons cross the tubes uncorrelated with the accelerator clock used as trigger time. The 25 ns jitter can be eliminated by using the time measured by the trigger chambers as a start time for the drift time measurement.
To simulate these effects, random time offsets in a predefined range are added to every drift time measurement in the two selected chambers (BOS5C04, BML3A01) before applying the autocalibration algorithm. The initial r(t) relationship and the value t_0 are unchanged. The r(t) accuracies achieved for different drift time uncertainties are summarized in Table 4.2.

Table 4.2: Dependence of the r(t) accuracy and number of iterations required on the accuracy of the drift time measurement. Random time offsets from different predefined intervals were added to each drift time before performing the autocalibration.

Time offset	BOS5C04			BML3A01		
intervals (ns)	ρ (μm)	$\hat{\rho}$ (μm)	Iterations	ρ (μm)	$\hat{\rho}$ (μm)	Iterations
$[0, 0]$	10.7	9.0	4	13.3	11.8	8
$[-1, 1]$	10.6	9.4	4	14.4	11.2	8
$[-2, 2]$	10.4	9.2	4	14.4	11.4	8
$[-3, 3]$	10.6	9.6	4	19.3	14.5	9
$[-4, 4]$	10.4	9.6	4	20.5	15.7	9
$[-5, 5]$	11.8	10.7	4	29.9	21.4	9
$[-10, 10]$	34.1	26.1	5	48.2	36.0	14
$[-15, 15]$	45.1	34.2	7	58.7	43.4	20*
$[-20, 20]$	73.0	53.5	20*	124.6	82.3	20*
$[-25, 25]$	158.0	95.6	20*	222.2	152.0	20*

*Interrupted after 20 iterations.

Time offsets up to ± 5 ns ($\rho = 11.8\,\mu$m) have no significant influence on the r(t) accuracy of the BOS chamber. The r(t) accuracy for the BML chamber on the other hand is already significantly degraded for the time offsets up to ± 3 ns ($\rho = 19.3\,\mu$m) and drops to $\rho = 30\,\mu$m for $\Delta t = \pm 5$ ns. The more difficult track configurations in the BML chamber lead to a higher sensitivity of the autocalibration to the precision of the drift time measurement. Correlated with degraded autocalibration precision is an increase of the number of iterations.
The average degradation $\Delta\rho$ and $\Delta\hat{\rho}$ of the r(t) accuracy is shown as a function of the maximum time offset (Δt) in Figure 4.20(a). Figure 4.20(b) shows the influence of the uncertainty in the drift time measurement on the calibrated r(t) relationship for an $\Delta t = \pm 5$ ns. To reach r(t) accuracies better than 30 μm for all chambers, the drift time has to be know with a precision of better than 5 ns including all corrections.

4.7.2 Effect of the Accuracy of the t_0 Determination

About 10 000 drift times are needed for a t_0-fit with an accuracy of better than 0.5 ns [54, 65]. The precise determination of t_0, especially a fitting per drift tube, needs larger statistics than the autocalibration (about $1 \cdot 10^6$ muons per chamber for a t_0-fit per tube), but is expected to be more stable in time than r(t). Hence t_0 and r(t) might be

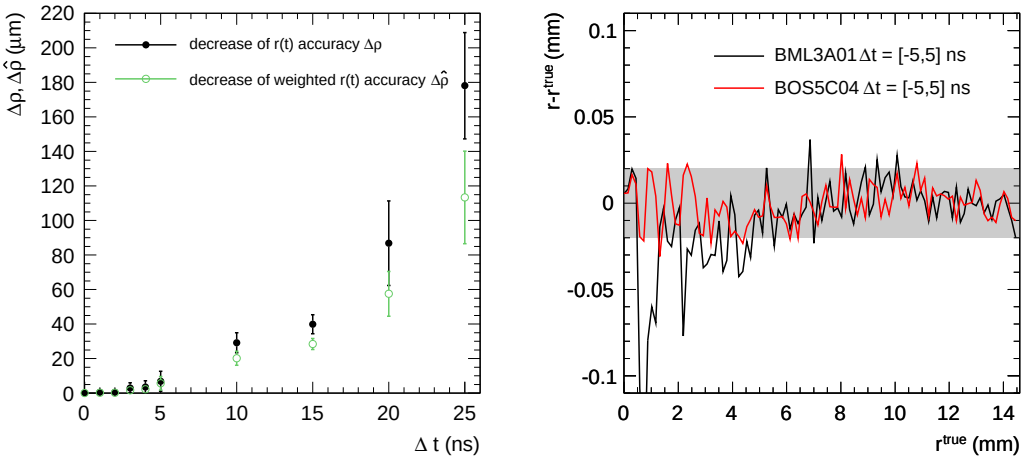

(a) (b)

Figure 4.20: (a) Degradation of the r(t) accuracy after autocalibration as a function of the maximum drift time offset (Δt). (b) Deviation of the calibrated from the true r(t) relationship as a function of r^{true} for maximum drift time offset of $\Delta t = \pm 5\,\text{ns}$.

determined with a different set of runs during ATLAS operation. To compensate eventual changes in the relative timing, t_0 is refit in the integration method to determine the starting point $r(t_0')$ only from the data which is used for the r(t) calibration. In case of $t_0' \neq 0$, the autocalibrated r(t) relationship has the starting point $r(t_0') = 0$ and a relative offset on the relationship to compensate for the change in t_0. To have sufficient statistics for an accurate t_0-fit, it is performed on the drift times of all tubes in the MDT chamber, neglecting the differences in between the single channels. How much this combination of channels affects the autocalibration is discussed in Section 4.7.3.
The question is how much an imprecise determination of t_0' affects the autocalibration accuracy. This dependence is shown for eight different offsets between $\Delta t_0' = -1\,\text{ns}$ and $\Delta t_0' = 1\,\text{ns}$ in Table 4.3. As the point $r(t_0')$ is included as a fit point in the parabolic extrapolation to the start-point of the r(t) relationship, the starting-point after autocalibration shifts according to

$$\Delta r(t_0') = \Delta t_0' \cdot v_{\text{drift}}(0), \tag{4.36}$$

where $v_{drift}(0) \simeq 40\,\mu\text{m}/\text{ns}$ is the electron drift velocity close to the wire. The r(t) relationship only changes in the region $r < 1\,\text{mm}$ (see Figure 4.21) and is thus only marginally affecting the precision of muon reconstruction, as the tube resolution $\sigma(r)$ increases to small radii. Hence $\hat{\rho}$ is nearly independent to changes of t_0'. The refit of t_0 during the integration method decouples the r(t) calibration from the tube wise and thus time dependent determination of t_0 and improves the stability of the r(t) calibration against changes in t_0.

4.7.3 Effect of t_0-Shifts within an MDT Chamber

The determination of t_0 will be performed per tube when the necessary statistics can be collected in a time of stable operational conditions (once per day at LHC design luminosity). As the muon rate will be too small for a per tube correction during the start-up

Table 4.3: Dependence of the r(t) accuracy on the precision of the t_0 refit during the integration method (t_0'). A constant time offset $\Delta t_0'$ was added to t_0' before performing the integration method and the autocalibration.

Time offset	BOS5C04			BML3A01		
intervals (ns)	ρ (μm)	$\hat{\rho}$ (μm)	Iterations	ρ (μm)	$\hat{\rho}$ (μm)	Iterations
0	10.7	9.0	4	13.3	11.8	8
-0.25	11.1	9.1	4	13.8	11.0	8
$+0.25$	10.5	9.0	4	13.3	10.7	8
-0.50	11.2	9.3	4	14.5	11.2	8
$+0.50$	10.3	8.8	4	13.3	10.7	8
-0.75	12.0	9.5	4	16.9	12.6	8
$+0.75$	11.1	9.1	4	13.9	10.8	8
-1.0	13.2	10.2	4	17.6	12.8	8
$+1.0$	12.0	9.4	4	15.2	11.4	8

phase of LHC, several channels are combined for one t_0-fit. Dependent on the available statistics, the combination of the tubes from one chamber, one multilayer or single mezzanine boards are possible. This implies the possibility of small time offsets in between the single channels and it shall be studied how these offsets influence the accuracy of the r(t) calibration.
To simulate these tube dependent offsets on the drift time, the following strategy will be followed:

- The single mezzanine boards are connected via twisted pair cables to the Chamber Service Module (CSM). According to the position of the mezzanine boards, these cables have different lengths, leading to different offsets in the drift time. As the mean t_0 over the full chamber is correct, the sum of all cable offsets is 0 (see Table 4.4).

- In addition a random time offset between -0.5 ns and 0.5 ns is added to each tube.

Table 4.4: Length of the twisted pair cables connecting the mezzanine boards of a standard BOS chamber with the CSM. The relative offset to the drift time Δt is calculated relative to the mean cable length of 0.88 mm.

Cable length (m)	1.30	1.00	0.67	0.50
Nb. of cables	3	6	8	1
Δt (ns)	+1.5	+0.4	-0.7	-1.3

The offsets applied to the drift time are shown as a function of the tube number in Figure 4.22(b) for the BOS5C04 chamber. The BOS chamber has 72 tubes per tube layer. Tube numbers smaller than 73 denote the tubes in the first layer of multilayer 1, tube numbers between 73 and 144 the second layer of multilayer 1, etc. The black line represents the relative offset which accounts only for the length of the twisted pair cables, while the grey bars show the applied offset on each drift tube including the random ± 0.5 ns shift. After applying the offsets to the drift times, the integration method was used to determine the initial r(t) relationship, before performing the autocalibration. In addition,

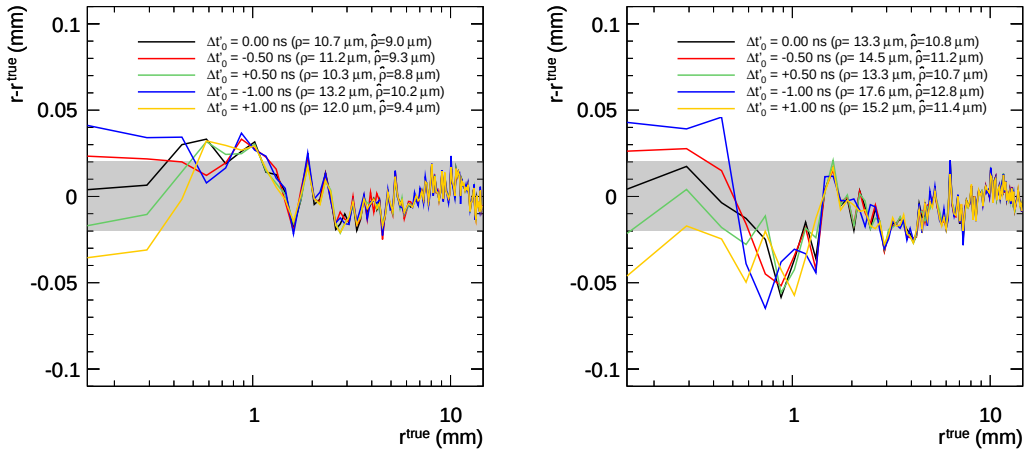

(a) BOS5C04 (b) BML3A01

Figure 4.21: Dependence of the r(t) accuracy after autocalibration on the precision of the t_0 refit in the integration method (t_0'). The difference ($r - r^{\text{true}}$) is shown as a function of r^{true} after the autocalibration for various $\Delta t_0'$ during the calibration of the BOS5C04 (a) and the BML3A01 (b) chamber. Note the use of a logarithmic scale of the x-axis.

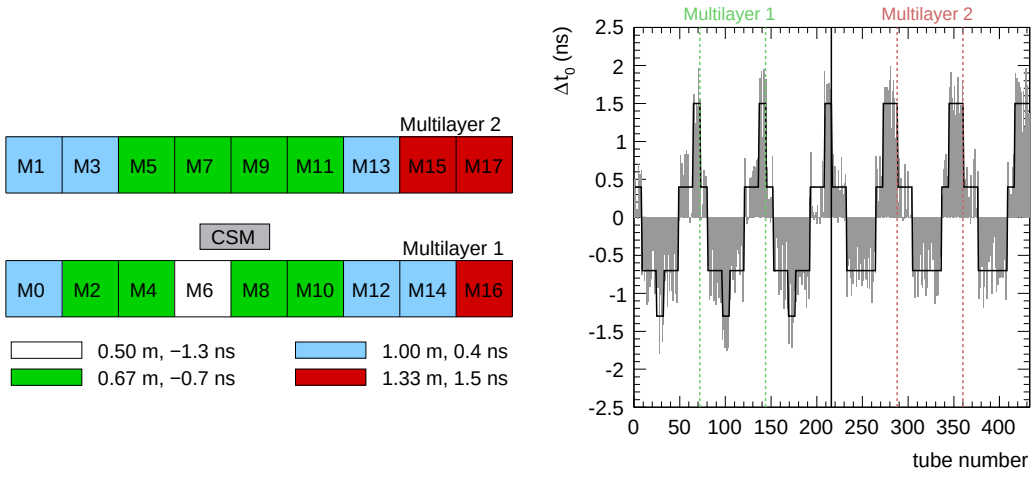

(a) (b)

Figure 4.22: (a) Schematic view of the read-out side of the BOS5C04 chamber with the position of the 18 mezzanine boards. The different colours correspond to the different lengths of the cables connecting the boards with the Chamber Service Module (CSM). (b) The corresponding offsets on the drift time is plotted in dependence of the tube number in. The grey bars show the applied shift, while the black line corresponds to the relative systematic offset due to the different cable lengths.

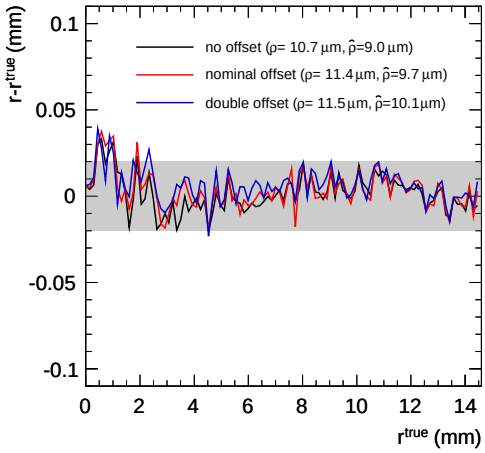

Figure 4.23: Deviation of the calibrated r(t) relationships from the correct one as a function of the true drift radii with and without shifting the drift time according to the length of the front-end cables.

the r(t) calibration has been tested a second time with double the size of the shifts—thus offsets correlating to double cable lengths and a per tube, random shift between -1 ns and 1 ns. The results are shown in Figure 4.23. The r(t) accuracy decreases only about 1 μm, thus a per chamber t_0 fit is not expected to decrease the precision of the r(t) calibration. It should be mentioned that grouping tubes for the t_0 fit decreases the intrinsic resolution of the drift tubes. Hence a tube wise fit cannot be avoided to reach the high intended momentum resolutions of the ATLAS muon spectrometer.

4.7.4 Effect of the Chamber Geometry

During the assembly of the MDT chambers, the anode wires have been positioned within a chamber with an accuracy of 20 μm [34]. Nevertheless, since the autocalibration uses track fits through both multilayers, small displacements of the multilayers with respect to each other can influence the calibration accuracy. The two largest effects on the accuracy of the track segment reconstruction are (see Figure 4.24):

- Relative shifts Δz of the multilayers with respect to each other in the direction perpendicular to the wires parallel to the tube layers.
- Relative rotations $\Delta\alpha$ of the two multilayers around the tube direction.

The relative position of the two multilayers of the BOS chambers, for example, have been measured to be within 20 μm (rms) in z-direction and within $\Delta\alpha < 20\,\mu$rad (rms) [46, 49, 73]. Thus their mechanical precision is on the same order required as r(t) accuracy.
To test the robustness of the autocalibration algorithm, multilayer 2 is shifted by up to 1000 μm and rotated by up to $\Delta\alpha = 1000\,\mu$rad with respect to multilayer 1. The r(t) accuracies achieved for the BOS5C04 and BML3A01 chambers are summarized in Table 4.5. The precision of the r(t) relationships changes only marginal even for the largest shifts and rotations. It can be concluded that the construction accuracies do not influence the performance of the autocalibration.

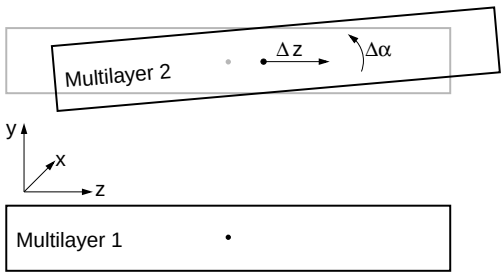

Figure 4.24: Illustration of relative displacements of the two multilayers of an MDT chamber definition of the local chamber coordinate system for barrel chambers. The local x-direction points along the tubes, y perpendicular to multilayer 1 towards the outside of the spectrometer and z perpendicular to the wires in the plane of multilayer 1.

Table 4.5: Dependence of the r(t) accuracy on shifts Δz and rotations Δr between the two multilayers of the selected MDT chambers.

Δz (μm)	BOS5C04			BML3A01		
	ρ (μm)	$\hat{\rho}$ (μm)	Iterations	ρ (μm)	$\hat{\rho}$ (μm)	Iterations
0	10.7	9.0	4	13.3	11.8	8
100	10.6	9.3	4	13.0	10.6	8
500	10.9	10.6	4	14.3	11.5	8
1000	13.3	13.5	4	17.8	14.4	9
$\Delta\alpha$ (μrad)	ρ (μm)	$\hat{\rho}$ (μm)	Iterations	ρ (μm)	$\hat{\rho}$ (μm)	Iterations
0	10.7	9.0	4	13.3	11.8	8
100	10.6	9.1	4	12.6	10.2	8
500	11.2	10.4	4	13.7	10.8	9
1000	12.1	11.9	4	18.6	14.0	9

4.8 Influence of the Accuracy of the r(t) Relationship on the Momentum Resolution

For transverse muon momenta above 100 GeV/c, the muon momentum resolution of the ATLAS detector is dominated by the performance of the muon spectrometer (see Figure 4.25). The goal is to achieve a momentum resolution of 10 % for 1 TeV/c muons including alignment and calibration uncertainties. The influence of the MDT calibration accuracy is evaluated in this section. The Monte Carlo sample of five million single muons with $p_{\mathrm{T}} = 4, 6$ and 10 GeV/c is used to determine t_0 values and r(t) relationships for all MDT chambers and to use these calibration constants to reconstruct 400 000 single muons with $p_{\mathrm{T}} = 1$ TeV/c simulated in the ATLAS software framework Athena [71] (version 14.2.25). The standalone muon momentum measurement in the muon spectrometer is performed using the STACO algorithm [74]. For a qualitative estimate of the influence of the r(t) calibration accuracy on the muon momentum resolution, the momentum measurement is performed for four different r(t) relationships,

- the r(t) relationships determined by the integration of the drift time spectrum for each chamber,

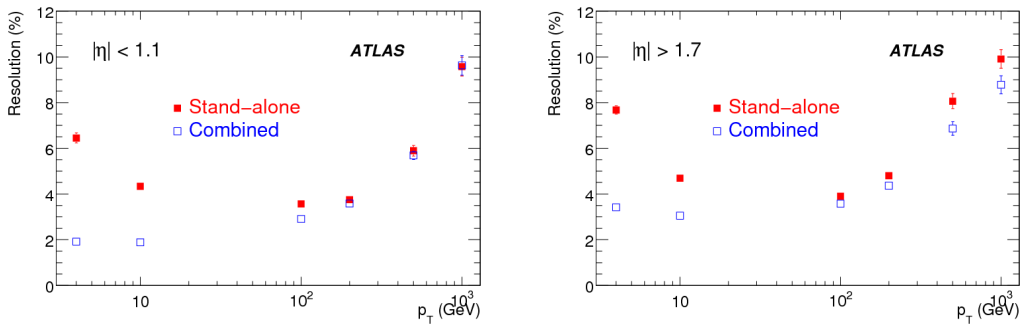

(a) (b)

Figure 4.25: Expected standalone and combined momentum resolution as a function of the transverse momentum for single muons with (a) $\eta < 1.1$ (barrel region) and (b) $\eta > 1.7$ (end cap region) [52].

- the r(t) relationship for each multilayer using the standard straight track autocalibration method,
- r(t) relationships per chamber determined by the analytical autocalibration with curved tracks,
- the correct r(t) relationship which is the standard for all ATLAS simulation studies.

The t_0-fit is performed for each chamber since there are no different offsets for individual drift tubes implemented in the simulation. For the correct r(t) relationship t_0 is not determined by fit, but the nominal value in the simulation used. Hence, the variations also include the uncertainty of the t_0 fit.

4.8.1 Average Momentum Resolution of the Muon Spectrometer at 1 TeV/c

The standalone momentum resolution of the muon spectrometer is estimated by comparing the inverse of the reconstructed and true muon transverse momenta:

$$x = \frac{1/p_{\mathrm{T}} - 1/p_{\mathrm{T}}^{\mathrm{true}}}{1/p_{\mathrm{T}}^{\mathrm{true}}}. \tag{4.37}$$

The width of the distribution of x is a measure of the muon spectrometer resolution. Several effects, like multiple scattering or the bending power of the magnetic field, depend on the detector region and add tails to the distribution of x. For a meaningful evaluation of the muon spectrometer resolution, these tails have to be taken into account. Two different methods have been used:

Single-Gaussian Fit The first approach has also used in [52] and consists of two steps. First, a Gaussian function is fit to the whole x-distribution. In the second step, the fit is repeated in restricting range

$$\langle x \rangle \pm 2\sigma_x \tag{4.38}$$

where $\langle x \rangle$ is the mean value of the first fitted function and σ_x its width. The width σ_s of the second Gaussian fit is taken as measure of the muon momentum resolution.
Figure 4.26 shows four x-distributions with the single-Gaussian fit corresponding to the muon reconstruction with the four different r(t) relationships. The widths σ_s of the fitted Gaussians are listed in Table 4.6.

The r(t) accuracies from the integration method are on the order of $\rho = (100 - 500)\,\mu$m

Table 4.6: Average standalone momentum resolutions for $p_T = 1$ TeV/c for different r(t) relationships. The resolution is defined as the width σ_s of a single-Gaussian function fitted in a $2\sigma_x$-window around the mean of the data-points.

r(t) relationship	All $\lvert\eta\rvert < 2.7$	Barrel $\lvert\eta\rvert < 1.1$	End cap $\lvert\eta\rvert > 1.7$
		σ_s (%)	
Integration method	10.57 ± 0.02	11.43 ± 0.04	8.27 ± 0.03
Standard Ac	9.78 ± 0.02	10.18 ± 0.03	7.70 ± 0.03
Analytic Ac with curved tracks	9.57 ± 0.02	9.98 ± 0.03	7.62 ± 0.03
True r(t) relationship and t_0	9.56 ± 0.02	9.98 ± 0.03	7.61 ± 0.03

only. Still an average standalone momentum resolution of $10.57 \pm 0.02\,\%$ is achieved. The improved r(t) relationships from the standard autocalibration method lead to a momentum resolution of $9.77 \pm 0.02\,\%$. Using the r(t) relationships from analytical autocalibration with curved tracks, the resolution is further improved to $9.57 \pm 0.02\,\%$ which almost reaches the resolution achieved with the true r(t) calibration and t_0 of $9.56 \pm 0.02\,\%$.

Double-Gaussian Fit Alternatively, a double-Gaussian function with common mean value $\langle x \rangle$ is fitted to the x-distribution,

$$C_1 \cdot e^{-\frac{1}{2}\left(\frac{x-\langle x\rangle}{\sigma_{d1}}\right)^2} + C_2 \cdot e^{-\frac{1}{2}\left(\frac{x-\langle x\rangle}{\sigma_{d2}}\right)^2}, \tag{4.39}$$

where C_1 and C_2 are the normalization constants and σ_{d1} and σ_{d2} the width of the two Gaussians. The double-Gaussian fits for the four different r(t) relationships are shown in Figure 4.27, the widths σ_{d1} and σ_{d2} are listed in Table 4.7.
As expected, both autocalibration methods are improving the width σ_{d1} of the narrow Gaussian compared to the integration method. Again, σ_{d1} and σ_{d2} agree for the analytical autocalibration and the true r(t) relationship.
It is interesting to note that the standard autocalibration does not improve σ_{d2} compared to the integration method in contrast to the analytical autocalibration. One can conclude that non-precise r(t) relationships of certain MDT chambers contribute to the tails of the x-distribution.
The results of this section show that the r(t) accuracy of the analytical autocalibration with curved tracks of the MDT chambers, including the t_0-determination does not deteriorate the momentum resolution of the muon spectrometer. For this study misalignment of the MDT chambers was not taken into account, the MDT chambers where at their nominal positions in the simulation. The quoted resolutions take into account only the intrinsic resolution of the drift tubes and multiple scattering.

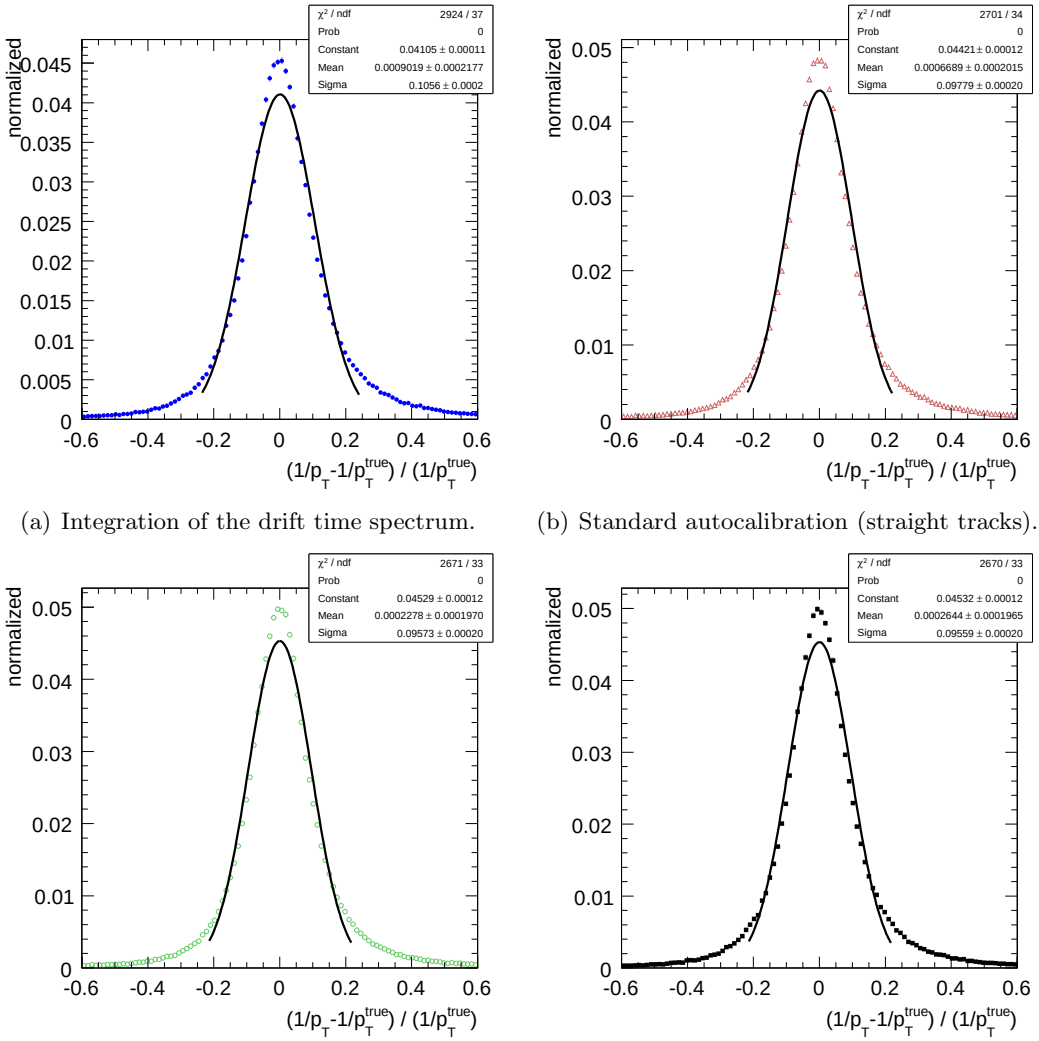

(a) Integration of the drift time spectrum.

(b) Standard autocalibration (straight tracks).

(c) Analytic autocalibration (curved tracks).

(d) Correct r(t) relationship and t_0.

Figure 4.26: Momentum resolution of the muon spectrometer for the standalone reconstruction of single muons with $p_T = 1\,\mathrm{TeV/c}$ with single-Gaussian fits for the four different r(t) relationships (see text).

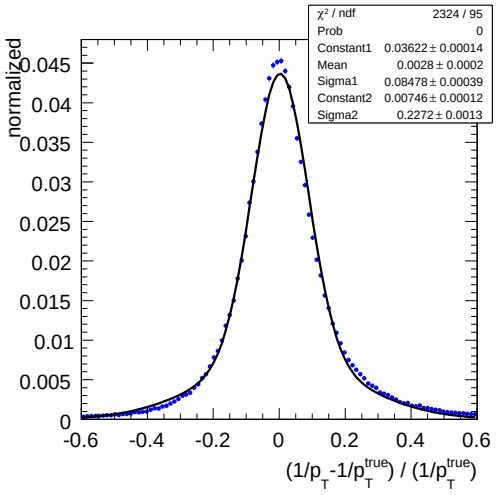

(a) Integration of the drift time spectrum.

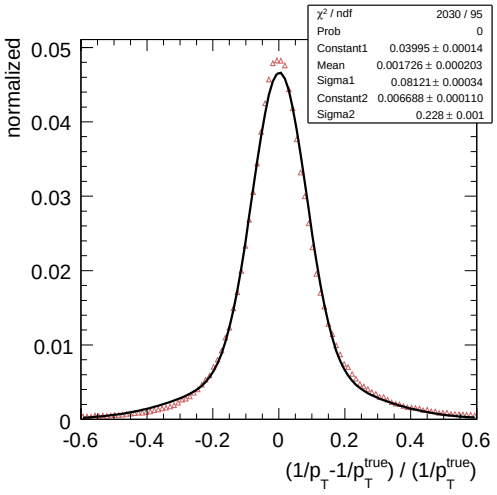

(b) Standard autocalibration (straight tracks).

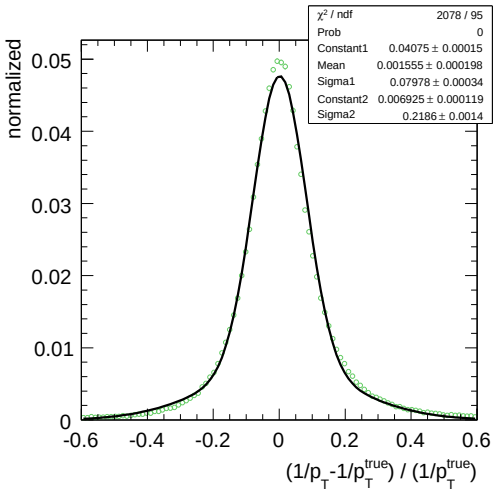

(c) Analytic autocalibration (curved tracks).

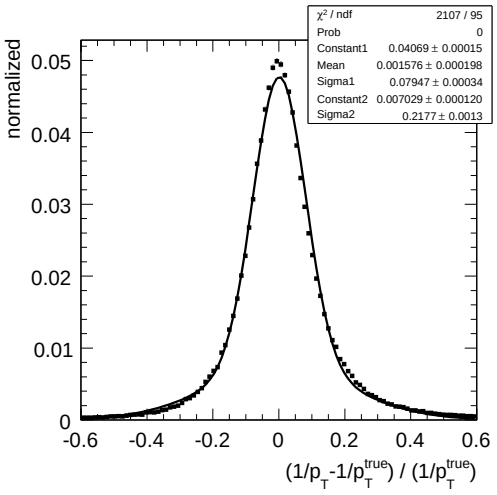

(d) Correct r(t) relationship and t_0.

Figure 4.27: Momentum resolution of the muon spectrometer for the standalone reconstruction of single muons with $p_{\mathrm{T}} = 1\,\mathrm{TeV/c}$ with double-Gaussian fits for the four different r(t) relationships (see text).

Table 4.7: Average standalone momentum resolutions for p_T= 1 TeV/c for different r(t) relationships. The resolution is measured by the widths of the two fitted double-Gaussians σ_{d1} and σ_{d2}.

r(t) relationship	All $\|\eta\| < 2.7$	Barrel $\|\eta\| < 1.1$	End cap $\|\eta\| > 1.7$
		σ_{d1} (%)	
Integration method	8.48±0.04	8.78±0.08	7.84 ± 0.03
Standard Ac	8.12±0.03	8.28±0.07	7.41 ± 0.03
Analytic Ac with curved tracks	7.98±0.03	7.98±0.07	7.31 ± 0.03
True r(t) relationship and t_0	7.95±0.03	8.01±0.07	7.31 ± 0.03
		σ_{d2} (%)	
Integration method	22.72±0.13	20.49±0.18	25.76 ± 0.37
Standard Ac	22.80±0.10	20.03±0.20	26.70 ± 0.40
Analytic Ac with curved tracks	21.86±0.14	18.59±0.18	26.05 ± 0.41
True r(t) relationship and t_0	21.77±0.13	18.90±0.20	25.98 ± 0.41

4.8.2 η- and ϕ-Dependence of the Momentum Resolution

To study in which part of the detector the autocalibration with curved tracks improves muon momentum resolution its η- and ϕ-dependence is analysed. The momentum resolution is defined in this section as the width of a single-Gaussian fit to the x-distribution (see Equation (4.37)). Different from the previous section, the fit range is not restricted to $\pm 2\sigma_x$ around the mean value here because the tails are less pronounced when not integrating over the whole detector. This leads to slightly larger resolution values.
The bending power $\int B \cdot dl$ of the toroid magnet system of the ATLAS muon spectrometer is shown in Figure 4.28 as a function of $|\eta|$. In the barrel part of the spectrometer ($|\eta| < 1.1$), it increases with $|\eta|$ and, as the momentum resolution is $\propto p/\int B \cdot dl$ (see Appendix A), also the momentum resolution improves with $|\eta|$. This effect continues in the end cap part of the spectrometer ($1.7 < |\eta| < 2.5$). Superimposed are several effects related to the detector layout and geometry:

$|\eta| < 0.1$ The decreased resolution around $|\eta| = 0$ is the result of gaps around $z = 0$ between chambers of the large sectors for cables and services for the inner detector and calorimeters.

$0.4 < |\eta| < 0.7$ Two main effects are responsible for the decreased momentum resolution in this detector region. One are gaps between chambers of the large sectors for services to the inner detector and access for detector maintenance: a 18 cm wide gap between the BIL3 and BIL4 chambers and missing BML4A13, BML4C13, BOL4A13 and BOL4C13 chambers.
The second reason is the difficult track configuration for track reconstruction and calibration of the MDT chambers. At $|\eta| = 0.55$, muons with high momentum cross the muon chambers at 30°. Two interesting observations can be made: First, imprecise r(t) relationships have a relatively large effect on the momentum resolution in this region as the track reconstruction is very sensitive to ambiguities if tracks are passing on the left- or

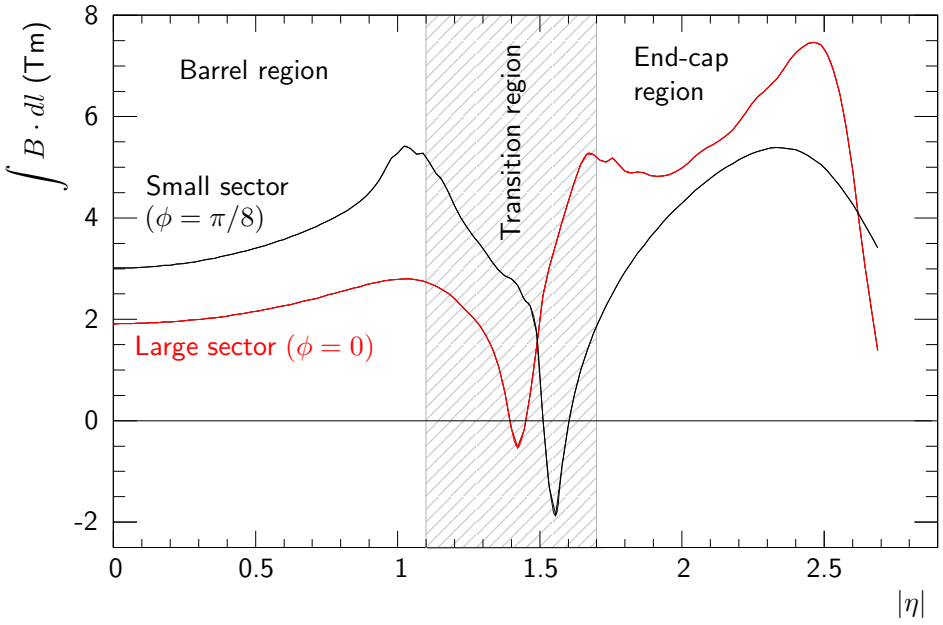

Figure 4.28: Integrated magnetic field strength of the ATLAS muon spectrometer as a function of $|\eta|$ [52].

the right-hand side of the anode wires of all or most of the drift tube layers. Second, the performance of the muon spectrometer in this region demonstrates the main advantage of the autocalibration with curved tracks with respect compared to the standard method, as it increases the momentum resolution for difficult tracks by about 3 % reaching the same performance as with the correct r(t) relationship.

$1.1 < |\eta| < 1.7$ In the transition region between the barrel and the end cap parts of the detector, a highly non-uniform magnetic field distribution and on average smaller number of chambers are along the muon path lead to the worst standalone momentum resolution in the spectrometer. The momentum resolution in this $|\eta|$-region improves when combining the measurements of inner detector and muon spectrometer. Furthermore, additional MDT chambers[3] are planned to be installed in the transition region in 2012 to improve the standalone measurement. Currently 10 out of 62 of these chambers are installed in the detector, but are not yet included in the detector simulation.

$2.5 < |\eta| < 2.7$ The loss of bending-power of the end cap toroid magnets combined with the fact that the EOL chambers do not cover this $|\eta|$-region, leads to a decrease of momentum resolution in the very forward region.

The dependence of the standalone momentum resolution for single muons with $p_T = 1\,\text{TeV/c}$ on the pseudorapidity η and the azimuthal angle ϕ is shown in Figure 4.30. For the muon reconstruction the calibration accuracies are taken into account using r(t) relationships determined by the autocalibration with curved tracks and fitted t_0 values. As

[3]MDT chambers from the types EES and EEL.

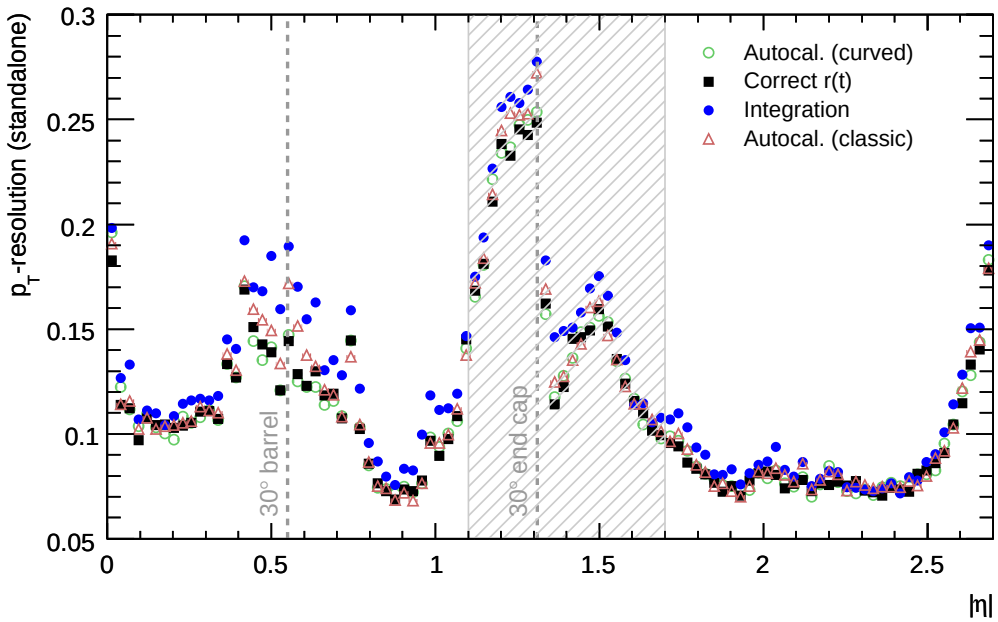

Figure 4.29: Standalone momentum resolution for single muons at $p_{\mathrm{T}} = 1\,\mathrm{TeV/c}$ as a function of $|\eta|$. The different markers represent the three different methods for the r(t) calibrations—Integration method, the two different autocalibration methods. For comparison, also the determined resolution achieved with the correct calibration constants are shown.

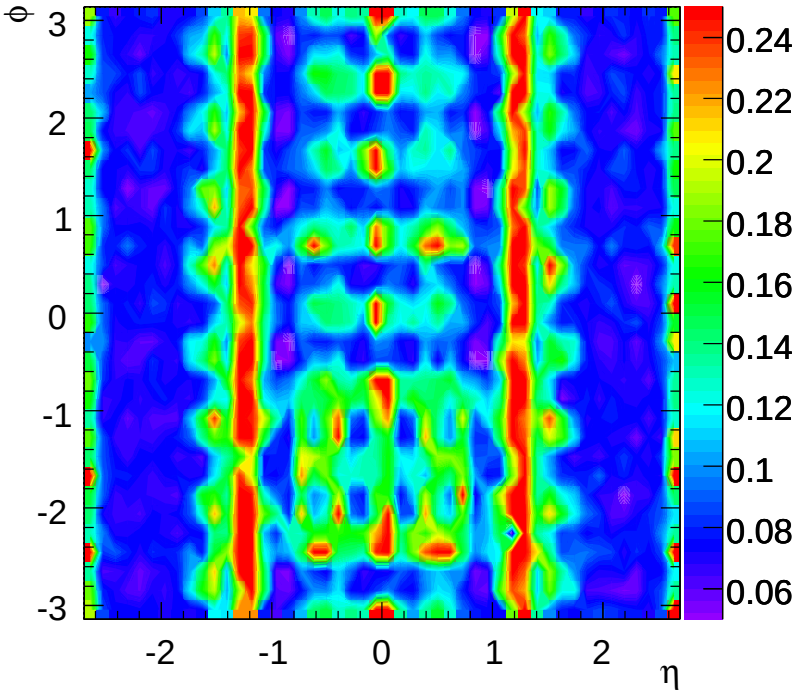

Figure 4.30: Standalone momentum resolution of the ATLAS muon spectrometer as a function of the pseudorapidity η and the azimuthal angle ϕ for single muons with $p_T = 1\,\mathrm{TeV/c}$ (see text).

shown in Tables 4.6 and 4.7, the influence of the calibration precision on the momentum resolution is negligible, if the autocalibration with curved tracks is used.
As the effect of MDT chamber misaligned is not included in the simulation, Figure 4.30 mainly points out the regions where the resolution is decreased by layout ond magnetic field effects. Clearly visible are the acceptance gaps in the large barrel sectors around $\eta = 0$ and close to $|\eta| = 0.55$. In addition, the larger bending power in the small barrel sectors is visible as well as the effect of the extra material in combination with an incomplete coverage in the feet region of the detector ($-2.5 < \phi < 1.5$). The two bands with resolutions larger than 24 % at $1.1 < |\eta| < 1.7$ are the result of the low average bending power and the still missing third layer of MDT chambers in the transition region. The high bending power in the end cap regions of the spectrometer combined with almost complete ϕ-coverage leads to the most accurate standalone muon momentum measurement in the TeV range .

4.9 Test of the Autocalibration with Cosmic Ray Muons

The last commissioning phase of the ATLAS detector before the first proton-proton collisions in November 2009 involved the detection of muons from cosmic rays. Triggered mainly by the RPC chambers more than $2 \cdot 10^8$ muons have been recorded during autumn

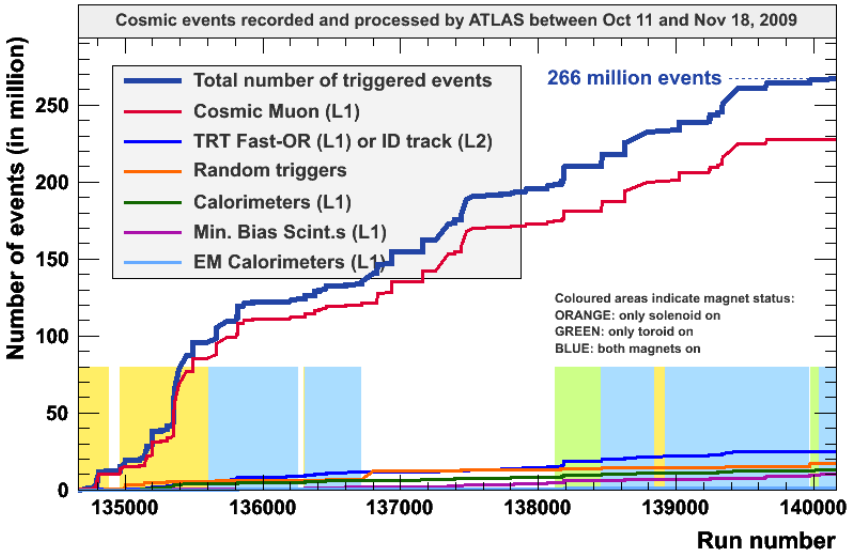

Figure 4.31: Integrated cosmic muon rate in the ATLAS detector versus run number for the cosmic data taking period in October/November 2009 with combined ATLAS sub-detectors. Periods with different magnetic field configurations are indicated.

2009 (see Figure 4.31) to test the functionality of all sub-detectors (combined cosmic runs). Data was taken with and without magnetic field during this period. These datasets provide the unique possibility to test the autocalibration with real data and to study the stability of the drift properties of the installed MDT chambers as well as the influence of the magnetic field.

4.9.1 Cosmic Muons in ATLAS

On the surface of the earth, muons are the most numerous charged particles originating from cosmic rays with an integral intensity of vertical muons above 1 GeV of about $1\,\mathrm{cm}^{-2}\mathrm{min}^{-1}$ at sea level. Most muons are produced in the atmosphere at a height of typically 15 km and loose on average 2 GeV due to ionization before reaching the ground. Their energy and angular distributions are convolutions of production spectrum, energy loss and decay rate. Muons with a momentum of 2.4 GeV/c, for example, have a decay length of 15 km. Due to energy losses on their way through the atmosphere it is reduced to 8.7 km. Hence, the mean muon energy at the surface is about 4 GeV. The angular distribution is $\propto \cos^2\theta$.
The ATLAS cavern is situated about 90 m below ground level. Thus cosmic muons with energies below about 30 GeV at the surface cannot reach the ATLAS detector but are absorbed in the rock and soil above. However, muons flying through one of the two access shafts with diameters of 12.5 m and 18 m reach the detector with less, or only minor energy losses. Hence, most of the cosmic muon tracks recorded in the detector are constrained to the directions of the two large shafts. Figure 4.32(a) shows a $y-z$ cross section of the ATLAS experimental cavern with 150 reconstructed cosmic muon tracks. The tracks have been measured with the 12 muon chambers from the middle barrel layer in the upper horizontal sector (BML, sector 5) and extrapolated to the surface without taking into account multiple scattering. The small gap without reconstructed tracks on the right detector side

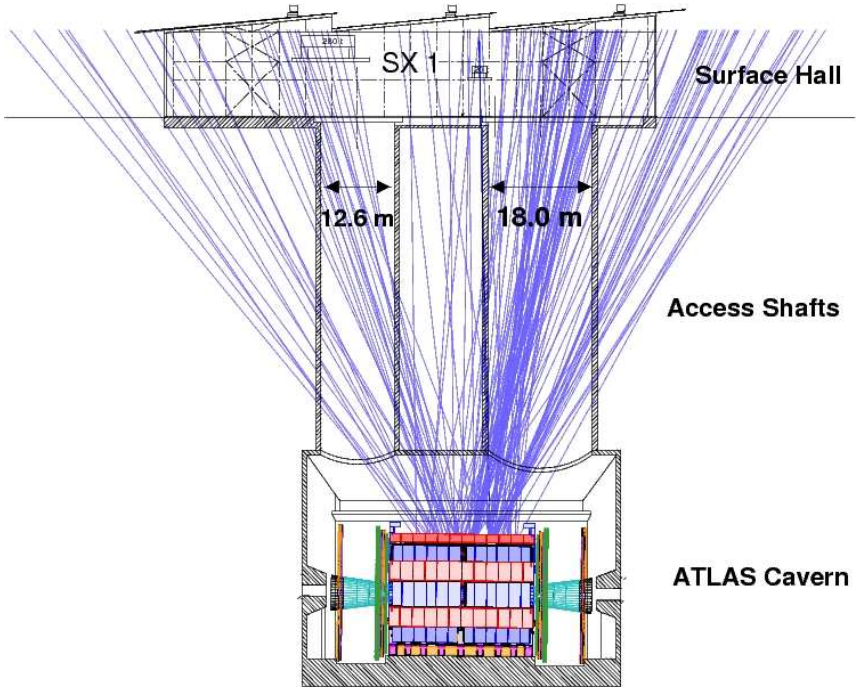

(a)

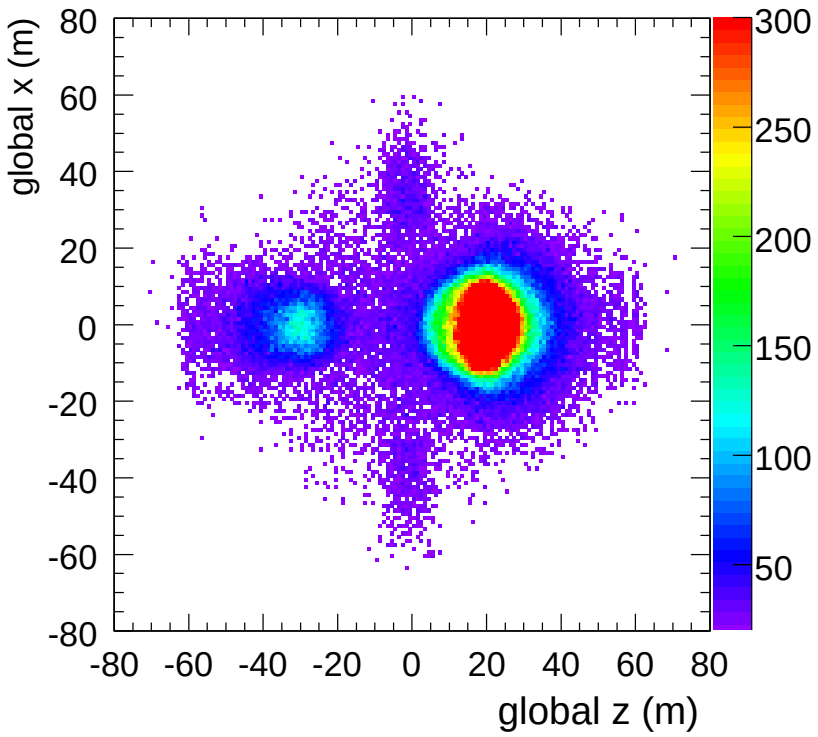

(b)

Figure 4.32: Cosmic muon tracks recorded with the MDT chambers of the upper sector of the ATLAS muon spectrometer.(a) Visualization of cosmic muon tracks in a cross section through the experimental cavern and the region above the detector. (b) Distribution of the extrapolated muon track coordinates to ground level. The accumulations of track points are due to access and elevator shafts through which the muons created in the atmosphere can reach the ATLAS cavern with less energy loss than through 90 m of soil.

is related to an un-powered RPC chamber during this data taking. In Figure 4.32(b), the origin of $1.5 \cdot 10^6$ muon tracks, reconstructed with the BML chambers in sector 5, at the surface ($x - z$ plane) are plotted. In addition to the two main access shafts, two other directions are favoured for the muons. They correspond to two elevator shafts connecting the experimental cavern with the surface.

4.9.2 Datasets from Combined Cosmic Runs

Two combined cosmic runs are chosen for the studies. One with the toroid magnets turned off and $9 \cdot 10^6$ measured muons, the other one with full magnetic field and $7 \cdot 10^6$ recorded events (see Table 4.8).

Table 4.8: Overview about the two selected cosmic runs.

Run number	Start time	End time	No. events	Solenoid	Toroid
135441	18.10.09 21:14 h	19.10.09 05:05 h	9 M	on	off
135816	20.10.09 22:48 h	21.10.09 07:24 h	7 M	on	on

For both run runs, most MDT chambers were powered and working with only 0.3 % of dead tubes (mainly due to problems in the HV distribution or broken wires). For two reasons, the recorded muons are not uniformly distributed over the spectrometer (see Figure 4.33). First, cosmic muons cross the ATLAS detector from top to bottom constrained by the access shafts (see previous Section). Therefore, most muons are recorded in the horizontal barrel sectors 5 and 13 and in sectors with small azimuthal angle, barrel sectors 3, 6, 12, 14. Secondly, a modified version of the low-p_{T} muon trigger was used for the data taking with cosmic muons. Hence, only muons crossing the two RPC planes of the middle barrel layer (RPC 1,2) or the two outer TGC planes (TGC 2,3) are recorded. For geometrical reasons, the probability that a muon crosses an MDT chamber decreases with increasing $|\eta|$ for the inner and outer layers of the barrel. The counting rate per chamber is proportional to the chamber size leading to lower rates in the inner compared to the outer chambers. In addition, several RPC chambers where turned off for these runs (for example for the BML2C05) significantly reducing the number of hits through the associated middle MDT chamber and corresponding chambers of the inner and outer layer.
The low hit rate in the end cap chambers is obvious from detector layout. The vertical TGC wheels trigger only relatively few muons. The small end cap wheel is situated inside the acceptance region of the RPC cosmic trigger. Thus the rate of cosmic muons recorded in the EIS and EIL chambers is the largest in the end cap region. As muons triggered by the upper RPC layers can cross the lower part of the middle end cap wheel (EML, EMS chambers), the muon rate in the respective lower sectors is larger than for the rest of the chambers triggered only by TGCs. The low rate of cosmic muons at large polar angles in the experimental cavern leads to counting rates close to zero in the EOS and EOL chambers.
A peculiarity of the data taking of cosmic muons is that the drift time measurement has to be adjusted for each event as the read out electronics is designed to measure times relative to the accelerator-clock. As cosmic muons are impinging the ATLAS detector asynchronous to the 40 MHz LHC clock, all measured drift times have a jitter correspond-

ing to an uniform distribution in a 25 ns interval. In addition, the spread of trigger times of triggers generated in different parts of the detector can be up to about 100 ns (4 bunch crossings) due to the then not yet optimized trigger synchronization. This effect can be corrected for by using the time information when the muon crossed the associated RPC chamber which has a precision of 2 ns.

4.9.3 Autocalibration with Cosmic Muons

Chamber BML1C05 which has a high muon rate (see previous section), will be used in this section to test the autocalibration with muons from the cosmic radiation. During the two selected runs $5 \cdot 10^5$ ($3 \cdot 10^5$) muon track segments without (with) magnetic field could be reconstructed in this chamber.

Residuals as a Measure of the Calibration Accuracy

Even though the angular distribution of the cosmic muons reaching the experimental cavern is restricted, the incidence angles of the cosmic muons are widely spread compared to muons originating from the interaction point. In particular, there is no region where muon incidence angles are restricted to an interval near 30°. Thus the track residuals and their dependence upon the distance between tracks and wires can be used as a qualitative measure of the calibration accuracy in the data:

- A non-accurate r(t) relationship affects the mean values of the residuals.
- A degradation of the time resolution increases the widths of the residual distributions.

Figure 4.34 shows the residual distributions after autocalibration as a function of the distance d between tracks and anode wires for cosmic muons (chamber BML1C05 without magnetic field) and for simulated single muons as comparison. The mean values of the residual distributions as a function of d agree within 20 μm to zero except for the asymmetric regions close to the wire and to the tube wall. The comparison of the mean values indicates that a r(t) accuracy of $\rho \simeq 11\,\mu$m for cosmic data, very similar to the result for simulated muons from the interaction region.
However, the residual distributions for cosmic muons have larger widths which points to a degradation of the time resolution. To determine the precision of the time measurement, the widths of the residual distributions in bins of d are determined by fitting Gaussians to them. The standard deviations $\sigma(\Delta(r))$ of the Gaussians are shown as a function of the distance d in Figure 4.35. In addition, the residuals for the simulated data are recomputed with random offsets on the drift time. Good agreement with the data is achieved, when smearing the time measurement in an interval of 4 ns which is in reasonable agreement from the precision of 2 ns of the trigger time correction together with small contributions from multiple scattering in material not included in the simulation and corrections for time slewing and for different t_0 for individual drift tubes not included in the data.

Stability of the r(t) Calibration

The stability of the r(t) relationship during a run depends on changes of the drift properties due to variations of temperature, gas mixture and ambient humidity. To validate the

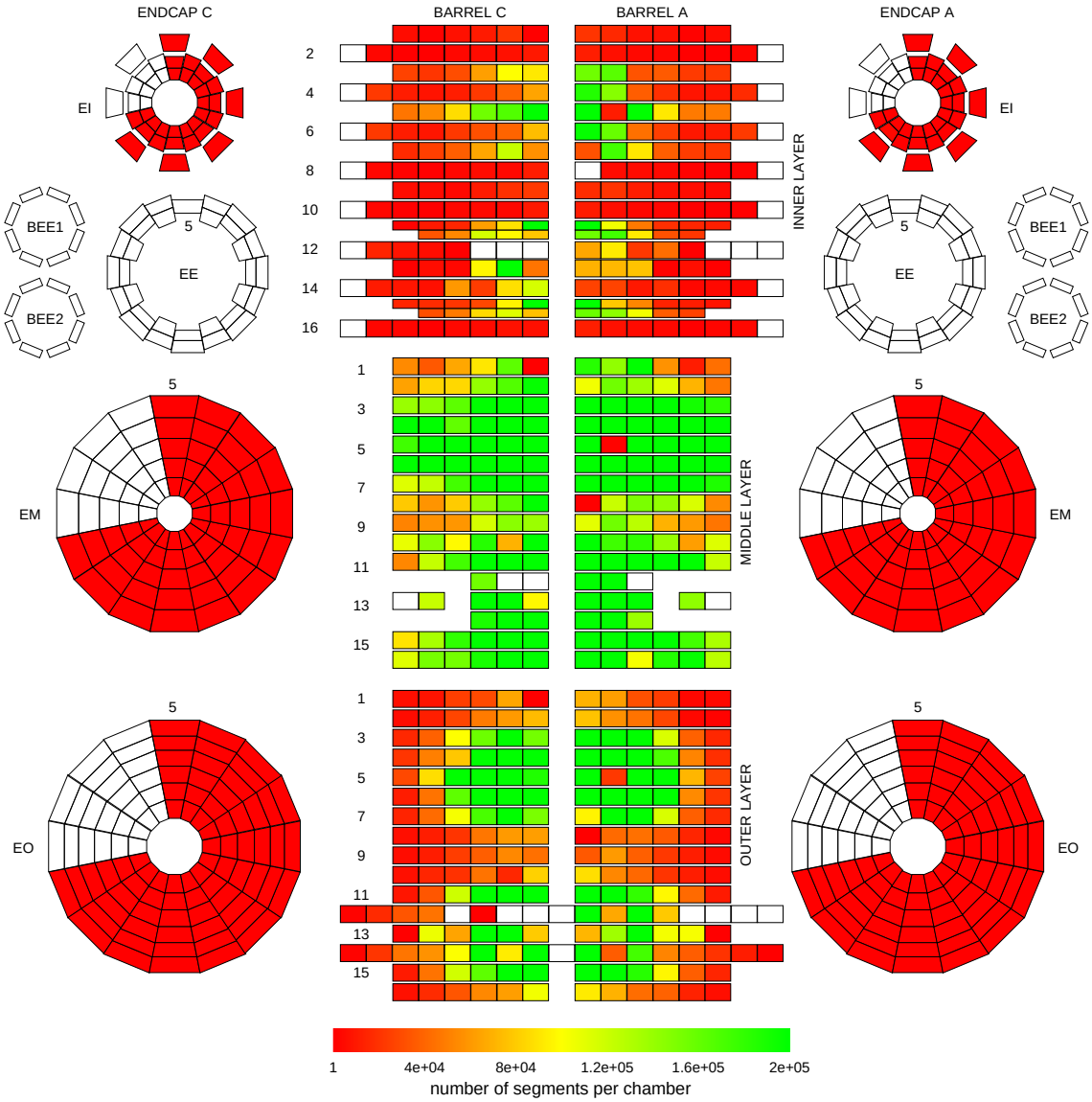

Figure 4.33: Number of hits per MDT chamber in the combined cosmic data run 135441. Most muons are recorded in the middle horizontal barrel layers. No data were available for the chambers marked white.

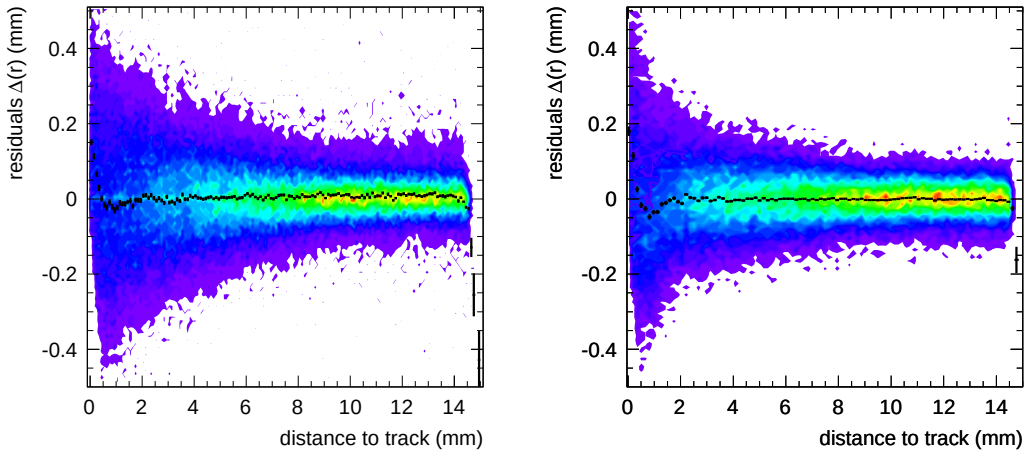

(a) (b)

Figure 4.34: (a) Residuals of cosmic muon tracks as a function of the distance between tracks and wires compared to (b) the residuals of simulated single muons after autocalibration in the BML1C05 chamber without magnetic field.

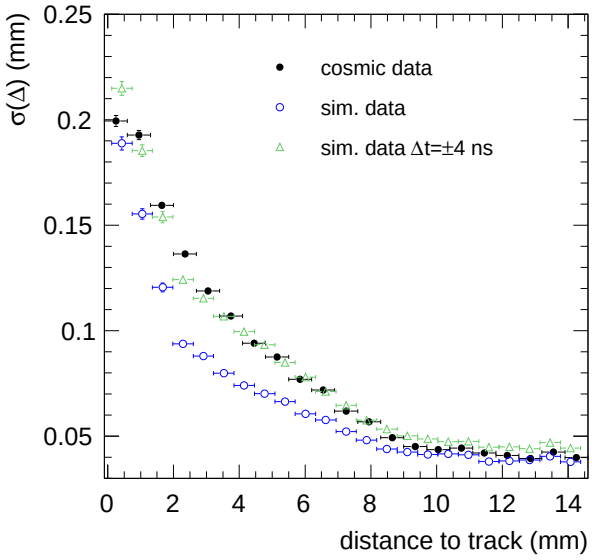

Figure 4.35: Width $\sigma(\Delta(r))$ of the residual distributions as a function of the distance between tracks and wires for cosmic muons and simulated muons with nominal and degraded (by ± 4 ns) time resolution.

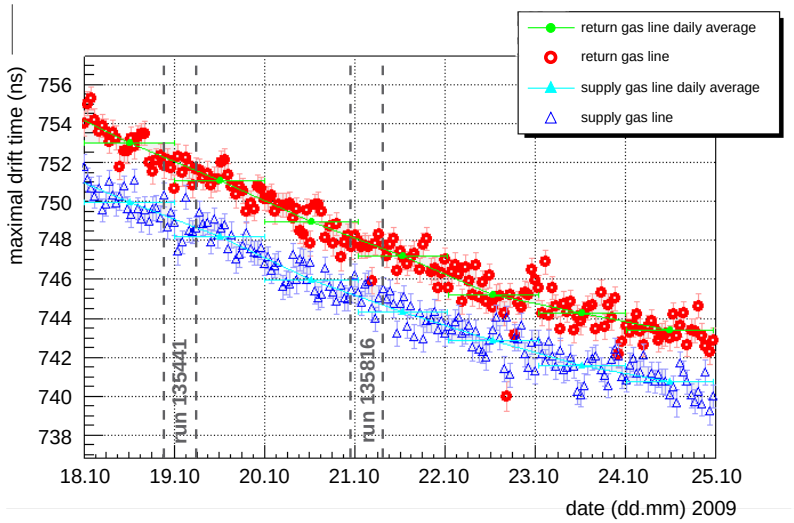

Figure 4.36: Maximum drift times measured with the gas monitoring chamber during the week of 18 October 2009. The drift times are corrected to a reference temperature of 20° C. The times of the two data taking runs are indicated.

accuracy of the autocalibration by means of cosmic muons with different sub-samples of a run, changes of temperature and gas-mixture have to be known:

- To monitor the gas composition with time, a dedicated drift chamber is used which is installed in the ATLAS gas supply building on the surface in the supply and in the return line of the MDT gas distribution system [75]. The test chamber measures the drift time spectrum with cosmic muons corrected to a nominal temperature of 20° C. The maximum drift times measured by the test chamber during the week of the two selected runs are depicted in Figure 4.36. They drop steadily from about 751 ns (755 ns) to 739 ns (743 ns) in the supply (return) gas line which can be traced to technical problems in the admixture of water to the gas mixture. During the time of each data taking, the maximum drift time changes by less than 1 ns, but there is a difference of about 4 ns between run 13541 and run 135816. Using a mean drift velocity of $\langle v(r) \rangle \approx 20\ ^{\mu m}/_{ns}$, the influence of the maximum drift time change Δt_{max} on the drift radius measured can be estimated by

$$\Delta r_{max} \simeq \langle v(r) \rangle \cdot \Delta t_{max} \tag{4.40}$$

  which predicts a change of the maximum drift radius by less than 20 μm during each run, but by about 80 μm in between the two selected runs.

- The average temperature of chamber BML1C05 was very stable and measured to 24.2° C (24.5° C) during run 135441 (135826) keeping the maximum drift time constant within 1 ns with $\Delta t_{max} = -2.34\ ^{ns}/_{K}$ [61].

The $5 \cdot 10^4$ track segments recorded in run 135411 are divided into five sub-samples with 10^4 segments each, sufficient to determine the r(t) relationship for each sub-sample by autocalibration including residual smoothing. The first sample serves as reference for which the r(t) relationships of the other four samples are compared to study systematic deviations due to changes in the drift properties. To restrict the sensitivity to changes in the

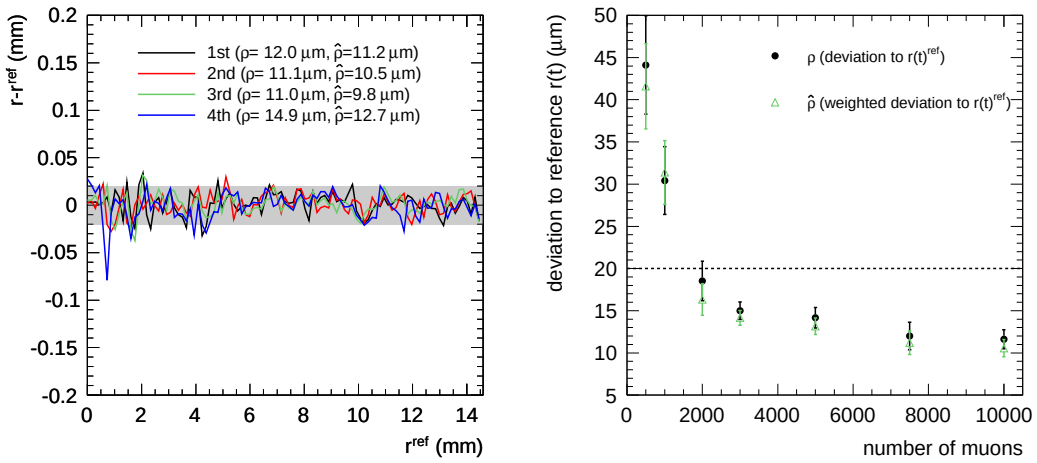

(a) (b)

Figure 4.37: (a) Stability of the r(t) relationship for the BML1C05 chamber during the eight-hour cosmic run 135441 divided into four sub-samples and (b) dependence of the autocalibration accuracy with respect to the reference r(t) relationship on the number of track segments needed for convergence (see text).

r(t) relationship, the full statistics is used for the t_0 fit, combining all tubes connected to the same mezzanine board (note that the starting point $r(t_0)$=0 of the r(t) relationship is still determined by a fit to the drift time spectrum for each sub-sample). The deviations from the reference r(t) relationship are plotted as a function of the drift radius in Figure 4.37(a). Systematic variations of the r(t) relationship during the run in the order of $2-3\,\mu$m can be observed, which is in agreement with the measured change of the maximal drift time due to changes in the gas-mixture during the same time.
As the maximum drift time is stable within $\Delta t_{\max} = 1\,$ns during the selected run, corresponding to few μm in the drift radius, the dependence of the autocalibration precision on the number of cosmic muon track segments can be studied in the following way:

- A reference r(t) relationship is determined using the first $2 \cdot 10^4$ segments of the run.
- The run is divided into five independent sub-samples, of 10^4 segments each from which always five r(t) relationships are determined with increasing statistics.
- The average quadratic and the average weighted quadratic deviations with respect to the reference r(t) relationship are calculated.

The average of the deviations over the five sub-samples are shown in Figure 4.37(b) as a function of the number of segments used per calibration. The result is in good agreement with the simulation (compare Figure 4.18) confirming the number of about 3000 muons needed for r(t) accuracies below 20 μm.

4.9.4 Autocalibration with Magnetic Field

The largest drift time variations within a calibration region are caused by non-uniform magnetic field distributions. The component $B_\perp$ of the toroid field perpendicular to the

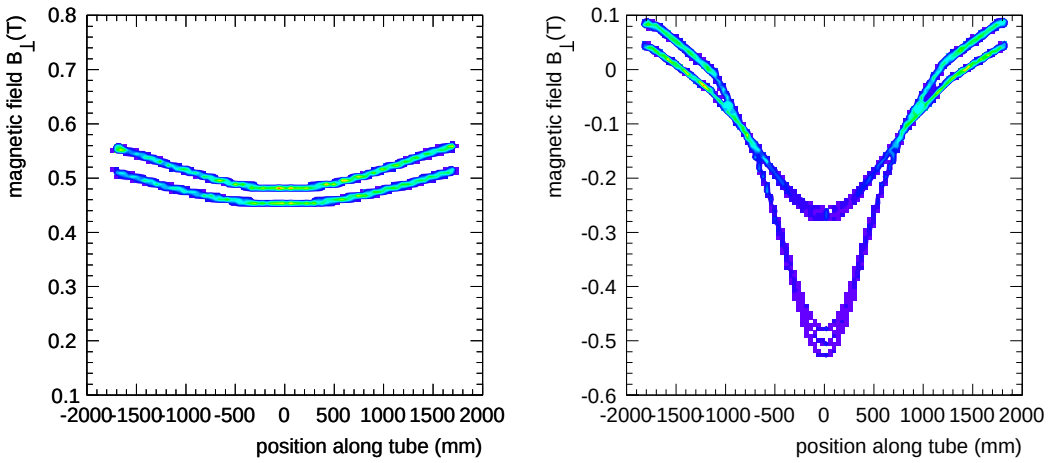

(a) BML1C05 (b) BOS1A06

Figure 4.38: Magnetic field component perpendicular to the drift direction as a function of the hit position along the tubes in the 2×3 layers for two selected barrel chambers. The differences between the multilayers are clearly visible.

drift path deflects primary ionization electrons on their way to the anode wire. Especially for the chambers of the small barrel sectors installed directly on the toroid coils the magnetic field is strongly varying along the tubes and perpendicular to the tube layers inducing variations of the measured drift times as a function of the hit position along the tubes in each layer. The strategy to cope with this effect is to correct each drift time measurement by the additional drift time due to the Lorentz-angle deflection according to (see Appendix D):

$$t(r, B_\perp) = t(r, B_\perp = 0) + \Delta t(r, B_\perp \neq 0). \tag{4.41}$$

The first term is the drift time without magnetic field $t(r, B_\perp = 0)$. The second term describes the change of the drift time $\Delta t(r, B_\perp \neq 0)$ due to the deflection from the straight drift path which can be determined by solving the Langevin equation describing the drift of electrons in the electric and magnetic field [62, 63]. The effect of inelastic scattering processes of the drifting electrons with the (CO_2) gas mixture is taken into account by introducing an additive correction to the exponent of the scattering term in the Langevin equation (see Appendix D). An approximate solution of the modified Langevin equation gives a parametrization of the magnetic field corrections to the drift time:

$$\Delta t(r, B_\perp \neq 0) = B_\perp^{2-\epsilon} \int_{r_{\min}}^{r} \frac{u_0^{1-\epsilon}(x_2)}{E^{2-\epsilon}(x_2)} dx_2, \tag{4.42}$$

where x_2 denotes the coordinate along the distance between muon track and wire, E the electric field and u_0 the drift velocity without magnetic field. This parametrization of the magnetic field effect agrees well with detailed Garfield simulations simulations [62] for proper choice of ϵ. From test beam measurements the parameter ϵ has been estimated for the operating conditions of the ATLAS drift tubes to be $\epsilon \simeq 0.1$ [62].
The precision of the drift time correction is tested for two different barrel chambers:

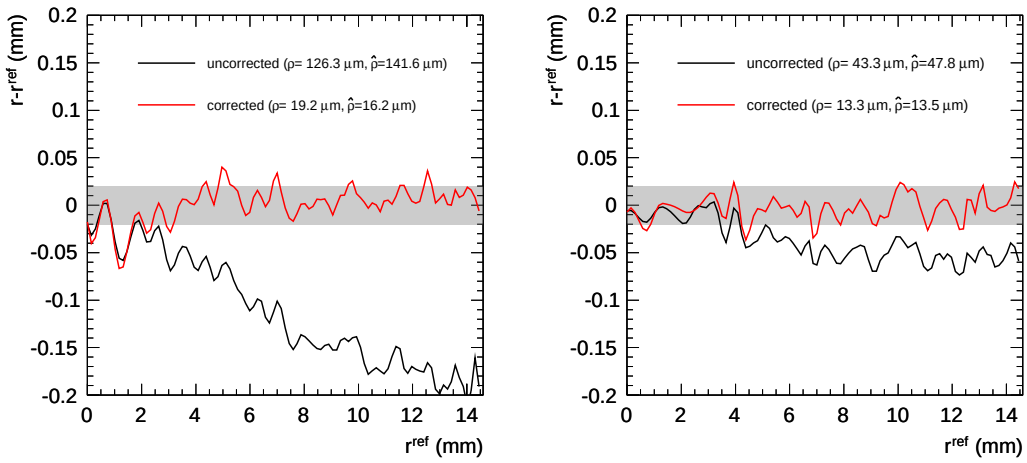

(a) BML1C05 (b) BOS1A06

Figure 4.39: Deviation of the r(t) relationship after autocalibration with cosmic muons with toroid field turned on with and without Lorentz-angle corrections from the reference r(t) relationship without magnetic field for (a) the BML1C05 and (b) the BOS1A06.

BML1C05, situated inside the barrel toroid with $B_\perp$ rather constant along the tubes (see Figure 4.38(a)) and BOS1A06, installed a barrel toroid coil leading to inhomogeneous magnetic field distribution along the drift tubes and perpendicular to the tube layers (see Figure 4.38(b)).
The precision of the Lorentz-angle correction is tested by comparing the r(t) relationship determined with the first 5000 muon segments from run 145816 (toroid magnet on) to a reference r(t) relationship determined for the same MDT chamber but calibrated using the last 5000 segments from run 135441 (toroid off). As discussed in Section 4.9.3, the water content of the gas mixture slightly changed in between the two runs while the temperature stayed stable. The change of the maximum drift time between the two runs is observed to be $\Delta t_{\max} \simeq 4\,\text{ns}$ corresponding to $\Delta r_{\max} \simeq 80\,\mu\text{m}$. The drift times for the reference r(t) relationship are corrected using the approximate formula:

$$t'_{ref} = t_{ref} - \frac{\Delta t_{\max}}{t_{\max}} \cdot t_{ref} \tag{4.43}$$

In Figure 4.39 the difference between the r(t) relationship after autocalibration in the magnetic field with and without Lorentz-angle correction according to Equation (4.42) and the reference r(t) relationship is shown for the BML1C05 and the BOS1A06 chamber. The mean magnetic field components perpendicular to the electron drift lead to average quadratic deviations of $\rho = 126\,\mu\text{m}$ and $\rho = 43\,\mu\text{m}$ for the BML1C05 and the BOS1A06 chamber, respectively. As expected, the difference is increasing with the radius to about $200\,\mu\text{m}$ and $50\,\mu\text{m}$, respectively at the tube wall while with Lorentz-angle correction there is good agreement ($\rho < 20\,\mu\text{m}$).

4.10 Summary

An improved autocalibration algorithm for the drift tubes of the ATLAS MDT chambers has been developed and tested. The algorithm is based on the reconstruction of curved muon track segments in both multilayers of the MDT chambers allowing for accuracies of the space-to-drift-time relationships of better than $20\,\mu$m. Special attention has been paid to the optimization of the method to converge reliably even at low statistics. Tests with simulated single muons corresponding to one hour of data taking at $\mathscr{L} = 10^{33}\,\mathrm{cm}^{-2}\mathrm{s}^{-1}$ give average squared accuracies between 5 and $20\,\mu$m and of better than $30\,\mu$m for 97 % and all of the chambers in the spectrometer, respectively. In addition, the simulated data was used to study systematic effects due to uncertainties in the drift time measurement and the t_0 fit as well as the mechanical precision of the chambers. The precision of the autocalibration with curved tracks was found to be very robust with respect to the studied effects.
Using the improved autocalibration method, no degradation of the momentum resolution with respect to the correct r(t) relationship is expected even at the highest muon energies. The r(t) calibration method has been validated with data of cosmic ray muons confirming the simulation results. Finally the accuracy of Lorentz-angle corrections to the measured drift times in the non-uniform toroidal field has been verified to be better than $20\,\mu$m with dedicated cosmic muon data taking runs.

Chapter 5

Search for Lepton Flavour Violating Decays $\tau \to \mu\mu\mu$ with the ATLAS Detector

With one year of data taking during the low luminosity phase ($\mathscr{L} = 10^{33}\,\mathrm{cm}^{-2}\mathrm{s}^{-1}$) at the LHC an integrated luminosity of about $10\,\mathrm{fb}^{-1}$ will be collected containing 10^{12} τ leptons within the ATLAS detector. For comparison, the total number of τ pairs produced at the e^+e^- B-Factories, experiments which set the current best upper limits for lepton flavour violating τ decays, is about three orders of magnitude lower. This high production cross section at the LHC motivates the search for such rare τ decays. The sensitivity of the ATLAS detector for the neutrinoless decay $\tau \to \mu\mu\mu$ is studied in this chapter.

5.1 Introduction

Since the discovery of the muon by Carl D. Anderson and Seth H. Neddermeyer in 1937 [76], charged-lepton flavour violation (cLFV) has always been an interesting topic in particle physics. First measurements by Hinks and Pontecorvo in 1948 showed that the decay $\mu \to e\gamma$ did not occur in cosmic radiation within their experimental sensitivity [77]. They could exclude this decay with a branching ratio $\mathcal{B}(\mu \to e\gamma) \gtrsim 10^{-2}$ and thus prove that the muon is not just an exited state of the electron.
After the discovery of the τ lepton by the group of Martin L. Perl in 1975 [78], also the cLFV τ decays such as $\tau \to \ell\gamma$ and $\tau \to \ell\ell\ell$ (with $\ell = e, \mu$) attracted the interest of the particle physicists. The corresponding limits on the branching ratios have been continuously improved ever since without finding any evidence for these decays.
With the observation of neutrino oscillations at the end of the 1990's, the existence of lepton flavour violation was proven. Still, the important question remains whether the rates of charged-lepton flavour violating decays are consistent with the predictions of the Standard Model with massive neutrinos and thus below experimental sensitivity for probably many decades, or considerably larger as predicted by numerous extensions of the Standard Model and therefore within experimental reach.
As explained in the theoretical introduction of this work (Chapter 2) the cLFV decay $\tau \to \mu\mu\mu$ is suppressed in the Standard Model by the GIM mechanism, resulting in branching ratios on the order of 10^{-14}. However with contributions from new heavy par-

Table 5.1: Current upper limits on a selection of charged lepton flavour violating decays. The limits on the μ decays have been set by experiments at the Los Alamos Meson Physics Facility (LAMPF), while the limits on the τ decays have been set by the B-physics experiments BELLE and BABAR. The given numbers and references are all quoted by the particle data group [1].

Decay	Branching ratio	Year	Reference
$\mu^- \to e^-\gamma$	$< 1.2 \cdot 10^{-11}$	1999	[81]
$\mu^- \to e^-e^+e^-$	$< 1.0 \cdot 10^{-12}$	1988	[82]
$\tau^- \to e^-\gamma$	$< 1.1 \cdot 10^{-7}$	2006	[83]
$\tau^- \to \mu^-\gamma$	$< 4.5 \cdot 10^{-8}$	2008	[84]
$\tau^- \to e^-e^+e^-$	$< 3.6 \cdot 10^{-8}$	2008	[85]
$\tau^- \to \mu^-e^+e^-$	$< 2.7 \cdot 10^{-8}$	2008	[85]
$\tau^- \to e^-\mu^+\mu^-$	$< 3.7 \cdot 10^{-8}$	2008	[86]
$\tau^- \to \mu^-\mu^+\mu^-$	$< 3.2 \cdot 10^{-8}$	2008	[85]

ticles in the loop processes responsible for the decays they could become experimentally accessible. Experiments with steadily increasing sensitivity have been performed in the last 50 years to search for cLFV decays as a hint of new physics. Even if none of the decays has been observed so far, the high precision measurements help to constrain the theories beyond the Standard Model, e.g. the parameter space of supersymmetric models.

The current best experimental upper limits on cLFV decay rates are in the range $10^{-7} - 10^{-12}$ depending on the decaying lepton (see Table 5.1). The limits on the τ decays are from the BELLE [79] and BABAR [80] experiments at e^+e^- B-Factories built for precision B-physics measurements.
At hadron colliders such as the LHC, the search for decays with muons in the final state are favoured due to the clean signature in the detector compared to electrons and photons. Due to the difficult discrimination from the huge background from light meson decays and the expected large pre-scaling factors for the low p_{T} single muon trigger, the sensitivity of the LHC experiments for $\tau \to \mu\gamma$ decays is relatively low. However, for multi-muon signatures lower momentum thresholds without pre-scaling are possible. Therefore, this work is focused on the decay $\tau \to \mu\mu\mu$. The investigation presented in this chapter is the first study of the sensitivity of the ATLAS detector for this rare τ decay. For the study of the sensitivity of the CMS detector see [87].

5.2 Simulation of the Decay $\tau \to \mu\mu\mu$

The analysis is based on Monte Carlo data. The simulation of physics processes in proton-proton collisions starts with the generation of the hard-scattering process followed by parton showering and hadronization. As the decay $\tau \to \mu\mu\mu$ was not available in any of the event generators of the ATLAS software framework Athena [71], it was implemented for this study using the following strategy:

- The program Pythia [88] is used to generate events in proton-proton collisions at $\sqrt{s} = 14\,\mathrm{TeV}$.

- Particles decaying leptonically or semileptonically are forced to decay to τ leptons (see Section 5.3).
- The generator is adjusted to treat τ leptons as stable particles.
- The $\tau \to \mu\mu\mu$ decay routine[1] is implemented in order to produce final states with three muons with uniform momentum distribution in the phase space. The four-momenta produced are further processed by the ATLAS detector simulation software (see Section 5.6).

According to [89], the contribution from the different theories beyond the Standard Model to $\tau \to \mu\mu\mu$ decays have no significant impact on the kinematics, i.e. ϕ, η and p_{T} distributions of the muons as well as ΔR of each pair of muons compared to pure phase-space decays. Effects related to the spin of the τ lepton are neglected in this study.

5.3 Production of τ Leptons at the LHC

The major sources of τ leptons at high energetic pp-collisions are:

- The leptonic charm decay $D_s^{\pm} \to \tau^{\pm}\nu_{\tau}$.
- Semileptonic B meson decays $B \to \tau\nu_{\tau}X$.
- Gauge boson decays $W^{\pm} \to \tau^{\pm}\nu_{\tau}$ and $Z^0 \to \tau^{+}\tau^{-}$.

The cross sections for D and B meson production are several orders of magnitude larger than the gauge boson production while the branching ratios for decays into leptons are similar for gauge bosons and D and B mesons. Thus D_s and B meson decays are the dominant sources of τ leptons at the LHC.

5.3.1 Production of τ Leptons in Heavy Meson Decays

The main source of τ leptons at the LHC are the decays of heavy mesons from the hadronization of $c\bar{c}$ or $b\bar{b}$ pairs. The inclusive τ production cross section due to heavy quark ($q = c, b$) decays is given by:

$$\sigma\left(pp \to q\bar{q} + X \to \tau + X\right) = \sigma\left(pp \to q\bar{q} + X\right) \cdot \frac{\text{number of events with } \tau\text{'s}}{\text{total number of events}}, \qquad (5.1)$$

where the fraction of events with τ leptons is determined from two Monte Carlo samples with 10^6 events each—one for $pp \to c\bar{c} + X$ and one for $pp \to b\bar{b} + X$. The $q\bar{q}$ production cross sections at $\sqrt{s} = 14\,\mathrm{TeV}$ are determined using the Pythia [88] event generator, version 6.420, with parton distribution functions CTEQ6L1 [90]. The ATLAS software provides a special tool for the production of heavy quark pairs. The ATLAS PythiaB interface to the Pythia generator allows for applying kinematic selection before and after hadronization. Only c-quarks with $p_{\mathrm{T}} > 4\,\mathrm{GeV}$ and b-quarks with $p_{\mathrm{T}} > 5\,\mathrm{GeV/c}$ in the pseudorapidity range $|\eta| < 4.5$ have been generated. The total τ production cross section

[1] The routine developed is part of the Pythia interface `PythiaExo_i` which is mainly used by the ATLAS exotics physics group and is part of the official release since Athena version 15.3.0.

Table 5.2: Leading order cross sections for the main sources of τ leptons at $\sqrt{s} = 14\,\text{TeV}$ and relative fraction of the τ-leptons produced via charm and beauty decays as calculated with the Monte Carlo program PYTHIA. In the last column the expected numbers of τ leptons produced are given for an integrated luminosity of $10\,\text{fb}^{-1}$.

Meson (M)	σ_τ	$\sigma_\tau/\sigma_{\text{tot}}$	$N(\tau)/10\ \text{fb}^{-1}$
B^0	$56.4\,\mu\text{b}$	0.40	$5.6 \cdot 10^{11}$
$B^\pm$	$55.0\,\mu\text{b}$	0.39	$5.5 \cdot 10^{11}$
$D_s^\pm$	$19.7\,\mu\text{b}$	0.14	$2.0 \cdot 10^{11}$
B_s^0	$9.9\,\mu\text{b}$	0.07	$1.0 \cdot 10^{11}$
$\sum$	$141.0\,\mu\text{b}$	1.0	$14.1 \cdot 10^{11}$

$\sigma_\tau = \sigma(M \to \tau + X)$, $\sigma_{\text{tot}} = \sigma(pp \to \tau + X)$

Table 5.3: NNLO values for inclusive cross sections of W and Z production with subsequent $W \to \tau\nu$ and $Z \to \tau\tau$ decays as calculated with the Program FEWZ [91,92] at the LHC ($\sqrt{s} = 14\,\text{TeV}$). In the last column the expected numbers of produced τ-leptons for an integrated luminosity of $10\ \text{fb}^{-1}$ are given.

Boson	σ_τ	$N(\tau)/10\ \text{fb}^{-1}$
Z^0	$2.02\,\text{nb}$	$4.04 \cdot 10^7$
$W^\pm$	$20.51\,\text{nb}$	$20.51 \cdot 10^7$

$\sigma_\tau = \sigma(pp \to W \to \tau\nu)$ or $\sigma(pp \to Z \to \tau\tau)$

from charm and beauty decays sums up to $\sigma_\tau \simeq 141\,\mu\text{b}$ corresponding to $1.4 \cdot 10^{12}$ τ leptons per $10\ \text{fb}^{-1}$ of integrated luminosity. Table 5.2 summarizes the contributions of individual charm and beauty meson decays. The decays $B^0 \to \tau + \nu_\tau + X$ and $B^\pm \to \tau + X$ are the two dominant production processes. PYTHIA only takes leading order processes into account, resulting in theoretic uncertainties of about 50 % on the $q\bar{q}$ production cross sections [91].

5.3.2 Production of τ Leptons by Gauge Boson Decays

PYTHIA 6.420 is also used for the generation of the τ leptons produced in gauge boson decays. However, to profit from new developments in the cross section calculations up to the next-to-next-to-leading order (NNLO) in perturbative QCD, the total cross sections were rescaled to the results from the program FEWZ [92] with the parton distribution functions CTEQ6.1 [52, 91]. To suppress low energetic Drell-Yan processes a cut on the generated invariant mass $\text{m}_{\tau\tau} > 60$ GeV is applied while no cut was used for the W production. The results are listed in Table 5.3 and the total cross section for τ leptons produced by gauge boson decays sums up to $\sigma_\tau = 22.53\,\text{nb}$, or about $2.5 \cdot 10^8$ τ's with $10\,\text{fb}^{-1}$ of collected data.

5.4 Signal Event Topology and Detector Acceptance

The topology of the signal events depends on the production channel. The large masses of the gauge bosons of $m_W \simeq 80.4\,\text{GeV}$ and $m_Z \simeq 91.2\,\text{GeV}$ lead to a minimum momentum

of about 40 GeV/c for the τ leptons. This leads to a mean muon momentum of about 13 GeV/c from subsequent $\tau \to \mu\mu\mu$ decays. The masses of the D_s and the B mesons are only $m_{D_s} = 1.97\,\text{GeV}$ and $m_{B^{0,\pm}} = 5.28\,\text{GeV}$ leading to muon momenta from $\tau \to \mu\mu\mu$ below 1 GeV/c. However, the mesons are created in the fragmentation of heavy quarks produced in highly energetic pp-collisions and thus carry high momenta leading to long tails in the momentum distribution of the muons from $\tau \to \mu\mu\mu$ up to several 10 GeV/c. Measuring events with only low energetic muons ($p_\text{T} < 6\,\text{GeV/c}$) is challenging for the following reasons. The mean energy loss of the muons in the inner detector and the calorimeters is 3 GeV. Hence, muons below this threshold do not reach the ATLAS muon spectrometer. Furthermore the momentum thresholds of the muon triggers have to be passed. In order to study the acceptance effects, $\tau \to \mu\mu\mu$ decays are selected with the following criteria from the different simulated data samples:

- Pseudorapidity range of the muon spectrometer: $|\eta| < 2.7$.
- Minimum muon momentum to pass the calorimeters: $p_\text{T} > 3\,\text{GeV/c}$.

The acceptance of the ATLAS trigger is in addition:

- Di-muon trigger: $2 \times p_\text{T} > 6$ GeV/c, $|\eta| < 2.4$.
- Single muon trigger: $p_\text{T} > 20$ GeV/c, $|\eta| < 2.4$.

The lowest muon trigger threshold without pre-scaling is 6 GeV/c for di-muon and 20 GeV/c for single-muon signatures in the pseudorapidity range $|\eta| < 2.4$. The fraction of events passing these criteria is the detector acceptance ϵ_acc.
The p_T distributions of the three muons from $\tau \to \mu\mu\mu$ decays in four selected τ production channels are depicted in Figure 5.1. The histograms are normalized for an integrated luminosity of $10\,\text{fb}^{-1}$ using $\mathcal{B}(\tau \to \mu\mu\mu) = 3.2 \cdot 10^{-8}$.
In only 0.07 % of the $D_\text{s} \to \tau\nu_\tau X$ events all three muons have transverse momentum larger than 3 GeV/c corresponding to an acceptance of $\epsilon_\text{acc} = 8.9 \cdot 10^{-4}$.
As the masses of the different B mesons are quite similar ($m_{B^{0,\pm}} = 5.28\,\text{GeV}$, $m_{B_s^0} = 5.37\,\text{GeV}$), only the muon p_T distributions for $B^0 \to \tau\nu_\tau$ events are shown (see Figure 5.2(b)). In 0.15% of the events all muons pass the minimum p_T threshold of 3 GeV/c resulting in an acceptance of $\epsilon_\text{acc} = 7.4 \cdot 10^{-4}$.
As expected, the p_T distributions are significantly shifted to higher p_T values for the gauge boson decays (see Figures 5.2(c) and 5.2(d)) and are peaking between 10 and 20 GeV/c for the two hardest muons leading to acceptances of $\epsilon_\text{acc} = 0.51$ for the W and of $\epsilon_\text{acc} = 0.56$ for the Z source.
In Figure 5.2 the pseudorapidity distribution of the four sources of $\tau \to \mu\mu\mu$ decays are depicted. It has to be mentioned that for the generation of D_s and B_0 events, pseudorapidities $|\eta| < 4.5$ of the heavy quarks are required while no cuts on η are applied for the gauge boson event generation.

5.4.1 Kinematic Properties of the Signal Events

By multiplying the τ production cross sections from Tables 5.2 and 5.3 with the corresponding acceptances ϵ_acc, the visible cross sections

$$\sigma_\text{vis}(\tau \to \mu\mu\mu) = \epsilon_\text{acc} \times \sigma_\tau \tag{5.2}$$

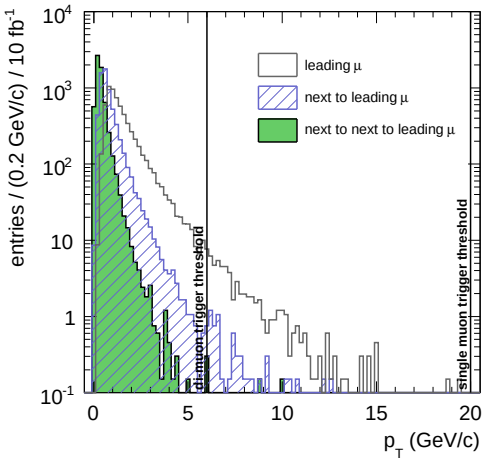

(a) $D_s \to \tau\nu_\tau X$ channel

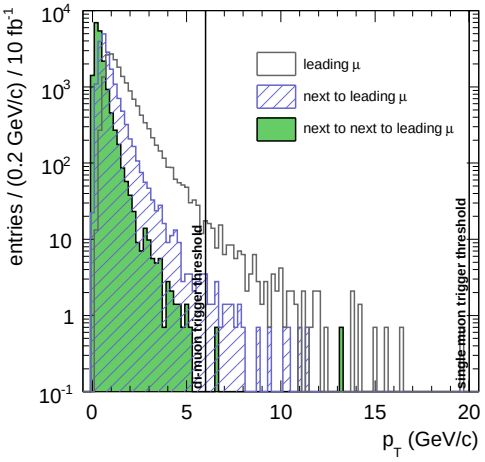

(b) $B^0 \to \tau\nu_\tau X$ channel

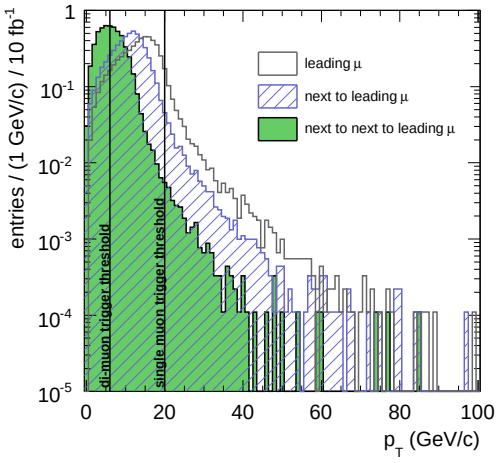

(c) $W \to \tau\nu_\tau$ channel

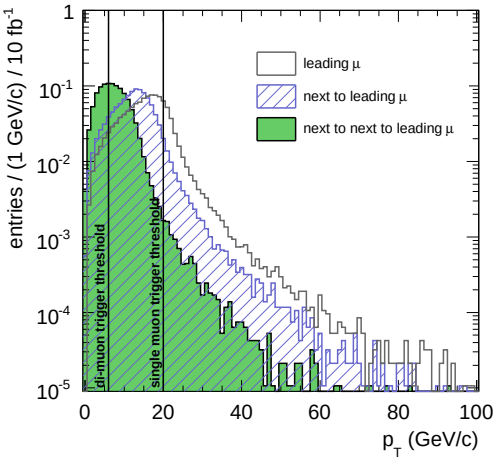

(d) $Z \to \tau\tau$ channel

Figure 5.1: Transverse momentum distributions of the three muons from $\tau \to \mu\mu\mu$ decays in four τ production channels after the $|\eta|$ acceptance cut. The single- and di-muon trigger thresholds are indicated.

Table 5.4: Production and visible cross sections (σ_τ as well as σ_{vis}) and expected numbers of τ leptons produced and of $\tau \to \mu\mu\mu$ decays for 10fb^{-1} using $\mathcal{B}(\tau \to \mu\mu\mu) = 3.2 \cdot 10^{-8}$.

τ-source	σ_τ (nb)	ϵ_{acc}	σ_{vis} (nb)	$N(\tau)/10\ \text{fb}^{-1}$	$N(3\mu)/10\ \text{fb}^{-1}$
$D_s^\pm$	$19.7 \cdot 10^3$	$8.9 \cdot 10^{-4}$	17.5	$17.5 \cdot 10^7$	6
B^0	$56.4 \cdot 10^3$	$7.4 \cdot 10^{-4}$	41.7	$41.7 \cdot 10^7$	13
$B^\pm$	$55.0 \cdot 10^3$	$6.8 \cdot 10^{-4}$	37.4	$37.4 \cdot 10^7$	12
$B_s^\pm$	$9.9 \cdot 10^3$	$7.2 \cdot 10^{-4}$	7.1	$7.13 \cdot 10^7$	2
Z^0	2.02	0.56	1.15	$2 \times 1.15 \cdot 10^7$	1
$W^\pm$	20.51	0.51	10.46	$10.46 \cdot 10^7$	3

$\sigma_{vis} = \sigma_\tau \times \epsilon_{\text{acc}}$

for $\tau \to \mu\mu\mu$ decays are determined (see Table 5.4). The number of signal events in the acceptance from the W decays is only about ten times smaller than the total number of $\tau \to \mu\mu\mu$ decays from hadron decays.
The different signal sources have the following kinematic properties:

- **Muon collimation:** Due to the large masses of the gauge bosons, the τ leptons from Z and W decays are strongly boosted implying the collimation of the three muons from $\tau \to \mu\mu\mu$ decays in a small cone with an average $\eta - \phi$ distance between two muons $\langle \Delta R_{\mu\mu} \rangle = 0.09$ (see Figure 5.3(a)) leaving a characteristic signature in the detector and offering efficient background suppression. This is different for the muons from the hadron decays to τ leptons which are low energetic.

- **Muon isolation:** The muons from the $\tau \to \mu\mu\mu$ decays from hadron sources are close to jets while the muons from gauge boson sources are isolated leaving a clean signature in the detector. In addition, the main backgrounds for $\tau \to \mu\mu\mu$ decays are from semileptonic charm and beauty decays and are thus very similar to the $\tau \to \mu\mu\mu$ decays from the hadron sources making background rejection more difficult.

- ***Z* mass constraint:** Requiring the $\tau^+\tau^-$ invariant mass to be consistent with the Z boson mass allows for good background suppression in the selection of $Z \to \tau^+\tau^-$ decays.

- **Missing transverse energy:** An important signature of $W^+ \to \tau^+ + \nu_\tau$ decays is missing transverse energy of on average $E_{\text{T}}^{\text{miss}} \sim 40$ GeV (see Figure 5.3(b)) due to the escaping neutrino balancing the p_{T} of the τ lepton which serves to suppress background of muons from charm and beauty decays.

From these considerations, the boson sources of $\tau \to \mu\mu\mu$ decays are preferable due to better signal-to-background ratio. Because of the larger production cross section, only the W channel is further considered in this work.

5.5 Background Processes

Every process with three strongly collimated muons and missing transverse energy in the final state constitutes a potential background to the search for $\tau \to \mu\mu\mu$ in the W channel. The by far dominating sources of prompt muons in ATLAS are charm and beauty decays.

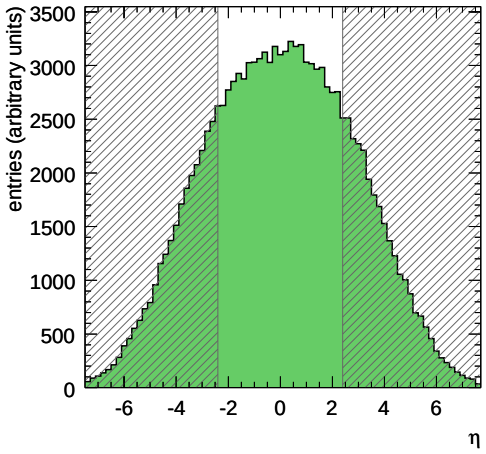

(a) $D_s \to \tau\nu_\tau X$ channel

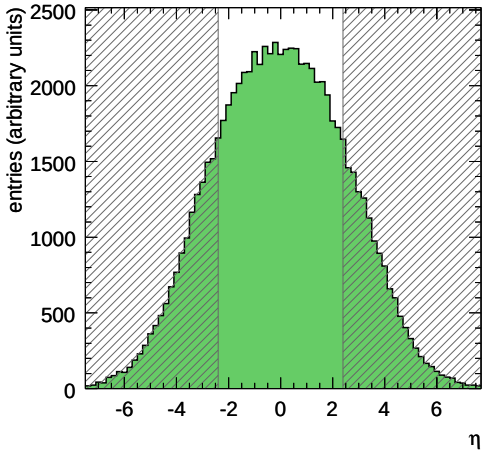

(b) $B^0 \to \tau\nu_\tau X$ channel

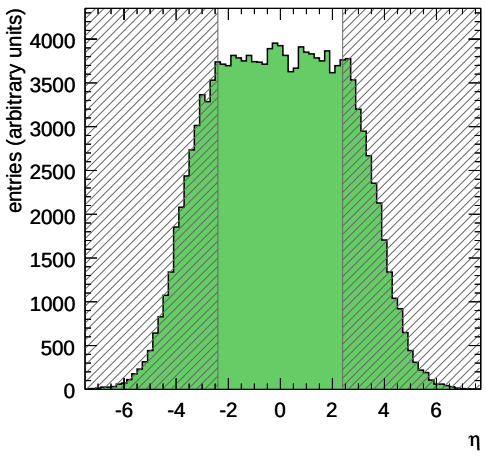

(c) $W \to \tau\nu_\tau$ channel

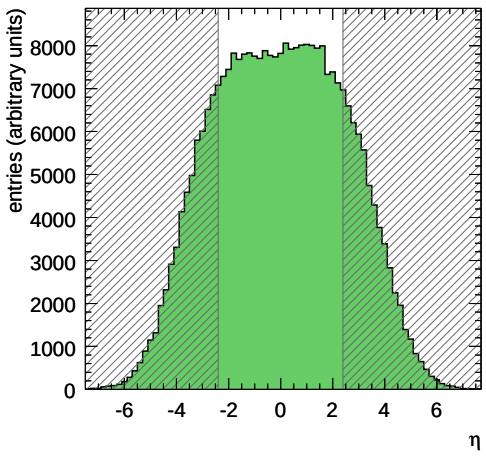

(d) $Z \to \tau\tau$ channel

Figure 5.2: Pseudorapidity distributions of the three muons from $\tau \to \mu\mu\mu$ decays for the four τ production channels before the p_{T} cuts. The shaded regions are outside the muon-trigger acceptance $|\eta| < 2.4$.

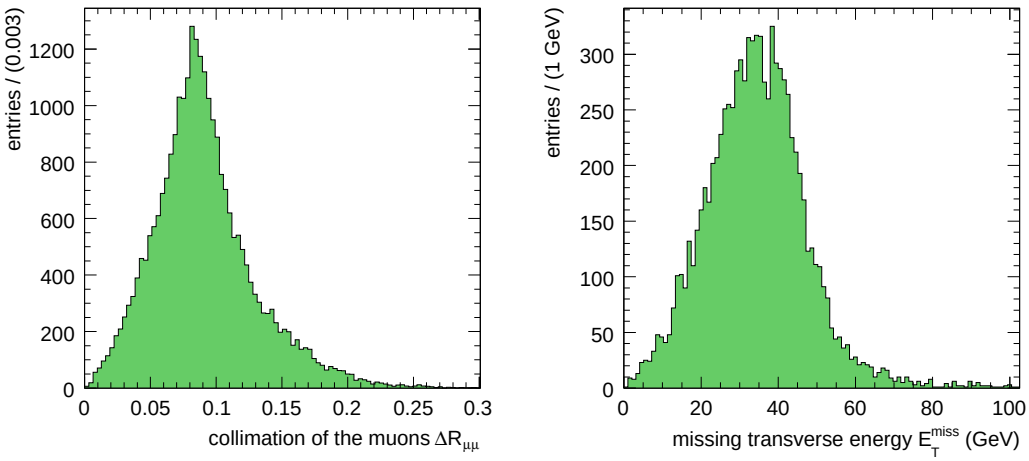

(a) (b)

Figure 5.3: (a) Distance in the $\eta - \phi$ plane for all pairs of muons in $\tau \to \mu\mu\mu$ decays from $W \to \tau\nu_{tau}$ decays and (b) the missing transverse energy distribution in these events.

Table 5.5: Branching fractions of tri-muon final states from D_s^+-decays [1] and the expected numbers of background events for $10\,\text{fb}^{-1}$.

D_s^+ decay	$\mathcal{B}_1$	Secondary Decays	$\mathcal{B}_2$	$\mathcal{B}_{\text{tot}} = \mathcal{B}_1 \cdot \mathcal{B}_2$	$N(3\mu)/10\,\text{fb}^{-1}$
$\phi\mu^+\nu_\mu$	$2.36 \cdot 10^{-2}$	$\phi \to \mu^+\mu^-$	$2.86 \cdot 10^{-4}$	$6.6 \cdot 10^{-6}$	$91 \cdot 10^6$
		$\phi \to \mu^+\mu^-\gamma$	$1.4 \cdot 10^{-5}$	$3.3 \cdot 10^{-7}$	$5 \cdot 10^6$
$\eta\mu^+\nu_\mu$	$2.90 \cdot 10^{-2}$	$\eta \to \mu^+\mu^-$	$5.8 \cdot 10^{-5}$	$1.7 \cdot 10^{-6}$	$22 \cdot 10^6$
		$\eta \to \mu^+\mu^-\gamma$	$3.1 \cdot 10^{-4}$	$9.0 \cdot 10^{-6}$	$124 \cdot 10^6$
		$\eta \to \pi^0\mu^+\mu^-\gamma$	$3 \cdot 10^{-6}$	$8.7 \cdot 10^{-8}$	$1 \cdot 10^6$
$\eta'\mu^+\nu_\mu$	$1.06 \cdot 10^{-2}$	$\eta' \to \mu^+\mu^-\gamma$	$1.03 \cdot 10^{-4}$	$1.1 \cdot 10^{-6}$	$15 \cdot 10^6$
Total				$1.9 \cdot 10^{-5}$	$258 \cdot 10^6$

In addition there are background combinations from in-flight decays of pions and kaons and of the muons due to punch through hadrons reaching the muon detector. The contributions of muons from direct W and Z decays are negligible due to their low production cross sections.

5.5.1 Background from Charm Decays

Processes with three collimated muons in the final states are semileptonic decays of $D_s^\pm$ mesons. The relevant decay chains with corresponding branching ratios are listed in Table 5.5. The branching ratio $\mathcal{B}_{\text{tot}}$ of tri-muon final states is on the order of 10^{-5}. The cross section for $c\bar{c}$-production at $\sqrt{s} = 14\,\text{TeV}$ at the LHC is $\sigma(pp \to c\bar{c} + X) = 5.3 \cdot 10^6\,\text{nb}$ with a probability of 26 % that a D_s meson is created in the hadronization process. Hence, about $2.6 \cdot 10^8$ such events will be produced for an integrated luminosity of $10\,\text{fb}^{-1}$.

$c\bar{c}$ events with D_s decay chains with the largest branching fractions,

$$D_s \to \phi\mu\nu_\mu \to (\mu\mu)(\mu\nu_\mu) \quad \text{and}$$
$$D_s \to \eta\mu\nu_\mu \to (\mu\mu\gamma)(\mu\nu_\mu),$$

have been generated with PYTHIAB. To increase the background statistics in the phase space of interest for the later analysis a dedicated three-muon filter ('$2\mu5\,\mu2$') requiring

- at least two muons with $p_\mathrm{T} > 5\,\mathrm{GeV/c}$ within $|\eta| < 2.5$ and
- at least one additional muon with $p_\mathrm{T} > 2\,\mathrm{GeV/c}$ within $|\eta| < 2.8$.

This pre-selection is necessary because of the large cross sections of the background processes in order to produce sufficient number of background events close to the signal region in a reasonable time. The disadvantage is the possible under-estimation of in-flight K and π decays as well as punch throughs.
The production cross sections of the two decays is further determined as:

$$\sigma_\mathrm{prod} = \sigma(pp \to c\bar{c} + X) \times \mathcal{B}_{tot} \times \epsilon \tag{5.3}$$

with the filter efficiency ϵ defined as the fraction of events passing the criteria defined above. The production cross sections of the selected background processes are summarized in Table 5.6.

5.5.2 Background from Beauty Decays

The second main background source are beauty decays. Three types of decays chains can be distinguished:

- Decays of b hadrons to D_s followed by the D_s decay chains from the previous section, e.g.

$$\begin{aligned} B_s \to & D_s + X, \\ & D_s \to \phi\mu\nu_\mu, \\ & \phi \to \mu\mu. \end{aligned}$$

- Semileptonic cascade decays of b hadrons, e.g.

$$\begin{aligned} B^- \to & D^0\mu^-\bar{\nu}_\mu, \\ & D^0 \to K^-\mu^+\nu_\mu, \\ & K^- \to \mu^-\bar{\nu}_\mu. \end{aligned}$$

- Semileptonic decays of two b hadrons, e.g.

$$\begin{aligned} B^- \to & D^0\mu^-\bar{\nu}_\mu, \\ B^+ \to & \bar{D}^0\mu^+\nu_\mu, \\ & \bar{D}^0 \to K^+\mu^-\bar{\nu}_\mu. \end{aligned}$$

Table 5.6: Overview of the signal and background Monte Carlo samples used in this analysis produced with PYTHIA. The cross sections σ_{prod} include the decay branching fractions as well as the filter efficiencies. The integrated luminosities corresponding to the numbers of produced events are given in the last column.

Channel	Secondary decays	Filter	σ_{prod} (nb)	Events produced	L (fb^{-1})
$W^{\pm}$	$W^{\pm} \to \tau\nu_{\tau}$ / $\tau \to \mu\mu\mu$	–	$5.5 \cdot 10^{-7}$	$2.5 \cdot 10^{4}$	–
$c\bar{c}$	$D_s^{\pm} \to \phi\mu\nu_{\mu}$ / $\phi \to \mu\mu$	$2\mu5\ \mu2$	$4.7 \cdot 10^{-3}$	$4.7 \cdot 10^{4}$	10.0
$c\bar{c}$	$D_s^{\pm} \to \eta\mu\nu_{\mu}$ / $\eta \to \mu\mu\gamma$	$2\mu5\ \mu2$	$8.1 \cdot 10^{-4}$	$4.5 \cdot 10^{4}$	55.6
$b\bar{b}$	$D^{\pm} \to \mu + X$	$\mu6\ 2\mu4$	$8.2 \cdot 10^{-3}$	$1.0 \cdot 10^{4}$	0.12
$b\bar{b}$	$D^{0} \to \mu + X$	$\mu6\ 2\mu4$	$4.2 \cdot 10^{-3}$	$1.0 \cdot 10^{4}$	0.24
$b\bar{b}$	$D_s^{\pm} \to \mu + X$	$\mu6\ 2\mu4$	$1.8 \cdot 10^{-3}$	$1.0 \cdot 10^{4}$	0.54
$b\bar{b}$	$B^{\pm} \to \mu + X$	$\mu6\ 2\mu4$	$1.3 \cdot 10^{-2}$	$1.0 \cdot 10^{4}$	0.08
$b\bar{b}$	$B^{0} \to \mu + X$	$\mu6\ 2\mu4$	$1.3 \cdot 10^{-2}$	$1.0 \cdot 10^{4}$	0.08
$b\bar{b}$	$B_s^{0} \to \mu + X$	$\mu6\ 2\mu4$	$1.8 \cdot 10^{-3}$	$1.0 \cdot 10^{4}$	0.56
$b\bar{b}$	–	$\mu6\ \mu4$	110.5	$1.0 \cdot 10^{6}$	0.01

In principle also $J/\psi \to \mu^+\mu^-$ decays accompanied by a third muon from a semileptonic weak decay have similar signature, but because of the difference between $m_{J/\psi} = 3.097\,\text{GeV}$ and $m_{\tau} = 1.777\,\text{GeV}$, that background can be fully suppressed by a $\mu^+\mu^-$ invariant mass cut.
The large number of possible beauty decay chains with three collimated muons in the final state requires a specific strategy for generating the background samples. Six datasets have been produced with one of the mesons $D^{\pm}, D^0, D_s^{\pm}, B^{\pm}, B^0$ and B_s^0 exclusively decaying into muons in all possible ways. To increase the statistics in the phase space close to the signal region, the following filter requirements (denoted as '$\mu6\,2\mu4$') have been applied to the muons:

- at least one muon with $p_{\text{T}} > 6\,\text{GeV/c}$ and
- at least two additional muons with $p_{\text{T}} > 4\,\text{GeV/c}$ and
- $\Delta R_{\text{min}} < 0.5$ where ΔR_{min} is the minimum $\eta - \phi$ distance of all possible muon pairs in tri-muon events.

In addition, an inclusive $b\bar{b}$ dataset with di-muon filter '$\mu6\,\mu4$' has been used. The filter requires at least two muons per event, with:

- $p_{\text{T}}^1 > 6\,\text{GeV/c}$ and $p_{\text{T}}^2 > 4\,\text{GeV/c}$.

This dataset contains also decays of the six special datasets and in addition covers other semileptonic decay chains of b hadrons as well as the background due to in-flight decays and punch through.

The cross sections of these background samples and the numbers of events produced are summarized in Table 5.6.

5.6 Simulation of the Detector Response

For a reliable Monte Carlo modelling of the data, a realistic simulation of the detector response is important. The simulation of the ATLAS detector is based on the GEANT4 toolkit [72] which provides a detailed description of the detector geometry, the propagation of the particles through the detector material as well as the magnetic field and realistic simulation of the response of the detectors, the read-out electronics and the trigger. The simulated data are processed by the same reconstruction algorithms as used for the real collision data. This so-called *full simulation* has been tuned with test-beam data and validated with cosmic muon date taken during the commissioning phase of the ATLAS experiment. However, due to the size and complexity of the detector, the time needed to simulate and reconstruct one event is typically several minutes on present CPUs. This is the reason for filtering background events in the signal region already at the generator level.

5.7 Trigger Performance

As explained in Section 3.4, the ATLAS trigger consists of three consecutive levels: level 1 (L1), level 2 (L2) and the event filter (EF). The signal event topology of $\tau \to \mu\mu\mu$ events implies two challenges to the trigger :

- The three muons are relatively low energetic with the p_{T} of the hardest muon peaking at about 14 GeV/c. Due to the large rates of low energetic single muons at the LHC and trigger rate limitations, the low p_{T} single muon L1 trigger will have to be pre-scaled. The small branching fraction of the signal decay, therefore, requires a dedicated trigger without pre-scaling. The following muon triggers can be considered without pre-scaling at a luminosity of $\mathscr{L} \simeq 2 \times 10^{33}\,\mathrm{cm}^{-2}\mathrm{s}^{-1}$ [52]:
  - 2MU6 for B-physics: at least two muons with $p_{\mathrm{T}} > 6\,\mathrm{GeV/c}$. To reduce the trigger rate, cuts on the $\mu^+\mu^-$ invariant mass corresponding to different B-physics signatures are performed at the higher trigger levels L2 and EF.
  - 2MU10: at least two muons with $p_{\mathrm{T}} > 10\,\mathrm{GeV/c}$.
  - MU20i: at least one muon at $p_{\mathrm{T}} > 20\,\mathrm{GeV/c}$. In addition, the muon is required to be isolated from nearby jets at the higher trigger levels L2 and EF.
- The $\eta-\phi$ distance between the three muons typically is $\Delta R < 0.2$. With a granularity of the L1 muon trigger of $\Delta\eta \times \Delta\phi = 0.1 \times 0.1$ (0.03×0.03) in the barrel (end caps), two of the muons are likely to fall into the same region of interest and are thus counted as one muon candidate.

5.7.1 Efficiency for $\tau \to \mu\mu\mu$ of the First-Level Muon Trigger

The design of the ATLAS first level muon trigger allows for six programmable p_{T} thresholds. For an instantaneous luminosity of $\mathscr{L} \simeq 10^{33}\mathrm{cm}^{-2}\mathrm{s}^{-1}$ the standard low and high p_{T} thresholds are 6 and 20 GeV, respectively [52]. Figure 5.4 shows the L1 trigger efficiencies for $\tau \to \mu\mu\mu$ events as a function of the transverse momentum p_{T}, pseudorapidity $|\eta|$ and azimuthal angle ϕ of the hardest muon. In addition, the trigger efficiencies in dependence

of the maximum $\eta - \phi$ separation ΔR_{max} between two of the signal muons is shown. The trigger efficiency is defined as the fraction of triggered to the total number of generated events without applying any other kinematic cuts.
For transverse momenta below 15 GeV/c, the total trigger efficiency is dominated by the di-muon trigger. The leading edge starts at about 5 GeV/c and reaches its maximum of 45 % at $p_{\text{T}} = 11$ GeV/c. For larger momenta, the di-muon trigger efficiency decreases to about 30 %. The reason for this behaviour is the strong collimation of the three muons which increases with the momentum of the τ lepton and thus with the leading muon p_{T}. If the $\eta - \phi$ distance between two muons becomes smaller than the size of the region of interest, the di-muon signature cannot be resolved anymore (compare also Figure 5.4(d)).
For transverse momenta larger than 16 GeV/c, the single muon trigger 'MU20' dominates the total trigger efficiency and a plateau of 52 % is reached for $p_{\text{T}} > 18$ GeV/c.
Within the geometrical acceptance of the trigger chambers ($|\eta| < 2.4$), the combined single and di-muon trigger efficiency is almost independent of the pseudorapidity (see Figure 5.4(b)). Only close to $|\eta| = 0$ the efficiency decreases due to holes in the RPC chamber coverage to allow passage of services for the inner detector. In the barrel ($|\eta| < 1.05$), the single and di-muon trigger show compatible efficiencies while the di-muon trigger efficiency increases towards larger pseudorapidities due to the finer granularity of the L1 trigger in the end cap part of the muon spectrometer.
Except for the feet regions of the detector ($\phi \simeq -1.1$ rad and $\phi \simeq -2.0$ rad) the trigger efficiency is independent of the azimuthal angle ϕ (see Figure 5.4(c)).
The efficiencies of the first-level muon trigger for $W \to \tau\nu \to \mu\mu\mu$ events are summarized in Table 5.7. For comparison, also the efficiency of the low p_{T} single-muon trigger 'MU6' ($p_{\text{T}}^{\mu} > 6$ GeV/c) is given.

5.7.2 Efficiency of the High-Level Triggers

The higher trigger levels (L2 and EF) use the full granularity of the ATLAS detector together with fast reconstruction algorithms to achieve the required rejection and maintain the event filter output rates of 200 Hz. In Figure 5.5 the efficiencies for $\tau \to \mu\mu\mu$ events of the event filter muon selections '2MU6' and 'MU20i' are shown as a function of the transverse momentum p_{T}, the pseudorapidity $|\eta|$ and the azimuthal angle ϕ of the hardest signal muon as well as of ΔR_{max}. The efficiencies are defined as the ratios of the number of $\tau \to \mu\mu\mu$ events passing L1, L2 and EF requirements to the total number of generated events. The better momentum resolution of the high-level triggers lead to an almost complete loss of efficiency of the high p_{T} threshold 'MU20i'. The efficiency of the di-muon trigger '2MU6' remains at about 30 % for momenta of the leading muon larger than 10 GeV/c.

The efficiencies of all muon triggers are listed in Table 5.7. As expected, the low p_{T} single-muon trigger 'MU6' has the highest efficiency, but cannot be used for this analysis due to expected high pre-scaling fraction. The high p_{T} single-muon trigger 'MU20' has a very low efficiency of 2.5 % only in the end caps. Due to the small $\eta - \phi$ distance between the signal muons, the efficiency even decreases below 1 % when applying the isolation cut on the higher trigger levels. This trigger will therefore not be used in this analysis.
The best suited trigger considered is '2MU6' with 24.3 % EF efficiency. It has to be considered that this trigger is only available with $\mu^+\mu^-$ invariant mass cut for B-physics

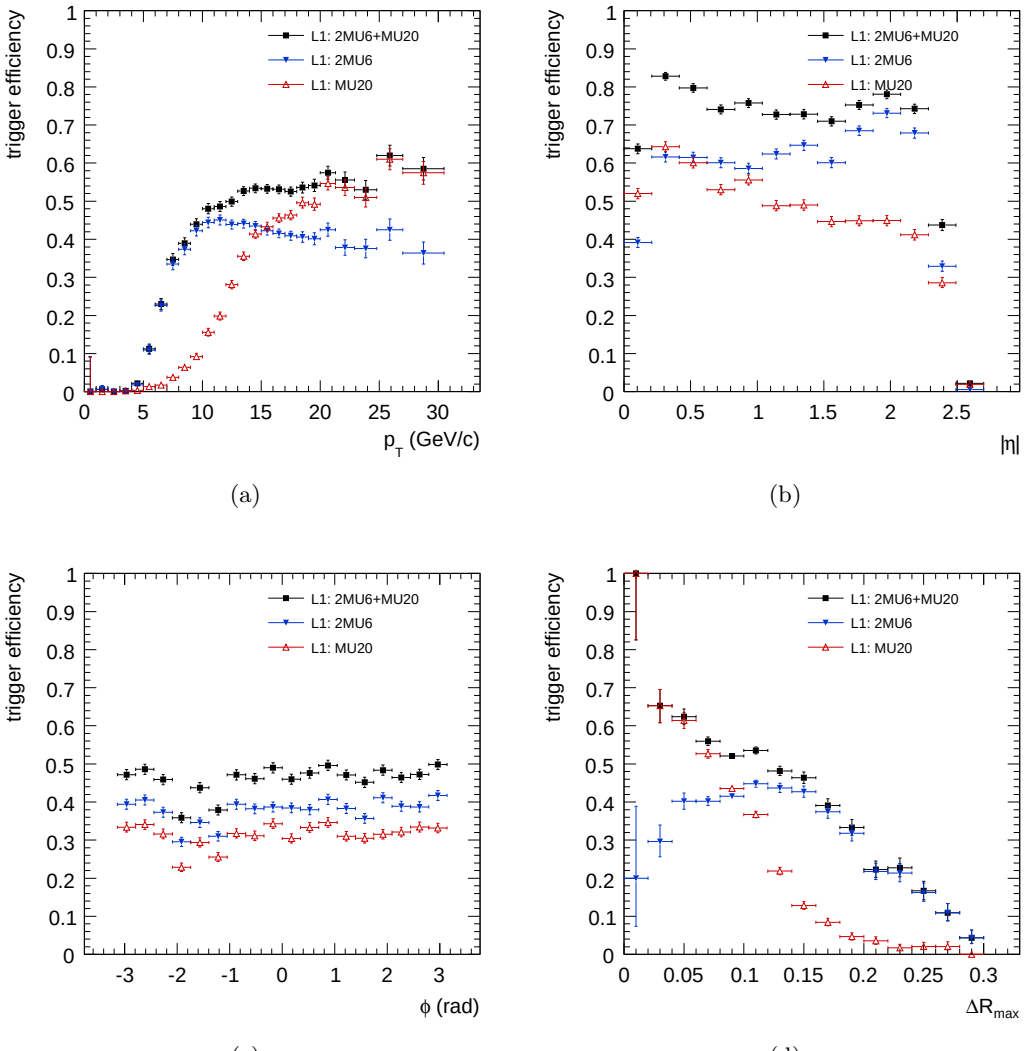

(a) (b)

(c) (d)

Figure 5.4: Efficiencies of the standard first-level muon trigger for the decay $\tau \to \mu\mu\mu$ as a function of (a) the transverse momentum p_{T} , (b) the pseudorapidity $|\eta|$ and (c) the azimuthal angle ϕ (c) of the hardest signal muon and (d) of the maximum distance ΔR_{max} between two of the signal muons.

Table 5.7: Efficiencies of ATLAS muon triggers for the lepton flavour violating decays $\tau \to \mu\mu\mu$ in $W \to \tau\nu_\tau$ events. The trigger '2MU10' and 'MU20i' use the L1 trigger thresholds of '2MU6' and 'MU20' respectively,

Trigger chain	Trigger efficiency (%)		
	L1	L2	EF
MU6	56.7 ± 0.3	49.2 ± 0.3	46.3 ± 0.3
2MU6	37.7 ± 0.2	26.7 ± 0.2	24.3 ± 0.2
2MU10		11.9 ± 0.2	10.8 ± 0.3
MU20	31.2 ± 0.2	5.0 ± 0.1	2.5 ± 0.1
MU20i		1.5 ± 0.1	0.7 ± 0.1
2MU6+MU20(i)	46.0 ± 0.2	27.2 ± 0.3	24.5 ± 0.3
2MU10+MU20(i)		12.7 ± 0.2	11.2 ± 0.2

final states so far. As B mesons and J/ψ have masses about two to three times as large as the mass of the τ lepton, all signal events would be rejected. Hence a dedicated L2 and EF trigger has to be implemented to profit from the low di-muon trigger threshold. If no dedicated trigger can be implemented and only the '2MU10' trigger can be used without pre-scaling at $\mathscr{L} = 2 \cdot 10^{33}\,\mathrm{cm}^{-2}\mathrm{s}^{-1}$ and an EF efficiency of 11 %.
In the following, the '2MU6' trigger without invariant mass cut will be assumed for the study of the lepton flavour violating decay $\tau \to \mu\mu\mu$.

5.8 Reconstruction of Physics Objects and Detector Performance

This section provides an overview of the reconstruction and of the associated detector performance for the physics objects used in this analysis: the muon reconstruction, the finding and fitting of the secondary vertex and the determination of the missing energy signature. A more detailed review on the reconstruction of all physics objects and the detector performance can be found in [34, 52].

5.8.1 Muon Reconstruction

In ATLAS, two different muon reconstruction algorithms are available called STACO [74] and MUID [93] which both exploit the information of all sub-detector systems. In this work the STACO algorithm is used. Nevertheless, the principle and performance of the two algorithms are very similar: in the muon spectrometer, track segments are reconstructed in each of the three layers of muon chambers. The segments are combined to a muon track, taking into account the material distribution traversed and the magnetic field along the muon trajectory. The track is extrapolated to the interaction point, applying corrections for the energy losses in the calorimeters and the inner detector. Within the acceptance of the inner detector ($|\eta| < 2.5$), the extrapolated track is matched with a track measured by the inner detector and both measurements are combined (combined muons) improving the momentum resolution in the p_T range where it is dominated by multiple scattering

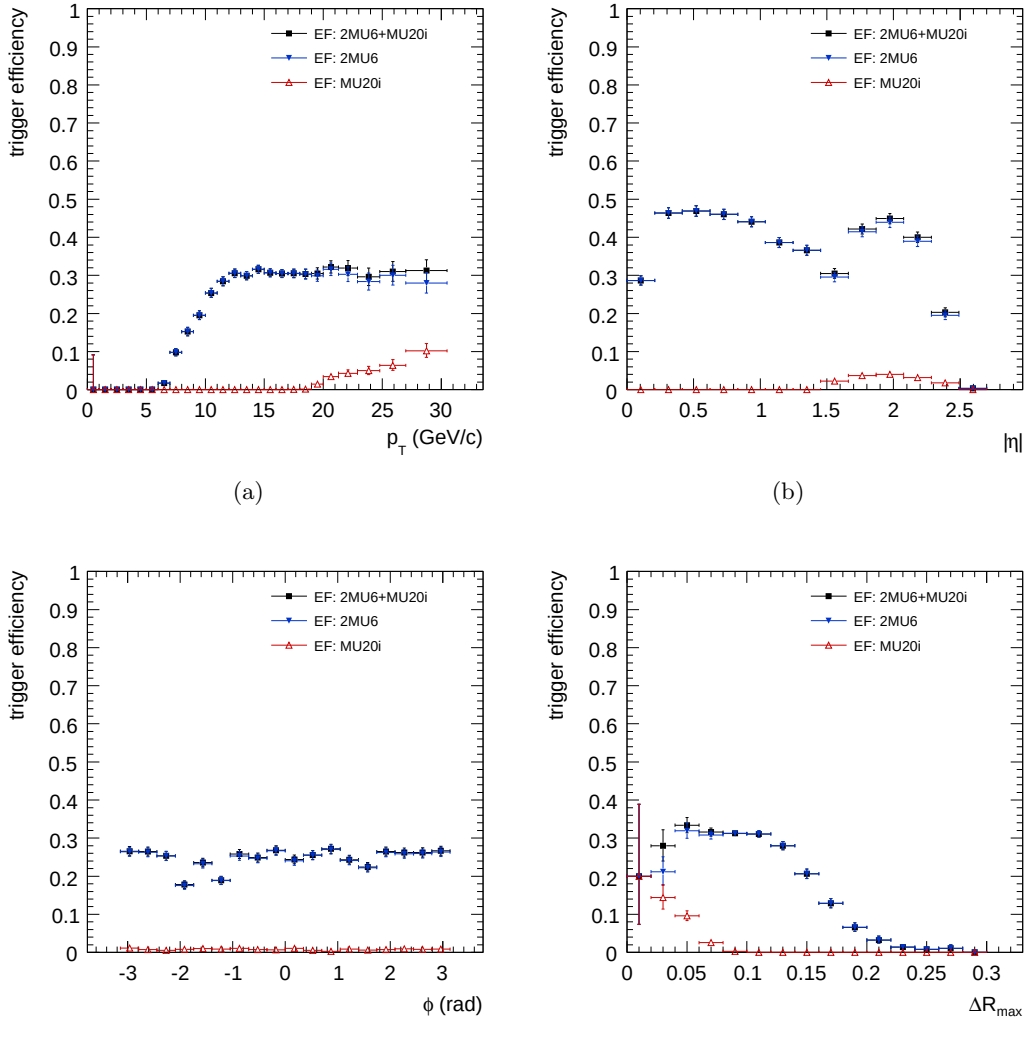

(a) (b)

(c) (d)

Figure 5.5: EF efficiencies for the decay $\tau \to \mu\mu\mu$ as a function of (a) the transverse momentum p_{T}, (b) pseudorapidity $|\eta|$ and (c) azimuthal angle ϕ of the hardest signal muon as well as of (d) ΔR_{max} between two of the signal muons.

($p_{\mathrm{T}} < 200\,\mathrm{GeV/c}$) and suppressing misidentification of particles escaping the calorimeter (punch through).
Low energetic muons often leave a track in the inner detector but, due to the energy loss in the calorimeters, have too low momentum to cross all three layers of muon chambers. To recover these muons, so-called tagging algorithms propagate all inner detector tracks with sufficient momenta to the innermost layer of the muon spectrometer and search for nearby segments. If a segment is sufficiently close to the extrapolated track the inner detector track is tagged as a muon. Tagging algorithms also improve the muon reconstruction efficiency in detector regions with less than three layers of precision muon chambers, e.g. in the transition regions between barrel and end caps. A disadvantage of muons reconstructed by the tagging algorithms is an increased number of misidentified muons. To still profit from the benefits of the tagged muons, the unique signal topology of $\tau \to \mu\mu\mu$ decays is used and a tagged muon is only considered if two combined muons with $\Delta R < 0.2$ with respect to the tagged muon are found. Adding these tagged muons increases the total signal efficiency by about 40 %.
The algorithms also reconstruct muons from hits in the muon spectrometer alone (standalone muons). Due to the increased misidentification rate, standalone muons are not used for this analysis.

To study the detector performance, the muon reconstruction efficiencies and misidentification rates are calculated with respect to the generated objects (Monte Carlo *truth* information). Muons with a (true and reconstructed) transverse momentum below $3\,\mathrm{GeV/c}$ as well as muons outside the inner detector acceptance ($|\eta| > 2.5$) are excluded. For each event, a unique matching is performed between reconstructed and true muons. Analogue to [52], the matching of two muons is quantified by the reference distance

$$D_{\mathrm{ref}} = \sqrt{\left(\frac{\phi_{\mathrm{reco}} - \phi_{\mathrm{true}}}{0.005}\right)^2 + \left(\frac{\eta_{\mathrm{reco}} - \eta_{\mathrm{true}}}{0.005}\right)^2 + \left(\frac{\Delta p_{\mathrm{T}}/p_{\mathrm{T}}}{0.03}\right)^2} \tag{5.4}$$

in phase space. The denominators are the average resolutions of the corresponding variable and consequently the two muons with minimal D_{ref} are matched. As all three signal muons are in a narrow cone, a strict requirement of $D_{\mathrm{ref}} < 10$ is used for correct matching (see Figure 5.6).
Two variables quantify the muon reconstruction performance of the ATLAS detector, the reconstruction efficiency

$$\text{efficiency} = \frac{N(\text{reconstructed muons with a matching truth muon})}{N(\text{truth muons})} \tag{5.5}$$

rate of misidentified muons:

$$\text{misidentification rate} = \frac{N(\text{reconstructed muons without a matching truth muon})}{N(\text{reconstructed muons})}. \tag{5.6}$$

It is obvious that high efficiencies together with low misidentification rates are intended.
Figure 5.7 shows the efficiency and the misidentification rate as a function of the reconstructed transverse momentum p_{T}, the pseudorapidity η and the azimuthal angle ϕ for the signal and the inclusive $b\bar{b} \to \mu\mu X$ background sample. For the η and ϕ dependence,

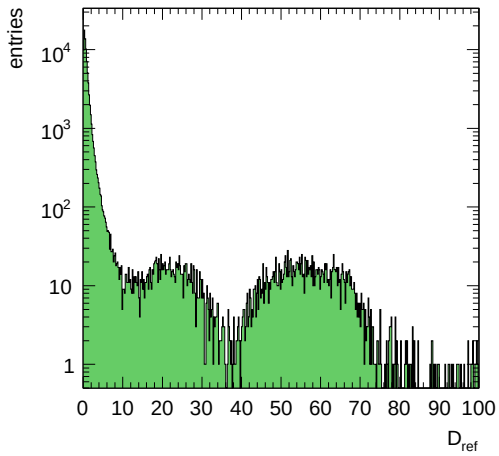

Figure 5.6: Minimum reference distance D_{ref} between reconstructed and true signal muons. The entries close to zero are correctly matched while the secondary maxima at $D_{\text{ref}} \simeq 20$ and $D_{\text{ref}} \simeq 55$ correspond to the other two nearby muons of the $\tau \to \mu\mu\mu$ decay.

a cut of $p_{\text{T}} > 4\,\text{GeV/c}$ was applied.
For both samples the efficiency increases with the transverse momentum and reaches a plateau for $p_{\text{T}} > 6\,\text{GeV/c}$. While the muon reconstruction efficiency for the background sample reaches 90 %, the efficiency for signal muons only reaches 80 %. Similar as the L1 efficiency, the reconstruction efficiency decreases at higher p_{T} values due to kinematic effects of the muon collimation (see Figure 5.7(a)). Around $\eta = 0$, the loss of efficiency is related to gaps in the muon spectrometer for service connections and around $|\eta| = 1.1$ to the lower coverage with muon chambers in the barrel-end cap transition regions (see Figure 5.7(c)). The efficiency only has two small dips as a function of ϕ in the region of the detector feet at $\phi = -2.1$ and $\phi = -1.0$ (see Figure 5.7(e)).
Noteworthy is the loss of efficiency at large $|\eta|$ which is more pronounced for the signal than for the background. The reason is once more the small distance ΔR between the signal muons which limits the possibility to separate the individual muon tracks. The mean distance between two signal muons is $\Delta R = 0.09$, independently of the pseudorapidity η while the polar angle $\Delta\theta$ between the muons, not Lorentz invariant in contrast to $\Delta\eta$, decreases with $|\eta|$. In Figure 5.8(a), $\Delta\theta$ between the leading and next-to-leading signal muon is shown as a function of $|\eta|$ of the leading muon. For $\eta = 0$, the mean angle between the muons is $\langle\Delta\theta\rangle = {}^{\langle\Delta R\rangle}/_{\sqrt{2}} = 0.07\,\text{rad}$ and decreases as $\arctan(e^{|\eta|})$ to $\langle\Delta\theta\rangle = 0.01\,\text{rad}$ at $|\eta| = 2.5$. In Figure 5.8(b) the muon reconstruction efficiency is shown as a function of $\Delta\theta$. It degrades for signal and background muons $\Delta\theta < 0.04\,\text{rad}$, the mean opening angle of the signal muons at pseudorapidities $|\eta| > 1.1$.
The average muon reconstruction efficiency is 79.8 ± 0.2 % for signal muons and 86.0 ± 0.02 % for muons of the background. The misidentification rates for both samples are well below 0.3 %.

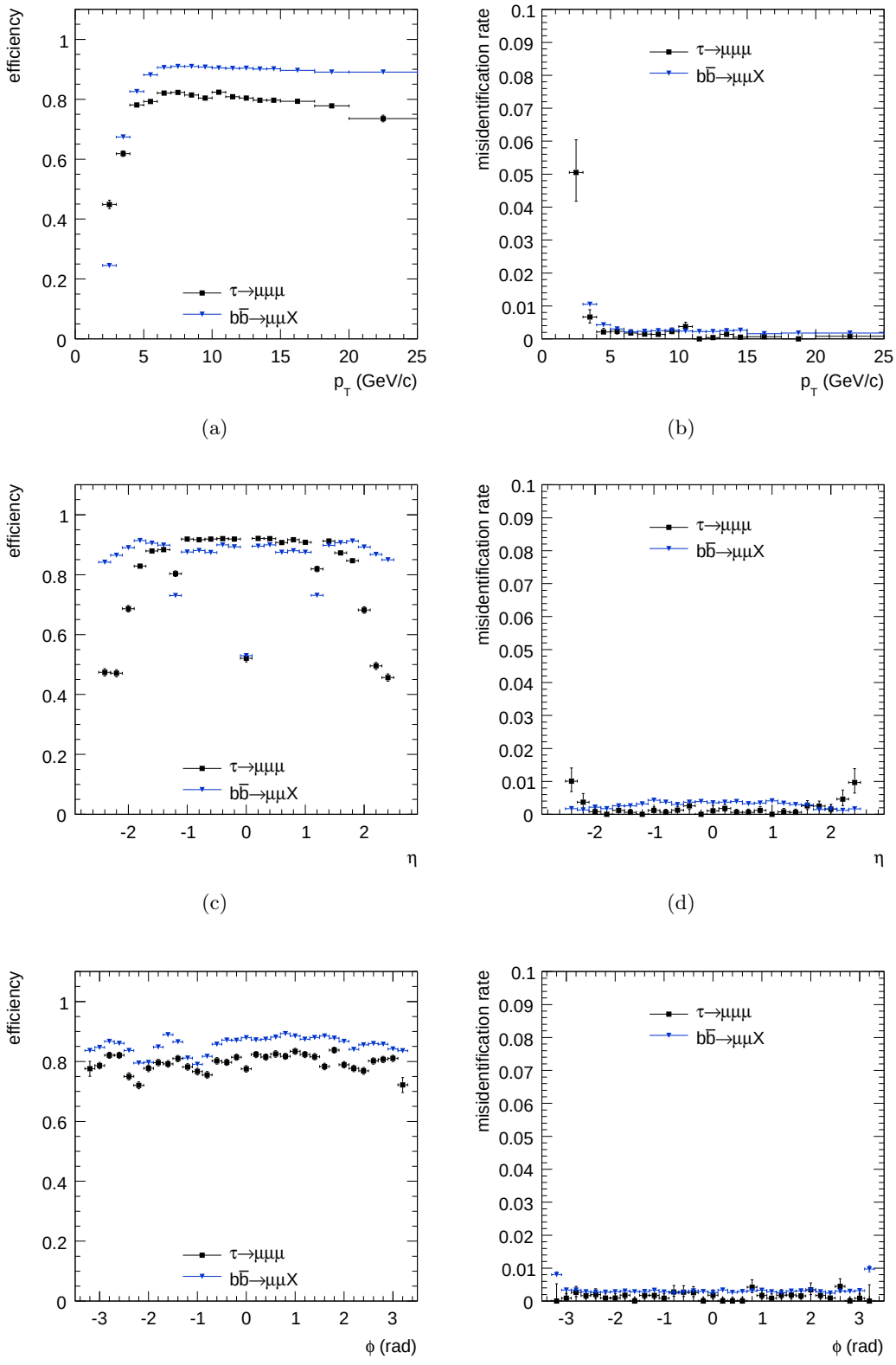

Figure 5.7: Muon reconstruction and identification efficiencies and misidentification rates as functions of p_{T}, η and ϕ, for the signal and the inclusive $b\bar{b} \to \mu\mu X$ background sample.

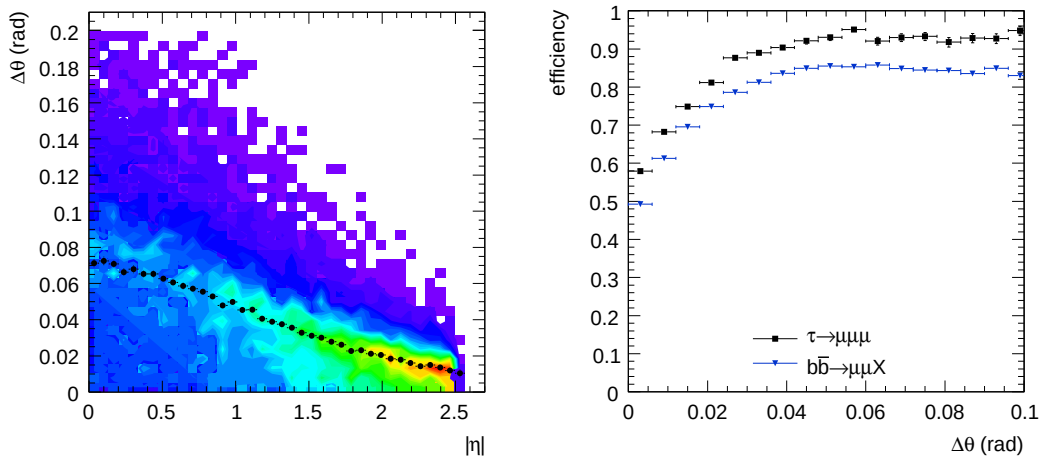

(a) (b)

Figure 5.8: (a) Angle $\Delta\theta$ between the two leading signal muons as a function of $|\eta|$ and (b) muon reconstruction efficiencies in signal and inclusive $b\bar{b} \to \mu\mu X$ background events as a function of $\Delta\theta$.

5.8.2 Reconstruction of the Secondary Vertex

The relatively long lifetime of the τ lepton ($c\tau = 87.11\,\mu$m [1]) allows for the reconstruction of its decay vertex using the inner detector tracks of the reconstructed muons. The mean decay length of the τ leptons originating from W boson decays amounts to about 2 mm due to time dilatation. Several algorithms are available in the Athena software framework to reconstruct the τ decay vertex (see [52] for a detailed description). The the so-called *FastVertexFitter*, based on the *Billoir* method [94] for the reconstruction of the decay vertex, is used in this analysis. Figure 5.9 shows the performance of the secondary decay vertex reconstruction. As expected, the transverse decay length of the τ lepton increases with its transverse momentum and is on the order of several millimetres (Figure 5.9(a)). The resolution of the reconstructed radial position of the τ decay vertex is 185 μm (see Figure 5.9(b)). Because of the strong collimation of the three muons, the reconstruction of the vertex position is challenging leading to long tails of the residual distribution.

5.8.3 Missing Energy Reconstruction

Neutrinos only interact weakly and thus escape the detector without trace. As the colliding protons do not have a transverse momentum component, the sum of the transverse momenta of the final-state particles has to vanish as well. Hence, the sum of the transverse energies of the detected particles equals the sum of the transverse energies of the invisible particles like neutrinos
In ATLAS, the calculation of the visible transverse energy ΣE_{T} is performed in the following way:

- Summation of all calorimeter cell energies.
- Addition of the absolute values of the muon transverse momenta, measured in the muon spectrometer only, in order to prevent double-counting of the muon energy

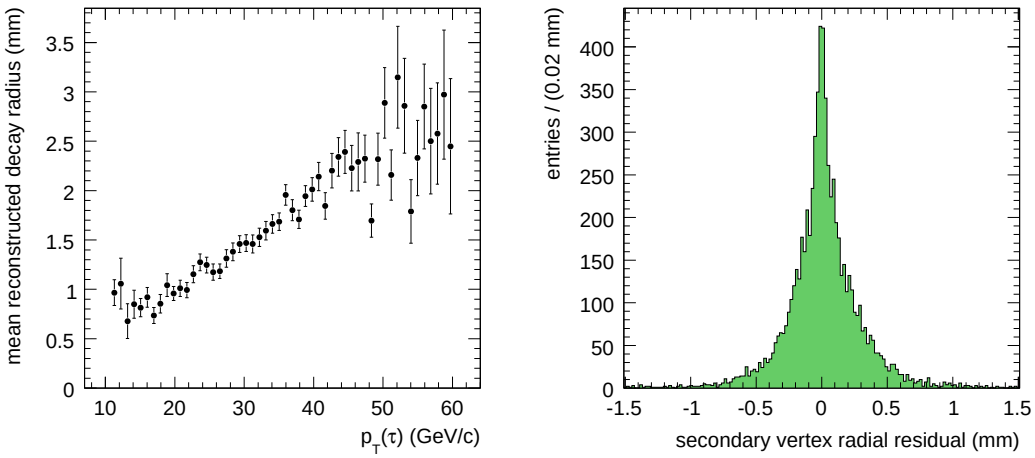

(a) (b)

Figure 5.9: (a) Reconstructed decay radius of the τ lepton as a function of its transverse momentum. (b) Residual distribution of the reconstructed with respect to the correct radial position of the τ decay vertex.

deposition in the calorimeter. To reduce the influence of misidentified muons, an associated track in the inner detector is required but not taken into account in the momentum measurement.

- Addition of the estimated energy loss of all particles in the inactive detector material.

In Figure 5.10, the expected resolution of the missing transverse energy $E_{\mathrm{T}}^{\mathrm{miss}}$ is shown as a function of the scalar sum of the transverse cell energies in the calorimeter and the muon transverse momenta ΣE_{T}. The resolution has been determined for simulated processes, including $W \to e\nu$ and $W \to \mu\nu$ production which have similar signatures as the signal events of this analysis. The $E_{\mathrm{T}}^{\mathrm{miss}}$ resolution is expected to be between 4 and 12 %.

5.8.4 Event Display of a $\tau \to \mu\mu\mu$ Decay

Figure 5.11 shows a simulated $\tau \to \mu\mu\mu$ decay in the ATLAS detector using the Atlantis event display software [95]. All three muons are detected in the barrel part of the muon spectrometer and reconstructed as combined muon tracks. One of the muons, denoted as μ_1, has opposite charge compared to the other two, μ_2 and μ_2 and is deflected in opposite direction in the bending plane of the magnetic fields, the $r-\phi$ plane in the solenoidal field of the inner detector and the $\eta-\phi$ plane in the toroid field of the muon spectrometer.

5.9 Signal Selection Criteria

In order to enhance the signal with respect to the background processes in the search for lepton flavour violating $\tau \to \mu\mu\mu$ decays, selection criteria described in the following are used.

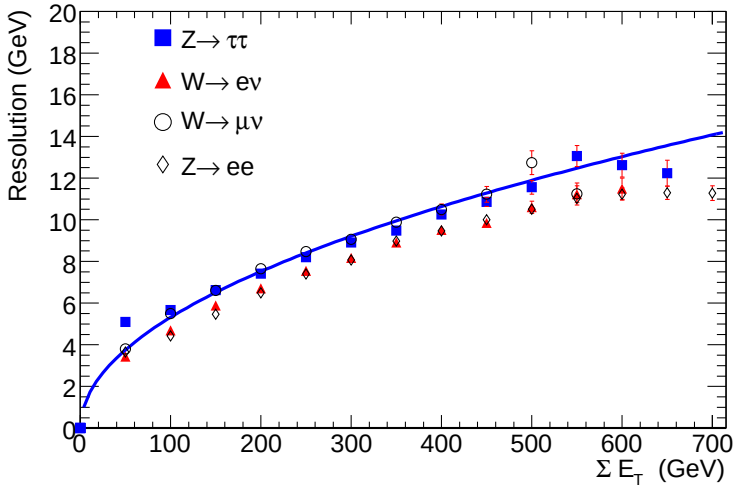

Figure 5.10: Expected resolution of the missing transverse energy $E_{\mathrm{T}}^{\mathrm{miss}}$ as a function of the total transverse energy $\Sigma E_{\mathrm{T}}$for different simulated processes [52].

5.9.1 Event Pre-Selection

The following loose pre-selection cuts have been applied to reduce the amount of data for the further detailed studies:

- At least three reconstructed muon tracks with $p_{\mathrm{T}} > 4\,\mathrm{GeV/c}$.
- At least two of the muons are combined muons.
- Tag muons are only accepted if two combined muons are closer than $\Delta R = 0.2$.
- The total charge of a muon triplet is ± 1.
- If more than one muon triplet is found, the one with invariant mass $m_{\mu\mu\mu}$ closest to $m_\tau = 1.777\,\mathrm{GeV}$ is selected.
- If $m_{\mu\mu\mu} > 2 \times m_\tau$, the event is rejected.

5.9.2 Signal Selection

For further separation of signal and background, a series of selection cuts is applied. The stacked distributions of the cut variables are shown for signal and background processes after pre-selection and after applying all other cuts in Figures 5.12–5.20. Due to limited Monte Carlo statistics, some cut values have been chosen relatively loose in order to keep enough Monte Carlo background events for the estimation of the expected background.
The data and background samples are normalized corresponding to an integrated luminosity of $10\,\mathrm{fb}^{-1}$ after about one year of data taking at an instantaneous luminosity of $\mathscr{L} = 10^{33}\,\mathrm{cm}^{-2}\mathrm{s}^{-1}$. For the signal normalization, the current best upper limit on the branching ratio $\mathcal{B}(\tau \to \mu\mu\mu) = 3.2 \cdot 10^{-8}$ is used. The six specially produced $b\bar{b}$ background samples (see Table 5.6) are combined to one dataset and will be denoted as

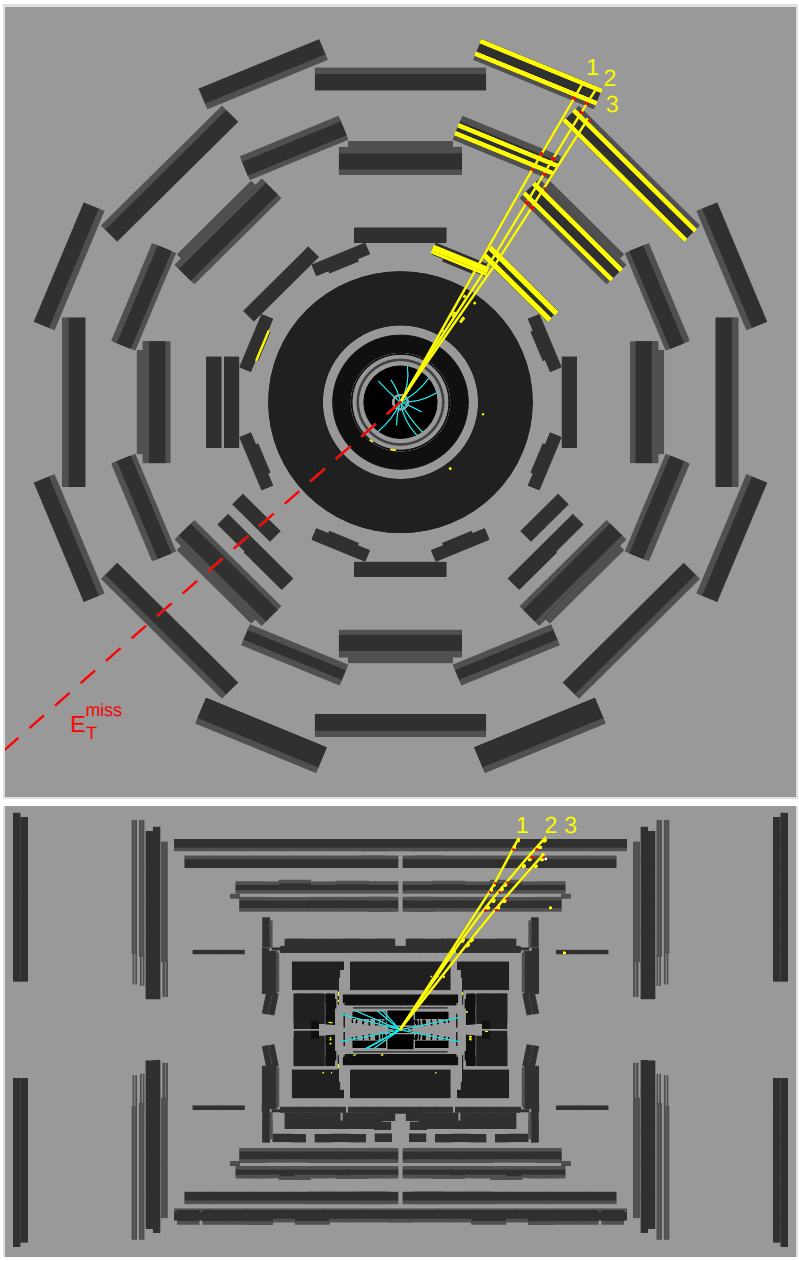

μ	Charge	p_T/E_T (GeV)	η	ϕ (rad)	$\Delta R_{\mu\mu}$
μ_1	$-$	12.77	0.619	1.015	0.067
μ_2	$+$	11.82	0.645	1.077	0.097
μ_3	$+$	17.77	0.719	1.014	
E_T^{miss}		40.076		3.867	

Figure 5.11: Event display of a simulated $\tau \rightarrow \mu\mu\mu$ decay measured with the ATLAS detector. The upper figure shows the $x-y$ $(r-\phi)$ projection and the lower the $y-z$ $(r-\phi)$ projection the detector.

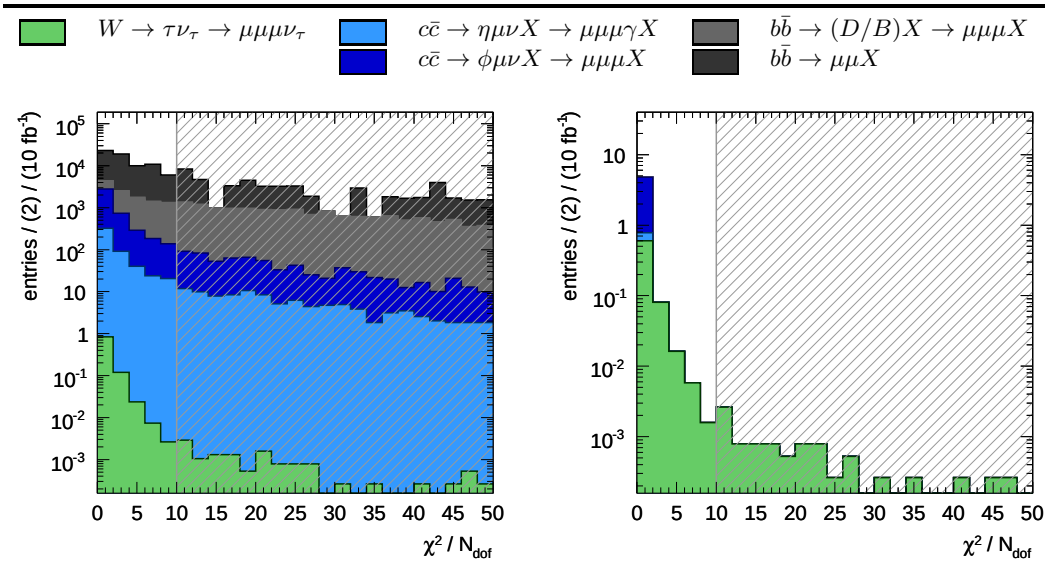

(a) (b)

Figure 5.12: Distributions of the quality parameter χ^2/N_{dof} of the τ decay vertex fit for signal and background events normalized to the number of events expected for $10\,\mathrm{fb}^{-1}$ (a) after pre-selection and (b) after all other selection cuts have been applied.

$b\bar{b} \to (D/B)X \to \mu\mu\mu X$. The efficiencies of trigger, pre-selection, and signal selection are summarized in Table 5.8.

Secondary Vertex Reconstruction

The τ leptons from W decays have a mean decay length of about 2 mm. The muon tracks in the inner detector are used to reconstruct the secondary decay vertices. Unfortunately, the lifetime of the τ lepton is with $\tau = 87.11\,\mu\mathrm{m}/c$ similar to the lifetime of D_s ($\tau = 150\,\mu\mathrm{m}/c$) and B mesons ($\tau \simeq 450\,\mu\mathrm{m}/c$) [1]. The decay length are even more similar taking into account the average boost of the decaying particles. Consequently, the distance between the primary interaction point and the secondary vertex of the three muons cannot be used to discriminate the signal against the background.
However, the muons of a $\tau \to \mu\mu\mu$ decay originate from the same vertex while the muons from the background processes are the decay products of two or three different particles leading to a worse quality of the vertex fit. Thus, the χ^2/N_{dof} of the secondary vertex fit (see also Section 5.8.2) is used as selection criterion. ϕ and η mesons decay almost instantaneously resulting in a common secondary muon vertex for charm decay backgrounds like $c\bar{c} \to D_s X \to (\eta/\phi)\mu\nu X \to \mu\mu\mu(\gamma)X$. Consequently, this criterion mainly rejects $b\bar{b}$ decay chains, for example

$$\begin{aligned} B^- &\to D^0\mu^-\bar{\nu}_\mu \\ B^+ &\to \bar{D}^0\mu^+\nu_\mu, \\ \bar{D}^0 &\to K^+\mu^-\bar{\nu}_\mu, \end{aligned}$$

with a relatively long decay length of the $\bar{D}^0$ meson ($c\tau = 103\,\mu\mathrm{m}$).
Figure 5.12(a) shows the χ^2/N_{dof} distributions for signal and background contributions

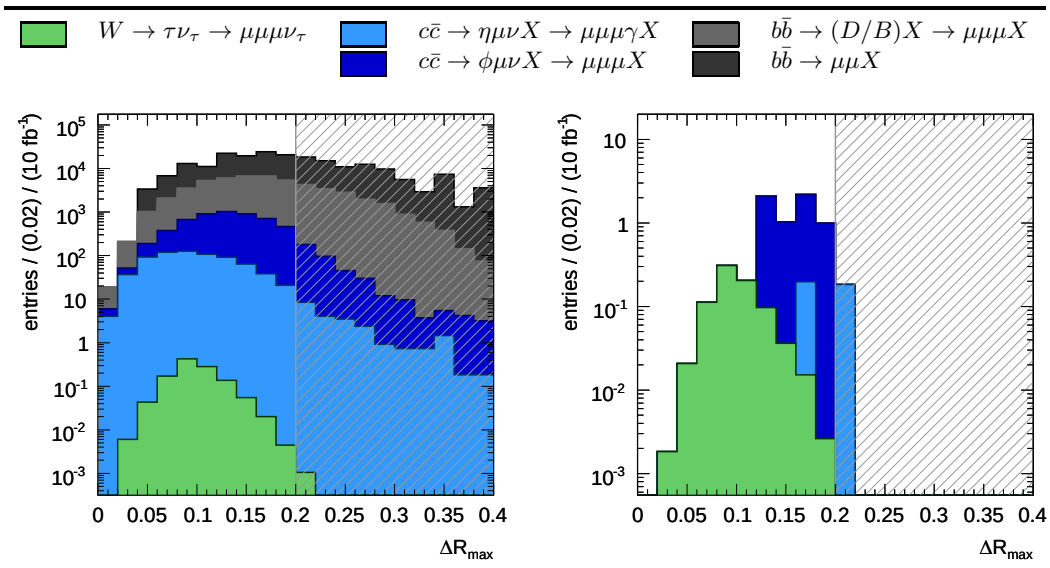

(a) (b)

Figure 5.13: Maximum $\eta - \phi$ distance $\Delta R_{\max}$ of any of the two pre-selected muons for signal and background events normalized to the number of events expected for $10\,\text{fb}^{-1}$ (a) after pre-selection and (b) after all other selection cuts have been applied.

corresponding to $10\,\text{fb}^{-1}$. In particular the $b\bar{b}$ backgrounds show a long tail in the χ^2/N_{dof} distribution while the signal and the $c\bar{c}$ backgrounds peak at $\chi^2/N_{\text{dof}} = 0$. Events with $\chi^2/N_{\text{dof}} > 10$ are rejected.

Collimation of the Muons

Due to the large mass difference between the W boson and the τ lepton is strongly boosted and the three muons from the $\tau \to \mu\mu\mu$ decay are strongly collimated. This special topology offers a good opportunity to reject the background where the probability of larger muon separation is increased. The maximum distance between two muons is required to be $\Delta R_{\max} < 0.2$. Figure 5.13 shows the $\Delta R_{\max}$ distributions after pre-selection and after all other cuts for signal and background combinations corresponding to $10\,\text{fb}^{-1}$.

Muon Isolation

With the τ lepton from W decay, the three signal muons are most likely isolated. In contrast, muons from the background processes are often surrounded by additional tracks and energy deposits in the calorimeters from close-by jets. Two different isolation criteria are used in this analysis, based on the energy deposits around the muon direction in the calorimeters and the other one based on the transverse energy of close-by tracks.
For the calorimeter isolation, the transverse energy $E_{\text{T}}^{\text{cone}}$ inside a cone of size $\Delta R = 0.2$ around each muon is measured. The maximum value for the three muons in an event is used as discriminating variable shown in Figure 5.14. Events with $E_{\text{Tmax}}^{\text{cone}} > 10\,\text{GeV}$ are rejected.
For the track isolation the total transverse energy of track inside cones of size $\Delta R = 0.2$ around each muon is determined excluding the other two muon from each cone. For the

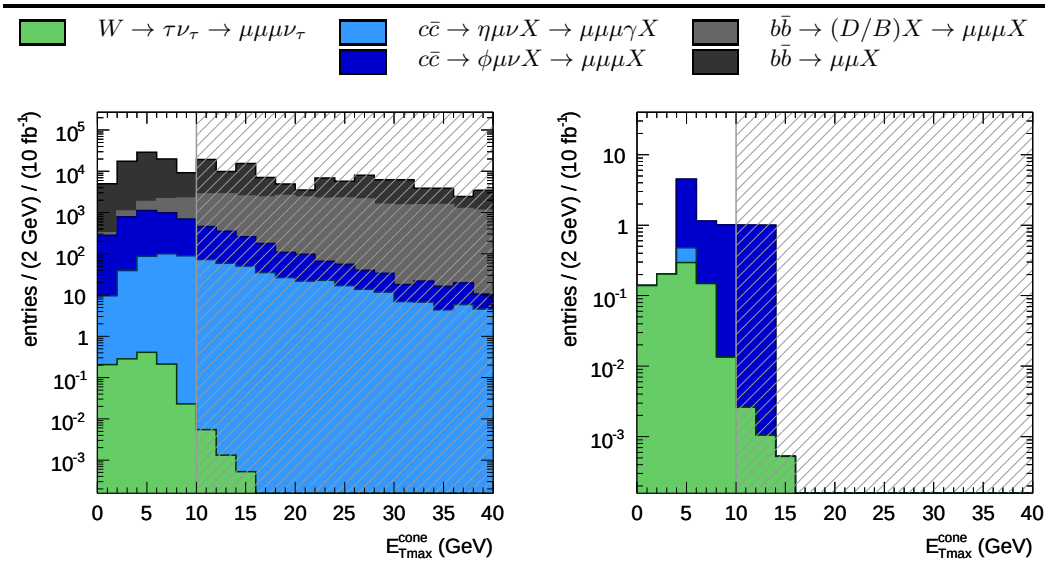

(a) (b)

Figure 5.14: Maximum transverse energy in the calorimeters in cones $\Delta R < 0.2$ around the three muons for signal and background events normalized to the number of events expected for $10\,\text{fb}^{-1}$ (a) after pre-selection and (b) after all other selection cuts have been applied.

signal events this corrected transverse cone energy $E_{\text{Ttrk}}^{\text{cone}}$ is small, while larger values are characteristic for background processes due to close-by jets (see Figure 5.15). Events with $E_{\text{Ttrk}}^{\text{cone}} > 5\,\text{GeV}$ are rejected.

Missing Transverse Energy

Compared to the background, the signal events are expected to have large missing transverse energy due to the escaping neutrino of the $W \to \tau\nu_\tau$ decay. Figure 5.16 shows the missing transverse energy of the signal and the background processes after pre-selection and after all other cuts have been applied. The cut $E_{\text{T}}^{\text{miss}} > 10$ was chosen relatively low in order to keep sufficient background events for reliable background estimation.

Transverse Mass

The invariant mass of the transverse momentum components of the three muons and of the missing transverse energy, the transverse mass m_{T}, is given by:

$$m_{\text{T}} = \sqrt{2|\vec{p}_{\text{T}}^{\,3\mu}||\vec{E}_{\text{T}}^{\text{miss}}| \cdot (1 - \cos(\Delta\theta))} \tag{5.7}$$

where $\vec{p}_{\text{T}}^{\,3\mu}$ denotes the vector sum of the transverse momenta of the three muons and $\Delta\theta$ the azimuthal angle between the directions of $\vec{p}_{\text{T}}^{\,3\mu}$ and of the missing transverse energy $\vec{E}_{\text{T}}^{\text{miss}}$. Proposed in [96], m_{T} is commonly used in the analysis of W boson production. The transverse mass distribution exhibits a Jacobian peak with maximum at the mass of the W boson. However, in the background events the missing energy mainly originates from neutrinos created together with the muons inside the jets. Hence m_{T} tends to be

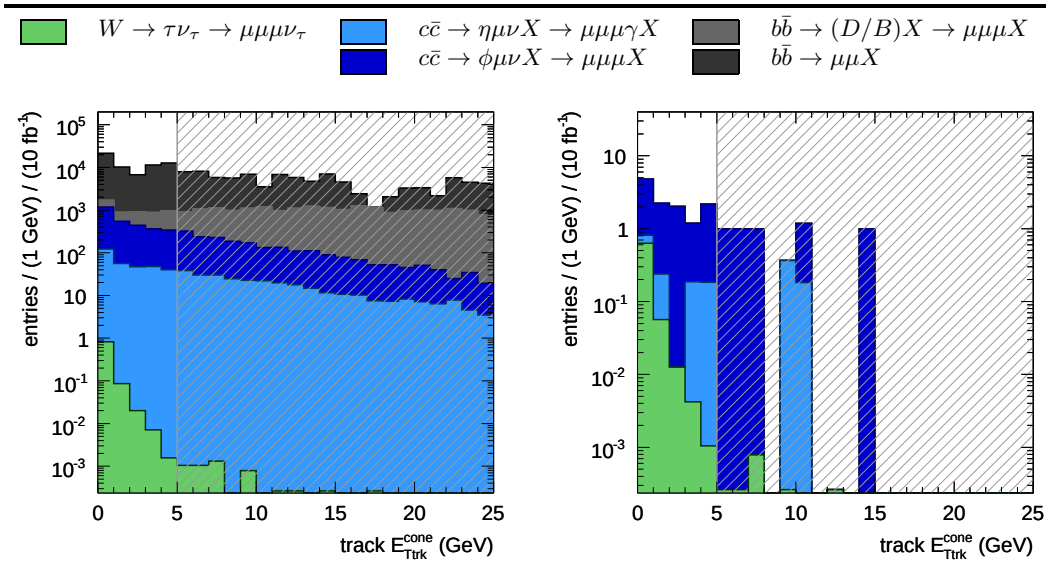

(a) (b)

Figure 5.15: Total transverse energy distributions of non-muon tracks in cones $\Delta R < 0.2$ around the three muons for signal and background events normalized to the number of events expected for $10\,\text{fb}^{-1}$ (a) after pre-selection and (b) after all other selection cuts have been applied.

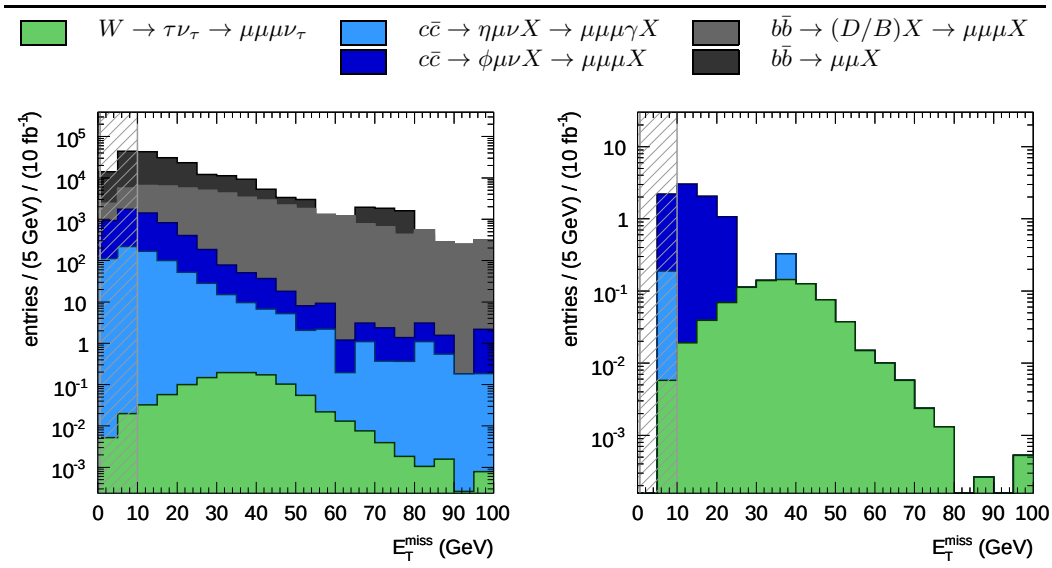

(a) (b)

Figure 5.16: Missing transverse energy distributions $E_{\text{T}}^{\text{miss}}$ for signal and background events normalized to the number of events expected for $10\,\text{fb}^{-1}$ (a) after pre-selection and (b) after all other selection cuts have been applied.

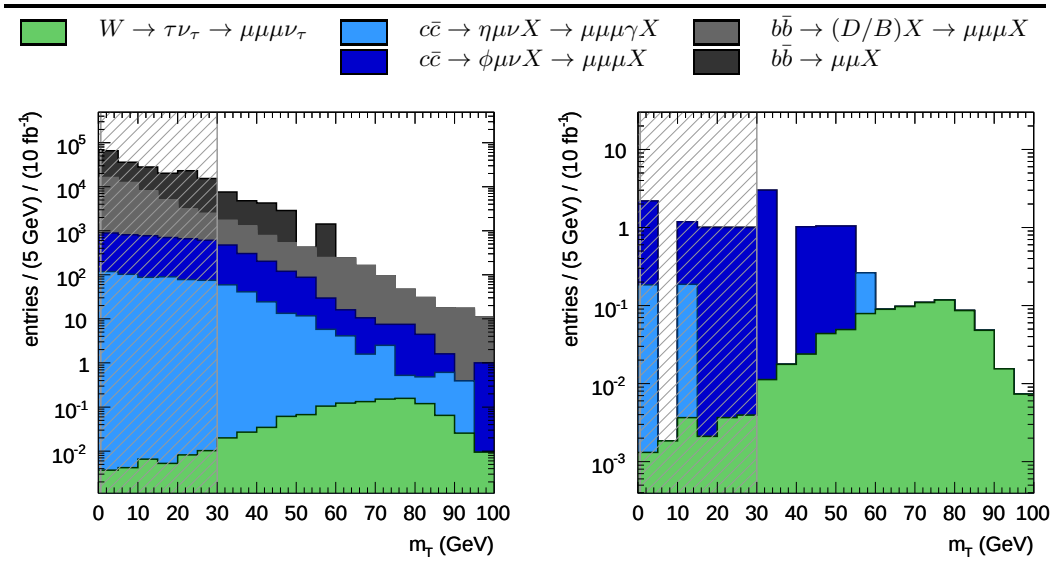

(a) (b)

Figure 5.17: Transverse mass distributions m_T for signal and background events normalized to the number of events expected for $10\,\mathrm{fb}^{-1}$ (a) after pre-selection and (b) after all other selection cuts have been applied.

small as shown in Figure 5.17 and events $m_\mathrm{T} < 30\,\mathrm{GeV}$ are rejected. Also this cut was chosen relatively loose in order to keep enough background events (see above).

Rejection of Light Mesons

Neutral η and ϕ mesons decaying into muon pairs can mimic the signal in combination with one additional close-by muon. If the invariant mass of an oppositely charged muon pair is consistent with the mass of the η or ϕ meson, the event is rejected. Both mesons appear as sharp resonances [1]:

$$m_\eta = 547.853\,\mathrm{MeV}, \quad \Gamma_\eta = 24\,\mathrm{keV}, \tag{5.8}$$
$$m_\phi = 1019.455\,\mathrm{MeV}, \quad \Gamma_\phi = 20\,\mathrm{keV}. \tag{5.9}$$

The width of the $\mu^+\mu^-$ invariant mass distributions is limited by the detector resolution. The width of the ϕ meson resonance is determined to be $\sigma(\phi) = 18.5\,\mathrm{MeV}$ by fitting a Gaussian to the di-muon mass distribution in the $c\bar{c} \to \phi\mu\nu X \to \mu\mu\mu X$ background events (see Figure 5.18(a)). Events within one standard deviation of the ϕ mass, $|m_{\mu^+\mu^-} - m_\phi| < 19\,\mathrm{MeV}$, are rejected.
No dedicated background sample was available for the decay chain $c\bar{c} \to D_s + X$, $D_s \to \eta\mu\nu_\mu$, $\eta \to \mu\mu$. Assuming the same invariant mass resolution as for the $\phi \to \mu\mu$ decays, events with $|m_{\mu^+\mu^-} - m_\eta| < 19\,\mathrm{MeV}$ are rejected.
In Figure 5.19 the invariant mass distributions of the all $\mu^+\mu^-$ pairs per event are shown after pre-selection and after all other selection cuts for the signal and background. For the background sample with $\phi \to \mu\mu$ decays, the ϕ mass peak is visible on top of the combinatorial background. No peak forms for the background sample with $\eta \to \mu\mu\gamma$ decays

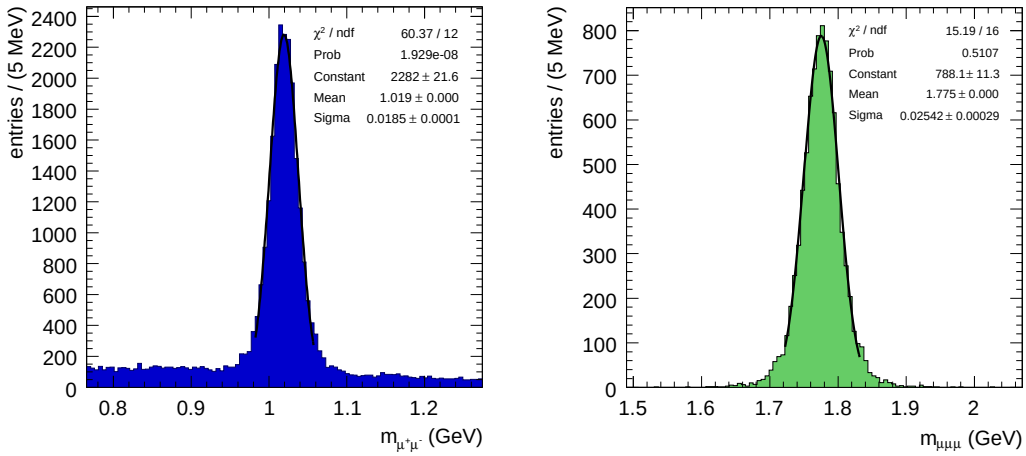

(a) (b)

Figure 5.18: Invariant mass distributions of two and three muons, respectively, in the decays (a) $\phi \to \mu^+\mu^-$ and (b) $\tau \to \mu\mu\mu$.

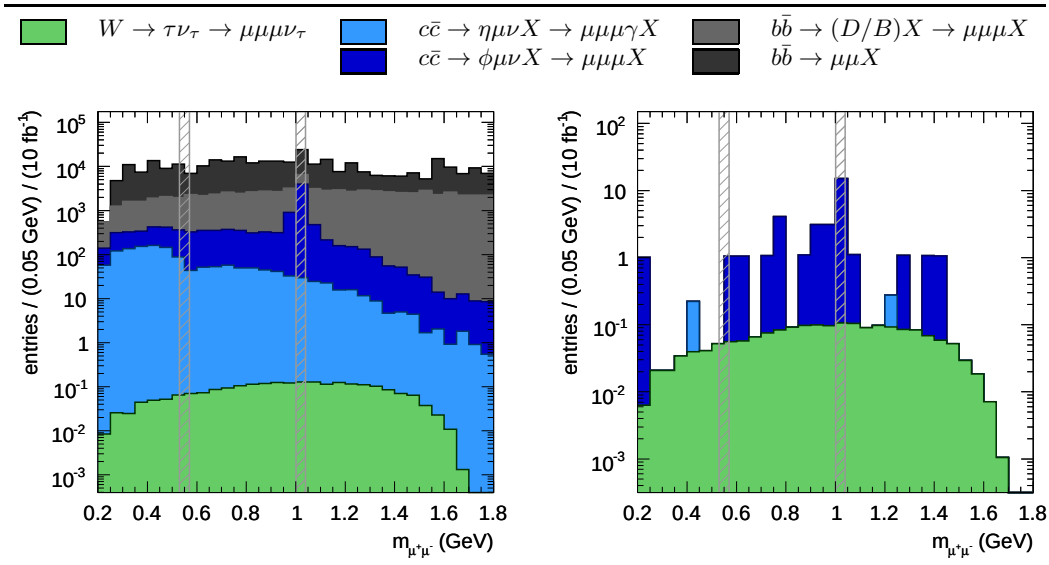

(a) (b)

Figure 5.19: Invariant mass distributions of all $\mu^+\mu^-$ pairs per event in signal and background events normalized for $10\,\mathrm{fb}^{-1}$ (a) after pre-selection and (b) after all other selection cuts have been applied. The excluded mass windows are indicated.

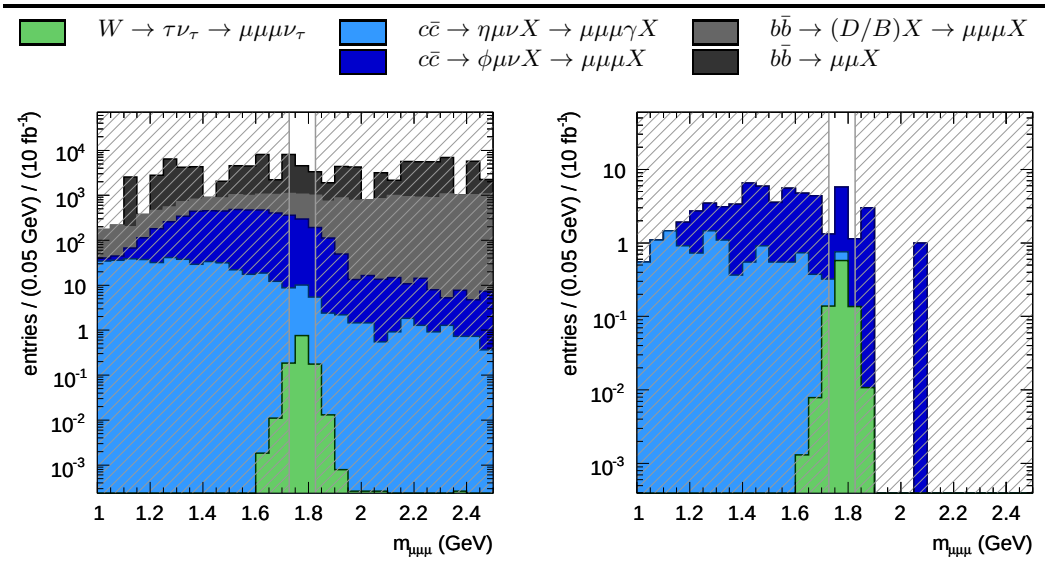

(a) (b)

Figure 5.20: Invariant mass distributions $m_{\mu\mu\mu}$ of the reconstructed muons in signal and background events normalized for 10 fb^{-1} (a) after pre-selection and (b) after all other selection cuts have been applied.

because the photon is not included in the invariant mass calculation.

τ-Mass Constraint

The invariant mass of the three muons from the $\tau \to \mu\mu\mu$ decay is distributed around the mass of the τ lepton with a width of 25 MeV determined from a Gaussian fit (see Figure 5.18(b)).
The invariant mass distributions of the three muons in signal and background events are shown in Figure 5.20. All events outside the two-standard deviation range around the τ mass $|m_{\mu\mu\mu} - m_\tau| < 50$ MeV are rejected.

Selection Efficiencies and Rejection Power

Figure 5.21 shows the evolution of the number of signal and background events with successively applied selection cuts for 10 fb^{-1} of integrated luminosity. The numbers and fractions of events surviving the different selection steps are listed in Table 5.8. After all cuts

$$\varepsilon = 12.2 \pm 0.2\,\% \tag{5.10}$$

of the signal events survive with a background rejection $(1.6 \pm 0.6) \cdot 10^5$.

5.10 Estimation of the Total $b\bar{b}$ Background Rate

None of the simulated $b\bar{b}$ background events survives the event selection. However, the total rate of background events from $b\bar{b}$ decay chains can be estimated by multiplying the number

Table 5.8: Summary of the total process of event selection. The Fraction indicates the absolute efficiency of each selection step.

Process	$\tau \to \mu\mu\mu$		$c\bar{c} \to \eta\mu\nu X \to \mu\mu\mu\gamma X$		$c\bar{c} \to \phi\mu\nu X \to \mu\mu\mu X$		$b\bar{b} \to (D/B)X \to \mu\mu\mu X$		$b\bar{b} \to \mu\mu X$	
	Events	Fraction	Events	Fraction	Events	Fraction	Events	Fraction	Events	Fraction
Production	25 000	1.00	45 000	1.00	47 000	1.00	60 000	1.00	$1 \cdot 10^6$	1.00
Trigger	6 132	0.25	7 713	0.17	8 712	0.19	34 420	0.57	114 409	0.11
Preselection	4 359	0.17	3 951	0.09	5 010	0.12	10 212	0.17	134	10^{-4}
Vertex $\chi^2/_{N_{\mathrm{dof}}}$	4 293	0.17	2 923	0.07	3 987	0.08	1258	0.02	56	10^{-5}
Muon collimation	4 289	0.17	2 841	0.06	3 720	0.08	845	0.01	33	10^{-5}
Muon isolation (calo.)	4 262	0.17	1 428	0.03	2 720	0.06	66	10^{-3}	10	10^{-5}
Muon isolation (track)	3 973	0.16	530	0.01	995	0.02	6	10^{-4}	4	10^{-6}
Missing E_{T}	3 885	0.16	233	0.01	429	0.01	5	10^{-4}	1	10^{-6}
Transverse mass	3 810	0.15	90	10^{-3}	169	10^{-3}	1	10^{-5}	0	0
Light meson rejection	3 325	0.13	82	10^{-3}	48	10^{-3}	1	10^{-5}	0	0
τ mass constraint	3 046	0.12	1	10^{-5}	6	10^{-4}	0	0	0	0
Total selection ($10\,\mathrm{fb}^{-1}$)	0.8		0.2		6.0		–		–	

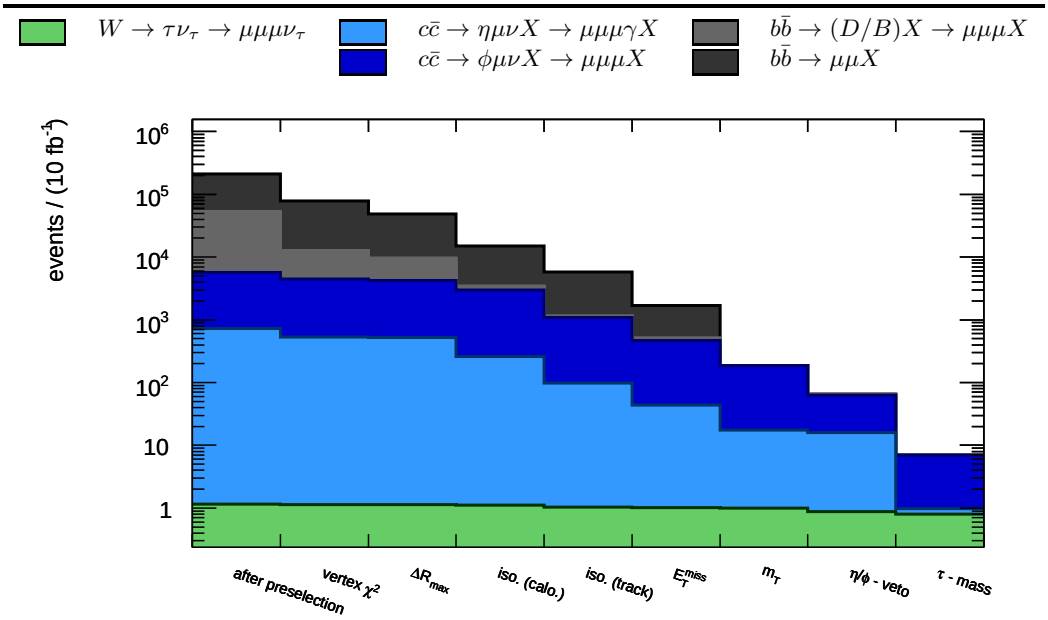

Figure 5.21: Evolution of the number of signal and background events with the applied selection cuts, normalized to $L = 10\,\text{fb}^{-1}$ of integrated luminosity.

of events remaining after the pre-selection by the efficiencies of uncorrelated selection cuts. Since some of the cut variables used in this analysis are strongly correlated, like, for instance, the missing transverse energy and the transverse mass, combined efficiencies of correlated selection cuts are determined. In order to increase the statistics for the determination of the individual cut efficiencies, the trigger selection is not applied before the pre-selection but introduced as additional selection criterion. The efficiencies are determined for the following groups of selection criteria:

- Trigger selection (event filter '2MU6').
- χ^2/N_{dof} of the vertex refit.
- Separation ΔR of the muons, calorimeter and track isolation.
- Missing transverse energy $E_{\text{T}}^{\text{miss}}$ and transverse mass m_{T}.
- Invariant di-muon mass $m_{\mu\mu}$ and invariant muon triplet mass $m_{\mu\mu\mu}$.

The cut on the separation of the muons influences the invariant mass distributions. However, this correlation was found to be weaker than the influence on the isolation criteria. In Table 5.9 the efficiencies are summarized for all background samples. The number of predicted events is the number of events after pre-selection (without trigger decision) multiplied by the product of the individual efficiencies (total efficiency). An accuracy of the background estimation of about 50 % is determined by comparing the numbers of predicted and the observed $c\bar{c}$ background events. Hence, the expected number of inclusive $b\bar{b} \to \mu\mu X$ events surviving all selection cuts for an integrated luminosity of $10\,\text{fb}^{-1}$ is

$$N(b\bar{b} \to \mu\mu X) = 6.4 \pm 3.2. \tag{5.11}$$

In comparison, the expected number of $b\bar{b} \to (D/B) + X \to \mu\mu\mu + X$ events surviving all selection criteria is negligible:

$$N(b\bar{b} \to (D/B)X \to \mu\mu\mu X) = 0.043 \pm 0.022. \tag{5.12}$$

The contributions of in-flight kaon and pion decays as well as fake muons from hadron punch through are suppressed in the six $b\bar{b} \to (D/B)X \to \mu\mu\mu X$ samples because of the forced existence of real muons. Therefore a likely explanation of the different predictions is that an important background contribution is di-muon $b\bar{b}$ events with a third fake muon.

5.11 Error Estimation

This section summarizes the statistical as well as the systematic uncertainties of the estimates of signal and background events after all selection criteria. The systematic uncertainties comprise theoretical uncertainties in the signal and background production cross sections as well as experimental uncertainties in the event selection efficiencies due to the imperfect knowledge of the detector performance.

5.11.1 Expected Statistical Uncertainties

For $10\,\mathrm{fb}^{-1}$ of integrated luminosity, the total number of signal events S (using $\mathcal{B}(\tau \to \mu\mu\mu) = 3.2 \cdot 10^{-8}$) and background events B (inclusive $b\bar{b} \to \mu\mu X$ and $c\bar{c} \to \mu\mu\mu X$, see Table 5.11) is expected to be

$$S = 0.8^{+1.1}_{-0.5}, \tag{5.13}$$

$$B = 12.6^{+3.5}_{-3.4} \tag{5.14}$$

using a Poisson confidence intervals of 84.13 % (corresponding to 1σ Gaussian propability) for the estimation of the statistical uncertainties.

5.11.2 Theoretical Uncertainties

The production cross section for the signal process $pp \to W + X \to \tau\nu_\tau + X$ has been calculated at next-to-next-to-leading order perturbation theory with a theoretical uncertainty of 1 % [92]. The imprecise knowledge of the parton distribution functions at LHC energies is with 8 % the dominant error contribution [91].
For the calculation of the production cross sections of the background processes, the leading-order event generator Pythia has been used accompanied by large theoretical uncertainties due to missing higher order corrections. As recommended in [91], a systematic uncertainty of 50 % is assigned to the cross sections of all background processes.

5.11.3 Expected Systematic Uncertainties

Monte Carlo Statistical Error

The Monte Carlo statistical error calculates according to the number of events surviving the selection criteria and scales with the integrated luminosity. For 3046 ± 55.2 signal

Table 5.9: Efficiencies of uncorrelated selection criteria used to estimate the background from $b\bar{b}$ decays.

	$b\bar{b}$							$c\bar{c}$	
Cuts	$\mu\mu X$	$B^0 \to 3\mu X$	$B^\pm \to 3\mu X$	$B_s \to 3\mu X$	$D^0 \to 3\mu X$	$D^\pm \to 3\mu X$	$D_s \to 3\mu X$	$\eta\mu\nu \to 3\mu\gamma X$	$\phi\mu\nu \to 3\mu X$
Trigger	0.199	0.541	0.544	0.547	0.553	0.527	0.546	0.212	0.231
Vertex $\chi^2/_{N_{dof}}$	0.481	0.179	0.207	0.206	0.186	0.162	0.202	0.795	0.837
Isolation + ΔR	0.036	0.003	0.002	0.001	0.001	0.003	0.002	0.199	0.222
$E_{\mathrm{T}}^{\mathrm{miss}} + m_{\mathrm{T}}$	0.052	0.061	0.063	0.086	0.081	0.082	0.115	0.161	0.150
$m_{\mu\mu} + m_{\mu\mu\mu}$	0.046	0.026	0.029	0.034	0.033	0.033	0.032	0.014	0.031
Total selection efficiency	$8.2{\cdot}10^{-6}$	$4.6{\cdot}10^{-7}$	$4.1{\cdot}10^{-7}$	$3.2{\cdot}10^{-7}$	$2.7{\cdot}10^{-7}$	$3.5{\cdot}10^{-7}$	$8.1{\cdot}10^{-7}$	$7.5 \cdot 10^{-5}$	$2.0 \cdot 10^{-4}$
Pre-selection w/o trigger	674	1940	1926	2061	2438	2263	2478	18598	21689
Events predicted	$5.5{\cdot}10^{-3}$	$8.9{\cdot}10^{-4}$	$7.9{\cdot}10^{-4}$	$6.7{\cdot}10^{-4}$	$6.7{\cdot}10^{-4}$	$1.6{\cdot}10^{-3}$	$2.0{\cdot}10^{-3}$	1.4	4.3
Events observed	–	–	–	–	–	–	–	1	6
Events ($\mathscr{L} = 10\,\mathrm{fb}^{-1}$)	6.4^*	0.011^*	0.011^*	0.001^*	0.003^*	0.013^*	0.004^*	$0.2^\dagger$	$6.0^\dagger$

* Number of predicted events scaled to $10\,\mathrm{fb}^{-1}$.
† Number of observed events scaled to $10\,\mathrm{fb}^{-1}$.

Table 5.10: Systematic uncertainties in the detector response for observables relevant for this analysis corresponding to an integrated luminosity of $10\,\mathrm{fb}^{-1}$ [52].

Observable	Relative uncertainty
Muon energy scale	$\pm 1\,\%$
Muon momentum resolution	$\sigma \oplus 0.011/p_\mathrm{T} \oplus 1.7 \cdot 10^{-4}$
Muon reconstruction efficiency	$-1\,\%$
Jet energy scale	$\pm 7\,\%$ ($\lvert\eta\rvert < 3.2$)
	$\pm 15\,\%$ ($\lvert\eta\rvert > 3.2$)
Jet energy resolution	$\sigma(E) \oplus 0.45\sqrt{E}$ ($\lvert\eta\rvert < 3.2$)
	$\sigma(E) \oplus 0.67\sqrt{E}$ ($\lvert\eta\rvert > 3.2$)

Monte Carlo events for $\mathcal{B}(\tau \to \mu\mu\mu) = 3.2 \cdot 10^{-8}$ after the selection cuts, the total number of signal events with Monte Carlo statistical error is

$$S = 0.800 \pm 0.014. \tag{5.15}$$

Due to the large cross sections of the background, only a rather low Monte Carlo statistics is available leading to:

$$N(c\bar{c} \to \eta\mu\nu X \to \mu\mu\mu\gamma X) = 0.2^{+0.2}_{-0.1}, \tag{5.16}$$

$$N(c\bar{c} \to \phi\mu\nu X \to \mu\mu\mu X) = 6.0^{+2.5}_{-2.4} \tag{5.17}$$

after scaling to $L = 10\,\mathrm{fb}^{-1}$ of integrated luminosity and using Poisson confidence intervals of 84.13 %. No events from the $b\bar{b}$ samples remain after the signal selection and the 50 % uncertainty of the cut factorization method is used instead (see Section 5.10).

Uncertainties in the Detector Performance

In addition the estimation of the signal and background event selection efficiencies with simulated data has to account for the imprecise knowledge of the detector response, for instance due to misalignment of detector components or additional material in the detector not included in the simulation. The detector performance can be measured with data with a precision depending on the recorded integrated luminosity. The systematic uncertainties in the detector response, as agreed in the ATLAS collaboration [52], corresponding to an integrated luminosity of $10\,\mathrm{fb}^{-1}$ are summarized in [52].
In the search for the cLFV decay $\tau \to \mu\mu\mu$, two observables are most relevant: the muon momentum and the missing transverse energy. Hence, the muon reconstruction efficiency, the momentum (energy) resolution and the energy scale have been varied independently for muons and jets, within the margins listed in Table 5.10. The uncertainty in the missing transverse energy $E_\mathrm{T}^\mathrm{miss}$ has been taken into account by varying the muon and jet energies and recalculating the $E_\mathrm{T}^\mathrm{miss}$ vector. Since additional information about the accuracy of the $E_\mathrm{T}^\mathrm{miss}$ measurement can be obtained from real data, only a 5 % variation in the jet energy scale has been used for the recalculation of the missing transverse energy.

Table 5.11 summarizes the experimental systematic variations in the expected numbers of events after applying all event selection criteria for the signal as well as for the background

Table 5.11: Expected numbers of events and their Poisson statistical error, Monte Carlo Gaussian (Poisson) statistical error, theoretical uncertainties on the cross sections [91] and experimental systematic uncertainties [52] corresponding to an integrated luminosity of $10\,\mathrm{fb}^{-1}$. $\mathcal{S}$ and $\mathcal{E}$ denote the effects of the shifts in the energy scale and lowered muon reconstruction efficiency, respectively. $\mathcal{R}$ denotes the effect of degradation of the energy resolution. The last column gives the squared sum of the individual systematic detector uncertainties. The influence of the detector effect could not be studied for the $b\bar{b}$ backgrounds due to low Monte Carlo statistics, but is not expected to be dominant in comparison to the 50 % theoretical and 50 % Monte Carlo statistical error, respectively.

Process	Expected events and stat. error	MC statistical error	Theoretical systematic error	Experimental systematic errors								
				Muons				Jets			$\sum$	
				$\mathcal{R}$	$\mathcal{S}^-$	$\mathcal{S}^+$	$\mathcal{E}$	$\mathcal{R}$	$\mathcal{S}^-$	$\mathcal{S}^+$		
$\tau \to \mu\mu\mu$	$0.80^{+1.1}_{-0.5}$	$\pm\,0.014$	$\pm\,0.064$	-0.026	-0.002	-0.002	-0.002	$+0.002$	$+0.001$	-0.001	-0.026	$+0.001$
$c\bar{c} \to \eta\mu\nu X \to \mu\mu\mu\gamma X$	$0.2^{+0.8}_{-0.1}$	$^{+0.2}_{-0.1}$	$\pm\,0.1$	$+0.2$	± 0	± 0	± 0	± 0	$+0.2$	± 0	-0.0	$+0.2$
$c\bar{c} \to \phi\mu\nu X \to \mu\mu\mu X$	$6.0^{+2.5}_{-2.4}$	$^{+2.5}_{-2.4}$	$\pm\,3.0$	$+2.0$	± 0	± 0	± 0	± 0	± 0	± 0	-0.0	$+2.0$
$b\bar{b} \to (D/B)X \to \mu\mu\mu X$	$0.04^{+0.52}_{-0.0}$	$\pm\,0.02$	$\pm\,0.02$	–	–	–	–	–	–	–	–	–
$b\bar{b} \to \mu\mu X$	$6.4^{+2.5}_{-2.4}$	$\pm\,3.2$	$\pm\,3.2$	–	–	–	–	–	–	–	–	–
Background combined	$12.6^{+3.5}_{-3.4}$	$^{+4.1}_{-4.0}$	$\pm\,6.3$								-0.0	$+2.0$

processes. In addition, the statistical and theoretical uncertainties are listed. The largest impact on the signal selection is from the 8 % theoretical uncertainty in the cross section and the 3 % uncertainty from the decreased muon momentum resolution. All other detector related uncertainties are well below 0.5 %. The expected number of signal events for $L = 10\,\mathrm{fb}^{-1}$ therefore is:

$$S = 0.80^{+1.1}_{-0.5}\,(\text{stat.}) \pm 0.014\,(\text{MC stat.}) \pm 0.064\,(\text{theo.})\ ^{+0.001}_{-0.026}\,(\text{sys.})$$

or

$$S = 0.80^{+1.1}_{-0.5}$$

assuming $\mathcal{B}(\tau \to \mu\mu\mu) = 3.2 \cdot 10^{-8}$.
A decrease of the muon momentum resolution leads to 0.2 additional $c\bar{c} \to \eta\mu\nu X \to \mu\mu\mu\gamma X$ events and two additional $c\bar{c} \to \phi\mu\nu X \to \mu\mu\mu X$ events for $L = 10\,\mathrm{fb}^{-1}$ after all selection criteria. The shift to lower values in the jet energy scale and the resulting change in the measurement of the missing transverse energy leads to 0.2 additional $c\bar{c} \to \eta\mu\nu X \to \mu\mu\mu\gamma X$ events. The impact of the experimental systematic error could not be evaluated for the $b\bar{b}$ background samples due to the low statistics of the simulated samples, but are small compared to 50 % theoretical uncertainty and 50 % precision on the estimation of these background processes. The expected total number of background events for $L = 10\,\mathrm{fb}^{-1}$ of integrated luminosity is

$$B = 12.6^{+3.5}_{-3.4}\,(\text{stat.})\ ^{+4.1}_{-4.0}\,(\text{MC stat.}) \pm 6.3\,(\text{theo.})\ ^{+2.0}_{-0.0}\,(\text{sys.})$$

or

$$B = 12.6^{+8.5}_{-8.2}.$$

For the combination of the systematic uncertainties, the positive and negative values are summed up in quadrature, respectively.

5.12 Upper Limit Estimation

The goal of this analysis is to study the sensitivity of the ATLAS detector for the lepton flavour violating decay $\tau \to \mu\mu\mu$ by estimating the achievable upper limit on the branching ratio $\mathcal{B}(\tau \to \mu\mu\mu)$ for $L = 10\,\mathrm{fb}^{-1}$ of integrated luminosity. In the following the *profile likelihood ratio* method employed for the evaluation of the upper limit is described and the expected upper limit determined taking into account systematic uncertainties.

5.12.1 Statistical Method

The estimated number of signal events s in the experiment is given by

$$s = \mathscr{L}\sigma_\tau \varepsilon \mathcal{B} \tag{5.18}$$

where L denotes the integrated luminosity, σ_τ the production cross section of τ leptons, ε the signal selection efficiency and $\mathcal{B}$ the branching fraction of $\tau \to \mu\mu\mu$. The number n of observed events follows a Poisson distribution with the mean value

$$E[n] = s + b \tag{5.19}$$

where b is the estimated number of background events.
The parameter of interest is the number of signal events s. The number of background events n_b is assumed to follow a Gaussian distribution with mean value $E[n_b] = b$ and standard deviation σ_{n_b} which takes into account the systematic uncertainties in the background estimate including Monte Carlo statistical errors. The product of the two probability distributions defines a likelihood function

$$L(s,b) = \frac{(s+b)^n}{n!} e^{-(s+b)} \cdot \frac{1}{\sigma_{n_b}\sqrt{2\pi}} e^{-\frac{(n_b-b)^2}{2\sigma_{n_b}}} \cdot \frac{1}{\sigma_{\varepsilon'}\sqrt{2\pi}} e^{-\frac{(\varepsilon'-\varepsilon)^2}{2\sigma_{\varepsilon'}}}. \tag{5.20}$$

In order to also account for the systematic uncertainties in the estimation of the signal efficiency ε, the likelihood function contains also a Gaussian probability density function centred at ε with a width corresponding to the uncertainty.
A hypothetical value of s is tested using the profile likelihood ratio

$$\lambda(s) = \frac{L(s,\tilde{b})}{L(\hat{s},\hat{b})}, \tag{5.21}$$

with $\hat{s}$ and $\hat{b}$ representing the maximum likelihood estimators of s and b, and $\tilde{b}$ the conditional maximum likelihood estimator of b when maximizing L for a specific value of s. The variable $\tilde{b}$ therefore depends on s. The profile likelihood ratio defined above always fulfils $0 \leq \lambda(s) \leq 1$. $\lambda(s) = 1$ implies a good agreement between data and the hypothetical value of s. To evaluate the agreement between data and the hypothetical value of s, the variable

$$q_s = -2\ln\lambda(\mathrm{s}) \tag{5.22}$$

is used. Large values of q_s imply poor agreement of s with the data while low values of q_s indicate good agreement. With the probability distribution function $f(q_s|s)$ of q_s the p-value corresponding to the observation $q_{\mathrm{s,obs}}$ is given by

$$p_s = \int_{q_{\mathrm{s,obs}}}^{\infty} f(q_s|s)dq_s. \tag{5.23}$$

To determine an upper limit on the number of signal events s_{up} at a particular confidence level CL (usually 90 % confidence level is used for upper limits of the lepton flavour violating τ decays [1]), the p-value from Equation (5.23) is calculated for different values of s. The range $[s_{\mathrm{low}}, s_{\mathrm{up}}]$ for which p_s is larger than or equal $1 - \mathrm{CL}$ defines the confidence interval for s and the upper limit s_{up}. The expected upper limit on the branching ratio $\mathcal{B}(\tau \to \mu\mu\mu)$ for $L = 10\,\mathrm{fb}^{-1}$of integrated luminosity is then given by

$$\mathcal{B}(\tau \to \mu\mu\mu) = \frac{s_{\mathrm{up}}}{\mathscr{L}\sigma_\tau\varepsilon} \tag{5.24}$$

with production cross section $\sigma_\tau = 22.51\,\mathrm{nb}$ (see Table 5.3) for τ leptons by W decays in pp-collisions and the signal efficiency $\varepsilon = 12.2\,\%$.

5.12.2 Results

The background estimate and the estimated signal efficiency ε are subject to rather large systematic uncertainties coming mainly from the theoretical error on the cross sections and the imperfect knowledge of the detector response and also from the limited Monte Carlo statistics. These uncertainties correspond to the widths of the Gaussian distributions in the likelihood function (Equation (5.20)). The positive and negative errors are added in quadrature and the larger value is taken as width of the Gaussian. Dominant contributions are the theoretical and statistical uncertainties of the Monte Carlo samples. However, measuring the background from data will significantly reduce the statistical uncertainty and the cross sections of charm, beauty and W production at LHC energies will be relatively precisely measured at an integrated luminosity of $L = 10\,\text{fb}^{-1}$. The knowledge of the detector response will improve during the data taking. The impact of the different systematic uncertainties is studied for four combinations of uncertainties:

- **No systematic uncertainties:** All observables are treated as perfectly known.
- **Detector systematics only:** Only the imprecise knowledge of the detector is accounted as uncertainties on the background estimate and signal efficiency.
- **Theoretical uncertainties and MC statistics:** The theoretical uncertainty of the cross section as well as the statistical uncertainties of the simulated data are included in the upper limit estimate.
- **Theoretical uncertainties, MC statistics and detector systematics:** All sources of uncertainties are included in the calculation of the upper confidence limit.

For the computation of the confidence interval, the TRolke package [97, 98] provided by the Root [99] analysis frame work was employed. The upper limit $\mathcal{B}(\tau \to \mu\mu\mu)$ is determined as a function of the number of observed events varied in a range $n = 8, ..., 20$ (see Table 5.12 and Figure 5.22). For $n = 13$ observed events (with $12.6^{+8.5}_{-8.2}$ expected background events) the upper limit on the branching ration is

$$\mathcal{B}(\tau \to \mu\mu\mu) < 5.9 \cdot 10^{-7}$$

including all systematic uncertainties. The theoretical and Monte Carlo statistical uncertainties reduce the sensitivity by factors of $2 - 10$ depending on the number of observed events. The influence of the imprecise knowledge of the detector response is less than 10 % in most cases.
With the expected sensitivity, an integrated luminosity of about $100\,\text{fb}^{-1}$ has to be collected by ATLAS to reach the current best upper limit of $\mathcal{B}(\tau \to \mu\mu\mu) < 3.2 \cdot 10^{-8}$ (90 % CL) of the BELLE experiment [85].

Table 5.12: Upper limits at a 90 % confidence level on the branching ratio $\mathcal{B}(\tau \to \mu\mu\mu)$ for $10\,\text{fb}^{-1}$ of integrated luminosity for a various number of events observed in the signal region.

Events observed	Without uncertainties	Detector systematics	Theoretical + MC statistics	Theo. + MC stat. + detector sys.
8	$4.0 \cdot 10^{-8}$	$7.1 \cdot 10^{-8}$	$3.5 \cdot 10^{-7}$	$3.7 \cdot 10^{-7}$
9	$9.1 \cdot 10^{-8}$	$1.2 \cdot 10^{-7}$	$3.9 \cdot 10^{-7}$	$4.1 \cdot 10^{-7}$
10	$1.4 \cdot 10^{-7}$	$1.7 \cdot 10^{-7}$	$4.4 \cdot 10^{-7}$	$4.6 \cdot 10^{-7}$
11	$2.0 \cdot 10^{-7}$	$2.2 \cdot 10^{-7}$	$4.9 \cdot 10^{-7}$	$5.0 \cdot 10^{-7}$
12	$2.4 \cdot 10^{-7}$	$2.7 \cdot 10^{-7}$	$5.3 \cdot 10^{-7}$	$5.5 \cdot 10^{-7}$
13	$3.0 \cdot 10^{-7}$	$3.2 \cdot 10^{-7}$	$5.8 \cdot 10^{-7}$	$5.9 \cdot 10^{-7}$
14	$3.4 \cdot 10^{-7}$	$3.7 \cdot 10^{-7}$	$6.2 \cdot 10^{-7}$	$6.4 \cdot 10^{-7}$
15	$3.9 \cdot 10^{-7}$	$4.1 \cdot 10^{-7}$	$6.7 \cdot 10^{-7}$	$6.8 \cdot 10^{-7}$
16	$4.4 \cdot 10^{-7}$	$6.6 \cdot 10^{-7}$	$7.1 \cdot 10^{-7}$	$7.3 \cdot 10^{-7}$
17	$4.8 \cdot 10^{-7}$	$5.1 \cdot 10^{-7}$	$7.6 \cdot 10^{-7}$	$7.7 \cdot 10^{-7}$
18	$5.3 \cdot 10^{-7}$	$5.6 \cdot 10^{-7}$	$8.0 \cdot 10^{-7}$	$8.2 \cdot 10^{-7}$
19	$5.8 \cdot 10^{-7}$	$6.0 \cdot 10^{-7}$	$8.5 \cdot 10^{-7}$	$8.6 \cdot 10^{-7}$
20	$6.3 \cdot 10^{-7}$	$6.5 \cdot 10^{-7}$	$8.9 \cdot 10^{-7}$	$9.1 \cdot 10^{-7}$

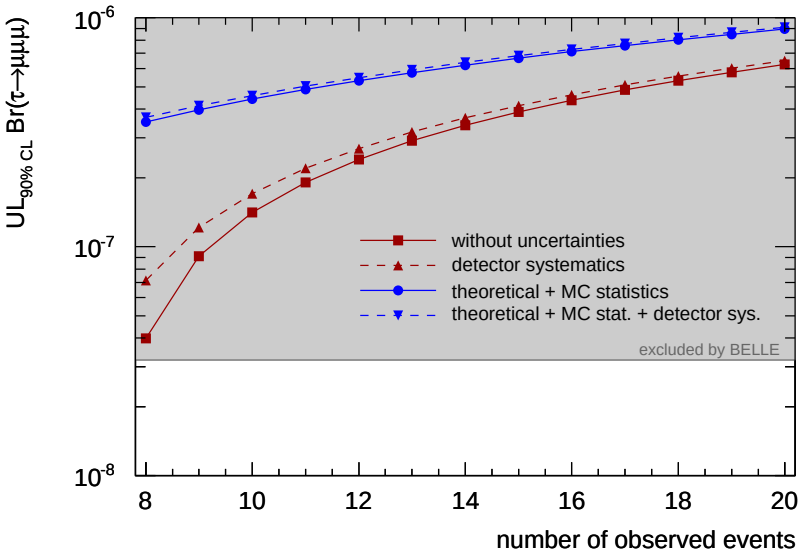

Figure 5.22: Expected sensitivity of the ATLAS detector on the branching ratio of the decay $\tau \to \mu\mu\mu$ originated by the W source as a function of the number of events observed in the signal region for an integrated luminosity of $L = 10\,\text{fb}^{-1}$. Four different predictions are depicted, including various combinations of statistical, theoretical and systematic detector uncertainties of the background processes as well as the signal efficiency.

Chapter 6

Summary

The Large Hadron Collider (LHC) is designed to provide proton-proton collisions at centre-of-mass energies up to $\sqrt{s} = 14\,\text{TeV}$. After several years of construction and commissioning, operation of the LHC has started in November 2009 with proton-proton collisions at $\sqrt{s} = 900\,\text{GeV}$ and $\sqrt{s} = 7\,\text{TeV}$. ATLAS, one of the two general purpose experiments at the LHC, has been built to probe a broad spectrum of physics processes of the Standard Model of particle physics and beyond.

The ATLAS physics goals require a muon momentum resolution of better than 10 % for muon energies up to about 1 TeV. For this purpose, ATLAS is equipped with a muon spectrometer comprising three superconducting air-core toroid magnets and 1150 precision drift tube (MDT) chambers measuring muon trajectories with better than $50\,\mu\text{m}$ position resolution. For muon momenta above 200 GeV, the accuracy of the calibration of the space-to-drift-time relationships of the MDT chambers is one of the main contributions to the muon momentum resolution. In this thesis, an improved method for the calibration of the drift tube chambers in magnetic fields has been developed using curved muon track segments. The space-to-drift-time relationship is determined for each chamber using solely the muon tracking information (so-called autocalibration). The performance of the improved autocalibration algorithm has been evaluated using a sample of simulated muon tracks corresponding to the number of muons delivered by a dedicated muon calibration data stream during one hour of ATLAS data taking. An accuracy of the drift distance measurement of better than $20\,\mu\text{m}$ ($30\,\mu\text{m}$) was achieved for 97 % (100 %) of the MDT chambers. It was shown that this calibration accuracy leads to negligible deterioration of the momentum resolution of the muon spectrometer.

Special attention has been paid to the investigation of systematic effects on the calibration accuracy including the resolutions of the trigger and drift time measurements as well as imprecise knowledge of the chamber geometries. The new method was found to be insensitive to these effects. The performance of the new autocalibration algorithm has been tested successfully with data of cosmic ray muons during the commissioning phase of the ATLAS experiment and is currently in use in ATLAS. The predicted calibration accuracies have been verified with and without magnetic field.

One of the measurements for which the high performance of the muon spectrometer is important is for the lepton flavour violating decay $\tau \to \mu\mu\mu$. The large τ production cross section at the LHC provides an excellent opportunity to search for rare τ decays. About 10^{12} τ leptons are produced per year already at the instantaneous luminosity of

$10^{33}\,\mathrm{cm}^{-2}\mathrm{s}^{-1}$ and centre-of-mass energy of 14 TeV. The dominant sources of τ leptons at the LHC are D_s and b hadron decays. Unfortunately, the trigger and reconstruction efficiency of $\tau \to \mu\mu\mu$ events is rather small due to the low transverse momentum of the muons. The number of τ leptons originating from gauge boson decays is considerably smaller ($\sim 10^8$) but the transverse momenta of the τ decay products is significantly increased due to the large mass difference between τ and gauge bosons. Therefore τ leptons from $W \to \tau\nu_\tau$ decays have been considered in this work.
The three muons from the signal decay provide a characteristic signature in the detector, but are strongly collimated with the lowest muon momentum likely below 10 GeV/c. This implies severe challenges for efficient triggering and reconstruction of the three signal muons. The production rate of low-energetic muons at the LHC exceeds the bandwidth and data storage capacity of the ATLAS readout system such that large pre-scaling factors have to be applied already at the first trigger level. To measure $\tau \to \mu\mu\mu$ events without limiting pre-scaling factors, di-muon triggers have to be employed. Depending on the momentum thresholds available in later data taking, a trigger efficiency of up to 24 % can be reached.
The main backgrounds are semileptonic decays of charm and beauty hadrons mimicking the signal process. The dominating processes are the decay chain $D_s \to \phi\mu\nu_\mu$, $\phi \to \mu\mu$ and $D_s \to \eta\mu\nu_\mu$, $\eta \to \mu\mu\gamma$. The event selection criteria suppress the background in the order of 10^5 for a signal efficiency of 12 %. The dominant systematic error is a 50 % theoretical uncertainty on the background production cross section at LHC energies. Taking also systematic uncertainties from an imprecise knowledge of the detector response into account an upper limit on the signal branching ratio at 90 % confidence level of $\mathcal{B}(\tau \to \mu\mu\mu) < 5.9 \cdot 10^{-7}$ can be reached for an integrated luminosity of $10\,\mathrm{fb}^{-1}$. The two dominant systematic uncertainties can be reduced by estimating the background contributions from data allowing for an increase in sensitivity by a factor of two. To improve the current best upper limit $\mathcal{B}(\tau \to \mu\mu\mu) < 3.2 \cdot 10^{-8}$ (90 % CL) from the BELLE experiment at the e^+e^- B-Factory KEK-B, about $100\,\mathrm{fb}^{-1}$ of data has to be collected by the ATLAS experiment.
This study applies for the low-luminosity phase of the LHC ($\mathscr{L} = 10^{33}\,\mathrm{cm}^{-2}\mathrm{s}^{-1}$) due to the assumptions about trigger thresholds and the neglect of pile-up effects. Applying the results of this study to operation at LHC design luminosity ($\mathscr{L} = 10^{34}\,\mathrm{cm}^{-2}\mathrm{s}^{-1}$) may be possible, but needs further investigations.

Appendix A

Precision Momentum Measurement with the ATLAS Muon Spectrometer

In a uniform magnetic field $B_\perp$, a charged particle with momentum p travelling perpendicularly to the field direction (see Figure A.1) follows a curved path with radius:

$$r\,[\mathrm{m}] = \frac{p_T}{k \cdot B_\perp} \frac{[\mathrm{GeV\ s}]}{[\mathrm{T\ m}]} \tag{A.1}$$

where $k = 0.2998$ m/s. From Figure A.1 one can see that:

$$\sin\frac{\alpha}{2} = \frac{l/2}{r} = k \cdot \frac{B_\perp l}{2p}. \tag{A.2}$$

Hence, in the approximation $\sin(\alpha) \approx \alpha$:

$$\alpha \approx k \cdot \frac{B_\perp l}{p}. \tag{A.3}$$

The sagitta s is with $\cos(\alpha/2) \approx 1 - \alpha^2/8$):

$$s = r - r\cos\frac{\alpha}{2} \approx r\frac{\alpha^2}{8}. \tag{A.4}$$

Inserting r from Equation (A.1) α from Equation (A.3), the following expression of the sagitta is found:

$$s = k\frac{B_\perp l^2}{8p}. \tag{A.5}$$

Depending on the muon energy, the momentum resolution is dominated either by the intrinsic resolution of the track-point measurements (by the MDT and CSC chambers) or by multiple scattering. In general, both effects combine to the momentum resolution.

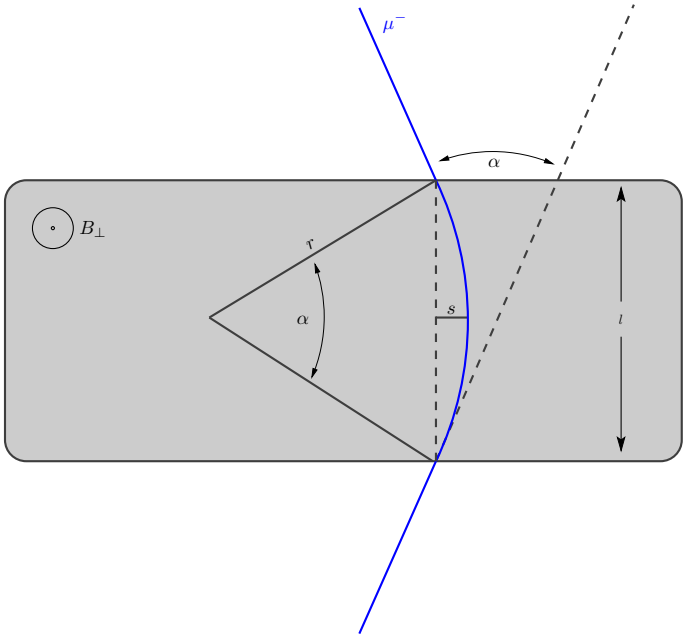

Figure A.1: Sketch of a muon trajectory crossing a perpendicular magnetic field $B_\perp$.

Effect of Intrinsic Detector Resolution

Since $s \propto 1/p$ the relative uncertainty of the momentum measurement is equal to the relative error on the sagitta measurement,

$$\frac{\sigma(p)}{p} = \frac{\sigma(s)}{s} \tag{A.6}$$

with equation A.4

$$\frac{\sigma(p)}{p} = \frac{8p}{kB_\perp l^2}\sigma(s) \tag{A.7}$$

and with

$$\sigma(s) = \sqrt{\frac{3}{2}}\sigma_{\text{TP}} \tag{A.8}$$

for three track-point (TP) measurements with equal precision σ_{TP} along the bent trajectory the momentum resolution of the ATLAS muon spectrometer becomesfor dominating detector resolution

$$\boxed{\frac{\sigma(p)}{p} = \sqrt{\frac{3}{2}}\frac{8p\sigma_{\text{TP}}}{kB_\perp l^2}} \tag{A.9}$$

To reach $\sigma(p)/p = 10\,\%$ for $p = 1\,\text{TeV/c}$ a chamber resolution including relative position uncertainty of

$$\sigma_{\text{TP}} = \sqrt{\frac{2}{3}}\frac{kB_\perp l^2}{8p} \cdot \frac{\sigma(p)}{p} \approx 50\,\mu\text{m} \tag{A.10}$$

is required for typical parameters of the ATLAS muon spectrometer($B_\perp \approx 0.5\,\text{T}$, $l \approx 6\,\text{m}$).

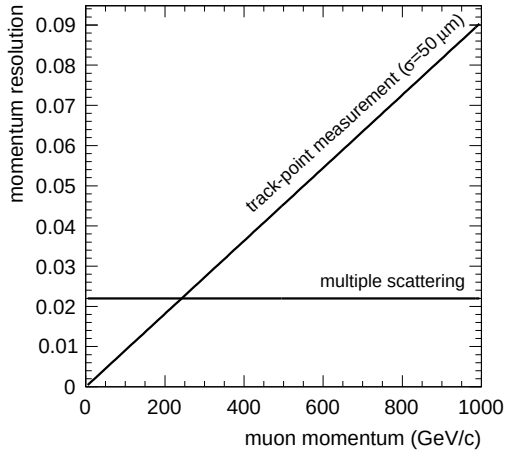

Figure A.2: Contribution of multiple scattering and precision of the track-point measurement to the momentum resolution of the ATLAS muon spectrometer. For momenta below about 250 GeV/c the resolution is dominated by multiple scattering.

Effect of Multiple Scattering

The effect of multiple scattering of the muons on their way through the spectrometer leads to an uncertainty in α of

$$\Delta\alpha = \frac{13.6\,\mathrm{MeV}}{p_T}\sqrt{\frac{l'}{X_0}} \tag{A.11}$$

where X_0 is the radiation length and l' the track length inside the material. The effect of multiple scattering (MS) on the momentum measurement is therefore

$$\frac{\sigma(p)}{p} = \frac{\Delta\alpha}{\alpha} \tag{A.12}$$

and with equation A.3

$$\frac{\sigma(p)}{p} = \frac{13.6\,\mathrm{MeV}}{k \cdot B_\perp l}\sqrt{\frac{l'}{X_0}}. \tag{A.13}$$

Hence, the momentum uncertainty due to multiple scattering is independent of the muon momentum and with $\sqrt{l'}X_0/\approx 1.5$ for the air-core magnet system of the muon spectrometer:

$$\frac{\sigma(p)}{p} \approx 2.2\,\%. \tag{A.14}$$

Which is the ultimate momentum resolutionachievable in the intermediate momentum range where energy loss fluctuations of the muons in the calorimeters are negligible. In Figure A.2, the two contributions to momentum resolution are plotted as a function of the muon momentum for typical parameters of the ATLAS muon spectrometer. The multiple scattering dominates for muon momenta below about 250 GeV/c, while the resolution of the track-point measurement dominates for higher momenta.

Appendix B

MDT Chamber Naming Scheme

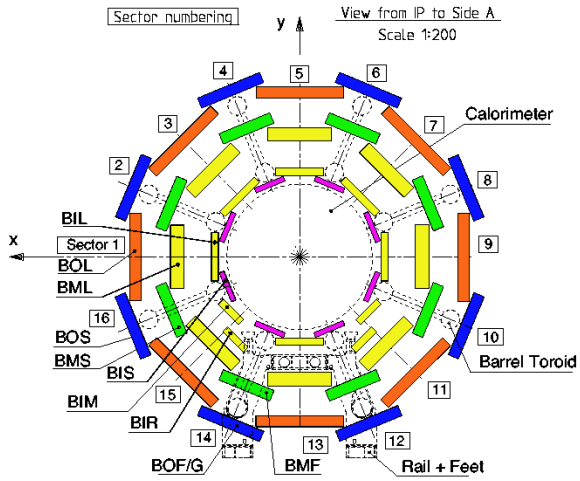

(a)

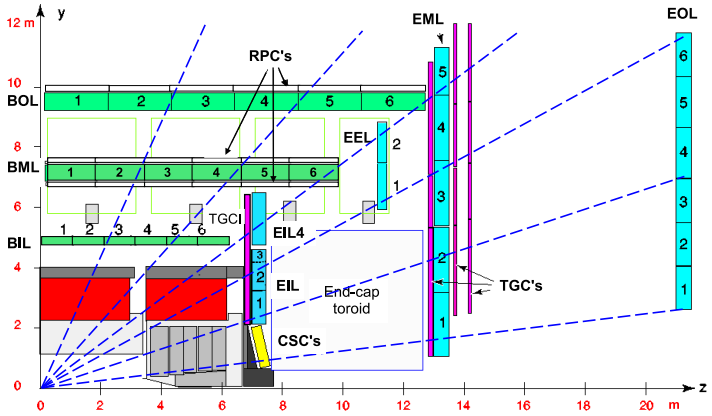

(b)

Figure B.1: Cross sections of the muon spectrometer (a) in the yz plane perpendicular to the beam pipe and (b) in the yz plane (one quadrant) which is the bending plane of the muons.

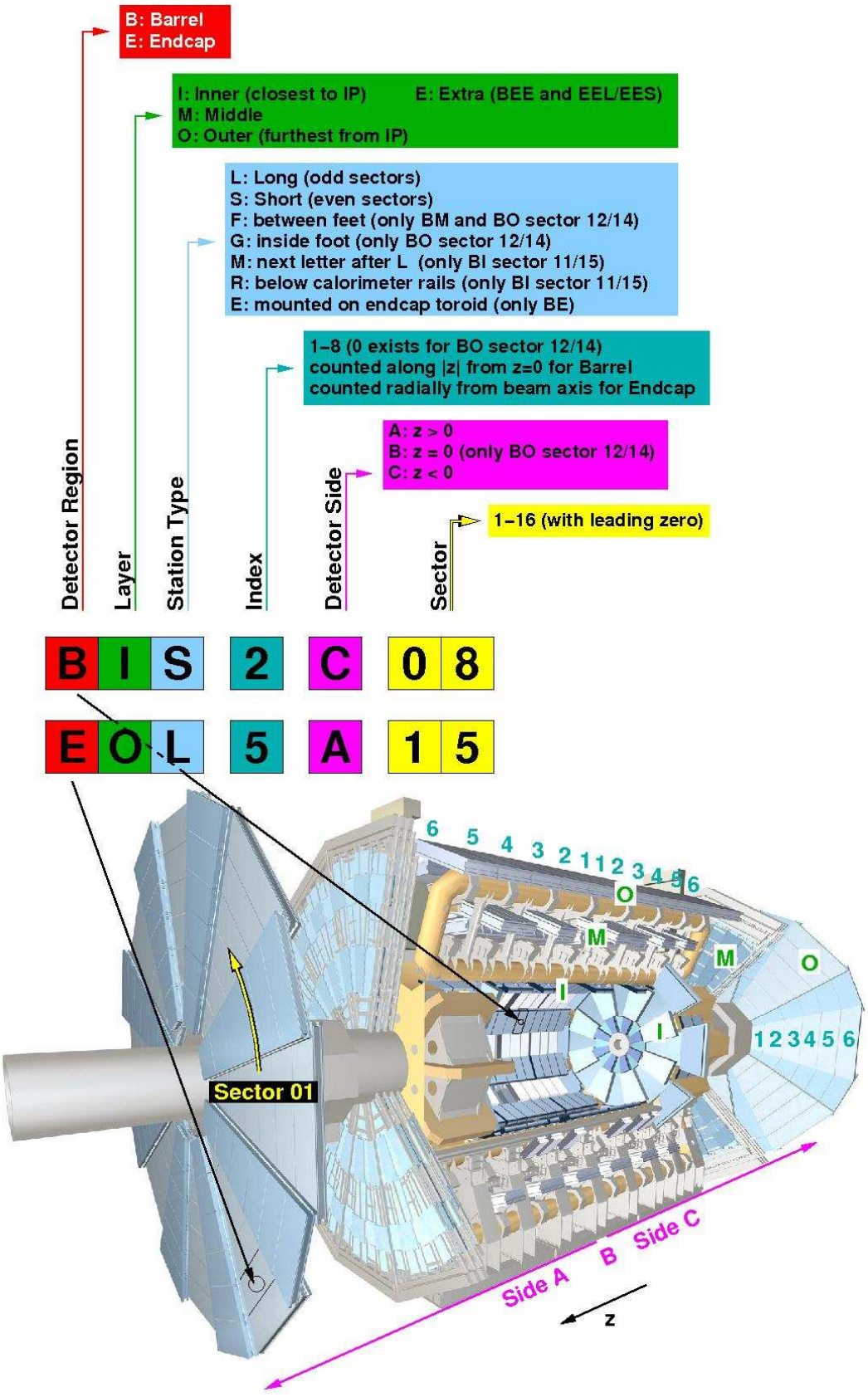

Figure B.2: Naming scheme of the ATLAS MDT chambers.

Appendix C

Autocalibration with Curved Tracks

The principle of the analytic autocalibration with curved tracks is described in Chapter 4. In this appendix the calculations to analytic expressions for the autocalibration algorithm are performed.

C.1 Analytic Expression for the Residual

The χ^2 function for the track fit is given by:

$$\chi^2 = \sum_{k=1}^{K} \frac{(r_k - d_k)^2}{\sigma^2(r_k)} \tag{C.1}$$

Where $r_k = r(t_k)$ is the drift radius determined from the drift time t_k via the initial r(t) relationship and $\sigma(r_k)$ the corresponding spacial resolution. d_k is the distance of closest approach between the track and the anode wire of the k$^{\text{th}}$ hit tube at (y_k^w, z_k^w). With a polynomial parametrization of the trajectory $y(z)$ at order P and

$$m_k := \frac{dy}{dz}(z_k^w) \tag{C.2}$$

(from the initial track fit) d_k has to good approximation the form (see Section 4.5.2):

$$d_k = \frac{1}{\sqrt{1+m_k^2}} \left| \underbrace{\sum_{p=0}^{P} \alpha_p u(z_k^w)^p}_{=y(z_k^w)} - y_k^w \right| \tag{C.3}$$

where the coefficients α_p are determined as free parameters in the fit. Inserting Equation (C.3) into (C.1), the χ^2 function becomes:

$$\chi^2 = \sum_{k=1}^{K} \frac{1}{\sigma^2(r_k)} \underbrace{\left[r_k - \frac{1}{\sqrt{1+m_k^2}} \left| \sum_{p=0}^{P} \alpha_p u(z_k^w)^p - y_k^w \right| \right]^2}_{:=A^2} \tag{C.4}$$

The minimum of the χ^2 function can be found analytically for this track parametrization. The gradient of the χ^2 function with respect to the parameters α_p has to vanish:

$$\frac{\partial \chi^2}{\partial \alpha_q} = \sum_{k=1}^{K} \frac{2A}{\sigma^2(r_k)} \left[-\frac{u(z_k^w)^q}{\sqrt{1+m_k^2}} \cdot \underbrace{sgn\left(\sum_{p=0}^{P} \alpha_p u(z_k^w)^p - y_k^w \right)}_{:=S_k} \right] \tag{C.5}$$

$$= \sum_{k=1}^{K} \frac{-2S_k}{\sigma^2(r_k)} \left[\frac{r_k u(z_k^w)^q}{\sqrt{1+m_k^2}} \frac{u(z_k^w)^q}{1+m_k^2} \left| \sum_{p=0}^{P} \alpha_p u(z_k^w)^p - y_k^w \right| \right] \tag{C.6}$$

$$= -2S_k \sum_{h=1}^{H} \frac{r_k u(z_k^w)^q}{\sigma^2(r_k)\sqrt{1+m_k^2}} + \frac{S_k u(z_k^w)^q z_k^w}{\sigma^2(r_k)(1+m_k^2)}$$

$$- \frac{S_k u(z_k^w)^q}{\sigma^2(r_k)(1+m_k^2)} \sum_{p=0}^{P} \alpha_p u(z_k^w)^p \stackrel{!}{=} 0 \tag{C.7}$$

with the result for the parameters α_p:

$$\sum_{p=0}^{P} \alpha_p \underbrace{\sum_{k=1}^{K} \frac{S_k u(z_k^w)^q u^p(z_k^w)}{\sigma^2(r_k)(1+m_k^2))}}_{:=M_{pq}} = \underbrace{\sum_{k=1}^{K} \frac{u(z_k^w)^q}{\sigma^2(r_k)} \left[\frac{r_k}{\sqrt{1+m_k^2}} + \frac{S_k y_k^w}{1+m_k^2} \right]}_{:=b_q} \tag{C.8}$$

which is a matrix equation which can be inverted to get

$$\alpha_p = \sum_{q=0}^{P} M_{pq}^{-1} b_q. \tag{C.9}$$

using Equations (C.3) and (C.9) the k$^{\text{th}}$ residuals $\Delta_k = r_k - d_k$ obtain the following analytic form:

$$\boxed{\Delta_k = r_k - \frac{1}{\sqrt{1+m_k^2}} \left| \sum_{p=0}^{P} \sum_{q=0}^{P} M_{pq}^{-1} b_q u(z_k^w)^p - y_k^w \right|.} \tag{C.10}$$

C.2 Sensitivity to the Measured Drift Radii

The sensitivity of Δ_k to changes of the drift radii $r_{k'}$ included in the track fit is given by:

$$\frac{\partial \Delta_k}{\partial r_{k'}} = \delta_{kk'} - \frac{S_k}{\sqrt{1+m_k^2}} \sum_{p,q=0}^{P} M_{pq}^{-1} u(z_k^w)_k^p \frac{\partial b_q}{\partial r_{k'}} \tag{C.11}$$

$$= \delta_{kk'} - \frac{S_k}{\sqrt{1+m_k^2}} \sum_{p,q=0}^{P} M_{pq}^{-1} u(z_k^w)_k^p \sum_{k''}^{H} \frac{u(z_k^w)_{k''}^q}{\sigma^2(r_{k''})\sqrt{1+m(z_k^w)_{k''}^2}} \delta_{k'k''} \tag{C.12}$$

$$= \underbrace{\delta_{kk'} - \frac{S_k}{\sigma^2(r_{k'})\sqrt{1+m_k^2}\sqrt{1+m(z_k^w)_{k'}^2}} \sum_{p,q=0}^{P} M_{pq}^{-1} u(z_k^w)_k^p u(z_k^w)_{k'}^q}_{:=D_{kk'}} . \tag{C.13}$$

Appendix D

The Lorentz Angle Correction Function

To describe the electron drift time in drift tubes with $ArCO_2$ gas mixture in the presence of a homogeneous magnetic field the following Cartesian coordinate system is used (see also Figure D.1):

- The x_2 axis is defined parallel to the shortest distance between muon track and anode wire.
- The x_3 axis is oriented parallel to the anode wire.
- The x_1 axis points in the direction perpendicular to the x_2 and x_3 axes which is the direction of the muon for perpendicular incidence.

The motion of an electron in an electromagnetic field is described by the Langevin equation:

$$\ddot{\vec{x}} = -\frac{\dot{\vec{x}}}{\tau} + \frac{e}{m_e}\vec{E}(x) + \frac{e}{m_e}\left(\dot{\vec{x}} \times \vec{B}\right) \tag{D.1}$$

where τ denotes the mean scattering time of the electrons on the gas molecules and $\vec{E}$ and $\vec{B}$ the electrical and magnetic field vectors inside the drift tube.
The first term on the right-hand side of the equation describes the deceleration of the electrons due to elastic scattering on the gas molecules. As the energies of the electrons are sufficient for the excitation of the CO_2 molecules (vibrations and rotations), part of the scattering processes is inelastic. To take this effect into account, the first term of the Langevin equation is modified with the power of $1 + \epsilon$ where Epsilon is determined by Garfield simulations [66] and test beam measurements [62] to be $\epsilon \simeq 0.1$:

$$\ddot{\vec{x}} = -\left(\frac{\dot{\vec{x}}}{\tau_\epsilon}\right)^{1+\epsilon} + \frac{e}{m_e}\vec{E}(x) + \frac{e}{m_e}\left(\dot{\vec{x}} \times \vec{B}\right), \tag{D.2}$$

The second term of Equations (D.1) and (D.2) is the acceleration in the electric field and the third term the acceleration of Lorentz force. In the simplified case that $\vec{B}$ is uniform

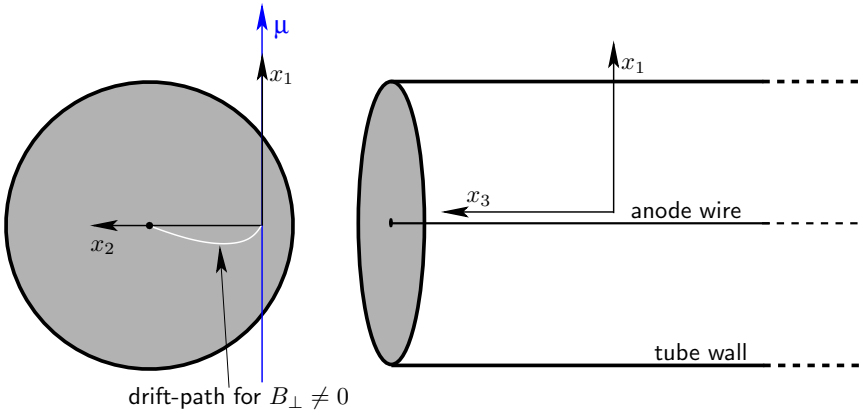

Figure D.1: Definition of the used coordinate system to calculate the electron drift in an electromagnetic field.

and has no component in x_1 direction Equation (D.2) can be written like:

$$\ddot{x}_1 = -\left(\frac{\dot{x}_1}{\tau}\right)^{1+\epsilon} + \frac{e}{m_e}E_1(\vec{x}) + \frac{e}{m_e}\left(\dot{x}_2 B_3 - \dot{x}_3 B_2\right), \tag{D.3}$$

$$\ddot{x}_2 = -\left(\frac{\dot{x}_2}{\tau}\right)^{1+\epsilon} + \frac{e}{m_e}E_2(\vec{x}) - \frac{e}{m_e}\left(\dot{x}_3 B_3\right), \tag{D.4}$$

$$\ddot{x}_3 = -\left(\frac{\dot{x}_3}{\tau}\right)^{1+\epsilon} + \frac{e}{m_e}E_3(\vec{x}) + \frac{e}{m_e}\left(\dot{x}_1 B_2\right). \tag{D.5}$$

For $t \gg \tau$ the equilibrium case is reached where the acceleration of the electrons in the electric field is compensated by the friction due to the elastic and inelastic scattering and the acceleration of the electrons can be neglected ($\ddot{x}_{1,2,3} \approx 0$). In addition, the drift path of the electrons is approximately parallel to x_2 if the magnetic field is not too strong. Thus the electric field along the drift path is

$$E_1(\vec{x}) \approx E_3(\vec{x}) \approx 0 \tag{D.6}$$

and

$$E_2(\vec{x}) \approx E(x_2) = \frac{U_0}{\ln\frac{r_{max}}{r_{min}}} \cdot \frac{1}{x_2} \tag{D.7}$$

where U_0 is the applied voltage, $r_{\min}$ denotes the radius of the wire and $r_{\max}$ the inner tube radius. For the further simplified case that $|\dot{x}_1| \ll |\dot{x}_2|$ and $B_1 = 0$, thus also $\dot{x}_3 = 0$ only two equations remain to describe the problem:

$$0 = -\left(\frac{\dot{x}_1}{\tau}\right)^{1+\epsilon} + \frac{e}{m_e}\dot{x}_2 B_3, \tag{D.8}$$

$$0 = -\left(\frac{\dot{x}_2}{\tau}\right)^{1+\epsilon} + \frac{e}{m_e}E(x_2) - \frac{e}{m_e}\dot{x}_1 B_3. \tag{D.9}$$

Solving the first equation for $\dot{x}_1$ and inserting it into the second (with $\frac{1}{1-\epsilon} \approx 1-\epsilon$) gives

$$0 = -\left(\frac{\dot{x}_2}{\tau}\right)^{1+\epsilon} + \frac{e}{m_e}E(x_2) - \left(\frac{e}{m_e}B_\perp\right)^{2-\epsilon}\tau\dot{x}_2^{1-\epsilon}. \tag{D.10}$$

or

$$\dot{x}_2\left[1 + \left(\frac{e}{m_e}B_\perp\right)^{2-\epsilon}\tau^{2+\epsilon}\dot{x}_2^{-2\epsilon}\right] = \left[\frac{e}{m_e}E_2(x_2)\right]^{1-\epsilon}\tau. \tag{D.11}$$

As this equation applies for all magnetic fields perpendicular to x_2, B_3 has been replaced by $B_\perp$. The right-hand side describes the drift velocity $u_0(x_2)$ without magnetic field in the case $\ddot{x}_2 = 0$ (compare Equation (D.4) in this case). Replacing approximately $\dot{x}_2 = u_0$ in the square bracket on the left-hand side gives:

$$\frac{1}{\dot{x}_2} = \frac{1}{u_0}\left[1 + \left(\frac{e}{m_e}B_\perp\right)^{2-\epsilon}\tau^{2+\epsilon}u_0^{-2\epsilon}\right] = \frac{\partial t}{\partial x_2}. \tag{D.12}$$

The the drift time as a function of r is calculated by integrating Equation (D.12):

$$t\left(r, \vec{B}\right) = t\left(r, \vec{B} = 0\right) + B_\perp^{2-\epsilon}\int_{r_{min}}^{r}\frac{u_0^{1-\epsilon}(x_2)}{E^{2-\epsilon}(x_2)}dx_2 \tag{D.13}$$

$$= t\left(r, \vec{B} = 0\right) + \Delta t(r, \vec{B} \neq 0). \tag{D.14}$$

Hence, the drift time can be separated into a term for the case without magnetic field and a correction term describing the Lorentz angle effect. This additional term depends only on the configuration of the electric and magnetic fields inside the tube and on the drift velocity u_0 without magnetic field.

Acknowledgements

This page is probably one of the most read of a thesis and I sincerely hope to mention everybody who supported me in any possible way during these last years. In case your name is missing here and feelings arise that this might be unfair, then please forgive me my carelessness and accept my apologies.
First I want to express my gratitude to my supervisor Hubert Kroha for the opportunity to do my diploma and my PHD thesis at the MDT group of the Max Planck Institute of physics. I thank him for giving me the possibility to stay at CERN for almost two years and to become part of the elected group of people who built-up this fascinating experiment and for always supporting me to participate in schools, workshops and conferences even if at the most far away islands.
I want to thank Jörg Dubbert, Oliver Kortner and Vadym Zhuravlov for guiding me through the jungle experimental high-energy physics sometimes is. This comparison particularly applies to the days and nights Jörg and I spent inside the ATLAS muon spectrometer hanging upside down to replace readout boards or hunting down evil pick-up noise. All three of them always showed much patience with me and had time for my questions and the following discussions, no matter how busy they were.
Thank you all the members of the MDT group for the last years together, but especially to Thies Ehrich and Sebastian Stern with whom i had the pleasure to share the office in Munich. Special gratitude i want to express to the *CERN Erasmus Group*, it was a pleasure to explore Geneva and its beautiful surroundings together and particularly to Steffen Kaiser for tough squash matches and multiple ascents of the Reculet.

Der größte Dank gebührt meiner Familie und meinen Freunden, die sich stets ungemein für meine Arbeit sowie deren Fortschritt interessierten und insbesondere für ihr Verständnis, dass manchmal vielleicht etwas zu wenig Zeit für sie übrig blieb. Ohne euch währe diese Arbeit nicht möglich gewesen. Besonderer Dank vor allem meinen Eltern Karin und Bernd v. Loeben, die mich nicht nur die letzten Jahre meiner Promotion, sondern während meiner gesamten Studienzeit unterstützt haben. Ebenso meiner Schwester Annette und meinem Schwager Thomas, dass sie mir stets moralisch Beistand geleistet haben und insbesondere für ihre tatkräftige Hilfe bei den Umzügen zwischen Ornex und München.

Impossible to fully express the feelings and the gratitude to the one special person in my life who is the source of all my motivation and my daily happiness. Not only during the last days it was you who gave me the force I needed. You were and are always with me Daniela, giving my the incredible feeling of being secure and confident whatever happens. Thank you so much for everything.

List of Figures

List of Tables

Bibliography

[1] Particle Data Group Collaboration, C. Amsler et al., *Review of particle physics*, Phys. Lett. **B667** (2008) 1.

[2] E. Noether, *Invariante Variationsprobleme*, Gött. Nachr. (1918) 235–257.

[3] H. Fritzsch, M. Gell-Mann, and H. Leutwyler, *Advantages of the Color Octet Gluon Picture*, Phys. Lett. **B47** (1973) 365–368.

[4] D. J. Gross and F. Wilczek, *Ultraviolet Behavior of Non-Abelian Gauge Theories*, Phys. Rev. Lett. **30** (1973) no. 26, 1343–1346.

[5] S. Weinberg, *Nonabelian Gauge Theories of the Strong Interactions*, Phys. Rev. Lett. **31** (1973) 494–497.

[6] S. Glashow, *Partial Symmetries of Weak Interactions*, Nucl. Phys. **22** (1961) 579–588.

[7] S. Weinberg, *A Model of Leptons*, Phys. Rev. Lett. **19** (1967) 1264–1266.

[8] A. Salam, *Weak and Electromagnetic Interactions*, originally printed in "Svartholm: Elementary Particle Theory, Proceedings of the Nobel Symposium held 1968 at Lerum, Sweden", Stockholm 1968, 367-377.

[9] P. Higgs, *Broken Symmetries and the Masses of Gauge Bosons*, Phys. Rev. Lett. **13** (1964) 508–509.

[10] ALEPH Collaboration, *Precision Electroweak Measurements and Constraints on the Standard Model*, `arXiv:0811.4682 [hep-ex]`.

[11] E. Konopinski and H. Mahmoud, *The Universal Fermi Interaction*, Phys. Rev. **92** (1953) no. 4, 1045–1049.

[12] R. Davis, *Report on the Homestake solar neutrino experiment*, Front. Phys. **5** (1993) 47–60.

[13] GALLEX Collaboration, M. Cribier et al., *Results of the whole GALLEX experiment*, Nucl. Phys. Proc. Suppl **70** (1999) no. 1-3, 284–291.

[14] GNO Collaboration, M. Altmann et al., *Complete results for five years of GNO solar neutrino observations*, Phys. Lett. **616** (2005) no. 3-4, 174–190.

[15] SAGE Collaboration, J. Abdurashitov et al., *Measurement of the solar neutrino capture rate in Sage*, Nucl. Phys. Proc. Suppl. **118** (2003) 39–46.

[16] Super-Kamiokande Collaboration, S. Fukuda et al., *The Super-Kamiokande detector*, Nucl. Instrum. Methods Phys. Res., A **501** (2003) no. 2-3, 418 – 462.

[17] B. Aharmim et al., *Determination of the ν_e and total ^8B solar neutrino fluxes using the Sudbury Neutrino Observatory Phase I data set*, Phys. Rev. C **75** (2007) no. 4, 045502.

[18] Super-Kamiokande Collaboration, T. Kajita et al., *Atmospheric neutrino results from Super-Kamiokande and Kamiokande: Evidence for nu/mu oscillations*, Nucl. Phys. Proc. Suppl. **77** (1999) 123–132, arXiv:hep-ex/9810001.

[19] KamLAND Collaboration, I. Shimizu et al., *KamLAND Results*, Nucl. Phys. Proc. Suppl. **188** (2009) 84–89. Proceedings of the Neutrino Oscillation Workshop.

[20] K2K Collaboration, K. Kaneyuki, *Recent results from K2K*, Nucl. Phys. Proc. Suppl. **145** (2005) 124–127.

[21] MINOS Collaboration, C. Howcroft, *Results from MINOS/NuMI*, Nucl. Phys. Proc. Suppl. **169** (2007) 326–330.

[22] OPERA Collaboration, N. Agafonova et al., *Observation of a first ν_τ candidate in the OPERA experiment in the CNGS beam*, arXiv:1006.1623 [hep-ex].

[23] S. Glashow, J. Iliopoulos, and L. Maiani, *Weak Interactions with Lepton-Hadron Symmetry*, Phys. Rev. D **2** (1970) no. 7, 1285–1292.

[24] X. Pham, *Lepton flavor changing in neutrinoless tau decays*, Eur. Phys. J. **C8** (1999) 513–516, arXiv:hep-ph/9810484.

[25] S. Martin, *A Supersymmetry Primer*, arXiv:hep-ph/9709356.

[26] J. Ellis et al., *A new parametrization of the seesaw mechanism and applications in supersymmetric models*, Phys. Rev. **D66** (2002) 115013, arXiv:hep-ph/0206110.

[27] A. Dedes et al., *Higgs mediated $B^0_{s,d} \to \mu\tau$, $e\tau$ and $\tau \to 3\mu$, $e\mu\mu$ decays in supersymmetric seesaw models*, Phys. Lett. **B549** (2002) 159–169, arXiv:hep-ph/0209207.

[28] N. Arkani-Hamed et al., *The littlest Higgs*, JHEP **07** (2002) 034, arXiv:hep-ph/0206021.

[29] M. Blanke et al., *Charged Lepton Flavour Violation and $(g-2)_m u$ in the Littlest Higgs Model with T-Parity: a clear Distinction from Supersymmetry*, JHEP **05** (2007) 013, arXiv:hep-ph/0702136.

[30] M. Blanke et al., *FCNC Processes in the Littlest Higgs Model with T-Parity: a 2009 Look*, Acta Phys. Polon. **B41** (2010) 657, arXiv:0906.5454 [hep-ph].

[31] R. Barbier et al., *R-parity violating supersymmetry*, Phys. Rept. **420** (2005) 1–202, arXiv:hep-ph/0406039.

[32] A. Akeroyd et al., *Lepton Flavour Violating tau Decays in the Left-Right Symmetric Model*, Phys. Rev. **D76** (2007) 013004, arXiv:hep-ph/0610344.

[33] L. Evans et al., *LHC Machine*, JINST **3** (2008) S08001.

[34] ATLAS Collaboration, G. Aad et al., *The ATLAS Experiment at the CERN LHC*, JINST **3** (2008) S08003.

[35] CMS Collaboration, R. Adolphi et al., *The CMS experiment at the CERN LHC*, JINST **3** (2008) S08004.

[36] ALICE Collaboration, K. Aamodt et al., *The ALICE experiment at the CERN LHC*, JINST **3** (2008) S08002.

[37] LHCb Collaboration, A. Augusto Alves et al., *The LHCb Detector at the CERN LHC*, JINST **3** (2008) S08005.

[38] A. Yamamoto et al., *The ATLAS central solenoid*, Nucl. Instrum. Methods Phys. Res., A **584** (2008) no. 1, 53–74.

[39] M. Aharrouche et al., *Energy linearity and resolution of the ATLAS electromagnetic barrel calorimeter in an electron test-beam*, Nucl. Instrum. Methods Phys. Res., A **568** (2006) no. 2, 601–623.

[40] B. Dowler et al., *Performance of the ATLAS hadronic end-cap calorimeter in beam tests*, Nucl. Instrum. Methods Phys. Res., A **482** (2002) no. 1-2, 94–124.

[41] J. Archambault et al., *Energy calibration of the ATLAS Liquid Argon Forward Calorimeter*, JINST **3** (2008) no. 02, P02002.

[42] C. Adorisio et al., *Ageing studies for the Atlas muon spectrometer drift tubes*, Nuclear Physics B - Proceedings Supplements **150** (2006) 168–171. Proceedings of the 9th Topical Seminar on Innovative Particle and Radiation Detectors.

[43] S. Zimmermann, *High Rate and Ageing Studies for the Drift Tubes of the ATLAS Muon Spectrometer*. PhD thesis, Albert Ludwigs Universität, Freiburg, 2004.

[44] D. Salvatore, *Intensive irradiation studies, monitoring and commissioning data analysis on the ATLAS MDT chambers*. PhD thesis, Università della Calabria, Cosenza, 2007.

[45] W. Blum, W. Riegler, and L. Rolandi, *Particle Detection with drift Chambers; 2nd ed.*

[46] F. Bauer et al., *Large-scale production of Monitored Drift Tube chambers for the ATLAS muon spectrometer*, Nucl. Instrum. Methods Phys. Res., A **518** (2004) no. 1-2, 69–72.

[47] A. Baroncelli et al., *Assembly and test of the BIL tracking chambers for the ATLAS Muon spectrometer*,
Nucl. Instrum. Methods Phys. Res., A **557** (2006) no. 2, 421–435.

[48] F. Bauer et al., *The first precision drift tube chambers for the ATLAS muon spectrometer*, Nucl. Instrum. Methods Phys. Res., A **478** (2002) no. 1-2, 153–157.

[49] R. Avramidou et al., *A high-precision X-ray tomograph for quality control of the ATLAS Muon Monitored Drift Tube Chambers*,
Nucl. Instrum. Methods Phys. Res., A **518** (2004) no. 1-2, 73–75.

[50] H. van der Graaf et al., *RasNiK, an Alignment System for the ATLAS MDT Barrel Muon Chambers: Technical System Description; Revised Version 2.0*,, NIKHEF, Amsterdam, 2000.

[51] Y. Arai et al., *ATLAS Muon Drift Tube Electronics*, JINST **3** (2008)
no. ATL-MUON-PUB-2008-008. ATL-COM-MUON-2008-010, P09001. 58 p.

[52] ATLAS Collaboration, G. Aad et al., *Expected Performance of the ATLAS Experiment: Detector, Trigger and Physics*. CERN, Geneva, 2008.

[53] C. Eck et al., *LHC computing Grid: Technical Design Report*. Technical Design Report LCG. Geneva, 2005.

[54] O. Kortner and F. Rauscher, *Automatic Synchronization of Drift-Time Spectra and Maximum Drift-Time Measurement of an MDT*, ATL-MUON-2005-012. ATL-COM-MUON-2002-006. CERN-ATL-COM-MUON-2002-006, CERN, Geneva, 2002.

[55] G. Avolio et al., *Test of the first BIL tracking chamber for the ATLAS muon spectrometer*, Nucl. Instrum. Methods Phys. Res., A **523** (2004) no. 3, 309–322.

[56] J. Dubbert et al., *Resolution and Efficiency of Monitored Drift-Tube Chambers with Final Read-out Electronics at High Background Rates*, ATL-MUON-2004-002, CERN, Geneva, Dec 2003.

[57] P. Bagnaia et al., *Calibration model for the MDT chambers of the ATLAS Muon Spectrometer*, ATL-MUON-PUB-2008-004. ATL-COM-MUON-2008-006, CERN, Geneva, Feb 2008. backup paper for Atlas Detector paper.

[58] M. Deile et al., *Resolution and efficiency of the ATLAS muon drift-tube chambers at high background rates*,
Nucl. Instrum. Methods Phys. Res., A **535** (2004) no. 1-2, 212–215. Proceedings of the 10th International Vienna Conference on Instrumentation.

[59] J. Dubbert et al., *Integration, commissioning and installation of monitored drift tube chambers for the ATLAS barrel muon spectrometer*,
Nucl. Instrum. Methods Phys. Res., A **572** (2007) no. 1, 53 – 56.

[60] D. Levin, *Investigation of Momentum Resolution in Straight vs Bent Large End-Cap Chambers*, ATL-MUON-2000-001, CERN, Geneva, Apr 1999. revised version number 1 submitted on 2000-01-03 11:50:03.

[61] A. Baroncelli et al., *Study of temperature and gas composition effects in rt relations of ATLAS MDT BIL Chambers*, ATL-MUON-2004-018, CERN, Geneva, Jul 2004.

[62] J. Dubbert et al., *Modelling of the space-to-drift-time relationship of the ATLAS monitored drift-tube chambers in the presence of magnetic fields*, Nucl. Instrum. Methods Phys. Res., A **572** (2007) no. 1, 50–52.

[63] J. v. Loeben, *Test und Kalibrierung der Präzisionsdriftrohrkammern des ATLAS Myonspektrometers*, Diploma thesis, Max Planck Institut für Physik and Technische Universität München, 2006.

[64] J. v. Loeben et al., *An efficient method to determine the space-to-drift-time relationship of the ATLAS monitored drift tube chambers*, Nuclear Science Symposium Conference Record, 2007. NSS '07. IEEE **1** (2007) 685–688.

[65] F. Rauscher, *Calibration of the ATLAS Muon Chambers*, ATL-MUON-PROC-2009-007. ATL-COM-MUON-2009-029, CERN, Geneva, Oct 2009.

[66] R. Veenhof, *GARFIELD-Simulation of gaseous detectors*, CERN Program Library, Reference: W5050 (1984) .

[67] S. Biagi, *A multi-term Boltzmann analysis of drift velocity, diffusion, gain and magnetic field effects in argon, methane and water vapour mixtures*, .

[68] P. Bagnaia et al., *Calib: a package for MDT calibration studies - User Manual*, ATL-MUON-2005-013. ATL-COM-MUON-2002-004, CERN, Geneva, 2002.

[69] M. Cirilli et al., *Results from the 2003 beam test of a MDT BIL chamber: systematic uncertainties on the TDC spectrum parameters and on the space-time relation*, ATL-MUON-2004-028. ATL-COM-MUON-2004-009. CERN-ATL-COM-MUON-2004-009, CERN, Geneva, 2004.

[70] M. Deile, *Optimization and Calibration of the Drift-Tube Chambers for the ATLAS Muon Spectrometer*. PhD thesis, Ludwig Maximilians Universität, München, 2000.

[71] Aad, G. and others, *ATLAS computing: Technical Design Report*. Technical Design Report ATLAS. Geneva, 2005. Revised version submitted on 2005-06-20 16:33:46.

[72] S. Agostinelli et al., *G4–a simulation toolkit*, Nucl. Instrum. Methods Phys. Res., A **506** (2003) no. 3, 250–303.

[73] F. Bauer et al., *Construction and test of MDT chambers for the ATLAS muon spectrometer*, Nucl. Instrum. Methods Phys. Res., A **461** (2001) no. 1-3, 17–20.

[74] S. Hassani et al., *A muon identification and combined reconstruction procedure for the ATLAS detector at the LHC using the (MUONBOY, STACO, MuTag) reconstruction packages*, Nucl. Instrum. Meth. **A572** (2007) 77–79.

[75] D. Levin et al., *Streamlined Calibration of the ATLAS Muon Spectrometer Precision Chambers*, ATL-MUON-PROC-2009-010. ATL-COM-MUON-2009-041, CERN, Geneva, Nov 2009.

[76] S. Neddermeyer and C. Anderson, *Note on the Nature of Cosmic-Ray Particles*, Phys. Rev. **51** (1937) no. 10, 884–886.

[77] E. Hincks and B. Pontecorvo, *Search for Gamma-Radiation in the 2.2-Microsecond Meson Decay Process*, Phys. Rev. **73** (1948) no. 3, 257–258.

[78] M. Perl et al., *Evidence for anomalous lepton production in e^+ e^- annihilation*, Phys. Rev. Lett. **35** (1975) 1489–1492.

[79] BELLE Collaboration, A. Abashian et al., *The Belle detector*, Nucl. Instrum. Methods Phys. Res., A **479** (2002) no. 1, 117–232.

[80] BABAR Collaboration, B. Aubert et al., *The BaBar detector*, Nucl. Instrum. Methods Phys. Res., A **A479** (2002) 1–116, arXiv:hep-ex/0105044.

[81] MEGA Collaboration, M. Brooks et al., *New Limit for the Family-Number Non-conserving Decay μ^+ to $e^+\gamma$*, Phys. Rev. Lett. **83** (1999) 1521–1524, arXiv:hep-ex/9905013.

[82] SINDRUM Collaboration, U. Bellgardt et al., *Search for the Decay $\mu^+ \to e^+e^+e^-$*, Nucl. Phys. **B299** (1988) 1.

[83] BABAR Collaboration, B. Aubert et al., *Search for lepton flavor violation in the decay $\tau^\pm \to e^\pm\gamma$*, Phys. Rev. Lett. **96** (2006) 041801, arXiv:hep-ex/0508012.

[84] BELLE Collaboration, K. Hayasaka et al., *New search for $\tau \to \mu\gamma$ and $\tau \to e\gamma$ decays at Belle*, Phys. Lett. **B666** (2008) 16–22, arXiv:0705.0650 [hep-ex].

[85] BELLE Collaboration, Y. Miyazaki et al., *Search for Lepton Flavor Violating τ Decays into Three Leptons*, Phys. Lett. **B660** (2008) 154–160, arXiv:0711.2189 [hep-ex].

[86] BABAR Collaboration, B. Aubert et al., *Improved limits on the lepton-flavor violating decays $\tau^- \to \ell^-\ell^+\ell^-$*, Phys. Rev. Lett. **99** (2007) 251803, arXiv:0708.3650 [hep-ex].

[87] M. Giffels, *Study of the sensitivity of CMS to the lepton flavour violating neutrinoless tau decay $\tau \to \mu\mu\mu$.* PhD thesis, Rheinisch-Westfälische Technische Hochschule, Aachen, 2009.

[88] T. Sjostrand et al., *PYTHIA 6.4 physics and manual*, JHEP **05** (2006) 026, arXiv:hep-ph/0603175.

[89] M. Giffels et al., *The lepton-flavour violating decay $\tau \to \mu\mu\bar{\mu}$ at the LHC*, Phys. Rev. **D77** (2008) 073010, arXiv:0802.0049 [hep-ph].

[90] J. Pumplin et al., *New Generation of Parton Distributions with Uncertainties from Global QCD Analysis*, JHEP **07** (2002) no. hep-ph/0201195. MSU-HEP-2001-11-01, 012. 44 p.

[91] S. Asai et al., *Cross sections for Standard Model processes to be used in the ATLAS CSC notes*, ATL-PHYS-INT-2009-003, CERN, Geneva, May 2008.

[92] K. Melnikov, *W Boson Production Cross Section at the Large Hadron Collider with $O(\alpha_s^2)$ Corrections*, Phys. Rev. Lett. **96** (2006) no. 23, 231803.

[93] T. Lagouri et al., *A Muon Identification and Combined Reconstruction Procedure for the ATLAS Detector at the LHC at CERN*, . revised version number 1 submitted on 2003-10-30 18:34:15.

[94] P. Billoir and S. Qian, *Fast vertex fitting with a local parametrization of tracks*, Nucl. Instrum. Methods Phys. Res., A **311** (1992) no. 1-2, 139–150.

[95] N. Konstantinidis et al., *The Atlantis event visualisation program for the ATLAS experiment*, .

[96] J. Smith et al., *Transverse Mass and Width of the W Boson*, Phys. Rev. Lett. **50** (1983) no. 22, 1738–1740.

[97] W. Rolke et al., *Limits and confidence intervals in the presence of nuisance parameters*, Nucl. Instrum. Methods Phys. Res., A **551** (2005) no. 2-3, 493–503.

[98] J. Lundberg et al., *Limits, discovery and cut optimization for a Poisson process with uncertainty in background and signal efficiency: TRolke 2.0*, Computer Physics Communications **181** (2010) no. 3, 683–686.

[99] R. Brun and F. Rademakers, *ROOT – An object oriented data analysis framework*, Nucl. Instrum. Methods Phys. Res., A **389** (1997) no. 1-2, 81–86.